SISSA   **ISAS**

SCUOLA INTERNAZIONALE SUPERIORE DI STUDI AVANZATI

INTERNATIONAL SCHOOL FOR ADVANCED STUDIES

The extragalactic sources at mm wavelengths and their role as CMB foregrounds

Thesis submitted for the degree of
Doctor Philosophiæ

CANDIDATE:
 Marcella Massardi

SUPERVISORS:
 Prof. Gianfranco De Zotti
 Prof. Ronald D. Ekers
 Prof. Luigi Danese

October 2008

Table of Contents

List of Figures

List of Tables

Published and submitted papers

The work presented in this thesis has been published (or submitted for publication) in the following scientific papers:

- "Radio source contamination of the Sunyaev-Zel'dovich effect in galaxy clusters",
  M. Massardi, G. De Zotti.
  Published in "Astronomy and Astrophysics", 2004, 424, 409

- "Realistic point source maps at Planck frequencies",
  M. Massardi, J. González-Nuevo, G. De Zotti.
  Proceedings of "CMB and Physics of the Early Universe" (CMB2006). 20-22 April 2006, Ischia, Italy.

- "Non–blind Catalog of Extragalactic Point Sources from the Wilkinson Microwave Anisotropy Probe (WMAP) First 3 Year Survey Data",
  M. López-Caniego, J. González-Nuevo, D. Herranz, M. Massardi, J. L. Sanz, G. De Zotti, L. Toffolatti, F. Argüeso.
  Published in "Astrophysical Journal Series", 2007, 170, 108

- "Observability of the virialization phase of spheroidal galaxies with radio arrays",
  M. Massardi, A. Lapi, G. De Zotti, R. D. Ekers, L. Danese.
  Published in "Monthly Notices of the Royal Astronomical Society", 2008, 384, 701

- "Statistical properties of extragalactic sources in the NEWPS Catalogues",
  J. González-Nuevo, M. Massardi, F. Argüeso, D. Herranz, L. Toffolatti, J. L. Sanz, M. López-Caniego, G. De Zotti.
  Published in "Monthly Notices of the Royal Astronomical Society", 2008, 384, 711.

- "The Australia Telescope 20 GHz Survey: The Bright Source Sample",
  M. Massardi and the AT20G group.
  Published in "Monthly Notices of the Royal Astronomical Society" 2008, 384, 775.

- "Blind and non-blind source detection in WMAP 5-year maps",
  M. Massardi, M. López-Caniego, J. González-Nuevo, D. Herranz, G. De Zotti, J. L. Sanz.
  Accepted for publication in "Monthly Notices of the Royal Astronomical Society".

- "Component separation methods for the Planck mission",
  S. Leach and part of the Working Group 2 of the Planck Consortium.
  Accepted for publication in "Astronomy and Astrophysics".

- "Imaging and polarimetry for the Biggest and Brightest sources in the Australia Telescope 20 GHz Survey",
  S. Burke and the AT20G group.
  Submitted for publication in "Monthly Notices of the Royal Astronomical Society".

Ai miei genitori
e a Paolo.

"Vino e musica rallegrano il cuore,
ma piú ancora lo rallegra l'amore della sapienza."
(Siracide, 40,20)

Introduction

The frequency range between 10 and 100 GHz (i.e. $30 \gtrsim \lambda \gtrsim 3$ mm), contains continuum signals of interest both for astrophysical and cosmological studies. The black body spectrum of the Cosmic Microwave Background (CMB), the relic radiation of the initial hot stages of the Universe, reaches its maximum close to this spectral range: for a CMB temperature of ~ 2.725 K (Mather et al. 1999) the black-body spectrum peaks at $\nu = 2.822kT/h \simeq 160$ GHz$\simeq 1.87$ mm. CMB observations confirmed the Big Bang scenario beyond any doubt, and the analysis of its angular power spectrum provides unique information about the properties and the evolution of the Universe and of the structures within it.

However, astrophysical continuum signals along our line of sight towards the CMB modify (like in the case of the Sunyaev-Zel'dovich effect) or contaminate (like the signals from the Milky Way or from other galaxies) the CMB signal, complicating the full exploitation of the CMB maps. The combined contamination from foregrounds reaches a minimum in the millimetric wavelength band, where the signal from the CMB is strong: for this reason the 10-100 GHz band is the most interesting spectral region for cosmological studies and is often called the 'cosmological window'. So, characterizing the foreground properties in the same observational frequency range of CMB observations, in addition to being of interest *per sé*, is of crucial importance to fully exploit the data collected by CMB-targeted missions.

The foreground minimum corresponds to the transition between the frequency region where radio (synchrotron and free-free) emissions dominate and the region where thermal dust emission takes over. In the case of extragalactic sources the dominant population shifts from radio sources to dusty galaxies. Note that extragalactic sources dominate the angular power spectrum of foreground emission on scales < 30 arcmin.

The inverse Compton scattering by hot electrons in ionized clouds modifies the CMB photon spectrum. The CMB spectral distortion along the line of sight of the clouds is well-known as the Sunyaev-Zel'dovich (SZ) effect (Sunyaev & Zel'dovich 1972, 1980, 1981; Birkinshaw 1999; Carlstrom et al. 2002). The so-called 'thermal' SZ effect appears as a decrement of the CMB brightness temperature at $\nu < 217$ GHz and as an excess at higher frequencies. If a ionized cloud is moving along the line of sight, the Doppler effect produces the kinetic Sunyaev-Zel'dovich effect. The thermal Sunyaev-Zel'dovich effect has been observed in galaxy clusters, but hot and dense gas clouds, according to standard models, are present also in the early stages of galaxy formation, and could generate potentially detectable SZ signals. Since the amplitude of the signal along the line of sight does not depend on the redshift of the cloud but only on its properties (density, size, peculiar velocity and

temperature) the SZ could give interesting information on the high redshift Universe and on structure evolution.

Observations with high sensitivity and resolution in this spectral region are a technological challenge, that is still not completely resolved.

- Shorter wavelengths require higher surface accuracy for the antenna. The surface accuracy, in fact, determines the upper limit of the wavelength range in which the antenna could be used because the phase error of a reflector with surface error ϵ is $4\pi\epsilon/\lambda$. A rms surface error of $\epsilon = \lambda/20$ corresponds to a surface efficiency $\eta_{surf} = e^{-(4\pi\epsilon/\lambda)^2} = 0.67$; to achieve it at 1 mm a surface error of 50 μm is required.

- The field of view of an antenna of size D is proportional to λ/D, i.e. it is smaller for higher frequencies. Because of this, high frequency surveys of radio sources are very time-consuming. For telescopes with diffraction limited fields of view, the number of pointings necessary to cover a given area scales as ν^2. For a given receiver noise, the time per pointing to reach the flux density level $S \propto \sigma_{\text{image}}$ scales as S^{-2}, so that, for a typical optically thin synchrotron spectrum ($S \propto \nu^{-0.7}$), the survey time scales as $\nu^{+3.4}$: a 20 GHz survey of synchrotron emitting sources takes more than 110 times longer than a 5 GHz survey with the same aperture covering the same area of sky to the same flux density level. This is the main reason why only few large area surveys of extragalactic radio sources exist at frequencies above 5 GHz.

- In the millimetric band the noise from the atmosphere becomes critical. The noise for a radiometer is expressed by the formula

$$\sigma = \frac{2T_{\text{sys}}}{A\eta\sqrt{\Delta\nu t}} \tag{0.1}$$

where T_{sys} is the so-called system temperature, A is the dish area, η is the efficiency of the system (antenna and receiver) $\Delta\nu$ is the bandwidth and t is the integration time (i.e. the time on source). The system temperature is a combination of the temperature of the source, of radiation from the atmosphere and the ground, and of noise from the device chain itself. Strong absorption lines from molecular oxygen block observations from the ground at $\sim$5 mm, but water vapour emission is the principal component of atmospheric emission and strongly contributes to dramatic rise of the T_{sys} with frequency. For this reason high and dry locations are strongly favoured for submillimeter telescopes. Interferometric observations may reach higher sensitivity than single dish observations thanks to the fact that correlation of the signals from the antennas can distinguish the signal over the noise, so that long integrations are possible without being limited by systematic errors. However, atmospheric turbulence may produce phase decorrelation and even small clouds are enough to decorrelate short wavelength signals.

- The synthesized beam size in an interferometer is proportional to λ/b where b is the maximum distance between the antennas, so for a given antenna configuration it is typically smaller at higher frequencies. The sensitivity of an observation of an object more extended than the beam size decreases with decreasing beam, because the

object is being resolved and there is less contribution to the flux density on the longer baselines. On the other hand, if short baselines are missing in the array configuration, the signal from the larger angular scales is lost. Interferometers are, in fact, usually well suited to pointlike objects and require careful set-up to deal with extended objects, expecially at high frequencies (selection of the array configuration, exploitation of mosaicking techniques...).

So, in summary, ground-based observations at mm wavelengths are strongly limited by atmospheric contamination. The problem could be partially overcome with interferometric observations. But, on the other hand, observing with interferometers requires a careful selection of the correct configuration of the antenna array to correctly measure flux densities on the source angular scales and obtain images of the objects. The small beam size at millimetric wavelengths makes large-area deep surveys extremely time-consuming. Satellite observations, that are crucial to investigate the CMB on all the angular scales, suffer limitations in resolution and sensitivity due to the small size of the antennas and the close packing of the receivers.

This thesis presents observational and theoretical/modelling work aimed at improving the characterisation of the extragalactic source populations in the millimetric band. A major part of the work consisted of participation in the Australia Telescope 20 GHz (AT20G) survey, the first multisteradian blind survey at frequencies above 5 GHz covering the whole Southern sky. It has been made possible by the fast scanning speed of the Australia Telescope Compact Array (ATCA[1]) and by the 8 GHz frequency bandwidth of a prototype analogue correlator. Thanks to follow-ups at 4.8, 8.6 and 20 GHz of the objects detected during the blind scans, we have investigated the spectral properties of a large sample ($\gtrsim$ 4800 sources) complete down to $\lesssim$80 mJy. During this thesis work we had the opportunity for substantial contributions to the observations and to the data reduction and analysis for the whole sample.

The exploitation of the extraordinarily rich information content of the AT20G data followed two routes: the investigation of a) the high frequency properties of extragalactic radio sources, and b) its potential to help cleaning the CMB maps, particularly those that will be provided by the Planck mission. There are indeed several obvious synergies between the AT20G survey and CMB experiments. As already mentioned, extragalactic sources are the main contaminant of CMB maps on scales < 30 arcmin. They must therefore be accurately subtracted to avoid biases in the estimate of cosmological parameters. The AT20G survey is, at present, the best suited survey for these purposes.

Also, the complex and poorly known statistical properties of the fluctuation field at the relatively poor angular resolution of CMB experiments strongly complicates the extraction of extragalactic sources from CMB maps and the assessment of the reliability and of the accuracy of flux estimates of candidate detections. We have investigated these issues on WMAP maps using the AT20G data as a benchmark.

In the framework of the Planck consortium we have contributed to the simulation of the radio source components for the so called Planck Sky Model (PSM), an all-sky simulation of the astrophysical and cosmological signals at all the Planck channels. Our

---

[1]www.narrabri.atnf.csiro.au

contribution included a simulation of the contamination of the SZ effect due to radio sources in clusters.

In addition to the study of extragalactic radio sources, we have devoted a substantial observational and modelling effort to the SZ effect. We have analyzed the possibility of detailed imaging of this signal in galaxy clusters from ground-based telescopes carrying out some observations of the galaxy cluster Cl J0152-1357 with the ATCA. Observing the SZ with a millimeter telescope can be challenging, even without considering any contamination, because of the faintness of the signal, distributed over the cluster region. Usually the SZ observations are combined with observations in other spectral bands to disentangle the information on temperature and density of the IntraCluster Medium (ICM). We have developed a simulator capable of reproducing the observations performed with any ground-based array of antennas. This helps both the planning of the observations and the interpretation of the results.

On the theoretical/modelling side, we have also analyzed the case of galaxy-scale SZ effects that should be produced in the early stages of galaxy formation when, according to current models, haloes of primordial gas virialize: we found that, despite the small angular scale, the produced SZ signal can be detectable by some next-generation radiotelescopes. Such detections could constrain the galaxy formation models and shed light on the earlier stages of galaxy evolution, unobservable in any other way.

The thesis is divided into three main parts. In the first part we have discussed the characterization of the radio source emission in the high radio frequency band. The second part has been devoted to investigating the Sunyaev-Zel'dovich effect focussing on its observability and on theoretical predictions for proto-galaxies. Finally, in the third part we have dealt with radio sources as a CMB foreground, with special reference to the Planck mission.

Part 1

Extragalactic radio sources

1 1   Radio Galaxies and QSO

The main emission mechanism in the radio band in extragalactic radio sources is synchrotron emission from relativistic electrons spiraling around magnetic fields in the source.

Throughout this thesis we will describe the spectral behaviour of these objects in the frequency range between ν_1 and ν_2 via the spectral index $\alpha_{\nu_1}^{\nu_2}$, adopting the convention that defines it as

$$\alpha_{\nu_1}^{\nu_2} = -\frac{\log(S_{\nu_1}/S_{\nu_2})}{\log(\nu_1/\nu_2)} \tag{1.1}$$

so that the flux density at frequency ν_x is $S_{\nu_x} \propto \nu_x^{-\alpha}$. Typically, sources with $\alpha_{\nu_1}^{\nu_2} < 0.5$ are referred to as 'flat' spectrum sources and those with $\alpha_{\nu_1}^{\nu_2} > 0.5$ as 'steep' spectrum sources. Objects with negative values for $\alpha_{\nu_1}^{\nu_2}$ are classified as 'inverted' spectrum objects. The observed spectra of radio sources frequently depart from simple power laws with fixed α.

In the millimetric band, most of the radio sources that dominate the low frequency source counts fade away. That is because the synchrotron spectrum is typically steep ($\alpha_{\nu_1}^{\nu_2} \sim 0.75$) at higher frequencies and electron energy losses enhance the steepening. In fact, the higher the energy of an electron, the less time it takes to radiate a given fraction of that energy (electron ageing), so that, since high frequency synchrotron emission is dominated by the high energy electrons, the spectrum is steepened at higher frequencies. Conversely, very young radio sources may have flatter than average radio spectra.

Another potential cause of spectral bending is opacity: as the optical depth rises, the source spectra bend. The result is a peak in the SED at roughly the frequency where the optical depth reaches unity. The frequency at which the spectral peak occurs depends on both the physical parameters of the emitting/absorbing region and its age; younger, more compact sources display this spectral turnover at higher frequencies (gigahertz peaked spectrum, GPS sources; Stanghellini et al. 1996).

Some compact sources can also show variability down to very short timescales. Synchrotron radiation is intrinsically highly polarized. Yet most radio sources observed at MHz or GHz frequencies are not. The lack of strong polarization may be due to random

alignment of the magnetic fields in the source or to Faraday depolarization of the emergent radiation (generally small in the millimetric band).

The so-called unified model of radio sources permits us to explain a wide variety of extragalactic discrete sources with a common scheme: an active galactic nucleus (AGN) with a black hole, an accretion disk around it, and axial jets (Urry & Padovani 1995). Many apparent differences between quasars, double-lobed radio sources, and other classes of radio sources are then determined by the orientation of the line of sight to the jet axis.

However, orientation to the line of sight cannot explain all the apparent differences between classes of radio sources and all the differences in the spectral behaviour. Other relativistic and hydrodynamic mechanisms should be invoked to describe the complexity of structures and emissions observed in these objects. In such a scenario, it is pretty clear that a net classification of the sources is almost impossible: classifying radio sources on the basis of their spectral properties is only a didactic exercise, useful to attempt a characterisation of the populations.

Trivially, flat- and inverted-spectrum sources (like Blazars or Gigahertz Peaked Spectrum sources) become more easily observable than steep-spectrum objects at high frequencies. As extensively discussed by many authors (Toffolatti et al. 1999, De Zotti et al. 1999, Bennett et al. 2003, Henkel & Partridge 2005), flat-spectrum AGNs and QSOs are expected to be the dominant source population in the range 30-100 GHz, whereas other classes of sources, and in particular the steep-spectrum sources, that dominate at low frequencies, are only giving minor contributions to the number counts at bright flux levels at higher frequencies.

In galaxies with active star formation, at wavelengths shorter than few millimeters, dust emission overwhelms the radio synchrotron emission, rising with spectral index $\alpha \simeq -3.5$. Dust emission becomes the most important signal in the far-IR band.

In this thesis we will focus more on the properties of the radio sources than on those of dusty objects in the millimetric wave band, even with the caveat that, at the upper frequency edge of the band, blind surveys should detect a combination of the two populations.

1 2   Observing and detecting radio sources at high radio frequencies

Important advances in the knowledge of the high radio frequency population were made recently thanks to the 15 GHz surveys with the Ryle telescope (Taylor et al. 2001; Waldram et al. 2003, 2007) covering $520 \, \mathrm{deg}^2$ to a flux density limit of 25 mJy and going down to 10 mJy in small areas. An all-sky compilation of 8.4 GHz observations for flat-spectrum radio sources identified in low frequency catalogues has been collected in the CRATES catalogue (Healey et al. 2007).

As a by-product of its temperature and polarization maps of the Cosmic Microwave Background (CMB), the Wilkinson Microwave Anisotropy Probe (WMAP) mission has yielded the first all-sky surveys of extragalactic sources at 23, 33, 41, 61 and 94 GHz (Bennett et al. 2003; Hinshaw et al. 2007), by blindly identifying sources in the maps. From the analysis of the first three years survey data the WMAP team has obtained a

catalogue of 323 extragalactic point sources, substantially enlarging the first-year one that included 208 extragalactic point sources detected above a flux limit of $\sim$ 0.8-1 Jy. Recently, 390 sources have been found in the 5-year data maps (Wright et al. 2008), down to a completeness limit of $\sim$ 1 Jy, but there is still little information in the flux densities range between 200 mJy and 1 Jy.

During this thesis we have participated in the AT20G collaboration. By exploiting the 8 GHz bandwidth of an analogue correlator connected to the ATCA it became possible to blindly survey the whole Southern sky at 20 GHz down to 50 mJy flux limit. A Pilot Survey (Ricci et al. 2004; Sadler et al. 2006) at 18.5 GHz was carried out in 2002 and 2003 with the ATCA. It detected 173 objects in the declination range $-60°$ to $-70°$ down to 100 mJy flux density limit. The Pilot project characterised the high-frequency radio source population and allowed us to optimise the observational techniques for the full Australia Telescope 20 GHz (AT20G) Survey. The full survey covers the whole Southern sky to a flux density limit of $\simeq$ 50 mJy: it began in 2004 and was completed in 2007, detecting more than 4800 sources. During the survey epoch we have been observing, reducing and analyzing the data for the blind survey at 20 GHz and the follow-ups for the detected sources at 20, 4.8 and 8.6 GHz. That produced an unprecedented set of data in total intensity and polarisation for a statistically significant sample of sources up to 20 GHz. In section 1 3 we will show the details of the blind scans and the results obtained for the 320 brightest ($S_{20GHz} > 0.50$ Jy) objects with declination below $-15°$ that constitute the Bright Source Sample (BSS).

In parallel, the NEWPS collaboration has developed a set of detection tools that could be used to exploit the WMAP data. A first non-blind detection exercise has been performed by selecting as targets the positions of the brightest sources ($S_{4.85GHz} > 500$ mJy) in the PMN and GB6 catalogues, complemented, in the regions uncovered by these surveys, with the positions of the brightest ($S_{\sim 1GHz} > 500$ mJy) objects in the NVSS and SUMSS. That produced the first version of the New Extragalactic WMAP Point Source catalogue (López-Caniego et al. 2007, González-Nuevo et al. 2008). Then blind and non-blind detections have been performed in the region of the AT20G BSS on the WMAP 5-year maps: the BSS was the benchmark to test the efficiency of the techniques and establish a detection procedure that, applied to the whole sky has produced the new version of the catalogue, the NEWPS_5yr. The analysis of the detection surveys on WMAP maps will be discussed in section 1 4

1 3   The Australia Telescope 20 GHz Survey

1 3.1   Observational techniques

1 3.1.1   Survey mode

The first phase of the observations is to make a set of blind scans. For an interferometric array the noise level in an image, in analogy with eq. 0.1, is given by

$$\sigma_{\text{image}} = \frac{k_B T_{\text{sys}}}{A\eta} \sqrt{\frac{2}{t \ N_{\text{base}} \Delta\nu \ n_{\text{pol}}}} \tag{1.2}$$
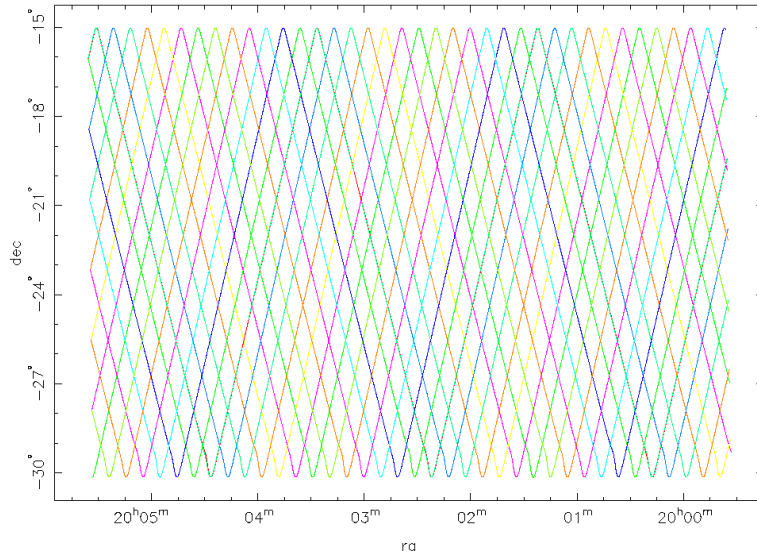
Figure 1 1 Plot of the scanning path for a declination region in a small hour angle bin. Different colors in this plot correspond to observations made on different days.

where N_{base} is the number of baselines, $\Delta\nu$ is the bandwidth and n_{pol} is the number of polarizations. Among the possible ways to improve the sensitivity (e.g. increasing the time on-source, using multi-beams focal planes, increasing the number of detecting antennas, using larger dishes, improving the receiver efficiency, increasing the bandwidth) we had the opportunity to increase the bandwidth of the Australia Telescope Compact Array (ATCA), by connecting it to an 8 GHz bandwidth wideband analogue correlator originally developed as part of a collaboration for the Taiwanese CMB experiment AMiBA (Lo et al. 2001) and now applied to 3 of the six 22 m dishes of the ATCA. We have also exploited the ATCA fast scanning capabilities (15 degrees min^{-1} in declination at the meridian). The lag-correlator measures 16 visibilities as a function of the differential delay for each of the three antenna pairs used. This wideband analogue correlator has no mechanism to allow for geometrical delay as a function of the position in the sky, so the scan has to be performed along the meridian corresponding to zero delay for the EW configuration used. There is no fringe stopping.

The scanning strategy consists in sweeping sky regions $10°$ or $15°$ wide in declination, using a whole Earth rotation to cover all the right ascensions in a zig-zag pattern. Each declination strip requires several days to be completely covered by moving the scanning path half a beam apart from day to day (see fig. 1 1). Along the scan, a sample is collected every 54 ms (3 samples per beam), enough to reach a rms noise of 12 mJy for each pointing. With this exceptional continuum sensitivity, along with precise and high speed telescope scanning capability, we can scan large areas of the sky, despite the small (~ 2.4 arcmin) field of view at 20 GHz. Scans with bad weather or occasional equipment error have been repeated, so that the sky coverage is 100 per cent at high flux levels. The separation of the tracks by a single beam width meant that each point on the sky falls within the FWHM of the primary beam of the telescope. Sky locations on the interior of

the scan region are covered twice each by this scanning strategy, once in a northward track and once in a (different) southward track. Towards the boundaries of the declination band the coverage becomes degraded and points are either covered only once, at the extreme edges, or twice with the same track.

Some regions (especially those close to the boundaries of the declination strips) suffer a higher noise level due to the change of velocity during the scanning path, so that the flux limit of real detections is higher. Some regions have been scanned more than average, so in these cases sensitivity is higher.

A primary calibrator was observed before each declination band is observed. This observation was a 'tracking' observation where the telescopes tracked the source individually, whilst the correlator remained phased for the meridian. This allowed for the mapping of the antenna and correlator response pattern (delay beam). Before and after each of the scans were observed (i.e. every 24 hours), a secondary calibrator was measured in a 'transit' observation. The telescopes and correlator were both fixed to the meridian as the calibrator passed by. This measurement provided a day-by-day measurement of the system response.

Candidate sources are identified by looking for the telescope response pattern within the delay channels in the time ordered data, correlated between the baselines. The correlator outputs for each set of 24-hour observations were interleaved and calibrated to produce maps. The overall rms noise in the maps reaches $\simeq 10$ mJy. Note that the overall rms noise is smaller than the noise for each pointing because it is the result of the average over the map of the combination of the scans. The candidate selection is then refined in the map.

All the sources detected in the scans that have known flux densities and positions (about 10 for each scan) are then used in a bootstrap process to refine the scan calibration. From this we produced an initial list of positions and flux densities for candidate sources brighter than 5σ (about 50 mJy). However, this detection is not enough to define a reliable catalogue with good estimations of flux densities.

Fainter sources, in fact, closer to the noise limit often have large positional uncertainties and the number of false detections at low flux limits is quite large. Detecting sources in the time ordered data only produces an overall candidate source to confirmed source detection rate as low as 30 per cent. Detections in maps improve this situation, but false detections are still possible, especially at the low flux density limits. Strong sources were also contributing to this low detection rate as, even though the source is easily identifiable, sidelobes of these sources appear at a level similar to the fainter sources, and thus introduce extra false sources. Filtering out the sidelobe detection of strong sources proved to be difficult. A strong source away from the primary beam center can produce a sidelobe nearer to the beam center that appears stronger than the source at the true position. However, many real sources have been observed at their sidelobe position and require additional observations to obtain accurate flux density and position measurements: for this reason the candidates have been followed-up at 20 GHz.

It was also possible to create a map of the sky that collects the properties of the observations: we estimate that at a flux level of ∼50 mJy 90 per cent of real sources are present in the map. The presence of a source within the survey map does not guarantee that it will be observed in the follow-up observations. The number of false sources that

Table 1 1 Follow-up observations to confirm candidate sources at 20 GHz (flagged as *C*), to observe them at 5 and 8 GHz (*O*) or to repeat previous bad quality observations (*R*). (*M*) refers to the observation run in which we observed the very extended sources in mosaic mode.

Epoch ref.	Declination range	Central Frequencies(MHz)	Array Configuration (shortest spacing [m])	Beamsize [arcsec]	Dates	Reason
1	$-50°, -30°$	18752, 21056	H214 (80)	10.7×10.7	21 Oct - 27 Oct 2004	C
1	$-50°, -30°$	4800, 8640	1.5C (77)	$8.3 \times 12.8\ 4.6 \times 7.13$	04 Nov - 08 Nov 2004	O
2	$-90°, -50°$	18752, 21056	H168 (61)	13.9×13.9	27 Oct - 31 Oct 2005	C
2	$-90°, -50°$	4800, 8640	1.5C (77)	$8.3 \times 8.8\ 4.6 \times 4.9$	12 Nov - 15 Nov 2005	O
3	$-90°, -30°$	18752, 21056	H214 (80)		29 Apr - 03 May 2006	R
3	$-90°, -30°$	4800, 8640	1.5D (107)		19 Jun - 23 Jun 2006	R,O
4	$-30°, -15°$	18752, 21056	H214 (80)	2.0×5.1	14 Oct - 17 Oct 2006	C
4	$-30°, -15°$	4800, 8640	1.5B (30)	$8.3 \times 21.1\ 4.6 \times 11.7$	09 Nov - 12 Nov 2006	O
5	$-90°, -15°$	18752, 21056	H214 (80)		11 May - 16 May 2007	R
5	$-90°, -15°$	4800, 8640	1.5C (80)		04 May - 10 May 2007	R,O
6	$-90°, -30°$	16704, 19392	H75 (31)	35.3×35.3	01 Oct 2006	M
7	$-15°, 0°$	18752, 21056	H214 (80)		26 Oct - 30 Oct 2007	C

were found by the source detection program meant that although we could obtain quite a complete sample down to $\sim$50 mJy at 20 GHz for the whole Southern sky, the amount of follow-up time to achieve the same limit is prohibitive. The time allocated for the follow-up was not enough to observe all the candidates so that it was decided to observe the stronger sources first, and then the fainter ones.

1 3.1.2 Follow-up mode

Most of the candidate sources selected in the first phase have been re-observed to confirm that they are genuine sources and to get accurate positions, flux densities, and polarisation information. Note that this procedure will exclude any fast (within few weeks) transient sources, if they exist. The follow-up has been performed with an hybrid array configuration (i.e., with some of the baselines on the NS direction) with the normal ATCA digital correlator with two 128 MHz bands centered at 18752 MHz and 21056 MHz and two polarisations. The combination of the two close bands could be considered as a single 256 MHz wide band centered at 19904 MHz, which is the reference frequency for our '20 GHz' observations.

The follow-up observations exploit the fast mosaic capabilities of the ATCA to reduce the slewing time between pointings. In our observing strategy each mosaic point is a pointing on a candidate source. The same source has to be observed more than once to improve the visibility plane coverage. The sources have been observed at least twice and in some cases up to 8 times at different hour angles. Up to 500 candidates could be followed-up in a day. A set of secondary calibrator sources are regularly observed between blocks of candidate sources. The follow-up is complete down to 100 mJy in the sky region with declination below $-15°$. The 20 GHz follow-up in the declination region between $-15°$ and

the equator has been partially degraded by bad weather, so that imaging has been possible only for sources below this declination range.

Within a couple of weeks, we observed the confirmed sources with an East-West extended array configuration with two 128 MHz bands centered at 4800 MHz and 8640 MHz to study their radio spectral properties. Those are the frequencies to which we will refer in the following as '5' and '8' GHz. In Table 1 1 we have summarized the array configurations used to observe sources or to replace previous bad quality data in the various sky regions. The simultaneity of observations at different frequencies is necessary to study the spectral properties of the sources, avoiding errors due to the source variability. The beam at 5 and 8 GHz in the $-15° < \delta < 0°$ is too elongated. For this reason we have decided not to follow-up this declination strip at lower frequency. The primary beam FWHM is 2.4, 5.5, and 9.9 arcmin at 20, 8, and 5 GHz, respectively.

We carried out observations dedicated to high sensitivity polarisation measurements in October 2006 with the ATCA on a sub-sample of the brightest observed sources, using the most compact configuration, H75 (Burke et al. submitted). This provided more accurate short-spacing measurements of flux densities at 20 GHz, imaging and integrated flux densities. Nine very extended sources have been selected from low frequency catalogues (PMN, Griffith et al. 1993, 1995, Wright et al. 1994, 1996, and SUMSS, Mauch et al. 2003, 2007) to be observed in mosaic mode to improve the flux density estimation at 20 GHz. The lack of mosaic observations at low frequencies for these objects does not allow us to use these data for spectral analysis.

1 3.2 Data reduction

1 3.2.1 The AT20G pipeline

We have developed a fully automated custom analysis pipeline to edit, calibrate, and reduce the data for all the follow-up observations (figure 1 2). This procedure has been developed to ensure consistent data quality in the final catalogued data. The software was built using the scripting language Python, and the underlying data reduction was done with the aperture synthesis reduction package Miriad (Sault et al. 1995).

After an initial manual inspection of the data to flag bad data, the pipeline generates the calibration solutions. Once source flux densities are calibrated, a set of processes is applied to determine positions, peak flux densities, extendedness, integrated flux densities, polarisation properties and to generate images. The final result is a list of confirmed (at more than 5σ confidence level) sources with all the available information and images for each epoch and for each frequency.

1 3.2.2 Data editing

An initial inspection of the correlator output is necessary in order to identify interferences or any problems in the data acquisition that may impair the data quality.

Weather conditions can seriously affect the quality of the data. Attenuation of the signal by atmospheric water vapour can decrease the sensitivity of the observations, and atmospheric turbulence can produce phase fluctuations that may produce visibility amplitude decorrelation. Data collected in periods of bad weather have to be removed. In
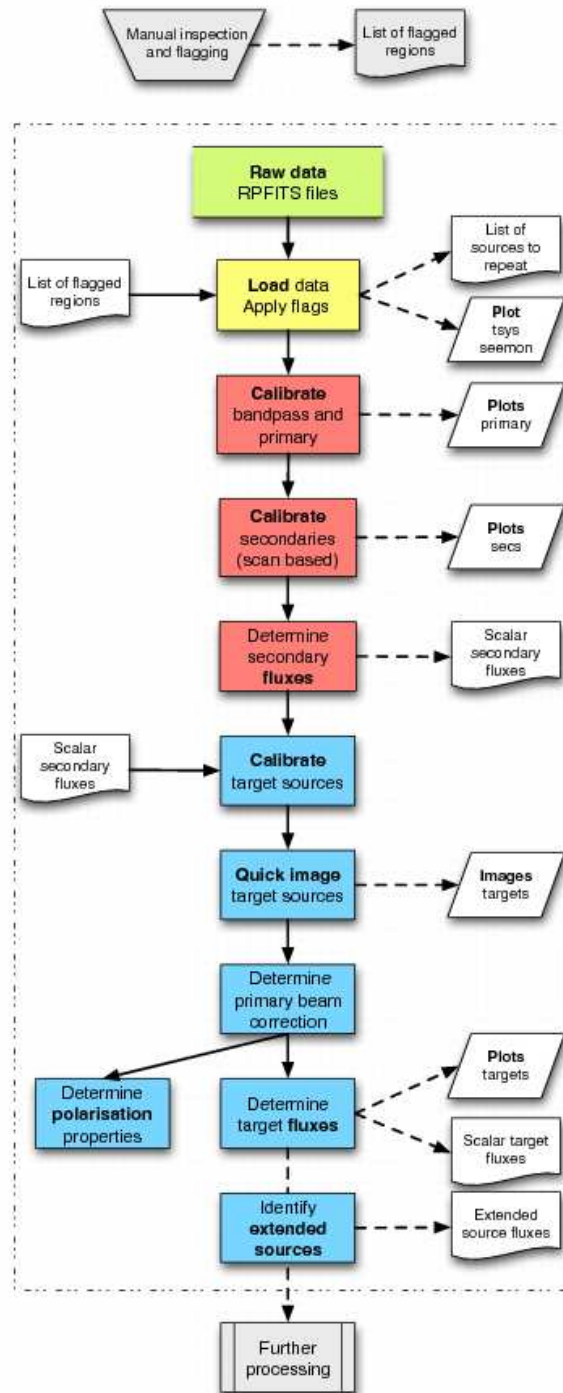
Figure 1 2 Diagram of the analysis pipeline process.

particular, calibrator data must be of high quality otherwise they introduce errors in the calibration solutions that affect the whole dataset (Thompson et al. 2001).

A seeing monitoring system is run at the ATCA site simultaneously with the main array. Two 40 cm dishes on a 240 m baseline monitor the differential phase variations in a geostationary satellite signal caused by tropospheric water vapour fluctuations. These fluctuations can be used to estimate the decorrelation in the interferometric data (Middelberg at al. 2006). In addition, the absorption due to atmospheric water vapour is estimated for each main antenna receiver by measuring the system temperature (T_{sys}) changes due to tropospheric emission. We used the seeing monitor data (to measure amplitude decorrelation) in conjunction with T_{sys} (to estimate tropospheric opacity) to develop semi-automatic flagging criteria. Specifically, we discarded data from all the periods in which there was decorrelation greater than 10 per cent. This improves the uniformity and data quality across all our observing epochs.

Flux densities of unresolved target sources suffering from significant decorrelation could still be recovered using triple product techniques, but imaging for these sources was not possible. Calibrators with significant decorrelation were excluded, and the blocks of target sources associated with those calibrator observations were also excluded. Very occasionally, bad weather required large blocks of data to be edited out and hence a small number of sources do not have near-simultaneous data at the lower frequencies (5 and 8 GHz).

1 3.2.3   Calibration

Primary flux calibration and bandpass calibration were carried out in the standard way using PKS B1934−63 as the primary and PKS B1921−293 as the bandpass calibrator.

For the secondary flux calibration we follow a non-standard procedure, which we describe here. Our follow-up observing schedule follows the pattern:

- a nearby secondary calibrator is observed for ~ 5 minutes

- a block of ~ 20 target sources are observed for ~ 40 seconds each

- the secondary calibrator is re-observed for ~ 5 minutes

This pattern is repeated throughout the observations. Hence we typically observed around ~ 50 secondary calibrators during one epoch of observations. To calculate an accurate flux density for each secondary calibrator we calculate the mean of the individual snapshot flux densities across the whole run excluding only a snapshot which has a flux density more than 2 standard deviations away from the mean. The rest of the snapshots are averaged to calculate the flux density for that secondary. Finally, each target source is calibrated using the secondary calibrator associated with its observing block. For each target source we calculate the position, flux density, primary beam corrections and Stokes parameters.

Full polarisation data (I, Q, U and V Stokes parameters) are determined for all of the target sources. These are calculated in the pipeline using a polarisation specific process. Firstly, a correction is applied for the time dependent phase difference (automatically monitored in real time at the telescope) between the orthogonal, linear antenna feeds (which are

referred to as x and y). After making this correction, a small residual xy-phase signal still remains. Because we have insufficient secondary calibrator data to accurately determine all the free parameters involved in instrumental polarisation corrections (e.g., leakages, residual xy-phase difference, and time-dependant gains), leakage terms were calculated using the primary calibrator, PKS B1934−638. The linear polarisation of this calibrator is known to be not variable and less than 0.2 per cent of the total source flux density at each of our observing frequencies. To determine the leakage terms, it was assumed to be unpolarised. We copied the leakage values to all the secondary calibrators, simultaneously calculating the time-dependent complex antenna gains, the residual xy phase differences, and the Q and U Stokes parameters of the calibrators. The polarisation calibration was then applied to the target sources.

1 3.2.4   Extended sources

If a source is extended more than several arcsec (depending on the array configuration) we will underestimate its total flux density using either the image peak or the triple correlation. We could use the shortest spacing or integrate the image over a larger area to recover the total flux density for an extended source, but this does not optimise the sensitivity for a point source. Hence we need an automatic procedure capable of distinguishing point-like sources from extended sources. To do this we exploited the properties of the observed phase closure, the vector combination of the phase of the correlated signal between each couple of antennas:

$$\Phi_{\rm cl} = \Phi_{1,2} + \Phi_{2,3} - \Phi_{1,3}. \tag{1.3}$$

The phase closure is null for a point source. It is also null for any flux density distribution that is an autocorrelation function such as a symmetrical Gaussian, but this is unlikely to occur for our sources.

In an array with more than three antennas the root mean square (rms) of the phase closure can be calculated for all the possible combinations of three antennas in the array. Analogously to the three antenna case, it is expected to be null for a point source: the phase closure rms is different from 0 if the source is extended or if there is more than one source in the beam area. Receiver noise will contribute to the phase closure errors but the phase closure rms does not depend on antenna based instrumental and atmospheric phase effects or on the position of the source in the field.

For each source we have compared the observed phase closure to the predicted phase closure due to receiver noise. This is determined by Monte Carlo simulations of our observations for point sources with receiver noise added. Then we have defined the *extendedness parameter* as the ratio of the predicted phase closure rms due to noise and the observed value. The discrimination between point-like and extended sources is for the extendedness parameter equal to 3, a good trade off, minimizing the wrong assignments to the two classes. An incorrect assignment will result in a flux density error of at most 20 per cent passing from one class to another. The largest errors are made for faint objects (well below 0.50 Jy).

With the 214 m array the threshold means that a source is extended if it has significant flux density (> 10 per cent) at 20 GHz on scales larger than 6 arcsec. The same

criterion could be applied to all the frequencies, but, in the following, we consider that a source is extended if its extendedness parameter is larger than 3 at 20 GHz. Although this method works pretty well down to low flux levels, it is not enough to correct for confusion due to faint sources especially at 5 GHz.

1 3.2.5 Source position

Source positions have been measured for the source centroid of the cleaned and restored images. Formal positional errors in right ascension and declination have been obtained by quadratically adding a calibration term (σ_{cal}) and a noise term (σ_{n}). We have statistically determined the calibration term by cross-matching 233 observations of the brightest objects in different epochs with the International Coordinate Reference Frame catalogue (ICRF, Ma et al. 1998). The VLBI-measured positions in the ICRF catalogue are accurate to $\leq 10^{-3}$ arcsec, so any discrepancy between the positions of our target sources and the ICRF positions can be attributed to positional errors in our sample. The rms positional error is 0.5 arcsec in right ascension and declination with small variations due to changing weather conditions. For the brightest objects the noise term is always negligible.

1 3.2.6 Flux density measurement

We have obtained the flux densities for bright point-like sources using the triple product method implemented in the Miriad task CALRED. The amplitude of triple product is the geometric average of the visibility amplitudes in a baseline closure triangle

$$A_{\mathrm{TP}} = \sqrt[3]{A_{1,2} \cdot A_{2,3} \cdot A_{3,1}} \tag{1.4}$$

and its phase is the phase closure (see eq. 1.3).

This way of measuring flux densities is particularly well suited for strong and point-like sources and it is able to recover the flux density lost in imaging because of phase decorrelation. We have derived formal flux density errors by adding quadratically a calibration term (gain error, σ_{gain}) and a noise term (σ_{n}). The gain error is a multiplicative term (i.e., it is proportional to the source flux density) and is a measure of the gain stability over time. We estimated σ_{gain} for each observational epoch and frequency from the scatter in the visibility amplitudes of the calibrators in each observing run. Such average values for the gain errors were found to be of the order of a few per cent. The noise term is an additive term strictly related to the interferometer noise which is proportional to the system temperature. Since no source has significant Stokes V, the rms noise levels in the V images have no gain error and are used as an estimate of the σ_{n} value for each target source.

For sources that have been defined as extended at 20 GHz, integrated flux densities at 5, 8 and 20 GHz have been estimated from the amplitude of the signal measured by the shortest baseline. Any source extended at 20 GHz is assumed to be extended at 5 and 8 GHz. Sources which are extended at 5 or 8 GHz but core-dominated at 20 GHz won't be considered as extended according to this procedure. In this case we are assuming a dominant point source and the flux densities at all the frequencies will be for the core and not the total source. The shortest baseline used in the follow-up (see Table 1 1) is 60 or 80 m so we still underestimate flux densities for sources larger than 20 arcsec. For extended

sources the error is increased by a factor equal to the square root of the number of baselines n_{base} (normally 10 for our 5-antenna follow-up arrays) to correct for the fact that the flux densities for these sources are estimated using only one (the shortest) baseline instead of n_{base}.

1 3.2.7   Polarisation

Images in Stokes U, Q and V are calculated for all the target sources using the calibration procedure described in § 1 3.2.3. Since no sources have detectable V at our sensitivity the V image is used to estimate the noise error. If a source is detected, P, the polarised flux, is calculated in the usual way $P = \sqrt{Q^2 + U^2}$ with no noise debias factor. For the intensity (I) we were able to avoid the effect of phase decorrelation by using the triple product but we don't have an equivalent measure for U and Q. However, the tropospheric phase decorrelation affects Stokes parameters Q and U in exactly the same way as Stokes I, so that we can use the triple product amplitude, I_{tp}, and the restored Stokes I image peak, I_{map}, to calculate the factor by which the flux density is reduced due to decorrelation $\chi = I_{\text{map}}/I_{tp}$. Then the corrected polarised flux is P/χ.

The error on P is $P_{\text{ERR}} = \sqrt{2}\sigma_V/\chi$, where σ_V is the noise error from the V image, i.e. assuming that both the errors on U and Q are equal to σ_V.

For the non-detections ($P < 3\sigma_V$) we calculate an upper limit on P setting U and Q to $3\sigma_V$ and calculating the value of P as above.

To avoid bias, P is always measured at the position of the peak in I for point sources. For extended sources we need to integrate the polarisation vectors over the source which is the same as the integrated value of U and Q. This has been done for the extended sources that have been observed in the mosaic mode, but at this time we have not determined the integrated polarisation for the slightly extended sources.

Unfortunately, an instrumental phase problem spoiled the phase measurements for May 2007 observations: for this epoch flux densities could be recovered with triple correlation techniques, but the polarisation information might be wrong, so it has been flagged.

1 3.3   The AT20G Bright Source Sample

From the confirmed sources observed in the period 2004-2007 we selected those with flux densities at 20 GHz above 0.50 Jy and Galactic latitude $|b| > 1.5°$ (the source tables are in the Appendix 1). At this flux density level, only PKS 0454-81 has been discarded because it hasn't passed the quality checks introduced in the pipeline of data reduction: its follow-up observations were seriously affected by bad weather, but the flux has been recovered by its observations as calibrator during the follow-ups. Some sources were observed at more than one epoch, in which case the flux density selection threshold has been applied to the measurements with the highest quality and the smallest primary beam correction. To minimize any selection bias caused by variability, sources were only included if they were above the threshold for the epochs with the highest quality observation. The final sample consists of 320 objects. The final distribution in coordinates, both equatorial
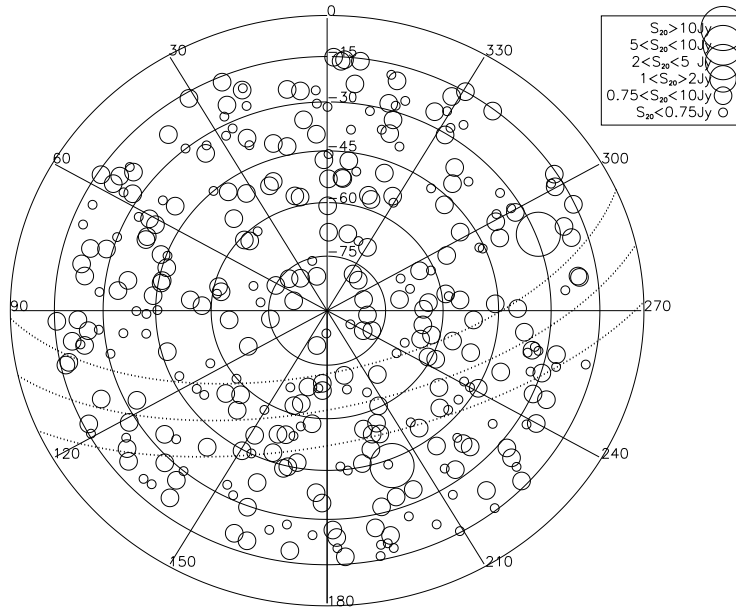
Figure 1 3 Equal area projection of the Southern sky in equatorial coordinates, showing the BSS sources. The symbols size of a symbol is a function of the flux density at 20 GHz, as in the inset. The dotted lines indicate the regions of Galactic latitude $b = \pm 10°$ and the Galactic plane.

and Galactic, is homogeneous (see fig. 1 3). The median errors in flux density estimation is 4.8 per cent at 20 GHz, and 2.5 and 1.5 per cent respectively at 8 and 5 GHz.

A small number of very extended sources are known to have 20 GHz flux density above our 0.50 Jy cut. These are discussed in § 1 3.3.2.

The differential source counts for the BSS (Fig. 1 4) are consistent with the 9C counts at 15 GHz (Waldram et al. 2003) and with the WMAP counts at 23 GHz (Hinshaw et al. 2007; López-Caniego et al. 2007), as well as with the predictions of the model by De Zotti et al. (2005). However, we must beware of resolution effects. The source detection technique is optimised for point-sources, and there is some bias against extended sources with angular sizes larger than about 30 arcsec. An outstanding case is Fornax A, one of the brightest sources in the Southern sky, which was missed by our survey because its compact nucleus (and any other compact component) is fainter than our blind scan detection limit (as was expected based on previous observations, e.g., Morganti et al. 1997) and its lobes are completely resolved by the 30-m baseline used for the blind scan.

By the same token, although no other bright source appears to have been completely missed by the AT20G Survey, the flux densities of the most extended objects may fall below our threshold because they are underestimated. To overcome this problem we have searched low-frequency catalogues for bright and extended sources, expected to have integrated 20 GHz flux densities above our 0.50 Jy threshold but missed by our selection (see § 1 3.3.2). For these sources we have made use of the information collected in mosaic mode during the October 2006 polarisation follow-up run (Burke et al., submitted).

Another source of uncertainty in the sample selection is variability, making sources
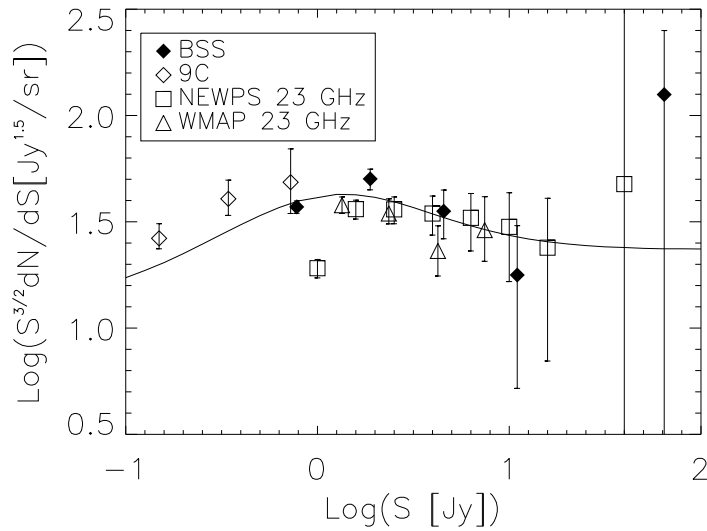
Figure 1 4 Differential source counts at 20 GHz, with their Poisson errors, normalised to Euclidean counts. The statistics are very poor above $\simeq 1$ Jy. The model by De Zotti et al. (2005) is also shown for comparison. Points from the 9C Survey (Waldram et al. 2003), and from the catalogues based on WMAP maps are also shown (WMAP, Hinshaw et al. 2007; NEWPS, López-Caniego et al. 2007).

move in or out of a given flux density bin, depending on the epoch of observations. Since we have been gathering flux density measurements made at different times we do not have a uniform view of the surveyed sky region. Only 30 BSS sources have more than one observation at 20 GHz in the 2002–2007 period (considering also the Pilot Survey observations), too small a sample for a meaningful analysis of variability for bright objects. However, Sadler et al. (2006) found, at 20 GHz and on timescales of a few years, a median debiased variability index, that takes into account the uncertainties in individual flux density measurements, of 6.9 per cent, uncorrelated with the flux density, with only a few sources more variable than 30 per cent. Also, a good fraction (201 sources corresponding to the 63 per cent of the sample) of our sources are ATCA calibrators and have therefore been observed repeatedly. Again, the variability turns out to be relatively modest. Since we selected the observation to which we applied the selection threshold on the basis of its quality and not on the basis of the flux density itself (i.e. the best observation is not necessarily that with the higher value of flux density) we minimize any bias towards higher flux density values that could affect the source counts.

1 3.3.1   Radio spectra

Figure 1 5 shows the so called colour-colour radio plot (Kesteven et al. 1977) for the BSS: it is the comparison of spectral indices at low and high frequencies. Only the almost simultaneous data have been used in this analysis: the sub-sample consists of 218 sources. The diagram shows the variety of spectral behaviours, with a relatively small
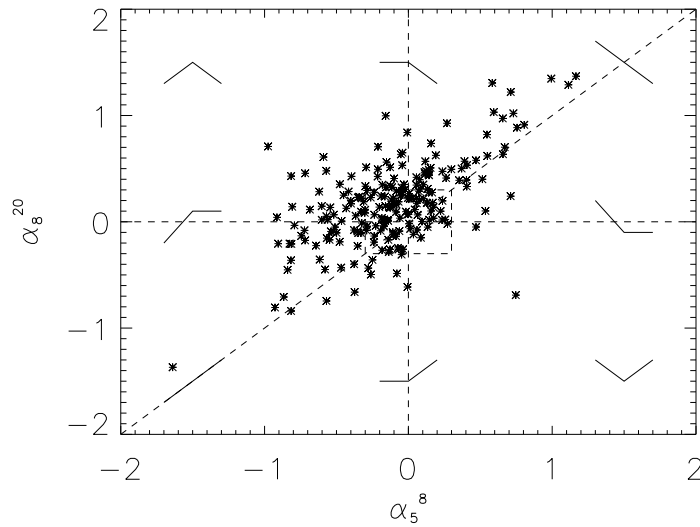
Figure 1 5 Colour-colour radio plot for the 218 BSS sources with near simultaneous observations: the comparison of the spectral behaviour in two ranges of frequencies shows the distribution of the spectral shapes in the whole sample. Power-law spectra sources lie on the dashed diagonal line. A general steepening of the spectra from low (5 to 8 GHz) to high (8 to 20 GHz) frequency is clearly shown by the large number of sources with $\alpha_8^{20} > \alpha_5^8$.

number of power-law spectra. Most of the points lie above the diagonal in Fig. 1 5, which implies that most sources steepen with increasing frequency[1]. The median of the difference of the spectral indices for the BSS is $\alpha_8^{20} - \alpha_5^8$ is 0.26 and the standard deviation of its distribution is 0.34 (see also Fig. 1 6). This implies that assuming a simple power law spectral index equal to α_5^8 to extrapolate from 8 to 20 GHz would result, on average, in a 27 per cent error in the flux density estimation. Thus, simple extrapolations in frequency using low-frequency spectral indices are highly unreliable.

The trend towards a steepening of spectral indices at higher frequencies is even clearer if we include low frequency data (see Fig. 1 7). The median spectral index between 1 and 5 GHz is -0.27 and increases to -0.11 between 5 and 8 GHz where the fraction of 'steep'-spectrum sources is $\simeq 8$ per cent. Between 8 and 20 GHz the median spectral index steepens to 0.16 and the fraction of 'steep'-spectrum sources almost doubles to $\simeq 15.5$ per cent. A similar behaviour has been reported by Bolton et al. (2004). It appears to be more significant at higher frequencies (cf. also González-Nuevo et al. 2008). An even larger steepening effect was found for a deeper ($S_{\text{lim, 20GHz}} > 150\,\text{mJy}$) selected sample of the AT20G Survey (Sadler et al. 2008).

In Table 1 2 we have classified the spectra on the basis of the spectral indices for the BSS between 5 and 8 GHz and between 8 and 20 GHz. Examples of spectra in total intensity and polarisation are plotted in Fig. 1 8, where the NVSS and SUMSS measurements at 1.4 and 0.843 GHz are also shown. Table 1 2 also gives the fractions of

---

[1]Remember that in our convention $S \propto \nu^{-\alpha}$
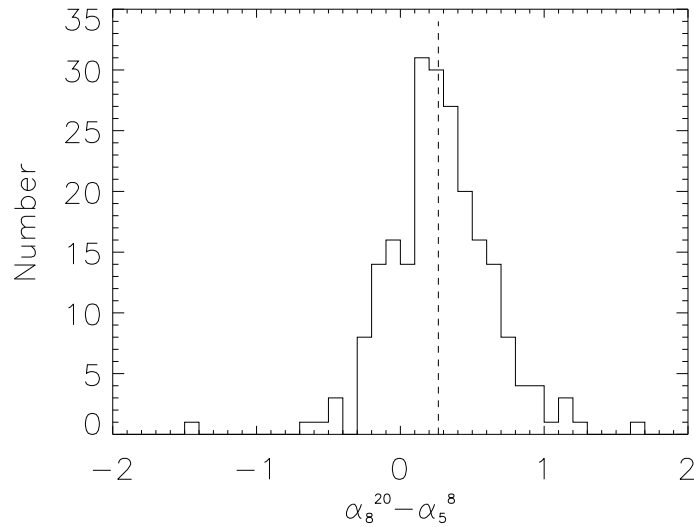
Figure 1 6 Distribution of the variation in spectral indices from the range 5-8 GHz to 8-20 GHz.

'steep'- and 'flat'-spectrum sources, based on the commonly used classification (spectral indices larger or smaller than 0.5). We have also defined a 'very' flat population of objects with both α_5^8 and α_8^{20} in the range $[-0.3, 0.3]$.

As expected, the 20 GHz BSS sample is dominated by flat-spectrum sources. The presence of spectral curvature provides valuable information about the physical conditions in a radio source. Two mechanisms which generate spectral curvature are the energy losses by synchrotron radiation causing steepening of the spectrum at high frequencies (e.g., Pacholczyk 1970) and effects due to the source structure in compact sources at lower frequencies which may be due to either free-free opacity or synchrotron self absorption. The clear evidence for spectral steepening of integrated flux density in the majority of the sources in the 20 GHz Bright Source Sample (Fig 1 5) and the increased spectral steepening observed at higher frequencies is in stark contrast to the lack of spectral steepening in the integrated flux density for radio sources in low frequency surveys (e.g. Laing and Peacock 1980). Spectral steepening in the resolved structure in radio source lobes is commonly seen and successfully modelled by a combination of energy losses and continual reacceleration in the lobes (e.g., Jaffe & Perola 1973, Subrahmanyan et al. 2006).

The spectral steepening of sources in the lower left quadrant in Fig. 1 5 could be due to synchrotron aging which would be much more rapid in the compact radio sources because the magnetic fields are higher. The class of flat and inverted spectrum objects which dominates the high frequency AT20G sample is quite different. The objects are small and maybe in a younger evolutionary phase which includes the 'Gigahertz Peaked Spectrum' (GPS) sources (e.g., O'Dea 1998, Stanghellini et al. 2001, Tinti & De Zotti 2006).

The BSS sample contains 64 objects (29.4 per cent of the 218 objects with simultaneous observations at 5, 8 and 20 GHz) with $\alpha_5^8 < \alpha_8^{20}$ and $\alpha_5^8 < -0.3$, i.e. peaking above

Table 1 2 Distribution of spectral shape for the 218 BSS sources with almost simultaneous 5, 8 and 20 GHz data. The abbreviations in the parentheses in the second column refer to the classification used to flag the sources according to their spectral behaviour in Table 2. In the third column there are the numbers of objects for each spectral class including a separate 'very flat' source class. No selection has been applied for flat sources to get the numbers in the last column (i.e. the values corresponds to the numbers of sources for each quadrant of the plot in Fig.1 5). See the text for details.

Spectrum		No.(%) incl. flat class	No.(%) excl. flat class
$\alpha_5^8 < 0,\ \alpha_8^{20} < 0$	Inverted (I)	39 (17.9)	58 (26.6)
$\alpha_5^8 < 0,\ \alpha_8^{20} > 0$	Peaked (P)	51 (23.4)	82 (37.6)
$\alpha_5^8 < 0,\ \alpha_8^{20} < 0$	Upturning (U)	2 (0.9)	9 (4.1)
$\alpha_5^8 < 0,\ \alpha_8^{20} > 0$	Steep (S)	44 (20.2)	69 (31.7)
$-0.3 < \alpha_5^8 < 0.3$ &			
$-0.3 < \alpha_8^{20} < 0.3$	'Very' Flat (F)	82 (37.6)	
$\alpha_8^{20} > 0.5$	Steep	34 (15.6)	
$\alpha_8^{20} < 0.5$	Flat	184 (84.4)	
$\alpha_5^8 > 0.5$	Steep	18 (8.3)	
$\alpha_5^8 < 0.5$	Flat	200 (91.7)	
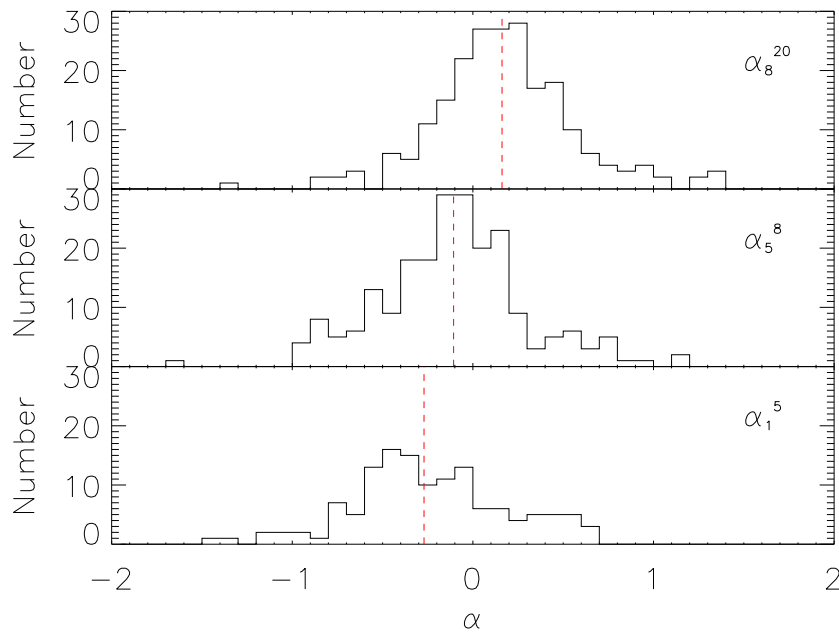
Figure 1 7 Distributions of spectral indices α_8^{20} (upper panel), α_5^8 (central panel), and α_1^5 (bottom panel) for the BSS. Data at ~ 1 GHz come from the NVSS. The red dashed lines correspond to the median values (respectively from the bottom to the top -0.27, -0.11, +0.16).
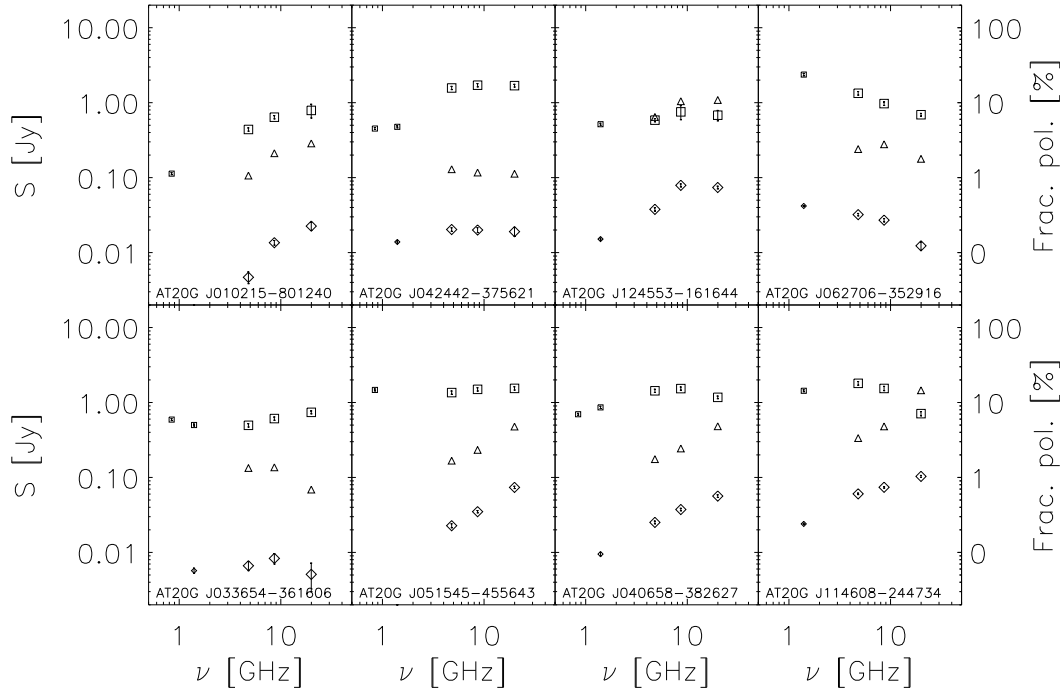
Figure 1 8 Some spectra as examples of the large variety of spectral behaviours in total intensity (squares) and polarisation (diamonds) for a set of point sources. We selected examples of inverted, flat, peaked and steep total intensity behaviours similar to (top panels) and different from (bottom panels) the polarisation behaviour. The triangles show the polarisation fraction. The low frequency values refer to data from SUMSS (0.843 GHz) and NVSS (1.4 GHz) catalogues in total intensity (small squares) and, where available, polarisation (small diamonds).

5 GHz. Tinti et al. (2005) argued that a large fraction of sources showing spectral peaks at several GHz are not truly young (GPS) sources but blazars where a flaring, strongly self-absorbed synchrotron component, probably originated at the base of the relativistic jet, transiently dominates the emission spectrum. Repeated simultaneous multifrequency measurements with time lags of a few years will be needed to discriminate among the two populations. Polarisation measurements are also a good discriminant, as true GPS sources generally have much lower polarisation levels than blazars (Orienti & Dallacasa 2008). The most unambiguous discrimination is however obtained with high resolution radio interferometry, observing the different milli-arcsec morphology of blazars and GPS sources. In Fig. 1 12 we have separated the sources with spectral peaks above 5 GHz.

1 3.3.2 Extended sources

The comparison of the extendedness parameters at different frequencies (Fig. 1 9) for the BSS sources confirms the expectation that the extended, steep-spectrum radio lobes are less and less prominent at higher frequencies. In Fig. 1 9 we can see three clear effects. There are point sources spread over a roughly circular area around a unit value of the extendedness parameter by measurement errors (a), a group of sources extended at 5 GHz
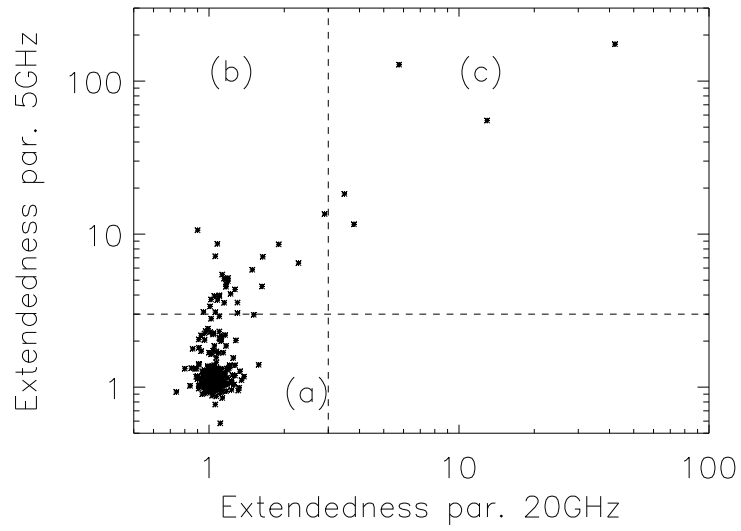
Figure 1 9 5 GHz versus 20 GHz extendedness parameter for the BSS. The horizontal and vertical dashed lines correspond to the threshold between pointlike and extended objects.
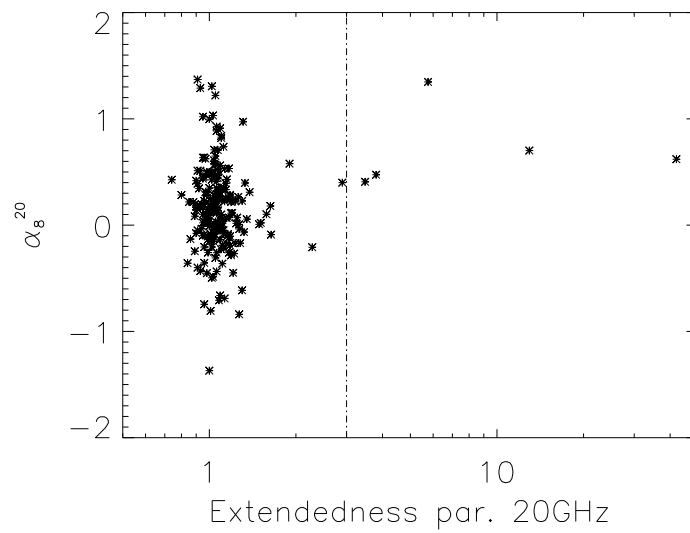
Figure 1 10 The spectral indices between 8 and 20 GHz versus the 20 GHz extendedness parameter for the BSS. The vertical dashed line corresponds to the threshold between pointlike and extended objects.

Table 1 3 Extended sources in the BSS. The first column lists the BSS sequential number. An 'M' indicates that they have been observed in mosaic mode. The 20 GHz flux densities in column 4 refer to the core region whereas those in column 5 are the integrated flux densities. For 3 sources observed in mosaic mode, we believe we have acquired the flux density values only for subregions, so we consider them as lower limits to the total integrated flux densities. P.A. is the position angle (in degrees) of the major axis of the source.

Seq. #	RA	δ	$S_{20\,GHz}$ core[Jy]	$S_{20\,GHz}$ [Jy]	$S_{8.6\,GHz}$ [Jy]	$S_{4.8\,GHz}$ [Jy]	$P_{20\,GHz}$ [Jy]	z	Size [arcmin]	P.A. [$^\circ$]
20M	01:33:57.6	-36:29:34.9	0.041 0.005	>1.86 ..	... ..	... ..	...	...	6.1	79
52	04:08:48.75	-75:07:20.1	...	0.86 0.14	2.64 0.42	4.74 0.75	...	0.693	0.1	45
69M	05:19:49.7	-45:46:44.2	1.33 0.07	8.52 0.11	... ..	... ..	1.400 0.016	0.0351	3.4	76
71	05:22:57.94	-36:27:30.4	...	3.91 0.59	6.57 1.04	9.07 1.43	...	0.0553	0.5	55
92	06:35:46.33	-75:16:16.9	...	3.24 0.51	4.82 0.76	5.54 0.87	...	0.653	0.2	90
100	07:43:31.60	-67:26:25.7	...	1.22 0.19	1.87 0.30	2.34 0.37	...	1.51	0.2	14
118	09:19:44.06	-53:40:05.1	...	0.94 0.15	1.69 0.27	2.5 0.39	...	...	0.3	40
157	12:05:33.37	-26:34:04.9	...	0.84 0.14	1.18 0.21	1.12 0.18	...	0.789	0.4	.
179M	13:25:27.7	-43:01:07.0	7.62 0.44	>59.3 ..	... ..	... ..	...	0.00183	10.9	34
182M	13:36:39.0	-33:57:58.2	0.21 0.04	>1.60 ..	... ..	... ..	...	0.01254	31	53
185	13:46:48.95	-60:24:29.0	...	5.30 0.84	6.14 0.97	6.58 1.04	...	...	16	.
216M	16:15:05.2	-60:54:25.5	0.19 0.05	3.84 0.04	... ..	... ..	0.169 0.011	0.01828	12.6	47
284M	21:57:06.08	-69:41:23.3	...	5.31 0.27	... ..	... ..	0.087 0.014	0.0283	1.2	20
310	23:33:55.28	-23:43:40.8	...	0.82 0.13	1.47 0.22	0.67 0.10	...	0.0477	21	-43
319M	23:59:04.70	-60:55:01.1	0.11 0.06	3.03 0.05	... ..	... ..	0.053 0.008	0.0963	6.3	46

Note: sources number 20, 69, 182, 284, 310 and 319 are characterized by a core and double lobes; 71, 92 and 100 have a core and a jet; 179 is the inner double lobe of the giant radio galaxy Centaurus A with total extent of 5 degrees; 216 is a wide angle tail source; 310 is the core region of a highly-extended radio galaxy: it is difficult to determine the correct size without a mosaic observation. References for the redshift are as in the Appendix in table 1.Useful references for the single sources are as follows. 20: Ekers et al. (1978); 69: Perley et al. (1997); 71: Birkinshaw et al. (2002);92: Schwartz et al. (2000); 182: Killeen et al. (1986); 284: Fosbury et al. (1998).

but dominated by a point core at 20 GHz (b), and a group of sources extended at both 5 and 20 GHz (c).

The median 8-20 GHz spectral index of the extended objects (0.62) is similar to sources found in low frequency samples (Fig. 1 10). In general, 8 of the 39 extended objects in the BSS at 5 GHz are extended also at 20 GHz (considering also 3 cases for which only non-simultaneous observations are available that do not appear in Fig. 1 9 and 1 10). To those we could add 7 extended sources at 20 GHz, for which we don't have low frequency data, but we know from other observations that they are extended also at low frequencies.

As anticipated in § 1 3.2.4 we have looked for extended sources missed by the BSS selection because they are either: 1) fully resolved (and therefore undetected) by the 60 m shortest antenna spacings used in the follow-up, or 2) had components (hot-spots, cores) which have been detected as separate sources in the AT20G follow-up or is marked in PMN as extended, with $S_{5\,GHz} > 0.90$ Jy (i.e. we expect any extended source with $S_{20\,GHz} > 0.5$ Jy to have a 5 GHz flux of $S_{5\,GHz} > 0.90$ Jy if it is steep with spectral index larger than 0.5, as would be expected by a conservative estimate for the spectral index of diffuse emission). An inspection of the SUMSS and of the PMN catalogues yielded 9 sources that are extended,

bright, and with 0.84–5 GHz spectral indices such that the expected integral flux densities at 20 GHz may be > 0.50 Jy, (that happens in 7 cases that are flagged with an 'M' in Table 1 3: PMN J0133-3629, Pictor A, Centaurus A, PKS 1333-33, PKS 1610-60, PKS 2153-69, PKS 2356-61) but were present in the initial BSS selection only if their core component has flux density above 0.50 Jy (see Table 1 3). All of these have been observed with the mosaic mode. For these sources we have integrated flux densities at 20 GHz but no flux densities at lower frequencies. Therefore we could not determine the extendedness parameter at low frequencies or the spectral indices for them, that are thus missing in Fig. 1 9 and 1 10. Except for Fornax A (whose compact component does not appear in the blind survey) and Centaurus B (for which the analysis of the mosaic observations is on-going), all the known bright extended sources in our area have been mosaiced. A summary of the properties of the extended sources in the BSS is in Table 1 3.

1 3.3.3 Polarisation

All the follow-up measurements include polarimetry. Once the low quality data have been removed from the sample, we take, as 'detections', measurements of integrated polarised flux at least 3 times higher than their errors (see § 1 3.2.7). We had a polarisation detection at 20 GHz for 213 BSS sources (34 cases are non detections, the others have low quality data in polarisation and the data have not been considered). The median fractional polarisation is 2.5 per cent, calculated considering also upper limits using Survival Analysis. The median polarisation degree is found to be somewhat lower at lower frequencies: it is 2.0 per cent at 8 GHz and 1.7 per cent at 5 GHz (see Fig. 1 13). A similar trend was found by Burke et al. (in prep.) for the sub-sample observed in October 2006 during the observation run dedicated to high sensitivity polarisation observations.

As can be seen from Fig. 1 8 the spectra for polarised flux density are very diverse and show little correlation with total flux density. This makes it even more difficult to predict high frequency polarisation properties from low frequency observations than it is to predict total intensity. There is no clear relation between the spectral properties of the sources and their polarised flux, nor there is any unique trend in the spectral behaviour of the total intensity and the polarised emission. The spectral shape in polarisation is often quite different from the spectral shape in total intensity at any flux level.

The matrices of spectra collected in Table 1 4 are complex. The diagonal cells refer to the sources that have polarised spectra similar to those in I (but, even if a source could be classified in the same spectral type in polarisation and total intensity, the spectral indices may be different in the two cases). The flat and peaked spectrum sources show a remarkable excess of rising polarisation spectra, whatever the spectral type in total intensity. For sources with peaked spectra, the polarised fraction generally decreases below the turnover frequency; an example of this behaviour in Fig. 1 8 (third panel, bottom row). There are several reasons why the polarised fraction might change with frequency, including:

- superposition of multiple components with different polarised spectra;

- depolarisation due to spatial variations in Faraday Rotation across the source;

- bandwidth depolarisation due to very high levels of Faraday Rotation.

Table 1 4 Distribution of spectral types in total intensity and polarized flux (Pol.) or polarisation fraction (m) for the 123 sources with almost simultaneous total intensity and polarisation detections at 5, 8 and 20 GHz. The spectral types are defined in Table 1 2.

$S \rightarrow$ Pol. $\downarrow$	U	I	F	P	S
U	0	2	7	1	2
I	1	7	16	10	3
F	0	0	5	1	2
P	0	7	24	13	5
S	0	1	6	2	8

$S \rightarrow$ $m[\%]$ $\downarrow$	U	I	F	P	S
U	0	5	9	5	7
I	1	4	14	13	4
F	0	0	6	2	3
P	0	4	18	2	3
S	0	4	11	5	3
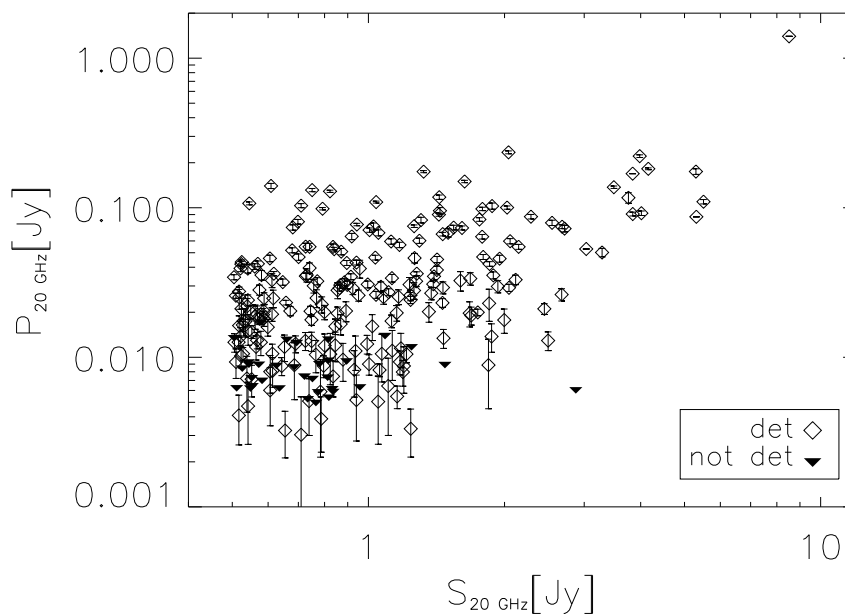
Figure 1 11 Integrated polarised flux as a function of total 20 GHz flux for the BSS. The bright source at $P = 1.4\,\mathrm{Jy}$ is Pictor A.
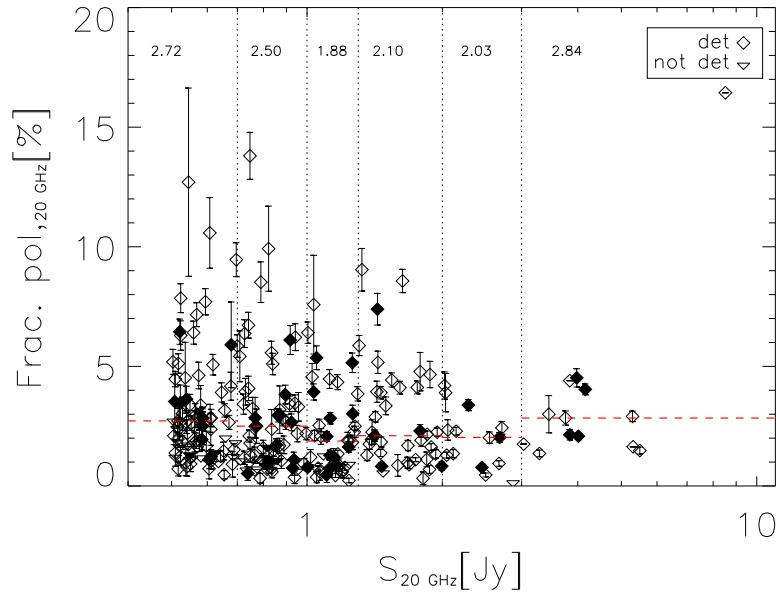
Figure 1 12 Fractional polarisation versus total 20 GHz flux density for the BSS. The dashed lines shows the median fractional polarization by bins of flux density (the dotted lines indicates the bin boundaries) for the full sample. Filled symbols refer to objects with $\alpha_5^8 < \alpha_8^{20}$ and $\alpha_5^8 < 0.3$. Values of the median fractional polarisation for each bin of flux density are on the top of the panel.

Figures 1 11 and 1 12 plot the polarised flux and fractional polarization as a function of flux density for the BSS as well as for the full sample. The data from our pilot observations (Sadler et al 2006) suggested a marginal trend for weaker sources to have higher fractional polarization. Although this seems to be present in Figure 1 12 the median fractional polarization as a function of flux density has no trend and indicates that the apparent effect is due to the increased density of points at lower flux levels. The sources with a peak in the spectrum above 5 GHz have lower fractional polarization at 20 GHz but this effect is not very pronounced. Fig. 1 13 shows the distribution of fractional polarisation at 5, 8 and 20 GHz for the BSS.

The images for the 7 mosaiced sources (see for example the image of Pictor A in Fig. 1.17(a)) have revealed clearly detected 20 GHz emission from all galactic nuclei except for that of PKS 2153-69. In all the cases, the fractional polarisation of the galactic core was either not detected or less than 1 per cent (in the case of Centaurus A and PKS 1333-33).

1 3.3.4   Low radio frequency counterparts and flux density comparisons for the BSS

Due to the lack of deep large area surveys at frequencies above 15 GHz the comparison of our results has to be done with low frequency catalogues. Because of variability between catalogue epochs a direct comparison can only provide hints on the spectral behaviour as discussed in the previous section. All 172 BSS sources in the sky region overlap-
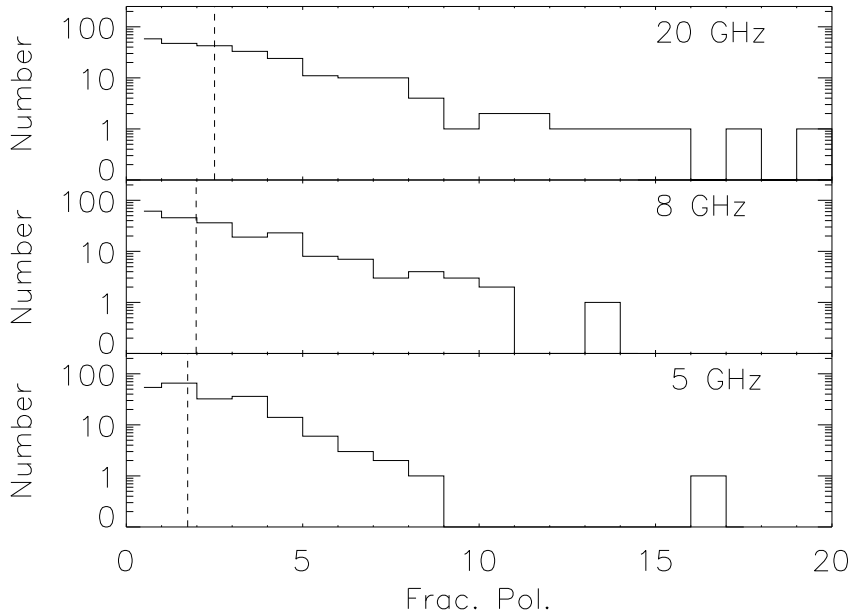
Figure 1 13 Distribution of fractional polarisation at 5, 8 and 20 GHz for the BSS. Dashed lines are the median values.

ping with the NVSS survey (Condon et al. 1998) have at least one counterpart in NVSS (within less than 1.2 arcmin from the position of the BSS source). A total of 156 BSS sources have a counterpart in SUMSS.

At 2.7 GHz we have cross-matched the BSS with the Parkes quarter Jy sample (Jackson et al. 2002) comprising sources with $\alpha_{2.7}^{5} \leqslant 0.4$. Of the 314 BSS sources in the overlapping declination range, 163 have a counterpart. At 4.85 GHz the cross-correlation with the PMN catalogue shows that 316 BSS sources have a counterpart in PMN. The four BSS sources without a PMN counterpart lie in the small regions of sky where the PMN survey was incomplete (see, e.g., Figure 2 of Wright et al. 1996). The 4.8 GHz flux densities from our observations have been used for comparison with these two catalogues (see Fig. 1 14 and 1 15). The closeness in frequency reduces the spectral effects and the scatter mainly results from variability. The few sources that fall below ~ 0.4 Jy have the most inverted spectra since our sample is flux limited at 20 GHz.

There are 88 BSS sources among the 185 sources monitored with the ATCA at 1.4, 2.5, 4.8 and 8.4 GHz at up to 16 epochs by Tingay et al. (2003). In addition to fractional polarisations at each frequency, and a measure of source extendedness, the multi-epoch monitoring enabled a variability index to be assigned for each frequency. The monitoring was done to support the VSOP Survey Program, and 87 BSS sources are included in the 5 GHz survey of bright compact AGN (Hirabayashi et al. 2000). Results from these space VLBI observations are presented by Scott et al. (2004) and Dodson et al. (2008).
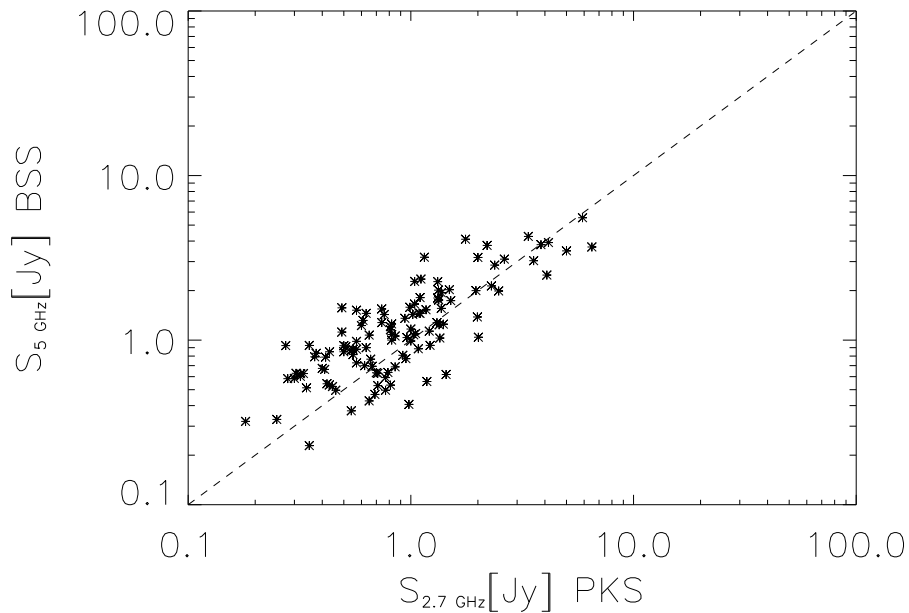
Figure 1 14 Comparison of 5 GHz flux densities with those at 2.7 GHz in the Parkes quarter Jy sample.

1 3.3.5   Interest of the BSS for CMB missions

The contamination due to point sources is a crucial limitation to the CMB power spectrum determination on small angular scales (less than ~ 30 arcmin), as we will extensively discuss in chapter 3. The variety of source spectral behaviours implies that, as mentioned, it is extremely difficult to make reliable flux density extrapolations from low to high frequency. Variability complicates the situation even more.

Also, the forthcoming Planck mission (that will be described in chapter 3 2) will be strongly confusion limited. According to López-Caniego et al. (2006), the 5σ detection limits range from $\simeq 520$ mJy at 30 GHz to $\simeq 180$ mJy at 100 GHz, while the rms noise levels are far lower (from $\simeq 19$ mJy at 30 GHz, Valenziano et al. 2007, to $\simeq 14$ mJy at 100 GHz, Lamarre et al. 2003): this means that there is a lot of astrophysical information in Planck maps below the confusion limit, that can be to some extent extracted, e.g. using stacking techniques, thanks to the full AT20G survey and follow-up observations at higher frequencies.

As a test of high frequency predictions from low frequency samples we selected a sample from the PMN catalogue with declination below $-30°$ and $|b| > 10°$ and cross-matched it with SUMSS to obtain the low frequency spectral behaviour. Then we divided it into sub-samples with different flux density limits at 5 and 1 GHz and/or different spectral indices at those frequencies. Finally, for each sub-sample we computed the fraction of PMN sources having a counterpart in the BSS (detection rate) and the fraction of BSS sources not having a counterpart in the PMN sub-sample (incompleteness).

There are 154 BSS sources with declination below $-30°$ and $|b| > 10°$ and 152 have a PMN counterpart. However, 35 PMN counterparts have flux density at 5 GHz
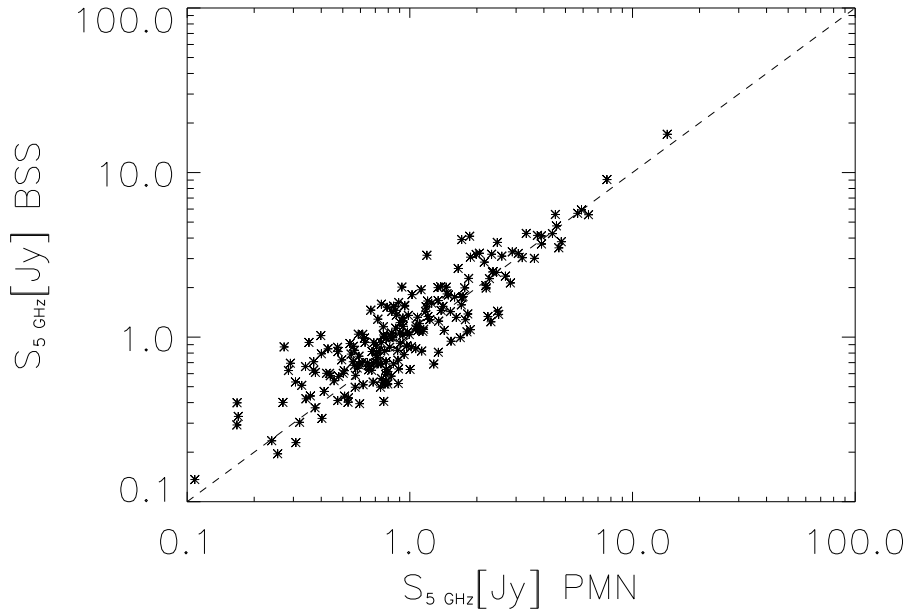
Figure 1 15 Comparison of 5 GHz flux densities with those in the PMN catalogue.

below 0.50 Jy, so that a low frequency selection threshold at 500 mJy would have lost them. Selecting only inverted sources ($\alpha_{0.843}^{4.85} < 0$, $\alpha_{0.843}^{4.85} < -0.25$, $\alpha_{0.843}^{4.85} < -0.5$) results in a low detection rate (3.6, 3.2, 3.0 per cent respectively) and a low completeness of the sample at high frequency (52.2, 22.2, 9.8 per cent respectively). A flux density selection at 5 GHz implies a decreasing 20 GHz completeness with increasing 5 GHz flux density threshold (from 90.2 to 71.9 per cent going from 250 to 500 mJy) with low, but increasing detection rate (from 11.3 to 27.5 per cent in the same flux density range): 289 PMN sources with a counterpart in SUMSS with declination below $-30°$ and $|b| > 10°$ have flux density above 500 mJy and no counterpart in the BSS. Combining spectral and flux density limits or adding further selection criteria at 1 GHz improves the detection rate but at the cost of a very low completeness of the high frequency sample. Thus, it is clear that low frequency catalogues could provide positions for constrained search techniques (cf. López-Caniego et al. 2007), but are inadequate to forecast the high frequency population.

The comparison of flux densities with WMAP map-based catalogues shows a good agreement in general (we used the NEWPS catalogue as in González-Nuevo et al. 2008 in Fig. 1 16). The epochs of observations partially overlap, but, since the WMAP maps have been averaged over three years, transient phenomena have been smoothed out.

The Bright Source Sample we have discussed is well-suited for CMB studies since its selection frequency is, so far, the closest to the spectral region of interest. It allows direct tests of source detection algorithms, quantifying the completeness, the fraction of spurious detections, the effective beam size (and therefore the flux calibration) and the possible presence of biases in flux density estimates. It also provides a rich list of candidate flux density and pointing calibrators over a large fraction (37 per cent) of the sky.

Finding suitable polarisation calibrators for CMB experiments is much more diffi-
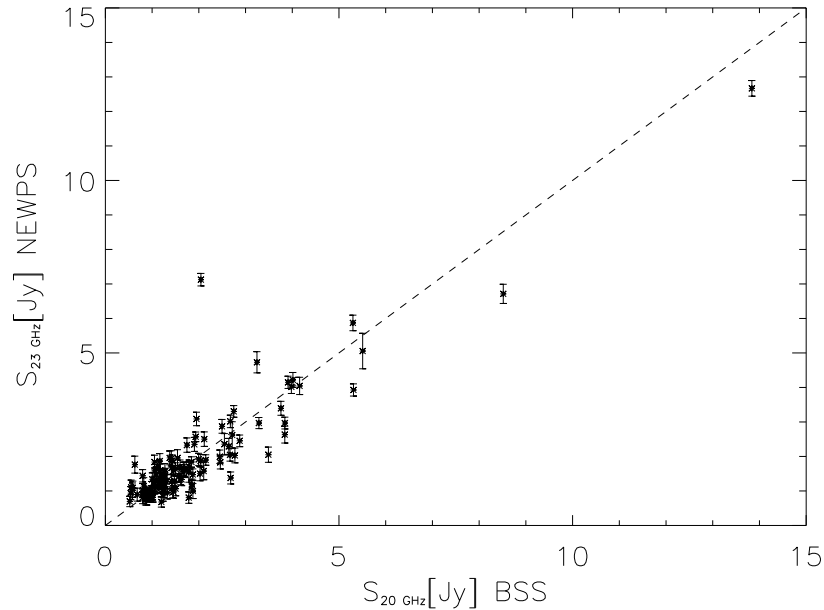
Figure 1 16 Comparison of the BSS 20 GHz flux densities with those in the NEWPS catalogue at 23 GHz.

cult. For example, the large low frequency beams of the Planck satellite (33 arcmin FWHM at 30 GHz) dilute the polarised signals by summing over differently oriented polarisation vectors. Thus, sources with large enough polarised flux density within such beams are very rare (Figs. 1 11 and 1 12).

The best candidate in this data set is Pictor A, which fits the Planck requirements in several ways. In total, the source size is of approximately 10 arcminutes and has ~ 1.4 Jy of integrated polarised intensity, dominated by the western hotspot. Because the hotspot is extended (see fig. 1.17(b)), its total and polarised emission should not change rapidly in time, making the source particularly useful for calibration in polarisation. Conveniently, Pictor A is located within 20 degrees of the South Ecliptic Pole.

1 3.3.6   Optical identifications and redshifts

All the available redshifts have been collected for the BSS from the 6dF (Jones et al. 2004) survey data and by searching in the Nasa Extragalactic Database (NED[2]). To optically identify objects in the Bright Source Sample, we searched the SuperCOSMOS catalogue (Hambly et al. 2001) near the positions of all sources. Objects within 10° of the Galactic plane were excluded from the analysis because the presence of foreground stars and Galactic dust extinction makes optical identifications incomplete in this region. This cutoff in Galactic latitude excluded 69 of the 320 BSS sources. Two other sources were also excluded from the optical analysis: sources 57 and 160 (according to the sequential numeration of the BSS source list, see Appendix 1) lie so close to bright foreground stars that no optical identification is possible from the DSS images. Also, source number 73 lies

---

[2]nedwww.ipac.caltech.edu

(a)

(b)
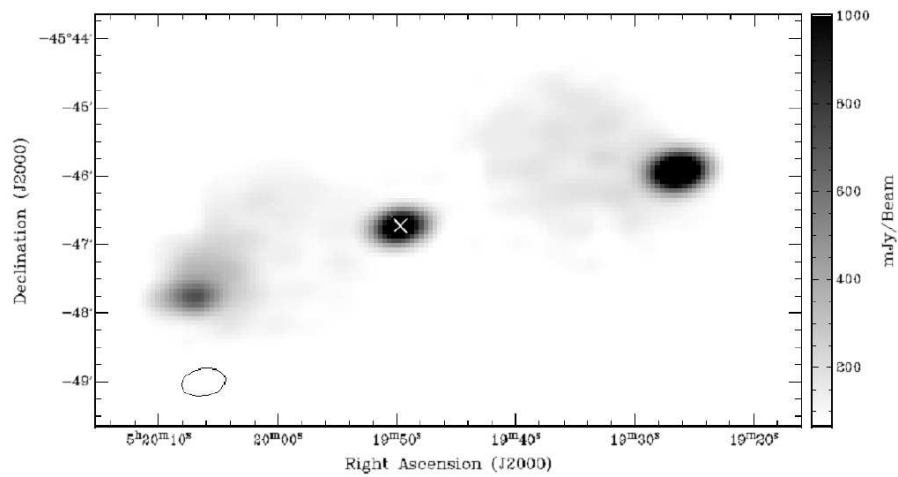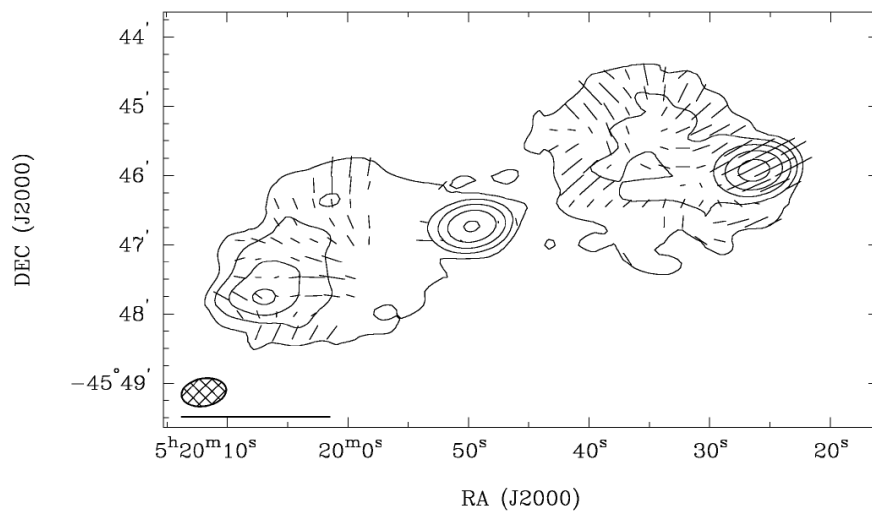
Figure 1 17 (a) Image at 18 GHz of Pictor A.(b) Polarisation vectors on a contour plot of the Pictor A region. The maximum in the image is 1.7 Jy.
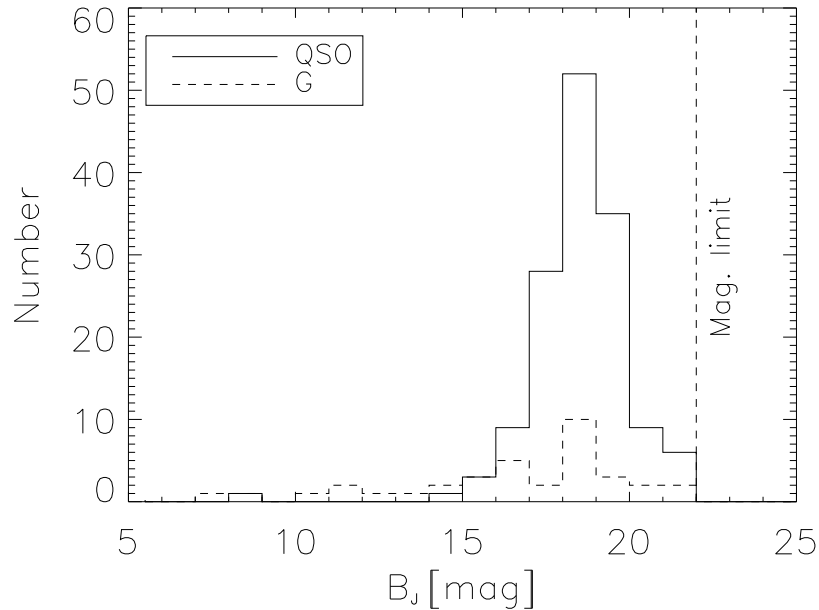
Figure 1 18 B-magnitude distribution for the BSS.

within the boundaries of the Large Magellanic Cloud and its identification is uncertain. An optical object was accepted as the correct ID if it is brighter than $B_J=22$ mag and lies within 2.5 arcsec of the radio position. Monte Carlo tests show that at least 97 per cent of such objects are likely to be genuine associations (Sadler et al. 2006).

We found a DSS identification for 238 of the remaining sources, 235 of which have $B_J \leq 22.0$ mag (identification rate of 94.5 per cent). On the basis of the SuperCOSMOS classification of each object as stellar or extended, there are 188 QSOs (75.5 per cent of the sample), and 47 galaxies (19 per cent). The median B_J magnitude is 18.6 for QSOs and 17.7 for galaxies (see Fig. 1 18).

We have also checked in the NASA Extragalactic Database (NED[3]) for optical identifications in order to distinguish between Galactic and extragalactic objects: none of the sources in the BSS which have a clear identification are Galactic objects (i.e. HII regions, planetary nebulae or SNRs).

After completing the optical identifications, we searched the NED for published redshifts. A listed redshift was accepted only if it could be traced back to its original source and appeared to be reliable. 177 of the 249 BSS objects (71 per cent) had a reliable published redshift, including three of the sources which are blank fields on the DSS (these objects were identified in deeper optical images by other authors).

The 72 objects without a published redshift include seven objects (sources number 10, 19, 30, 42, 85, 221 and 278) which have a redshift listed in NED. In these cases, we were either unable to trace back to the original source, or considered the redshift to be unreliable for other reasons (PKS 0332−403, source 42, was previously discussed in this regard by

---

[3]http://nedwww.ipac.caltech.edu/
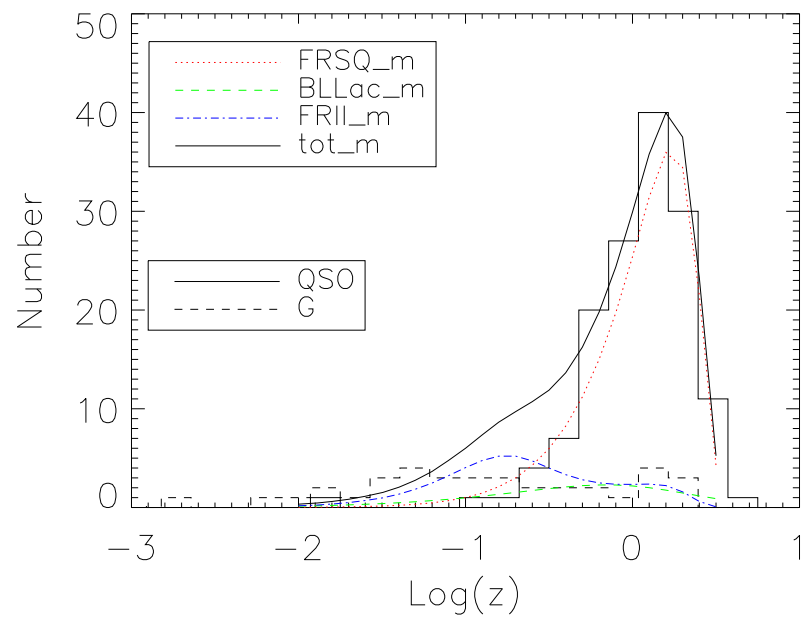
Figure 1 19 Redshift distribution for the BSS. The model by De Zotti et al. (2005) has been overlapped for comparison.
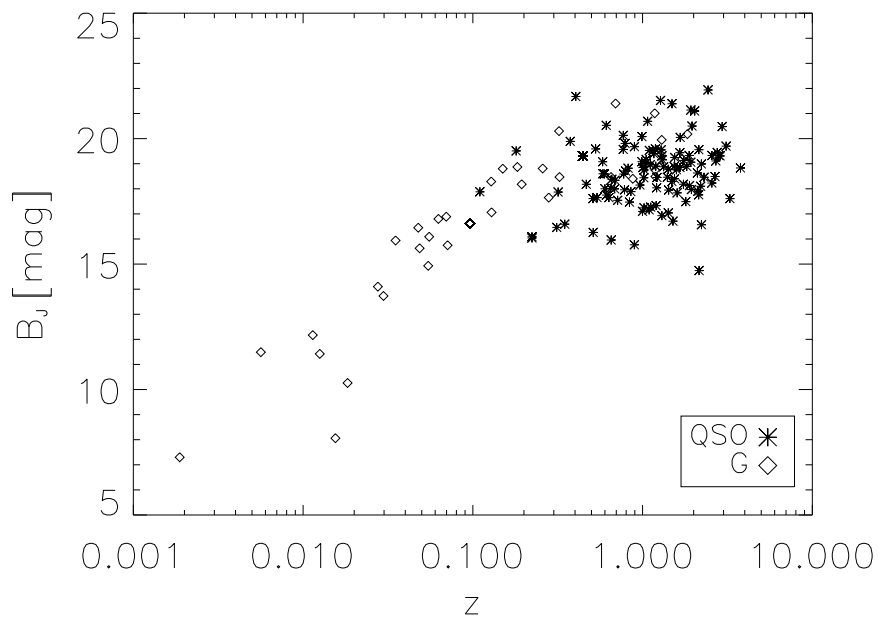
Figure 1 20 B-magnitude versus redshift for galaxies and QSO in the BSS.
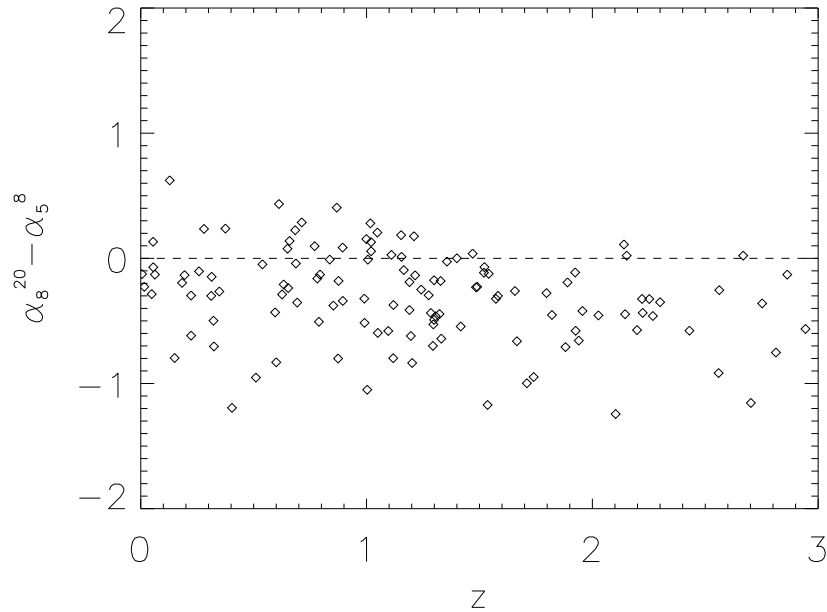
Figure 1 21 Plot of the difference between spectral indices α_8^{20} and α_5^8 with redshift.

Shen et al. 1998).

Redshifts for two BSS objects (sources number 33, a QSO at $z =0.466$ QSO, and 313, a QSO at $z =0.626$ based on a single broad emission line identified as MgII) were obtained from a pre-release version of the final redshift catalogue from the 6dF Galaxy Survey (Jones et al. 2004). The redshift for source 138 has been measured with the ESO 3.6 m telescope (Edwards private communication).

Optical spectra of nine other BSS sources were obtained at the ANU 2.3 m telescope in April and June 2007 by R.W. Hunstead (private communication). Redshifts were measured for seven of these objects (sources number 77, 98, 140, 162, 166, 208 and 246). The spectra of two other objects (number 68 and 78) showed a featureless optical continuum from which no redshift could be measured.

Among the 186 objects with redshifts (75 per cent of the sample), 144 are QSOs, 36 are galaxies and 6 are unclassified. The median redshift is 1.20 for the QSOs and 0.13 for the galaxies(Fig. 1 19). No correlation is observed between redshift and total 20 GHz flux density or polarised flux. As noted by Sadler et al. (2006) there is a correlation between redshift and optical magnitude for galaxies in the AT20G sample, but this does not apply to the AT20G quasars (see Fig. 1 20).

Six BSS objects with good–quality optical spectra (either from the published literature or from unpublished 6dF/2.3 m data), have no measured redshift because the spectra are featureless. Such objects generally fall into the BL Lac class, though it is possible that some of them fall in the 'redshift desert' at $z \sim 1.5 - 2.2$ where QSOs show no strong lines in the optical.

The correlation between the difference of the spectral indices at high and low frequencies ($\alpha_8^{20} - \alpha_5^8$) with redshift (Fig. 1 21) shows a clear curvature in the spectra.

Since the median redshift of the QSO in the sample is 1.20, the steepening is occurring at frequency $\nu > 50\,\mathrm{GHz}$ in the rest frame, and grows steeper to above $\nu > 70\,\mathrm{GHz}$ in the rest frame for the objects at $z \sim 2.5$.

Although this correlation with redshift is most simply explained as the combination of increased spectral curvature with frequency and the changes in the rest frame frequency it should be noted that the BSS sample does not cover a large enough flux range to break the degeneracy between distance and power so it could also be a correlation with power. Further investigation of this correlation clearly needs the deeper sample, and would also benefit from more complete redshift information, since there may be selection effects in the sub-samples with existing redshift information.

1 3.4   Summary: the AT20G survey Bright Source Sample

The BSS is a complete sample of 320 AT20G sources with flux density $S_{20\mathrm{GHz}} > 0.50\,\mathrm{Jy}$, $|b| > 1.5°$. Almost simultaneous 5 and $8\,\mathrm{GHz}$ observations have been used for spectral behaviour analysis. Information on polarisation is available at all the frequencies. We found that the median fractional polarisation is slightly increasing with frequency (from 1.7 at 5 GHz to 2.5 per cent at 20 GHz).

Neither the high frequency total intensity nor the polarisation behaviour can be estimated from low frequency information. We examined a set of issues that support this statement:

- the colour-colour plot shows a broad range of spectral shape: most sources' spectra are not power-law so do not allow easily extrapolations from one frequency to the other;

- the comparison with low frequency selected samples showed that by increasing the constraints on the low frequency sample the number of low frequency objects recovered also at high frequency increased, but that the completeness of the predicted high frequency sample gets poorer. It is necessary to fine tune the conditions on the low frequency sample to obtain a good trade-off between completeness and correct source identification rate, but there is no way to select a low frequency sample that guarantees that all the sources will constitute a complete high frequency sample at sensible flux density limits;

- the polarisation spectral shape does not agree in all the cases with that in total intensity: the lack of knowledge on polarisation properties, together with unpredictable polarisation spectral behaviour, make any forecast extremely difficult.

It is clear that actual high frequency samples are much better than trying to predict them from lower frequencies. So, the Bright Source Sample constitutes an unprecedented collection of information at 20 GHz, that will be of importance by itself and for any future observations at high radio frequencies. The whole AT20G Survey, in fact, will improve the radiosource population knowledge to much lower flux densities. Analysis of the full sample is on-going and preliminary results confirm what we have found for the Bright Source Sample.

This amount of information will be of crucial interest for the next generation telescopes, to provide good sample of calibrators, and for the CMB targeted missions, as a

test for point source detection techniques, as a help in point-source removal in any component separation exercise, and as a list of candidate pointing, flux, and possibly polarisation calibrators.

With the analysis presented here we find interesting new physical effects from this sample:

- spectral steepening is common in this class of objects;

- the spectral steepening correlates with redshift, possibly due to changing rest frame frequency;

- sources with spectral peaks in the GHz range are common in this sample and have high depolarisation on the low frequency side of the peak.

1 4 The New Extragalactic WMAP Point Source (NEWPS) Catalogue

An important byproduct of CMB experiments is information on point sources, whose millimeter-wave properties, as mentioned, are poorly known. On the other hand, a careful extraction of point sources from CMB maps is crucial since they are the main foreground contaminant on small angular scales (less than $\sim 30'$; De Zotti et al. 1999; Toffolatti et al. 1999).

The WMAP mission has produced the first all-sky surveys of extragalactic sources at 23, 33, 41, 61 and 94 GHz. The analysis of first year data yielded a sample of 208 extragalactic sources detected above a flux limit of $\sim$ 0.8-1 Jy (Bennett et al. 2003), with an estimated completeness limit of ~ 1.2 Jy at 23 GHz (Argüeso et al. 2003; De Zotti et al. 2005). The sample size has been steadily increasing as the WMAP survey successfully progressed: 323 sources were found in the 3-yr maps (Hinshaw et al. 2007; we will refer to this sample as WMAP_3yr), and 390 in the 5-yr maps (Wright et al. 2008; WMAP_5yr sample). The approach used by the WMAP team for source extraction can be summarized as follows. The temperature map pixels were first weighted by $N_{\rm obs}^{1/2}$, $N_{\rm obs}$ being the number of independent observations per pixel, and then filtered in harmonic space by the global matched filter $b_l/(b_l^2 C_l^{\rm CMB} + C_l^{\rm noise})$, where b_l is the transfer function of the WMAP beam response, $C_l^{\rm CMB}$ is the CMB angular power spectrum, and $C_l^{\rm noise}$ is the noise power spectrum. Peaks with signal-to-noise ratio (SNR) greater than 5 (note that the 'noise' here is the global rms fluctuation in regions outside the processing mask) in any band were then interpreted as source detections. The peaks are fitted in real space, i.e. in the unfiltered maps, to a Gaussian profile plus a planar baseline to estimate the flux densities. The flux densities in the other channels are given if their SNR > 2 and the source width falls within a factor of two of the true beam width.

Several other attempts to improve the source detection have been presented. Nie & Zhang (2007) applied cross-correlation techniques to clean the WMAP first-year residual maps and identify foreground residuals which have been associated to radio sources: they detected 101 sources of which 26 where not in the WMAP 1-year catalogue (25 of them do not appear even in the WMAP_3yr catalogue, but 5 of them are in the LMC region).

Chen & Wright (2008), combining the 61 and 94 GHz WMAP temperature maps to cancel the 'noise' due to the CMB anisotropy signal, found 31 sources in the first year maps and 64 in the 3-year co-added maps, of which 21 are not in WMAP_3yr. The same $V - W$ internal linear combination technique was used by Wright et al. (2008) to find 99 sources in the region with $|b| > 10°$, 64 of which are in WMAP_5yr, 17 can be identified with known sources, 17 are in complex Galactic emission regions, and 1 is unidentified.

It has been shown that wavelet techniques are well suited to detect sources in CMB maps (Cayón et al. 2000, Vielva et al. 2001a, 2003, González- Nuevo et al. 2006, López-Caniego et al. 2006). González-Nuevo et al. (2006) have discussed a natural generalization of the (circular) Mexican Hat wavelet, obtained by iteratively applying the Laplacian operator to the Gaussian function, which was called the Mexican Hat Wavelet Family (MHWF). They demonstrated that the MHWF performs better than the standard Mexican Hat Wavelet (Cayón et al. 2000) for the detection of extragalactic sources in CMB anisotropy maps. In a subsequent work (López-Caniego et al. 2006) the MHWF has been applied to the detection of compact extragalactic sources in simulated CMB maps. In that work it was shown, in particular, that the second member of the MHWF, called the MHW2, at its optimal scale, compares very well with the standard Matched Filter (MF); its performances are very similar to those of the MF and it is much easier to implement and use. López-Caniego et al. (2006) compared the two techniques, MF vs. MHW2, by exploiting realistic simulations of CMB anisotropies and of the Galactic and extragalactic foregrounds at the nine frequencies, between 30 and 857 GHz, of the ESA Planck mission, considering the goal performances of the Planck Low and High Frequency Instruments, LFI and HFI.

As a first approach we have performed non-blind detections (López-Caniego et al. 2007, González-Nuevo et al. 2008) exploiting the MHW2 filter to obtain estimates of (or upper limits to) the flux densities at the WMAP frequencies for a complete all-sky sample of 2491 sources with $|b| > 5°$, brighter than 500 mJy at 5 GHz in the PMN or in the GB6 (Gregory et al. 1996) catalogues, or at 1.4 or 0.84 GHz in regions not covered by 5 GHz surveys but covered by either the NVSS or the SUMSS. This work yielded 5σ detections of 380 extragalactic sources in the WMAP 3-yr maps, including 98 sources not present in the WMAP_3yr catalogue. The results were organized in the NEWPS_3yr (New Extragalactic WMAP Point Source) catalogue.

Then we have extended the analysis to the WMAP 5-yr data, carrying out both a 'blind' and a 'non-blind' source search using the MHW2. A particularly delicate issue that we will address is the estimate of the 'noise' to be used to derive the SNR and hence the nominal flux limit for source detection, in the presence of a highly inhomogeneous fluctuation field. This analysis is important also in view of defining the optimal source extraction strategy for the Planck mission.

The strong inhomogeneity and non-Gaussianity of the fluctuation field, which in the best CMB experiments is dominated not by the instrumental noise but by sources below the detection limit and by small-scale structure in the Galactic emission, is a serious hindrance for source detection techniques. Since the statistical properties of such fluctuation field are poorly known, the reliability of source detections and the real uncertainties on flux estimates are difficult to quantify, even in the case of relatively high SNR's. It is well known (Eddington 1913; Hogg & Turner 1998) that the skewness of the distribution of Poisson

Table 1 5 Summary of the main properties of the blindly and non-blindly (NB) samples detected on WMAP maps discussed in this work. Values in the square brackets refer respectively to [23, 33, 41, 61] GHz. Note that we have investigated 2 different blind approaches: a 'simple' blind (SB) and a 'combined' blind (CB); details are in the text.

Sample ID	NEWPS_3yr	NEWPS 5-yr NB
Method	non-blind	non-blind
Maps epoch (year)	3	5
Input positions (for NB)	5 GHz catalogues	NEPWS_3yr_3σ
Sky coverage	All sky with $|b| > 5°$	All sky with $|b| > 5°$
SNR > 3 detections	[759, 564, 535, 365]	[712, 585, 537, 312]
SNR > 5 detections	[349, 223, 217, 135]	[366, 262, 246, 122]
median flux density error [mJy]	[182, 219, 214, 251]	[168, 207, 196, 249]
min flux density at SNR > 5[mJy]	[712, 995, 861, 995]	[754, 888, 861, 950]
Sample ID	NEWPS 5-yr SB	NEWPS 5-yr CB
Method	simple blind	combined blind
Maps epoch (year)	5	5
Sky coverage	All sky with $|b| > 5°$	All sky with $|b| > 5°$
SNR > 3 detections	[1826, 2279, 3001, 3441]	[1302, 1345, 1575, 1308]
SNR > 5 detections	[454, 304, 285, 155]	[399, 279, 265, 143]
median flux density error [mJy]	[167, 206, 196, 249]	[168, 206, 194, 247]
min flux density at SNR > 5[mJy]	[695, 874, 831, 1082]	[744, 876, 854, 963]

fluctuations due to unresolved sources may strongly bias flux estimates with SNR < 5, and the effect is larger for steeper source counts. Source clustering and small-scale structure of the Galactic emission may substantially worsen the problem for low resolution experiments, such as those aimed at mapping the CMB. Simulations of Planck observations (Leach et al. 2008) show that both the fraction of spurious detections and the incompleteness level may be of several percent, even at flux limits corresponding to SNR $\geq$ 5.

Fortunately, the Bright Source Sample discussed in the previous sections, offers the opportunity of an empirical assessment of the completeness and the reliability of samples extracted from the WMAP 23 GHz map in the same area. Follow-up observations at 20 GHz have yielded very accurate flux measurements, allowing us to determine the accuracy of flux and error estimates at the nearby WMAP frequency of 23 GHz. The lessons learned from the comparison of the results of the analysis of 23 GHz maps with the AT20G data provided an useful guidance for the investigation of WMAP all-sky data also at the other WMAP frequencies. We have limited our study to the first 4 WMAP channels, leaving aside the 94 channel because of the normalization problems discussed by López-Caniego et al. (2007) and González-Nuevo et al. (2008).

1 4.1   Detection techniques

The MHW2 is the second member of the Mexican Hat Wavelet filter family (González-Nuevo et al. 2006). It is obtained analytically applying the Laplacian opera-

tor twice on the 2D Gaussian function. It operates locally removing simultaneously the large scale variations originated in the diffuse Galactic foregrounds as well as the small scale noise. The scale at which MHW2 operates can be easily optimized so that the signal-to-noise ratio (SNR) of the sources is maximized. This scale is obtained numerically in an easy way for any given sky patch.

After filtering, the flux is estimated at the position of the maxima. The wavelet can be normalized in such a way that the intensity value at the maxima is equal to the flux of the source. This estimation of the flux is, on average, unbiased. The normalisation of the wavelet is very sensitive to the assumed profile of the signal. In López-Caniego et al. (2007) it was shown how it is possible to go beyond the Gaussian approximation, using the symmetrized radial beam profiles provided by WMAP. We have used the updated 5 year beam profiles for the 5-year data analysis.

In the *simple blind* (SB) approach we look for objects above a given SNR anywhere in the patch. In the *non-blind* (NB) approach, whereby we are looking for WMAP sources at the positions of previously known sources, the patch is chosen so that the source position is right at the center of the patch, and we measure the SNR there. Finally, the *combined blind* (CB) approach consists in producing, for each source detected with the blind approach, new patches centered at the source positions, and in re-estimating the SNRs.

An end-to-end code reads in an input parameter file containing the specific characteristics of the maps to be studied, reads in the input map in FITS format, extracts the patches to be analyzed using the tangential plane approximation, finds for each patch the optimal scale of the wavelet, filters each of them with the MHW2 code, produces a list of detections above a given SNR, converts the positions of the detected objects from the tangent plane to the sphere, and, finally, combines the detections into a single output file.

In the input parameter file we specify how to obtain the patches needed for the analysis. In the general case, the code divides and projects the sky into a sufficient number of square patches such that the whole sky is not only fully covered, but also there is a sufficient amount of overlap among the patches to allow cuts of the borders of the image, if needed. The size of the patches in the sky, the pixel size and the amount of overlap among patches are specified in the parameter file. We have used flat projected patches of $14.6° \times 14.6°$, each containing 128×128 pixels. The pixel area is $6.87' \times 6.87'$, corresponding to the HEALPix resolution parameter $N_{size} = 512$. The patch making routine is part of the CPACK library[4]. There is also the option of inputting the list of coordinates of the centers of the patches, corresponding to the known positions of the sources in the cases of the non-blind and of the combined blind approaches. In the following subsections we will describe in detail how the algorithms work for each approach.

1 4.1.1   Simple blind approach

The program reads in the input parameter file and the map in FITS format and calculates the number of flat patches to be extracted and the coordinates of their centers. For our choice of the input parameters ($14.6° \times 14.6°$ patches with $3°$ overlap) the program extracts 371 flat patches. Next, the code loops over each of them, finding the optimal

---

[4]http://astro.ic.ac.uk/∼mortlock/cpack/

scale, filtering the maps with the MHW2 at such optimal scale and detecting objects with SNR ≥ 3. For each patch a temporary catalogue is obtained, and for each object, the flux at the position of the corresponding peak is estimated. Finally, the temporary catalogues are combined into a final one, removing duplications (in the case of multiple detections of the same source we select the one with the brightest flux, that normally corresponds to the most accurate position).

The rms of the map is obtained via a three step process. First, in order to avoid border effects after filtering, a 15 pixel border around the maps is flagged. Second, all the maxima in the image are identified and a histogram of their values is obtained. Then, the 5 per cent brightest maxima are masked, flagging the pixels within a 2 FWHM radius from the position of the maxima. Finally, the rms of the map is calculated excluding the flagged pixels.

1 4.1.2   Non-blind approach

In the non-blind approach the patches to be analyzed are centered at the positions of the objects we want to investigate. Since the position of the source is already known, the goal is to get a good characterization of the noise rms level in the vicinity of the source. The algorithm goes as for the blind approach, with the following differences: i) we have an additional input file, containing the coordinates of the objects; ii) we look for maxima within a circle around the patch center, with 1 FWHM radius; iii) the rms fluctuation level is estimated taking into account only a corona around the patch center, with inner radius of 1 FWHM and an outer radius of 3 FWHM.

In practice, the amplitude of the central maximum (if any) gives an estimate of the source flux, and to compute the rms noise we apply the flagging of pixels at the border, the search of maxima, and the flagging of the 5 per cent brightest, only to the corona. In this way, we try to get a more accurate estimate of the noise in the vicinity of the object of interest, avoiding the contamination by other bright nearby objects.

The application of this approach builds on the work by López-Caniego et al. (2007) who have looked for signals in WMAP 3-year maps at the positions of 2491 sources forming a complete sample mostly selected at 5 GHz, briefly described in section 1 4.2. They detected 369 of these sources with SNR ≥ 5 in at least one WMAP channel. The detection efficiency is therefore of only 14.8%. The lower noise level in WMAP 5-year data can allow the SNR ≥ 5 detection of somewhat, but not much, fainter sources. Thus, in the analysis of the 5 year maps, we limited our non-blind search to the 933 sources in the López-Caniego et al. (2007) associated to SNR ≥ 3 peaks in the 3-yr maps.

As discussed below, the AT20G Bright Source Sample (BSS), complete to $S_{20\,\mathrm{GHz}} = 0.5\,\mathrm{Jy}$ and covering about $1.5 \times 10^4\,\mathrm{deg}^2$, is particularly useful to test the performances of our detection algorithms. Our non-blind approach was applied to this sample.

1 4.1.3   Combined blind approach

The combined blind method can be regarded as a two-step iterative method. The first step follows the procedure described in §1 4.1.1 and produces as output a list of coordinates that are fed to the non-blind scheme of §1 4.1.2. In this way we hoped to

Table 1 6 Summary of the large-area surveys of point sources used to generate the initial catalogue.

Frequency	Catalogue	S_{lim}(mJy)	DEC range	Angular resolution	References
	GB6	18	0　　− +75	3.5'	Gregory et al. 1996
	PMNE	40	- 9.5 − +10	4.2'	Griffith et al. 1995
4.85 GHz	PMNT	42	-29　− - 9.5	4.2'	Griffith et al. 1994
	PMNZ	72	-37　− -29	4.2'	Wright et al. 1996
	PMNS	20	-87.5 − -37	4.2'	Wright et al. 1994
1.4 GHz	NVSS	2.5	-40　− +90	45"	Condon et al. 1998
0.843 GHz	SUMSS	18	-50　− -30	45"cosec$|\delta|$	Mauch et al. 2003
		8	-90　− -50	45"cosec$|\delta|$	

combine the potential of the blind detection with the advantages of the local noise estimation of the non-blind method.

1 4.2　The non-blind NEWPS_3yr

A summary of the multi–steradian surveys that we have used[5] is given in Table 1 6. The highest frequency for which an almost complete sky coverage has been achieved is $\simeq$ 5 GHz, thanks to the combined 4.85 GHz GB6 and PMN surveys with an angular resolution of 3.5′ and 4.2′, respectively, and a flux limit ranging from 18 to 72 mJy. The CRATES catalogue at 8.4 GHz (Healey et al. 2008) was not available when we made this exercise, and in any case it only contains flat spectrum sources. Deeper and higher resolution surveys have been carried out at 1.4 (NVSS; FIRST, Becker et al. 1995) and 0.843 GHz (SUMSS); altogether these surveys cover the full sky.

Since 'flat-spectrum' AGNs are expected to be the dominant source population in the millimetric wavelength band, whereas other classes of sources, and in particular the steep-spectrum sources which increasingly dominate with decreasing frequency, are only giving minor contributions to the number counts at WMAP frequencies and sensitivities (De Zotti et al. 2006), we chose to adopt 5 GHz as our reference frequency, and used lower frequency surveys to fill the 'hole' at 5 GHz.

Altogether, the catalogues listed in Table 1 6 contain over 2 million sources, but we already know that for only a tiny fraction ($\sim 2 \times 10^{-4}$) of them the WMAP data can provide useful information. Applying the MHW2 at the positions of all these sources would be extremely inefficient. Therefore, we decided to work with a complete sub-sample containing sources with $S_{5\mathrm{GHz}} \geq 500\,\mathrm{mJy}$. This limiting flux corresponds to about 2–3 times the mean noise in the filtered images we will be dealing with. To fill the 5 GHz 'holes' we have picked up NVSS or SUMSS (in the region not covered by the NVSS) sources brighter than 500 mJy at the survey frequency. In this way we obtained an all-sky sub-sample of 4050 objects. After having removed sources in the strip $|b| \leq 5°$, and in the LMC region

---

[5]A new version of the SUMSS has been released in March 2008 in which the source number has been almost doubled, but it was not yet available when the initial catalogue has been prepared, so we will refer in this section to the 'old' version by Mauch et al. (2003).

(i.e. inside the circle of 5.5° radius centered at $\alpha = 5^h23^m34^s.7$, $\delta = -69°45'22''$, J2000; $l = 280.47°$, $b = -32.89°$) and the well-known Galactic sources outside of these zones (Taurus A, Orion A & B, and the planetary nebula IC 418/PMNJ0527-1241) we are left with 2491 objects making up our 'Input Catalogue' (IC). Note that some Galactic objects are still present in the selected IC.

Of the 381 sources that we detected with the non-blind technique at signal-to-noise level larger than 5 (NEWPS_3yr_5σ sample) only 283 are listed in the WMAP_3yr catalogue. As expected, the a priori knowledge of source positions has allowed us to significantly increase the detection efficiency with respect to the WMAP_3yr results. Also, for 39 (26+13) WMAP sources our approach yields a signal-to-noise ratio < 5.

In addition, as already mentioned, there are 25 WMAP sources left out by our low-frequency selection, but included in our analysis. Only 12 of them are detected at signal-to-noise ratio≥ 5 by our approach, and only 3 have 23 GHz flux densities above the estimated completeness limit of 1.1 Jy. Of our 12 sources with signal-to-noise ratio≥ 5, 10 have low-frequency flux densities $\geq 270\,\mathrm{mJy}$ (8 of them are above 340 mJy) and may well be variable sources, that happened to be in a particularly 'high' phase at the time of WMAP observations. The source with $S_{5\mathrm{GHz}} = 120\,\mathrm{mJy}$ has an inverted spectrum (i.e. a spectrum rising with frequency) and the last one, with $S_{5\mathrm{GHz}} = 38\,\mathrm{mJy}$, may be a spurious detection.

The flux estimates showed small systematic differences, increasing with frequency, with those obtained by the WMAP team. These differences were attributed to different approximations of the beam shapes. In fact, the beams are complex and asymmetrical. Taking also into account that sources are observed with different beam orientations, it is clear that the effective beam areas and, therefore, the flux calibrations, are uncertain.

To check the calibration of López-Caniego et al. (2007) fluxes we have looked for ground based measurements of NEWPS_3yr_5σ sources at frequencies close to the WMAP ones, finding small but appreciable systematic differences. This prompted us to investigate in more detail the calibration problem, by comparing with ground-based measurements at the closest frequencies and by directly estimating the effective beam areas for the brightest sources.

In fact, the correction factors to the flux density introduced by the effective beam areas calculated using the symmetrized beam profiles given by the WMAP team are [1.05, 1.086, 1.136, 1.15] at [23, 33, 41, 61] GHz, respectively. The comparison of fluxes determined from the WMAP 5-year maps with those listed in the NEWPS_3yr catalogue shows good agreement if the same calibration, described in González-Nuevo et al. 2008, is applied. The same correction factors have been applied also in the following analysis of the 5 year maps.

1 4.3 Blind vs non-blind detection on the 5-year WMAP maps: comparison with AT20G data

The prior knowledge of source coordinates has the obvious advantage that source detection algorithms need to determine only one parameter, i.e. the source flux, while blind detection must deal also with the 2 additional parameters defining the source position, and are exposed to be misled by source blending or small-scale structure in the Galactic
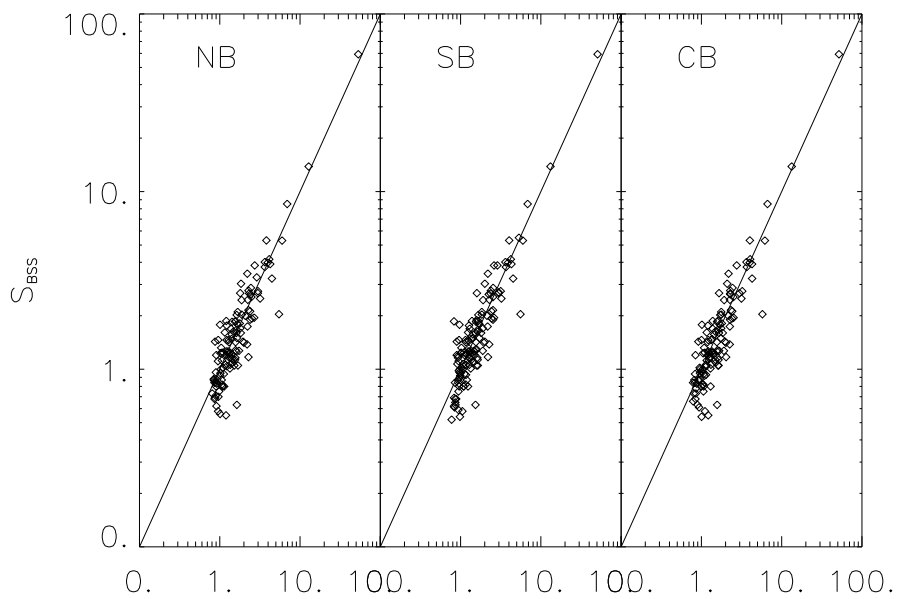
Figure 1 22 Comparison of flux densities estimated from WMAP maps with our 3 methods with the AT20G ones. The agreement is good except for the systematic offset at faint flux densities (see text for a discussion).
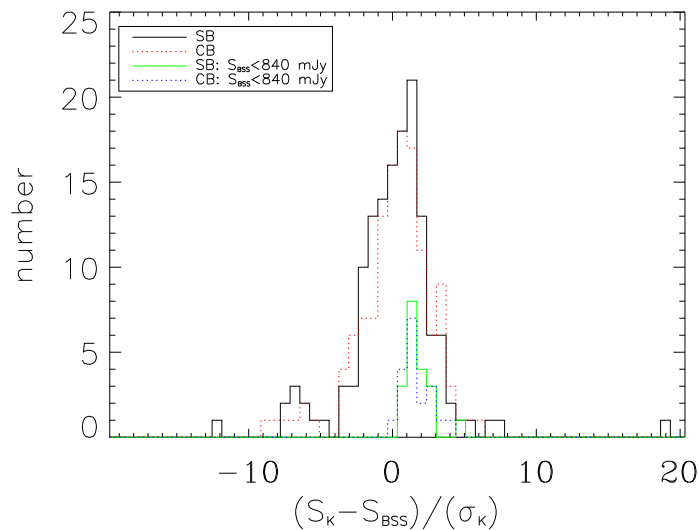
Figure 1 23 Distribution of the ratio of 'true' to estimated errors. $S_{\rm BSS}$ is the ATCA flux density, measured with very high SNR, that we assume to be the 'true' value. $S_{\rm K}$ and $\sigma_{\rm K}$ are our flux and error estimates from the WMAP K-band map with the SB and CB methods (see inset). The histograms labeled $S_{\rm BSS} < 840\,{\rm mJy}$ in the inset include only the faint sources whose $S_{\rm K}$ is systematically higher than $S_{\rm BSS}$ (see Fig. 1 22).

emission.

On the other hand, catalogues obtained from a non-blind approach are liable to various possible sources of incompleteness ensuing from the selection that has produced the input catalogue. The latter may have been generated by a survey at a different frequency (generally lower than WMAP's), with different angular resolution (generally much higher than WMAP's), carried out at a different epoch. A lower frequency survey may easily miss sources with strongly inverted (i.e. increasing with increasing frequency) spectra. High angular resolution observations (especially the interferometric ones) are insensitive to extended sources, or may pick up only their compact spots, while the sources may be much brighter at the WMAP resolution. Observations at different epochs may catch variable sources in different stages, so that a source that is too faint to be included in the input catalogue may be detected by WMAP, and vice versa.

The AT20G Bright Source Sample (BSS) minimizes the problems mentioned above: i) it has been selected at 20 GHz, i.e. at a frequency close to that of the WMAP K-band channel; ii) the survey has been carried out from 2004 to 2007, i.e. in a period overlapping that of WMAP 5-year maps (obtained averaging over the data collected in 2001-2006). As pointed out by Sadler et al. (2006), on a 1-2 yr time-scale, the general level of variability at 20 GHz appears to be low. The only completeness problem of the BSS for our analysis is related to the size $(2.4')$ of the 20 GHz ATCA primary beam. The ensuing incomplete sampling of extended sources will be discussed in the following. Because of its properties, the AT20G BSS constitutes an excellent benchmark against which we may test the performances of blind and non-blind detection techniques applied to the WMAP 23 GHz maps.

Thus, first of all we have performed the Simple Blind (SB) and Combined Blind (CB) searches on the WMAP 5-yr 23 GHz maps and analyzed the results over the area of the AT20G BSS $(\delta < -15°)$, cutting out the Galactic plane region $(|b| < 5°)$. This cut removes 26 of the 320 BSS sources. Of the remaining 294 sources, 124 have $S_{BSS} > 1\,$Jy. Next we repeated the search non-blindly, on patches centered at the BSS source positions on the WMAP K-band map. The non-blind technique detected 125 sources (96 with $S_{20\,GHz} > 1\,$Jy) with SNR > 5; the mean flux density error is of 212 mJy and the minimum detected flux density is of 767 mJy.

The association of peaks in WMAP maps with BSS sources was made adopting a search radius of $21.35'$, i.e. equal to $\sigma = \text{FWHM}/2\sqrt{2\ln 2}$ for FWHM $= 50.277$ arcmin. The position of a detection is given by the coordinates of the pixel where a local maximum is found. The median of the distances of the SB detections from the real positions of the sources (given by the AT20G BSS) is $3.7'$ (for the combined blind it is $3.3'$), so the positions are typically correct within a pixel for most ($\sim 83\%$) of the objects (the pixel size for the WMAP maps is $6.87'$).

The simple (combined) blind search recovers 140 (128) BSS sources: 114 (115) are in common with the non-blindly detected sample, but 26 (13) BSS sources have been detected only blindly. 14 (27) BSS sources with $S_{BSS} > 1\,$Jy remain undetected at SNR > 5 level (but all show up as local maxima with a lower SNR). Flux estimations are consistent with the BSS measurements, at least for the brightest objects. The faintest BSS sources with $S_{BSS} > 1\,$Jy undetected at SNR > 5 level are mostly underestimated: that is probably because they lie over a negative peak of noise. Furthermore, the search yielded 41 (30)
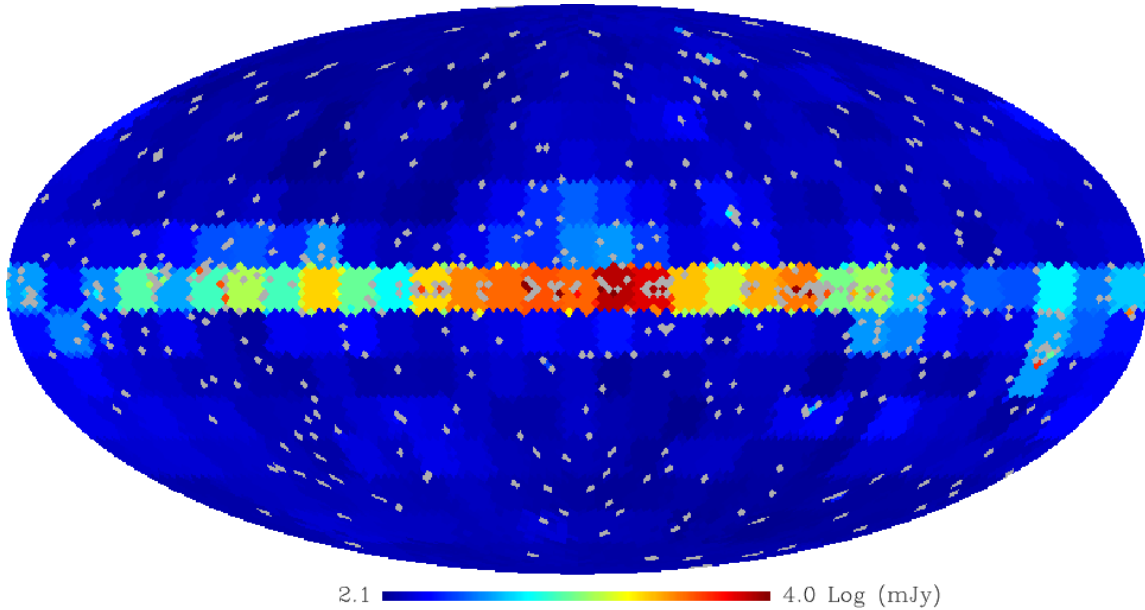
Figure 1 24 Map (Mollweide projection in Galactic coordinates) of σ_{pixel} for the SB approach. The pixel area is of $\simeq 3.36\,\mathrm{deg}^2$ (HEALpix pixelization with $N_{side} = 32$). The patches and the 3° overlaps among detection patches are discernible.

detections of objects that are not in the BSS.

1 4.3.1 Accuracy of flux density and error estimates

A comparison of the flux densities derived from the WMAP maps with those measured by the AT20G survey is shown in Fig. 1 22. The agreement is generally good, except for the faintest levels ($S_{BSS} < 840\,\mathrm{mJy}$) where the WMAP fluxes are systematically higher. Since there are no indications that the faint sources are extended and may therefore be resolved by the AT20G, the discrepancy is likely due to a swelling of the peak at WMAP resolution when the sources happen to be on top of large positive fluctuations due to other components (noise, Galactic emission, CMB). There is no obvious way to identify sources affected by this problem using WMAP data only, and this is another instance of the importance of complementary, higher resolution data. Such sources are not found in particularly contaminated regions; on the contrary, the associated noise values are generally rather low.

The comparison with AT20G flux densities, measured with very high SNRs, that we assume to be the 'true' values, with the flux and error estimates from WMAP maps with our 3 methods allow us to assess also the reliability of error estimates. The results are illustrated by Fig. 1 23. After having removed the sources with $S_{BSS} < 840\,\mathrm{mJy}$, whose fluxes are systematically overestimated, the median ($S_{BSS} - S_K$) is 124 mJy for the simple blind and 41 mJy for the combined blind respectively. The error on the median has been estimated as (Arkin & Colton 1970) $\sigma_{median,\ \Delta S} = 1.2533/[\sum_i (1/\sigma_{K,i})^2]^{1/2}$. The median of ($S_{BSS} - S_K$)/$\sigma_K$ is 0.77 for the simple blind and 0.40 for the combined blind respectively. The standard deviation of ($S_{BSS} - S_K$)/σ_K is 2.0 for the SB and 2.4 for the CB sample; more

than 94% of the sources lie within 3 standard deviations from the mean (both including and removing the sources with $S_{\mathrm{BSS}} < 840\,\mathrm{mJy}$. The fact that the rms differences between the BSS fluxes, S_{BSS}, and our estimates from WMAP K-band maps, S_{K}, are about twice the average σ_{K} is not surprising. As pointed out by López-Caniego et al. (2007), by applying the optimum filters to WMAP temperature maps we get an average amplification of the SNR, or equivalently, a damping of the fluctuation level, by a factor of almost 3. In other words, the noise level in the original map, that determines the true uncertainty on the flux estimate, is substantially higher than that in the filtered map, used to estimate σ_{K}. The ratio of the two noise levels is a measure of the detection efficiency of the adopted algorithm.

1 4.3.2 Reliability of detections

As mentioned above, the SB (CB) approaches yielded 41 (30) detections without a BSS counterpart. To check whether these sources are real we have looked for counterparts in the NASA Extragalactic Database (NED[6]). The search yielded 15 (12) extragalactic and 9 (4) Galactic sources. The BSS is biased against Galactic sources, mostly because they are generally extended; in fact no known Galactic source is included in it. It has also completely missed the very extended extragalactic source Fornax A (detected in WMAP maps). All the other extragalactic sources that have been detected by our blind techniques were also detected by the AT20G survey, but below the BSS flux density threshold. Since accurate estimates of the total flux density of the other known extended sources in the area have been obtained with ATCA observations in the mosaic mode, the discrepancy cannot be attributed to resolution effects, and in fact there is no indication that the sources in question are extended. We therefore conclude that the K-band fluxes are overestimated, probably because these sources happen to be on top of positive fluctuations of noise and/or Galactic and/or CMB signals within the WMAP beam.

The 17 (14) objects that do not have a consistent counterpart in the NED may be knots in the Galactic emission, as suggested by the fact that 14 (9) of these sources are at $|b| < 20°$. To better characterize the sky regions more liable to the occurrence of spurious detections we have produced a 23 GHz noise map (Fig. 1 24) with pixels size of $\simeq 3.36\,\mathrm{deg}^2$, corresponding to the HEALPix $\mathrm{N_{size}} = 32$ (the size of patches discussed above corresponds to $\mathrm{N_{size}} = 4$). Figure 1 25 shows that a $\pm 10°$ Galactic cut removes almost all the most contaminated pixels, but also some clean regions. The $\pm 5°$ Galactic cut that we have used so far seems to be a better compromise between removing very dirty regions and saving clean ones. However, the selection could be improved by selecting a mask for contaminated regions exploiting the information given by the noise map itself.

As illustrated by Fig. 1 26, most (but not all) of the objects that do not have a consistent counterpart in the NED lie in regions where the noise level is relatively high. Dropping areas with $\sigma_{\mathrm{pixel}} \geq 1.5\sigma_{\mathrm{median}} = 253\,\mathrm{mJy}$ at 23 GHz, where $\sigma_{\mathrm{median}} = 169\,\mathrm{mJy}$ is the median noise level for all pixels at $|b| > 5°$, removes 17 (11) sources, of which 9 (5) are doubtful objects, at the cost of losing $\simeq 7\%$ of the sky region with $|b| > 5°$ covered by the AT20G BSS (the remaining area amounts to 3.77 sr). This criterion is a good trade-off between completeness and reliability of the sample, and we will adopt it for the all-sky

---

[6]http://nedwww.ipac.caltech.edu/
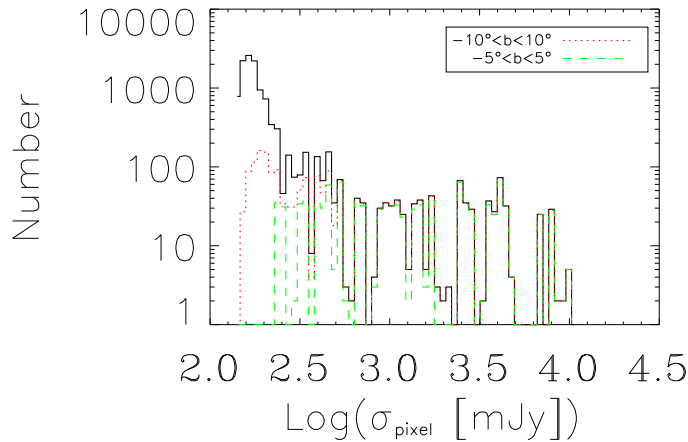
Figure 1 25 Distribution of the values of σ_{pixel} (pixels size of $\simeq 3.36\,\mathrm{deg}^2$) over the whole sky (solid line), the region within $|b| < 10°$ (dotted line), and the region within $|b| < 5°$ (dashed line).

analysis. As for the reliability, only 8 (9) sources detected by the SB (CB) approach in regions with $\sigma_{\mathrm{pixel}} < 1.5\sigma_{\mathrm{median}}$ do not have a consistent low-frequency counterpart. If they are all spurious, the sample reliability is 95.5% (94.3%).

1 4.3.3 Completeness

The inhomogeneity of the fluctuation field translates into a spatially varying effective depth of the survey. Correspondingly, the effective area to be used to derive the source counts decreases with decreasing flux limit. This is illustrated by Fig. 1 24 showing the map of the noise within the $\simeq 3.36\,\mathrm{deg}^2$ pixels, (σ_{pixel}). Note that σ_{pixel} is approximately the same in all the pixels within a detection patch and vary on the edge of it because of the overlap among patches. The regions of both higher (Galactic plane, Orion region, Ophiuchus complex, LMC, ...) and lower (Ecliptic pole regions) fluctuation levels can be clearly discerned (particularly in the colour version).

Our final sample is almost 100% complete over the unmasked BSS area above 2 Jy (only 1 source with $S_{\mathrm{BSS}} = 2.06$ Jy is detected with SNR < 5 level). Considering only detections by the simple (combined) blind methods, the completeness is 89% (80%) above 1 Jy; it increases to 91% (82%) including the non-blind detections. The decrease in the detection fraction with decreasing flux density is consistent with the decrease of the effective area (Fig. 1 27).

1 4.3.4 Simple blind vs combined blind approach

The performances of SB and CB methods are similar. The SB method recovers with SNR > 5 more sources also in highly contaminated regions, but in those regions the fraction of spurious detections is also higher. Hence, choosing among the two approaches
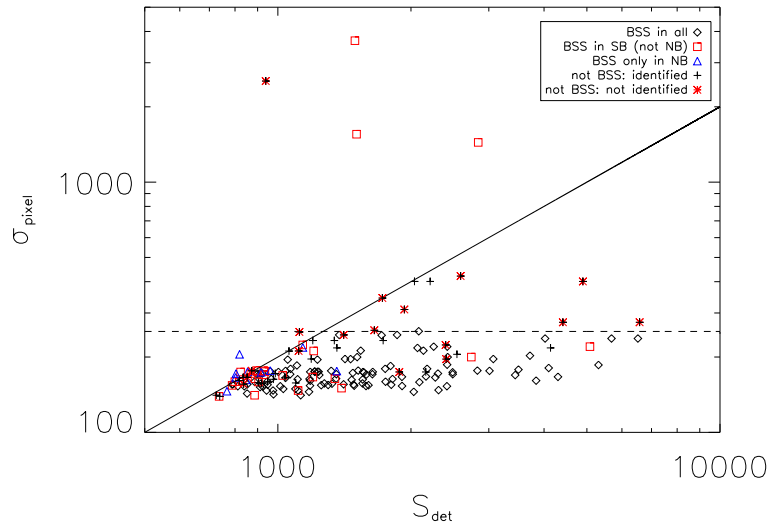
Figure 1 26 Noise at the source position versus flux density at 23 GHz estimated with the SB approach. The dashed line corresponds to 1.5 times the median noise for the pixels at $|b| > 5°$. The solid line corresponds to $S_K = 5\sigma_{pixel}$. 11 sources have $S_K < 5\sigma_{pixel}$ and correspond to SNR > 5 detections in highly contaminated pixels ($\sigma_{pixel} \gg \sigma_K$; remember that σ_K is computed over a much larger area than σ_{pixel}.).

amounts to choosing among slightly higher completeness (SB) and slightly higher reliability (CB). On the whole, there is no clear advantage in adopting the more complex CB approach, and we will no longer consider it.

1 4.4 Blind and non-blind source detection on all-sky WMAP 5-yr maps.

The analysis of the BSS sample, described above, provides useful guidance for the analysis of all-sky WMAP 5-yr maps at 23, 33, 41 and 61 GHz, to produce the NEWPS_5yr catalogue. For each map we have performed the following steps.

- We have carried out a simple blind search over the whole sky.

- We have produced maps of the mean noise values per pixel corresponding to $N_{size} = 32$, σ_{pixel}, and computed the median of such values for $|b| < 5°$, σ_{median}.

- We have masked all the pixels with noise level $> 1.5\sigma_{median}$, which, as found in the previous analysis, contain most of the doubtful detections.

- We have taken all the sources with SNR > 5 outside the masked area as true detections.

- By counting the number of pixels for which $5\sigma_{pixel}$ is smaller than any given flux density limit, S_{lim}, we obtain the effective area, as a function of S_{lim}, to be used to

Table 1 7 Summary of the properties of the NEWPS_5yr_5σ catalogue. Areas with $\sigma_{\mathrm{pixel}} > 1.5\sigma_{\mathrm{median}}$ have been left aside.

	Total	23 GHz	33 GHz	41 GHz	61 GHz
σ_{median} (mJy)		169	206	196	250
Area selected [sr]		10.32	11.12	11.24	11.25
Simple blind detections		405	281	275	147
Additional non-blind detections		28	26	26	14
Total number of objects $|b| > 5°$	516	433	307	301	161
Total number of objects with $|b| < 10°$	51				
Total number of objects within the LMC boundaries	10				
Total number of identified Galactic objects	27	11	14	21	10
Total number of identified extragalactic objects	457	406	281	268	147
Total number of objects missing a consistent counterpart	31	16	12	12	4
Number of sources in WMAP_5yr	352				
Number of sources only in WMAP_5yr	36				
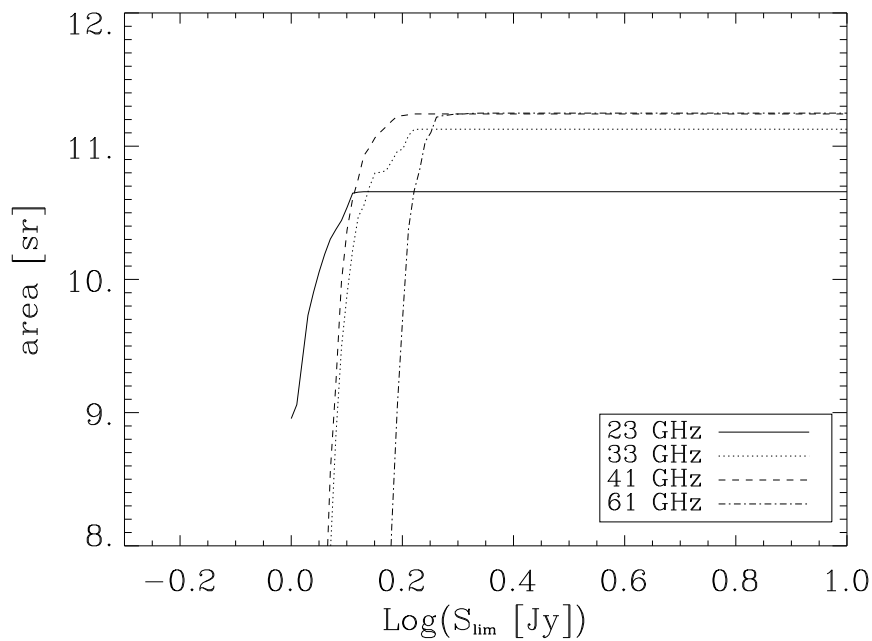
Figure 1 27 Effective area as a function of the flux limit $S_{\mathrm{lim}} = 5\sigma_{\mathrm{pixel}}$.
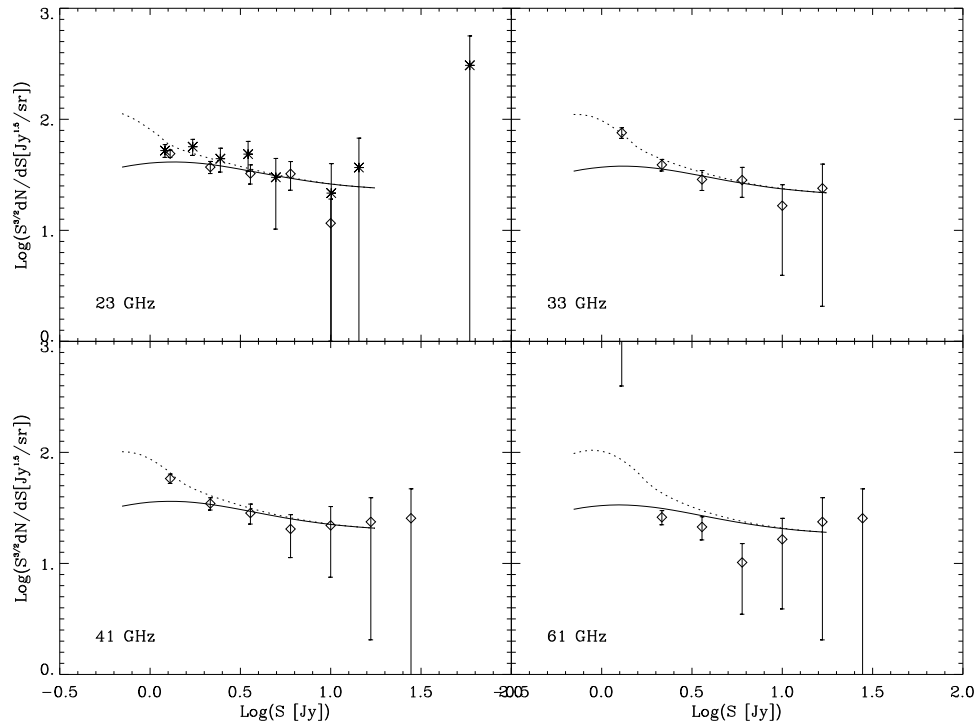
Figure 1 28 Differential WMAP counts, normalized to $S_{\mathrm{Jy}}^{-2.5}$, estimated from the WMAP data (diamonds). The 23 GHz counts are compared with the ATCA 20 GHz ones (asterisks). The solid line shows the predictions of the model by De Zotti et al. (2005). The dotted line illustrates the effect of the Eddington bias by showing the model counts convolved with a Gaussian error distribution with $\sigma = 0.34, 0.42, 0.4, 0.5$ Jy at 23, 33, 41, and 61 GHz, respectively. The value of σ at 23 GHz was obtained by comparison with the BSS measurements. At higher frequencies we assumed that the true errors on flux measurements are twice the median errors yielded by the simple blind approach, as found at 23 GHz. The convolution has been computed integrating down to a minimum flux equal to $S/10$.

estimate the differential source counts (see Fig. 1 27). The maximum effective area is given, for each WMAP channel, in the second row of Table 1 7.

Next, we carried out a non-blind search on the 5-yr WMAP maps at the positions of sources in the NEWPS_3yr_3σ sample. This search has produced 28 additional SNR > 5 detections at 23 GHz.

The main properties of the NEWPS_5yr_5σ catalogue, including SNR > 5 detections obtained with both the blind and the non-blind approach, are summarized in Table 1 7. The sample totals 516 sources detected in the regions where $\sigma_{\mathrm{pixel}} \leq 1.5\sigma_{\mathrm{median}}$. A search in the NED yielded 457 identifications with extragalactic sources and 27 identifications with Galactic objects. Only for 32 objects no consistent counterparts were found. Even if they are all spurious, the reliability of our sample is of 93.8%, close to that found from the comparison with the BSS sample. The source list and a list of notes on the identification of individual sources is in the Appendix 2 and 2.1.

Identifications have been performed by searching within a beam radius and in the region surrounding the source position in the NED. The database provides mainly data

Table 1 8 The differential normalized source counts ($\log(S^{3/2}dN/dS[\mathrm{Jy}^{1.5}/\mathrm{sr}])$) of WMAP sources for each channel per bin of $\log S[\mathrm{Jy}]$. Note that no correction for Eddington bias has been applied(see the text for details).

log S [Jy]	23 GHz	33 GHz	41 GHz	61 GHz
0.1	$1.69^{+0.03}_{-0.03}$	$1.87^{+0.04}_{-0.05}$	$1.77^{0.04}_{-0.04}$	$3.51^{0.27}_{-0.91}$
0.3	$1.57^{+0.05}_{-0.06}$	$1.59^{+0.05}_{-0.06}$	$1.54^{0.05}_{-0.06}$	$1.42^{0.06}_{-0.07}$
0.5	$1.51^{+0.08}_{-0.09}$	$1.46^{+0.08}_{-0.10}$	$1.45^{0.08}_{-0.10}$	$1.33^{0.09}_{-0.12}$
0.8	$1.51^{+0.11}_{-0.15}$	$1.45^{+0.11}_{-0.16}$	$1.31^{0.13}_{-0.26}$	$1.01^{0.17}_{-0.47}$
1.0	$1.06^{+0.22}_{-1.06}$	$1.22^{+0.19}_{-0.63}$	$1.34^{0.17}_{-0.47}$	$1.22^{0.19}_{-0.63}$
1.2		$1.38^{+0.22}_{-1.06}$	$1.37^{0.22}_{-1.06}$	$1.37^{0.22}_{-1.06}$
1.4			$1.41^{0.26}_{-11.41}$	$1.41^{0.27}_{-11.41}$

drawn from low frequency catalogues, and only few well-known bright objects have data from observations throughout the whole radio spectral band. For this reason, a source was considered a counterpart for our detections only if the low frequency flux density and/or the spectral behaviour are consistent with the observed flux densities at the WMAP frequency channels (e.g. flux density at 5 GHz above 500 mJy, inverted spectrum between 1 and 5 GHz ...). If, for example, in the region of a detection no compact object can be considered as a counterpart and/or there was an extended structure that may affect the flux estimation, then we consider that there is no clear counterpart to the detection and it is a candidate spurious object. Note that this approach guarantees the reliability of the final catalogue, but does not diminish the power of the detection tool, that correctly detects also the small scale contribution from extended structures, but is not suited to distinguish them from compact sources.

Of the 388 WMAP_5yr sources in the sky region covered by the NEWPS_5yr_5σ catalogue, 352 have been recovered. All the other 36 have detections below our SNR > 5 threshold. On the other hand, the NEWPS_5yr_5σ catalogue contains 164 objects not in WMAP_5yr. 31 of the new sources are among those that do not have consistent counterparts in low frequency catalogs and may therefore be spurious.

Of the 64 sources detected by Chen & Wright (2008) in the 3-yr catalogue, 50 are in our NEWPS_3yr at 61 GHz. All the 64 objects have been recovered in the present analysis, but 6 of them are below the SNR = 5 threshold. Our NEWPS_5yr_5σ catalogue also includes all the sources detected by Nie & Zhang (2007) outside the LMC region and at $|b| > 5°$, not present in the 3-year WMAP catalogue.

The counts of WMAP sources for each channel are presented in Table 1 8 and in Fig. 1 28. They have been estimated calculating the effective area over which each source could have been observed (Fig. 1 27) and summing the inverse areas in the flux density bin of interest (Katgert et al. 1973). Error estimates use the approximation formulae for a Poisson statistics recommended by Gehrels (1986), with an effective number of sources

$$n_{\mathrm{eff}} = \frac{(\sum_i (1/A_i))^2}{\sum_i (1/A_i)^2} \ . \tag{1.5}$$

As expected, the counts are systematically overestimated at the faintest flux densities, by effect of the Eddington bias (Eddington 1913, Murdoch et al. 1973). At 23 GHz, the De Zotti et al. (2005) model suggests that the overestimate is of about 15% at 2 Jy, and rapidly increases with decreasing flux (it is $\simeq 30$ per cent at 1.5 Jy, and reaches a factor of almost 2 at 1 Jy).

The NASA Extragalactic Database (NED) provided values of redshift for 385 sources.

The redshift distribution for the latter subsample is shown in Fig. 1 29, where the dashed, dotdashed and solid histograms refer to QSOs, galaxies and to the total, respectively. The median redshift of the sample is 0.86 (0.058 for the 80 Galaxies with redshift, 1.037 for the 301 QSOs). We have also plotted, for comparison, the redshift distributions predicted by the De Zotti et al. (2005) model for different source populations. The agreement is generally good, except for the dip in the data around log(z)=-1, where the model predicts a little bump due to Fanaroff-Riley type II (FR II) sources. The reason of this discrepancy is unclear. The most obvious option is that FR II sources are not correctly modelled, but other possibilities, such as a large-scale inhomogeneity in the distribution of bright radio sources, cannot be ruled out.

A similar behaviour has been found for the NEWPS_3yr data by González-Nuevo et al. (2008).

1 4.5 The NEWPS catalogue: discussion and conclusions

We have analyzed the efficiency in source detection and flux density estimation of *blind* and *non-blind* detection techniques based on the MHW2 filter applied to the WMAP 5-year maps. Comparing with a complete sample of radio sources, the AT20G Bright Source Sample, selected at 20 GHz, close to the lowest WMAP frequency, with very high signal-to-noise flux measurements, and almost contemporary to the WMAP survey, we estimated the completeness, the reliability, and the accuracy of flux density and error estimates for the samples detected with the two approaches.

We found that flux density estimates are unbiased except at the faintest flux densities ($S_{\mathrm{BSS}} < 840\,\mathrm{mJy}$), where the fraction of the source intensity peaks amplified by positive fluctuations due to other components (Galaxy, CMB, noise) within the WMAP beam becomes substantial and the source counts are correspondingly overestimated. This is a manifestation of the Eddington bias, enhanced by the fact that the true errors on flux density estimates turn out to be about a factor of 2 higher than the errors estimated by our procedure (see §1 4.3.1). The difference is due to the filtering of the maps that increases the signal-to-noise ratio by smoothing the fluctuation field. No clear-cut criterion capable of identifying sources affected by this problem using only WMAP data was found. However, the estimate of the true uncertainties obtained by comparison with the high signal-to-noise AT20G measurements, and the information on counts of sources below the WMAP detection limit provided by the AT20G (Massardi et al. 2008; Ricci et al. 2004) and 9C (Waldram et al. 2003) surveys at nearby frequencies allow us to correct the WMAP source counts. In the K-band, the downward correction is of about 15 per cent at 2 Jy, and rapidly increases to a factor of almost 2 at 1 Jy.

At higher flux densities most (17 out of 19) of probably spurious detections are at
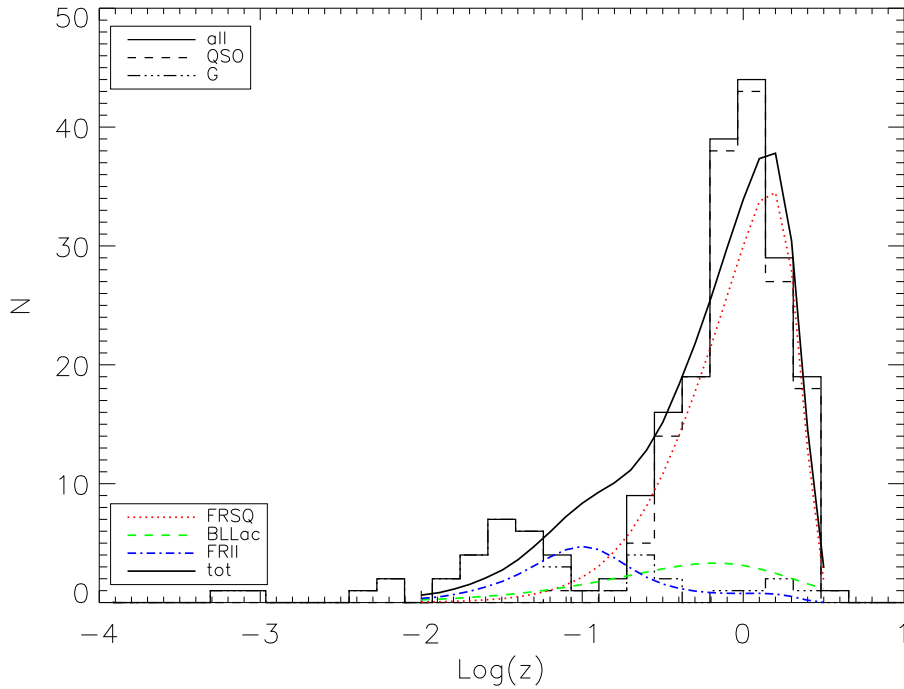
Figure 1 29 Redshift distributions of all the 381 sources of the NEWPS_5yr sample with a measure of redshift in the NED, the QSOs only and the galaxies (solid, dashed and dot-dashed histograms, respectively). The dotted, dashed and dot-dashed curves display, for comparison, the predictions of the model by De Zotti et al. (2005) for Flat-Spectrum Radio QSOs, BL Lacs, FR II sources, while the solid line shows the total.

relatively low Galactic latitudes ($|b| < 20°$), suggesting that the observed intensity peaks are largely due to small scale in the Galactic emission. Excluding the areas where the rms fluctuations are more than 50 per cent higher than the $|b| > 5°$ median approximately halves the number of dubious candidates, at a modest cost ($\simeq$ 7–10 per cent) in terms of useful area. If all dubious sources are spurious, the reliability of the sample is 95.5 per cent.

The blind detection approach applied to the all-sky WMAP maps, excluding the Galactic plane region ($|b| < 5°$) and the areas where the rms fluctuations are more than 50 per cent higher than the median value at $|b| < 5°$, has found 488 candidate sources with SNR > 5 in at least one WMAP channel. The non-blind approach has added 28 further objects, raising the total to 516, to be compared with the 388 sources listed in the WMAP 5-yr catalog (Wright et al. 2008). Almost all (484) sources in our sample were previously catalogued extragalactic (457) or Galactic (27) objects. The remaining 32 candidate sources do not have counterparts in lower frequency all sky surveys with comparable flux densities and may therefore be just high peaks in the distribution of other components present in the maps. If they are all spurious, the reliability of the sample is 93.8 per cent.

Part 2

The Sunyaev-Zel'dovich effect

2 1 The Sunyaev-Zel'dovich effect signal on various angular scales

The Sunyaev-Zel'dovich (SZ) effect is a powerful tool to study cosmology and the properties of the structures where it is observed (see Sunyaev & Zel'dovich 1972, 1980 and 1981, Birkinshaw 1999, Carlstrom et al. 2002). Since, as we will show below, the SZ effect depends only on the properties of the electron distribution and, if not integrated over the angular size of the cloud, it is independent of the distance of the cloud, it is a well-suited tool to investigate objects permeated by ionized gas clouds at any redshift.

Galaxy clusters are the most massive virialized object ever observed. They are permeated by hot dense completely ionized gas that constitutes the IntraCluster Medium (ICM). At 20 GHz the SZ effect signal is of the order of 1 mJy or less for a galaxy cluster with electron density $n_e \sim 10^{-3}$ cm^{-3} and temperature $T_e = 10^7$ K. For this reason, galaxy clusters are the only SZ sources observable with the available telescopes.

Different models (White & Frenk 1991; Kauffmann et al. 1993; Cole et al. 1994; Somerville & Primack 1999; Benson et al. 2003; Granato et al. 2004) describe galaxy formation as the virial collapse of massive clouds of primordial gas at redshift $z > 2$. Collapsing, the gas grew denser and hot enough to inverse Compton scatter the CMB photons. All the mentioned methods adopt a similar mass function of dark matter halos, a cosmological gas to dark matter ratio at virialization, and assume that all the gas is heated to the virial temperature. A SZ effect is produced on the galaxy angular scales: the amplitude of the signal strongly depends on the mass of the virializing cloud but it is not easily observable with existing telescopes, as we will show in the next chapters.

Let's review here some of the main properties of the Sunyaev-Zel'dovich effect.

2 1.1 The thermal Sunyaev-Zel'dovich effect

The Compton scattering of the CMB with hot ionized gas heats the radiation and moves the energy of the photons from the Rayleigh-Jeans to the Wien region of the spectrum (see figure 2.1(a)).

The spectral distortion consists in an increase of photon energies which implies a
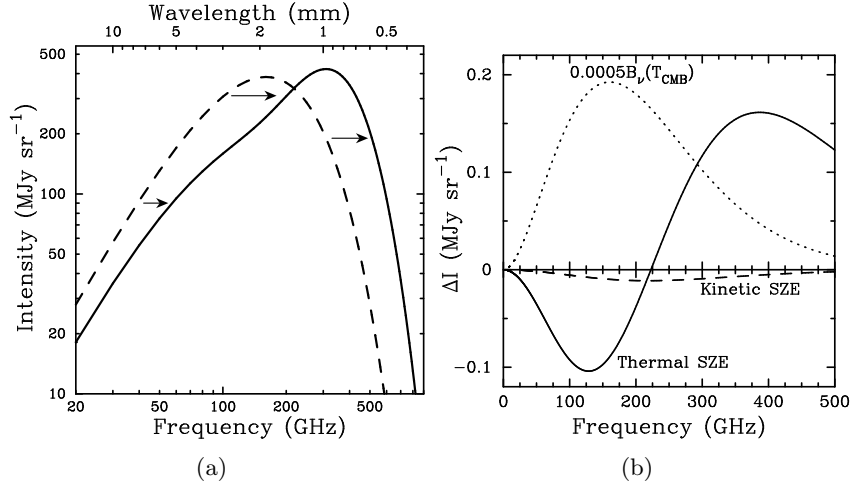
Figure 2 1 (a) The CMB spectrum undistorted (dashed line) and distorted by the SZ effect (solid line) in a cluster 1000 times more massive of a typical massive galaxy cluster. (b) Spectral distortion of the CMB due to the SZ effect for a typical cluster ($T_e \simeq 10$ keV, $y = 10^{-4}$, $v_e \simeq 500$ km s^{-1}) compared with the scaled spectrum of CMB (dotted line) (Carlstrom et al. 2002).

decrease of the CMB brightness temperature at low frequencies ($\nu < 218$ GHz for $T_{\mathrm{CMB}} = 2.728$ K for a thermal distribution of electrons; the threshold depends on the Lorentz factor of the electrons in case they are relativistic) and an increase at high frequencies. For a distribution of non-relativistic electrons (see figure 2.1(b)):

$$\frac{\Delta T_{\mathrm{CMB}}}{T_{\mathrm{CMB}}} = (x \coth (x/2) - 4)y \tag{2.1}$$

where $x = h_{\mathrm{P}}\nu/(k_B T_{\mathrm{CMB}})$ and y is the comptonization parameter

$$y = \frac{k_B \sigma_T}{m_e c^2} \int dl\, n_e T_e \tag{2.2}$$

σ_T being the Thomson cross-section and m_e the electron mass. In the Rayleigh-Jeans region ($x << 1$) eq. (2.1) simplifies to

$$\frac{\Delta T_{\mathrm{CMB}}}{T_{\mathrm{CMB}}} \simeq -2y. \tag{2.3}$$

The SZ signal corresponds to an unresolved flux

$$S_{tSZ} = 2\frac{(k_B T_{\mathrm{CMB}})^3}{(h_{\mathrm{P}}c)^2}g(x)Y \tag{2.4}$$

where

$$g(x) = \frac{x^4 e^x}{(e^x - 1)^2}\left(x \coth (x/2) - 4\right) \tag{2.5}$$

and Y is the surface integral of the comptonization parameter.

The amplitude of the distortion depends only on the properties of the electron cloud: in the case of thermal electrons it is proportional to the integral of the electron

pressure along the line of sight (y), and is independent of distance[1]. This is why the SZ effect is a powerful tool for investigating high redshift structures, their evolutionary properties, and, combining it with other observations (in particular in the X-ray band), distances of the clouds and cosmological issues.

2 1.2   The kinetic Sunyaev-Zel'dovich effect

If the electron cloud has a proper velocity with respect to the CMB rest frame there is an additional spectral distortion due to Doppler effect, called 'kinetic' SZ effect and given by

$$\frac{\Delta T_{\rm CMB}}{T_{\rm CMB}} = -\tau_e \left(\frac{v_e}{c} \right) \tag{2.6}$$

where v_e is the component of proper velocity along the line of sight and τ_e is the optical depth of the cloud.

The kinetic Sunyaev-Zel'dovich effect is due to scattering of CMB photons by an ionized cloud moving with peculiar velocity v. The associated flux density is (Carlstrom et al. 2002):

$$S_{kSZ} = -\frac{v_p}{c} \, 2 \frac{(k_B T_{\rm CMB})^3}{(h_{\rm P} c)^2} h(x) \int \tau_e d\Omega \tag{2.7}$$

where

$$h(x) = \frac{x^4 e^x}{(e^x - 1)^2}, \tag{2.8}$$

τ_e is the optical depth, v_p is the line-of-sight component of the velocity, and the surface integral of τ_e is carried out over the solid angle of the moving cloud. The resulting CMB spectrum is shifted towards higher (lower) temperatures for negative (positive) velocities (where negative means towards the observer). The function $h(x)$ has a maximum at $\nu = 218$ GHz where the thermal effect vanishes.

As can be seen in figure 2.1(b) for typical values of density, temperature and v_e in a cluster the kinetic effect is usually smaller than the thermal SZ effect. The signature of the kinetic SZ effect signal depends on the direction of v_e, and can be distinguished from the thermal effect for $\nu \sim 218$ GHz. Its study provides information on the proper motions of the gas clouds.

2 2   The SZ effect in galaxy clusters

Clusters of galaxies, the most massive virialized objects in the Universe, are permeated by a completely ionized gas with electron temperatures $T_e \sim 10^7$-10^8 K and densities $n_e \sim 10^{-3} cm^{-3}$ (Rosati et al. 2002, Sarazin 1988).

The SZ effect from clusters provides information on the cluster properties and can also be used to obtain important cosmological constrains (Birkinshaw & Lancaster 2005).

---

[1]Note that Y, the integral of y over the angular size of the cloud, depends on the cloud angular diameter, and hence on its distance.

- The total thermal SZ flux is proportional to the total thermal energy content of the cluster gas. Observations of the SZ effect provide direct model-independent measures of the thermal energy of the gas which depends on the cluster gravitational potential, if the gas is in hydrostatic equilibrium. The SZ effect is independent of the cluster redshift so that it can be exploited to study clusters up to very large distances, tracing the evolution of cluster potential wells in order to constrain the models of cluster formation.

- The SZ effect is a particularly effective tool to estimate the gas mass, since it is proportional to the electron density, while X-ray fluxes are proportional to n_e^2 and are therefore highly sensitive to the gas clumping factor $C = \langle n_e^2 \rangle / \langle n_e \rangle^2$, that may be much larger than 1. Total cluster masses can be derived through gravitational lensing data or from the gas distribution and the electron temperature, assuming hydrostatic equilibrium. Comparing the SZ effect-derived gas mass with the total mass, we can derive the gas fraction, which, locally, is approximately equal to the baryon mass fraction, since there are about ten times more baryons in the gas than in the galaxies. Because of the depth of the cluster potential well, the baryon fraction in clusters reflects the baryonic mass fraction in the Universe, and provides therefore a good estimate of the latter.

- If observations have high enough resolution and sensitivity, the SZ effect is a source of information on the ICM structure. The ICM is metal enriched and is therefore, at least partly, made of gas stripped from the member galaxies, which, in the early phases of their evolution, probably also had a cosmic baryon fraction, while the fraction of baryons in stars is ~ 10 per cent of the cosmic value. The history of stripping of the gas from galaxies is not well known, and it may be that a good fraction of gas was lost by galaxies after the cluster virialization epoch, thought to occur typically at $z \sim 1$. By combining SZ effect with X-ray measurements for clusters at different redshift up to $z \sim 1$, it would then be possible to learn about the evolution of the ICM and of the gas content of member galaxies.

- Merging is an important ingredient of the currently standard hierarchical scenario for cluster formation, and the merging rate increases rapidly with redshift. A manifestation of merging are strong shocks, implying substantial clumping of the gas. Again, coupling X-ray with detailed SZ effect measurements of clusters at different redshifts would allow us to investigate the evolution of the cluster structure and to test the merging rates predicted by hierarchical models.

  As already mentioned, the SZ effect provides a measure of thermal energy content of the gas, and is therefore a powerful tool to study cooling and heating processes. Merging is a potentially important heating source, but is not the only one. Kinetic energy injected in the ICM by supernovæ during the early phases of evolution of member galaxies, or by nuclear activity (jets of radio sources and strong winds from radio quiet active nuclei) and thermalized in the ICM are other important heating sources. On the other hand, cooling can be important in the densest parts of the clusters, particularly in their cores. SZ effect measurements are essential to study all these phenomena.

Current theories of structure formation predict that clusters form hierarchically via merger of smaller structures (Borgani et al 2001). X-ray observations revealed that high redshift ($z > 0.5$) clusters are much more morphologically complex, less virialized and dynamically more active than low-redshift clusters (Jeltema et al. 2005). Studies of $z > 0.8$ clusters evidenced clumpy and elongated structures that suggest that they are close to the epoch of cluster formation (Rosati et al. 2004)

- The comparison of SZ effect and X-ray emission is also a way to deduce cluster distances, bypassing the traditional distance scale ladder (Cavaliere et al. 1977, Silk et al. 1978). In fact, as discussed by Cavaliere et al. (1979), the SZ effect decrement in brightness is independent of the distance of clusters while the X-ray flux decreases with distance squared being $F_X = \frac{L_X}{4\pi D_L^2}$ with D_L the luminosity distance and

$$L_X \propto \left(\frac{\Delta T_{SZE}}{T_{CMB}}\right)^2 \theta_c D_A f(T, r) \tag{2.9}$$

where $\frac{\Delta T_{SZE}}{T_{CMB}}$ is the SZ effect temperature distortion, $\theta_c = r_c/D_A$ the core radius of the galaxy distribution, D_A the angular diameter distance and $f(T, r)$ is a function depending on the properties of the gas distribution and the shape factor for X-ray luminosity and SZ effect distortion which can be obtained from observations. Finally

$$D_L = 1.9 \; 10^{39} \; (\frac{\Delta T_{SZE}}{T_{CMB}})^2 F_X^{-1} \theta_c \; (1+z)^{-2} f(T, r). \tag{2.10}$$

Combining SZ and X-ray data we can obtain the distances directly from observable quantities (X-ray flux, SZ effect decrement, electron temperature and angular dimensions; see Birkinshaw & Lancaster 2005, Carlstrom et al. 2002, Majumdar & Subrahmanyan 2000).

Measurements on a single cluster at a redshift $z << 1$ ($D_L \simeq cz/H_0$) provide good absolute estimates of the Hubble constant H_0. Observations of a much more distant cluster ($z \simeq 1$) would give information on the deceleration parameter q_0. In principle these properties may be used to construct a 'Hubble diagram' of angular diameter distances versus H_0 (see figure 2 2). This technique is independent of cluster evolution, so it is a useful way to measure distances also for high redshift objects where the Hubble diagram strongly depends on the underlying cosmology. But the existing observations have not enough sensitivity to discriminate among cosmological models.

A study of a large number of clusters with well-known X-ray fluxes over a large redshift range would constrain the dark energy density and its evolution. A blind deep SZ effect survey of clusters can provide a fairly direct indicator of how many clusters of a given mass have assembled at any redshift and the cluster count and redshift distribution can set constrains on σ_8 and Ω_M once we know the initial phases of cluster formation (which can be tested by the cluster counts).
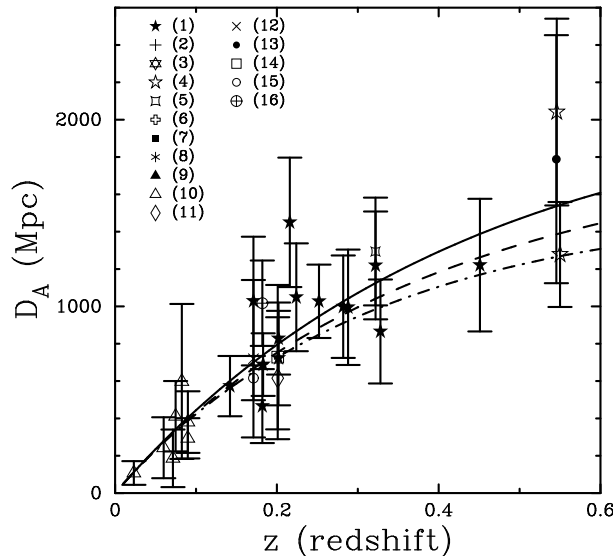
Figure 2 2 SZ effect-determined distances versus redshift. The theoretical relation is plotted for three different cosmologies assuming $h = 0.6$: $\Omega_M = 0.3$ and $\Omega_\Lambda = 0.7$ (solid line), $\Omega_M = 0.3$ and $\Omega_\Lambda = 0.0$ (dashed line) and $\Omega_M = 1.0$ and $\Omega_\Lambda = 0.0$ (dot-dashed line)(Carlstrom et al. 2002).

2 2.1 Observing the SZ effect in clusters.

For a typical cluster in the Rayleigh-Jeans region of the spectrum, where it is usually observed, the SZE signal is $\lesssim 1$ mK (Birkinshaw 1999, Birkinshaw & Lancaster 2005, Carlstrom et al. 2002). In the millimetric band it corresponds to flux densities of the order of few mJy or less, on the typical angular scales of clusters (few arcmin for redshift $0.3 < z < 1$).

The kinetic SZ effect signal is about a tenth of the thermal effects at low frequencies, for velocities of the order of $v = 1000$ km s^{-1}, but with a maximum close to the minimum of the thermal effect.

Existing telescopes could reach the required sensitivity levels in hours of observations. However, the beams are often smaller than the angular size of the clusters.

Clusters need to be carefully selected to have efficient measurements. The angular size of the cluster is a crucial element to plan observations. Small angular scale SZ effects fill only partially the beam so that the signal brightness is decreased by beam dilution over the beam area. If a cluster is too extended, single dish beam-switching and position-switching techniques may require wide movements from the cluster position to a reference area uncontaminated by the cluster. Other movements are required to observe quite often suitable well-known calibrators to have real-time calibration. Large dish movements are usually pretty slow. Large offsets mean large effects due to the atmosphere changing from a position to the other, and changing with time during the telescope slewing. To have reasonable measurements, in fact, the atmospheric and system conditions, that are measured in the reference position and towards the calibrators, should remain stable over large time intervals.

Existing interferometers are not well suited for extended objects, being tailored to obtain high resolution. Interferometers working at high frequencies typically have more resolution than optimum for cluster SZ observations. An array without shadowing has a filling factor $<< 1$ so will always have more resolution than a single dish of the same area. However, the correlation technique allows a better control of systematics and noise. A convenient observational set-up must allow the recovery of some short spacings (to have observations on larger scales within the beam): for this reason SZ-dedicated arrays are usually characterized by packed small dishes (BIMA-OVRO). In the next sections, by showing the simulations and the observations of Cl J0152-1357 we will more deeply investigate the suitable configurations for antenna arrays. Short spacings could be observed together with some larger baselines to measure simultaneously any astrophysical source of confusion.

Clusters are overdensities of galaxies, so they are also overdensities of radio and IR sources whose emission contaminates the SZ signal. The lack of information about galaxy populations at high frequency makes it difficult to estimate the contamination effect at the observational frequency ν, especially because most of the contamination is due to faint objects difficult to observe directly. An attempt of statistical extrapolation of information from low frequency radio source catalogues to high frequencies has been done by Massardi & De Zotti (2004; see also Lin & Mohr 2007, and Coble et al. 2007).

Since powerful radio sources are normally associated with early-type galaxies and these preferentially reside in clusters, a strong over-density of radio sources, which could partly fill the SZ dip in the Rayleigh-Jeans region, is naturally expected in clusters. And, indeed, radio sources were found to be the major contaminant of experiments using centimeter-wavelength receivers (Cooray et al. 1998; LaRoque et al. 2003).

In Massardi & De Zotti (2004) we found, for example, for observations at 30 GHz with angular resolution matching the assumed cluster radius of 1.7 Mpc (h = 0.65) a mean contamination of ~ 13.5 μK at $z = 0$ and of ~ 3.4 μK at $z = 0.5$. The contamination increases by a factor of 1.5 within 0.25 Mpc from the cluster center, but drops with frequency (see fig. 2.3(b) and 2.3(a)). We also found that the mean radio luminosity function of sources in clusters does not show any evidence for cosmological evolution up to $z \simeq 0.4$: that is at odds with the predictions of the pure luminosity evolution models by Dunlop & Peacock (1990), indicating that either the evolutionary behaviour of sources in clusters and in the field differ or that such models overestimate the radio source evolution at low redshifts.

No significant differences between the properties of sources in clusters and in the field have emerged. The shape of our estimated radio luminosity function is very similar to the local luminosity function in the field at the same frequency (1.4 GHz), determined by Magliocchetti et al. (2002). The mean density is however about 3000 times higher, a factor that corresponds to the matter overdensity in clusters formed at $z \simeq 1.5$.

The extrapolation of the luminosity function at 30 GHz is consistent with the results obtained by Lin et al. (2008) observing radio sources in a sample of 139 X-ray selected galaxy clusters.

More difficult and uncertain is the situation in the determination (both as statistical estimation and measurement) of IR galaxies contributions because FIR catalogues are typically not deep enough, and, especially for the dust component, the contamination depends on the properties of each single cluster.

(a)

(b)
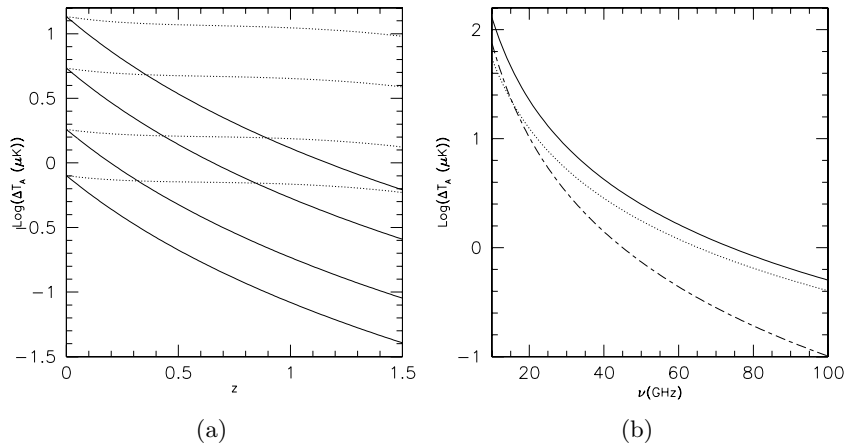
Figure 2 3 (a) Mean contamination of the SZ signal (in antenna temperature) by radio sources as a function of cluster redshift for 4 frequencies, 30, 44, 70, and 100 GHz (from top to bottom). At each frequency, the solid line refers to the case of no-evolution, the dotted line to the pure luminosity evolution models for steep- and flat-spectrum sources described in Sect. 3.4.1 of Dunlop & Peacock (1990). (b) Frequency dependence of the total emission (in terms of antenna temperature) from cluster sources for $z = 0.15$, the median redshift of our cluster sample. The dashed and dotted lines correspond to steep- and flat-spectrum sources, respectively, while the solid line shows the total.

Up to now over 100 clusters have SZ effect measurements but only a small fraction of them at high redshift ($z > 0.3$). Surveys are planned with upcoming instruments like the Atacama Cosmology Telescope (ACT, Kosowsky et al. 2006), the South Pole Telescope (SPT, Ruhl et al. 2004), the Array for Microwave Background Anisotropies (AMiBA, Lo et al. 2001), and the One Centimetre Radiometer Array (OCRA, Browne et al. 2000). The next generation of telescopes (both ground based like ALMA[2] and SKA and on satellites like Planck) will offer the possibility of increasing by large factors the number of detected clusters and are expected to exploit the potential of the SZ effect as a source of cosmological information.

2 2.2   Simulating SZ effect in galaxy clusters

In order to disentangle the information about the ICM density and its temperature, the observation of the SZ effect in a given cluster should be compared with observations in other bands (usually X-ray band observations are used). We have attempted a new approach that on one hand could help to determine the possibilities of a radiotelescope in SZ observations and on the other hand could detach the radio observation from those in other spectral regions: we suggest to apply a simulation of the whole observation to a model of the cluster.

That allows also to predict the difficulties of the observation and plan a suitable observational strategy. Observations with radio telescopes are usually described in the Fourier space by the coordinate system (u, v, w), where w is the line of sight (i.e. the (u, v)

---

[2]In particular, the ALMA-J sub–array of 12 7–m and 4 12–m antennas that will provide the shortest baselines to the full array.

is a plane perpendicular to the line of sight centered on the pointing position) and distances are measured in wavelengths. Roughly speaking, an interferometer array observes tracks (more details about this will be given in §2 2.3) on the (u, v) space, that correspond to the local (i.e. assuming planar projection approximation) Fourier transform of the signal within the observed field of view. The distances from the origin of the u and v axes are usually referred to as 'spacings'. Because of Fourier transform relations, smaller spacings correspond to signal on the larger angular size and are observed by the most closeby antennas. So, to observe signal over large angular sizes (e.g. extended objects, like the nearer clusters), antennas should be closely packed, whereas for high resolution antennas should be on long baselines (some VLBI experiments exploit ground based and satellite antennas to have the longest spacings possible).

Since common simulating tools are well suited for point sources or extended object assuming a gaussian profile of the signal, they are not useful in the SZ case which has a peaked profile in the Fourier space (see fig. **??**). For this profile the array configuration is crucial: shorter spacings can detect the stronger signal but lose resolution, whereas longer spacings, on which the signal is fainter, could add signal on smaller angular scales, but also sidelobe structures in the image. So a compromise should be carefully tuned. The optimum configuration for interferometric observations of the SZ effect is a compact group of several small antennas, but with few distant elements that can investigate the smaller angular scales to remove contamination.

To model the signal from the cluster we have assumed that the cluster is described by a spherically symmetric density profile described by an isothermal β model (Cavaliere et al. 1976)

$$\rho(r) = \rho_0 \left(1 + \left(\frac{r}{r_c} \right)^2 \right)^{-\frac{3}{2}\beta} \tag{2.11}$$

where r_c is the core radius.

A 2D FFT of the model convoluted with the telescope primary beam response function produces the model map on the UV plane. The telescope tracks generated by the given configuration select the observed visibilities. The inverse Fourier transform of the selected visibilities generates the simulated image. Mosaicking could help to recover the source structures but works properly on scales smaller than the beam size.

We have tried the capabilities of the simulator on a set of existing and projected arrays. The simulator is being developed and will benefit from the application to the analysis of the data of the difficult observation of the SZ effect of Cl J0152-1357, a massive high redshift galaxy cluster. The observational campaign is still on-going, so the results are only preliminary.

2 2.3 The case of Cl J0152-1357: SZ effect observations for a massive galaxy cluster.

We selected Cl J0152-1357 as the first target for an observational campaign of SZ effect observations with the ATCA. It is one of the most massive ($M_{tot} = 1.1 \times 10^{15} M_\odot$) galaxy clusters known at high redshift ($z = 0.823$). It was discovered in the ROSAT Deep Cluster Survey, observed in the Wide Angle ROSAT Pointed Survey, and catalogued in the

Bright SHARC survey. X-ray with BeppoSax, Chandra and XMM (Maughan et al., 2003, 2006, Huo et al. 2004), optical (Burbidge et al. 2006, Girardi et al. 2005, Demarco et al. 2005 Kodama et al.2005, Jorgensen et al. 2005), IR (Marcillac et al. 2007), and weak lensing (Jee et al. 2005) observations showed the complex structure of this cluster. X-ray and weak-lensing observations demonstrate that it is a non relaxed cluster with a complex substructure with two main sub-clumps, 95" apart and several other smaller structures probably merging together at least in two main directions. The cluster SZE was detected by Joy et al. (2001) with the BIMA millimeter interferometer at 28.5 GHz. BIMA had a resolution of 151" × 88" which was not enough to observe the internal structure in this cluster. The recent study of the SZ effect with archival SCUBA data (Zemcov et al. 2007) hasn't improved the knowledge of the gas details.

The ATCA had been used to attempt some observations of SZ effect (Liang et al. 1993) at 8 GHz: as mentioned, the small beam size at higher frequencies makes it difficult to recover enough signal. For this reason it is necessary that targets for observations are carefully selected. Cl J0152-1357 appeared well suited, thanks to the existing X-ray and SZ observations, and the complex structure could be resolved by the ATCA high resolution.

In July 2005 we had a 24 hour observation with the ATCA in the H75 configuration using five of the six 22 m antennas: in the H75 configuration, a hybrid of EW and NS stations, which is the most compact available for the ATCA (10 baselines from 30.6 m to 89.2 m corresponding to the range 1.6 -5 kλ). We used two adiacent 128 MHz bands at 18.5 GHz. The primary beam FWHM was $\simeq$ 3.4 arcmin. The beam size is 58.4" × 35.5". We made a mosaic of two pointings with centers on the X-ray position of each of the sub-clusters (NE: 01:52:44.18 -13:57:15.84; SW: 01:52:39.89 -13:58:27.48). The mosaic recovers some spatial frequencies shorter than 30 m. PKS 1964-638 was used as flux calibrator, PKS 1921-293 as bandpass calibrator and a nearby bright phase calibrator (PKS 0130-171 or PKS 0202-172) has been observed every 10 minutes on each sub-clump. We processed the data with Miriad (Sault et al. 1995).

We also had a 3 hours observation at 1.4 GHz with the hybrid configuration H214 of ATCA (6 antennas spacings from 89 to 4500 m) to check for traces of non-thermal emission from shocks.

The peak of the ATCA image appears (as expected from X-ray observations) close to the NE subclump (01:52:44.04 -13:56:43.84), that is the hottest and densest, but significantly displaced towards North from the X-ray peak. The signal to noise ratio in this point is 3.5. The SW peak is fainter and we have only signal to noise ratio equal to 1.5 in its position (01:52:38.68 -13:58:35.8).

The extended SZ effect signal in the uv-plane is strongest on the shortest spacings. The longer spacings improve the resolution and are sensitive to any substructure of the cluster, but have a lower signal to noise ratio. To improve the overall uv coverage we combined the ATCA data with the BIMA data (courtesy of M. Joy and J. Carlstrom) which adds shorter spacings. BIMA observations were made with nine 6.1 m antennas in a closely packed configuration (from 8 to 140 m) at 28.5 GHz with 0.8 GHz of bandwidth. This added spacings down to 0.6 kλ (see fig. 2 4). Even though short spacings have high noise because the BIMA dishes are only 6.1 m they are important because the signal strength is much higher.
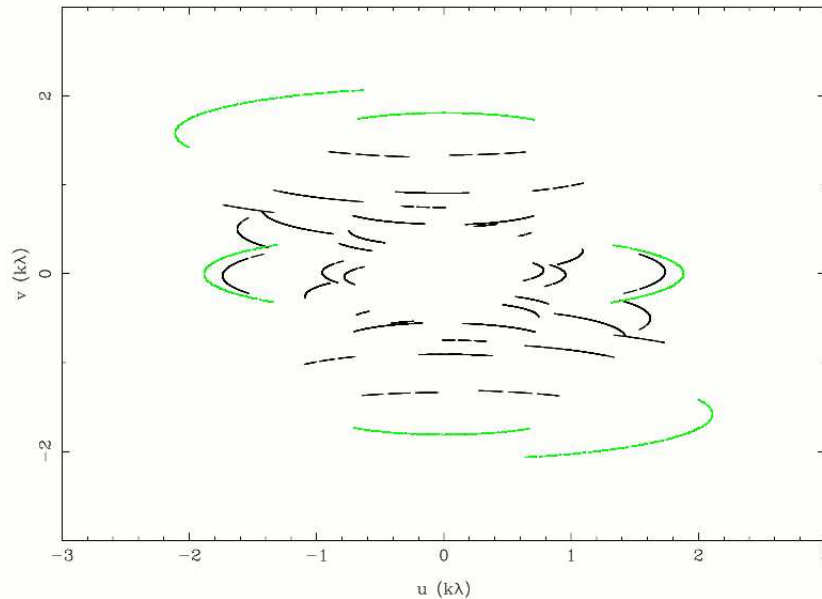
Figure 2 4 UV coverage for ATCA data (green lines) and BIMA (black lines). Note that BIMA covers shorter spacings than ATCA.

Thus, the combination of ATCA and BIMA data improved the sensitivity for ATCA observations and the resolution for BIMA ones. The data combination has been done correcting the amplitudes for the small wavelength difference and then using a range of relative weighting schemes to explore the trade-off between optimising the signal to noise ratio or the sidelobes. The best combination has been obtained by weighting the two images for their rms noise and the combined non deconvolved image shows a 5.6-signal-to-noise-ratio negative peak $\Delta I = -232\mu$Jy/beam in the region of the NE clump (RA: 01:52:44.214 δ:-13:56:45.84) and a signal of -146μJy/beam, corresponding to a 3.1 signal to noise ratio, in the SW clump region at 58.4" $\times$ 35.5" resolution and of -147μJy/beam in the SE region (see fig. 2 5).

Despite the combination of BIMA and ATCA and the selection of only the shortest baselines of the ATCA configuration we still have significant sidelobes from the NE peak which affect the region of the SW peak and the SE region, so that it is hard to estimate the real emission from these regions.

The debate in the literature about the nature of the SE region between the two subclumps is still open: it could be either a further sub-clump as the galaxy distribution suggests (Kodama et al. 2005), or a trace of a merging front among the two main sub-clumps (Maughan et al. 2003). Unfortunately our 20 cm SZ observations are unable to solve the enigma. As pointed out in literature (see for example Feretti 2003, or the case of 1ES0657-56 in Liang et al. 2000) merging clusters often show non-thermal radio relics or haloes due to synchrotron emission in the merging front region. Such structures should be detectable with high resolution lower frequency observations that are much more sensitive to non-thermal emission. The image at 20 cm has an rms of 4.8 mJy/beam and doesn't show any emission in the cluster region. At the level of sensitivity of our observations we
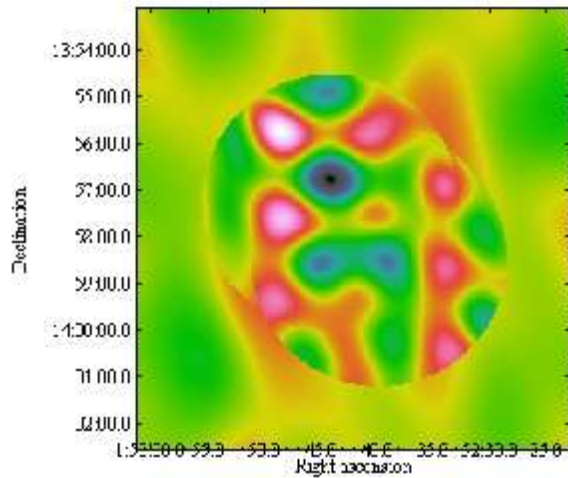
Figure 2 5 Cl J0152-1357 using combined but non deconvolved image: BIMA and ATCA images have been corrected for the different primary beam, the frequency and combined weighting for the rms noise of the images. The peak is $-231.9 \pm 43.85 \mu$Jy/beam.

have no trace of any of these structures, so we don't have any clear evidence for strong merging in the system.

The position of the NE peak in the SZ image doesn't agree with the X-ray peak of emission (see fig. 2 2.3 and 2 2.3), but is in good agreement with the galaxy distribution, as can be seen in Kodama et al. (2005) and Maughan et al. (2006) and with the weak-lensing-based mass distribution Jee et al. (2005). Furthermore, it is well-known that the peaks of the galaxy distribution do not coincide, in this cluster, with the X-ray emission peaks (Hou et al. 2003). Unexpectedly, our SZ effect peaks seems to better align with the galaxy distribution rather than with the X-ray emission.

The merging system could justify the differences between X-ray and galaxy distribution or weak lensing images. The different time scales on which the effects of merging could move from gas to the dark matter and to galaxies could explain the different distribution of the different components. The directions of the merging fronts seem to cross exactly in the region of the NE peak we detected. In that region density and temperature distributions are probably combined in a complicated way. In a relaxed isothermal structure we expect that the signal from the SZ effect and the free-free emission have overlapping peaks, even if SZ observations are much more sensitive to the low density regions than X-ray ones. In this case the merging fronts could produce shocks that drive the X-ray peak towards the densest regions whereas the SZ signal could come from less dense ones. The distribution of cold and hot fronts could emphasize the differences.

The agreement of SZ signal and galaxy/mass distribution is probably due to the fact that the region behind the strongest merging front has not yet reacted to the density perturbations that will modify also the galaxy distribution.

Furthermore, Burbidge et al. (2007) recently suggested an extension of the cluster structure towards the North-East to incorporate a QSO found at the same redshift 14 arcmin apart: it suggests that the structure of the cluster is more extended in the NE direction

(a)   (b)
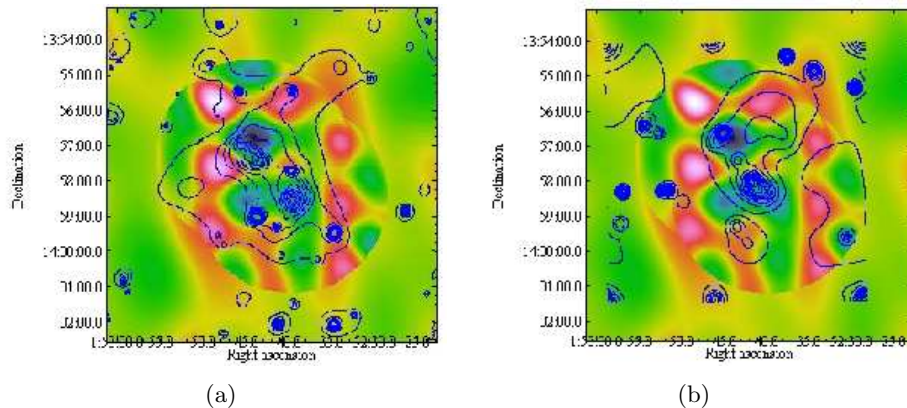
Figure 2 6 (a) Smoothed contours of X-ray surface brightness and (b) contours of constant galaxy number density derived from the AAT K-band images (Maughan et al. 2006) overlaid on the SZ effect combined but non deconvolved image.

than what shown by the X-ray observations.

The observations in the SW peak provide a further confirmation to these conclusions: the SW peak is less perturbed by the other subclumps and in this case SZ emission and X-ray overlap pretty well. If we consider the NE peak as a genuine detection and the signal in the SW region as an upper limit of the real signal, we could generate a deconvolved image with all the flux in the NE peak. However, the non-linear deconvolution at this low S/N is not unique so we have preferred to work with the images with no deconvolution (i.e. the dirty image).

The poor signal to noise ratio and the presence of sidelobes in the final image led us to develop a model of the SZ structure and simulate the UV plane response to compare it directly with the observed data.

2 2.3.1   The simulation of Cl J0152-1357

To better understand the properties of this system we developed a simulated observation, by producing a model of the SZ effect signal from Cl J0152-1357 which includes its complex substructure. For the simulations we assumed a Λ-CDM cosmology with h=0.7, $\Omega_\lambda = 0.7$, $\Omega_m = 0.3$ and $\Omega_b = 0.04$: at the cluster redshift, 1 arcmin corresponds to 458 kpc. We have assumed spherical symmetry for the sub-clumps.

Our simulation software can also reproduce mosaic observations including data combinations from different telescopes like the one we made among BIMA and ATCA data. Thus we were able to reproduce our data with the correct resolution and distribution of sidelobes, using the expected rms noise to estimate the noise both in the visibilities and in the image plane.

To built the correct model we had a huge number of degrees of freedom: number of sub-clumps, presence of merging-fronts, and for each sub-clumps the central position and density, the parameter for the β–model of density distribution (eq. 2.11), the physical dimension, the core radius and the temperature. The selection of the range of validity for all

Table 2 1 Best fitting model for Cl J0152-1357, after preliminary analysis.

	NE	SW
RA	01:52:44.214	01:52:39.89
δ	-13:56:45.84	-13:58:27.48
ρ_{gas} [g/cm^{-3}]	3.3×10^{-3}	5.3×10^{-3}
T_e [keV]	6.0	5.0
β	0.74	0.57
r_c [arcsec]	33.	11.6
$M_{1.4\ Mpc,\ gas}$ [$M_\odot$]	$7. \times 10^{14}$	4.5×10^{13}

the input parameters of the model was based on literature data. We described the cluster in terms of substructures, ignoring their interactions. According to the X-ray observations only the NE and SW subclumps show a strong signal. But the galaxy distribution shows the presence of a subclump close to the position of the SE signal in our observations. To define which is the case, we tried several combinations with 2 or 3 subclumps. Note that even if for simplicity we have selected the ranges of parameters on the basis of existing data it would have been possible to run a random scan for them until the model that better fits the observations is found (i.e. the model that minimize the χ^2 in the image or in the uv-plane).

The NE subclump has to be assumed to be in a different position with respect to the X-ray peak of emission to obtain a good agreement between observations and the simulation.

The comparison between observations and the simulation and between the different fitting models has been performed both in the UV plane and in the image plane. In the image plane each pixel is correlated to the others so that the error analysis is complicated. In the visibility domain each visibility is independent and has well defined noise associated with it. That provides a comparison which is independent of the spacings, gridding, weighting and deconvolution used and gives an effective estimation of the quality of our simulations. In particular we plan to compare the set of different simulations by calculating a χ^2, comparing the observations at a given distance on the UV plane with the simulated value in the same position. In this way we'll perform a comparison along the observed tracks. A preliminary attempt suggested that by changing in the model the physical position of the NE peaks toward North, according to the observed displacement from X-ray observations, the χ^2 improves. This kind of analysis indicates that the observed displacement can be real. The parameters of the best fitting model are in table 2 1 and simulated images are in figure 2 7 and 2 8. The signal in the SE region seems to be mainly due to an effect of sidelobes due to the NE and SW peaks. Of course, better observational data are necessary to finalize this analysis.
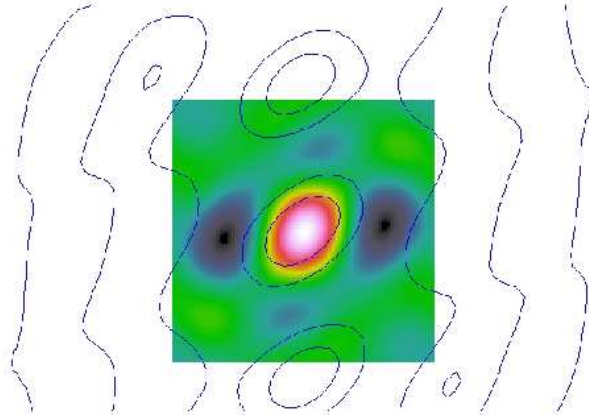
Figure 2 7 Comparison between the synthesized beam of ATCA observations and the simulated one and their profiles.
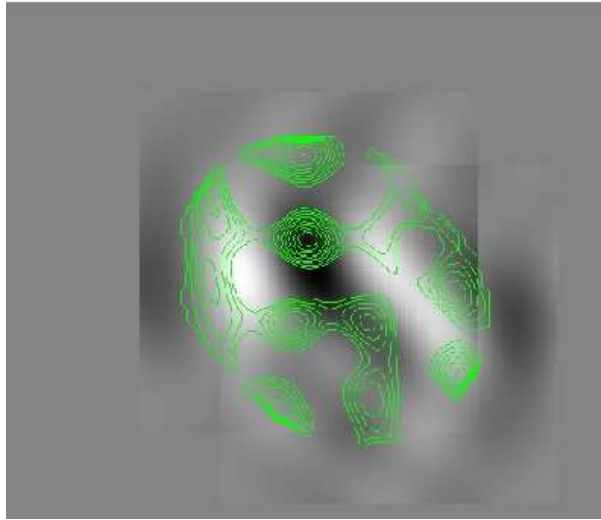
Figure 2 8 Comparison between the simulated and the observed images (contours) in the case of shifted NE peak.

2 2.3.2   Summary and new observations

The SZ effect is a powerful tool for investigating high redshift structures. As an attempt to exploit the possibility of the existing telescopes we have observed a high redshift (z= 0.823), massive ($M = 1.1 \times 10^{15} M_\odot$) galaxy cluster: Cl J0152-1357. Its complexity allowed us to investigate possible new approaches for SZ investigation in clusters.

The observations with the ATCA had too poor a sensitivity, so that we combined it with the BIMA data: the ATCA data could improve the resolution of the BIMA observations, while the latter have more signal on the shorter spacings.

We got a 5.6 σ signal in the region of the NE main sub-clump, but the SZ image of Cl J0152-1357 showed a shift of the SZ peak toward the North with respect to the X-ray position of the NE sub-clump. X-ray and weak-lensing observations demonstrate that Cl J0152-1357 is a non relaxed cluster with a complex substructure with several subclumps

and at least two merging fronts. The directions of the fronts seems to cross exactly in the region of the NE clump. In that region density and temperature distributions are probably combined in a complicated way.

The complicated structure seen in this cluster could provide insight into the mechanisms that are active in early stages of cluster formation but with only a few sigma detection of an unexpected offset between the SZ and X-ray peak, and a very complex data analysis involving two telescopes, mosaics and UV plane modeling, further investigation is required to confirm our preliminary results.

A new observational campaign will be run with the new Compact Array Broad Band (CABB) system that is expected to provide better signal to noise ratio. This will allow us to use, for the first time, SZ observations to measure cluster substructures.

We considered using the new higher frequency 7 mm system of the ATCA but although the SZ flux density is higher this is more than offset by the higher resolution, poorer UV coverage and higher T_{sys}.

Hence, the optimum frequency is still 18 GHz. Future observations at 35 GHz will be interesting because we get comparable signal to noise at higher resolution, but at this stage we need a convincing detection of the SZE in the sub-clumps at the 18 GHz resolution before we consider higher frequency and potentially higher resolution observations.

With 2 GHz bandwidth on even one CABB band we will improve the signal to noise ratio on the ATCA visibilities by a factor of 2.8 for the same observing time. This gives a dramatic improvement in the ATCA data alone from a signal to noise ratio of 3.5 to ~ 10, and this will be further improved with the addition of the low resolution BIMA data needed to correctly image the extended component.

The comparison with the simulation will define the possibility of getting information about structures without any further observation in other bands.

2 3   The SZE in the early stages of galaxy formation

A satisfactory theory of galaxy formation requires a good understanding of the complex physical processes governing the collapse of primordial density perturbations and the early stages of galaxy evolution. Measurements of the galaxy luminosity and stellar-mass functions up to substantial redshifts have highlighted that these functions show conspicuous differences with respect to the halo mass functions predicted by the cold dark matter (CDM) theory with the "concordance" cosmological parameters. At the low-mass end, the halo mass functions is much steeper than the galaxy luminosity function. As discussed by many authors (Larson 1974: Dekel & Silk 1986; Cole 1991; White & Frenk 1991; Lacey & Silk 1991; Kauffmann et al. 1993; Cole et al. 1994; Somerville & Primack 1999; Granato et al. 2001; Benson et al. 2003), the relative paucity of low-luminosity galaxies may be attributed to the quenching of star formation in low-mass halos by energy injections from supernovae and stellar winds, and by photoionization of the pre-galactic gas. This leads to the conclusion that efficient star formation must await the collapse of massive halos. On the other hand, the above processes have little effect on very massive halos, which, in the absence of additional relieving mechanisms, would convert too large a fraction of gas into stars, yielding too many bright galaxies, with wrong metallicities (Thomas et al. 2002; see

Benson et al. 2003 and Cirasuolo et al. 2005 for discussions of the effect of quenching mechanisms). An effective cure for that is the feedback from active nuclei (AGNs), growing at the galaxy centers (Granato et al. 2001, 2004; Bower et al. 2006; Croton et al. 2006)[3].

During their very early evolutionary phases, massive proto-galaxies are expected to contain large amounts of hot gas, but the gas thermal history is obscure. According to the standard scenario (Rees & Ostriker 1977; White & Rees 1978), the proto-galactic gas is shock heated to the virial temperature, but this view has been questioned (Katz et al. 2002; Binney 2004; Birnboim & Dekel 2003; Keres̆ et al. 2005), on the basis of independent approaches: analytic methods, a high-resolution one-dimensional code, smoothed particle hydrodynamics simulations. The general conclusion is that only a fraction, increasing with halo mass, of the gas heats to the virial temperature. The hot gas is further heated by supernova explosions and by the AGN feedback, and may eventually be pushed out of the halo. Keres̆ et al. (2005) and Dekel & Birnboim (2006) find that there is a critical shock heating halo mass of $\sim 10^{11.4}$–$10^{12} M_{\odot}$, above which most of the gas is heated to the virial temperature, while most of the gas accreted by less massive halos is cooler.

The large thermal energy content of the hot proto-galactic gas in massive halos makes this crucial evolutionary phase potentially observable by the next generation of astronomical instruments through its free-free emission and the thermal and kinetic Sunyaev-Zel'dovich effects (Oh 1999; Majumdar et al. 2001; Platania et al. 2002; Oh et al. 2003; Rosa-González et al. 2004; De Zotti et al. 2004). In this section we investigate the detectability of this proto-galactic gas exploiting an up to date model. For the purposes of the present analysis, the adopted model can be taken as representative of the most popular semi-analytic models (White & Frenk 1991; Kauffmann et al. 1993; Cole et al. 1994; Somerville & Primack 1999; Benson et al. 2003), that all adopt a similar mass function of dark matter halos, a cosmological gas to dark matter ratio at virialization, and assume that all the gas is heated to the virial temperature.

Even if some single dish telescopes have the required theoretical sensitivity, especially at mm and sub-mm wavelengths (e.g. LMT/GTM, GBT at 3 mm, Rosa-González et al. 2004) these continuum observations will be hampered by fluctuations in tropospheric emission. Interferometric array observations offer a better trade off between angular resolution, sensitivity and control of systematics (Birkinshaw & Lancaster 2005) together with larger fields of view, and allow us to work at lower frequencies where the sources of contaminations from backgrounds and foregrounds are lower and may be better estimated. For this reason we focus mainly on the capabilities of next generation interferometers: the Square Kilometer Array (SKA)[4], the Atacama Large Millimeter Array (ALMA)[5], the Expanded Very Large Array (EVLA)[6], the new 7 mm capability of the Australia Telescope Compact Array (ATCA). We note that the situation for galaxy scale SZ detection is quite different from that for cluster SZ detection. Cluster SZ signals are stronger and have much larger

---

[3]Note that the AGN feedback invoked by Granato et al. is radically different from that advocated by Bower et al. and Croton et al.. The former is a property of all AGNs and is attributed to a combination of radiation pressure (especially line acceleration) and gas pressure. The latter is associated to the radio active phase of quasars ('radio mode' feedback).

[4]http://www.skatelescope.org/

[5]http://www.alma.info/

[6]http://www.aoc.nrao.edu/evla/

angular scales than optimum for the interferometer arrays and are best observed with single dishes at high quality sites (Carlstrom et al. 2002).

We adopt a Λ-CDM cosmology with $h = 0.71$, $\Omega_m = 0.27$, $\Omega_\lambda = 0.73$, $\Omega_b = 0.04$, $\sigma_8 = 0.8$, consistent with the results from WMAP (Spergel et al. 2006).

2 3.1   Outline of the model

We adopt the semi-analytic model laid out in Granato et al. (2004), with the values of the parameters revised by Lapi et al. (2006) to satisfy the constraints set by the AGN luminosity functions.

The model is built in the framework of the standard hierarchical clustering scenario, taking also into account the results by Wechsler et al. (2002), and Zhao et al. (2003a; 2003b), whose simulations have shown that the growth of a halo occurs in two different phases: a first regime of fast accretion in which the potential well is built up by the sudden mergers of many clumps with comparable masses; and a second regime of slow accretion in which mass is added in the outskirts of the halo, without affecting the central region where the galactic structure resides. This means that the halos harboring a massive galaxy, once created even at high redshift, are rarely destroyed. At low redshifts they are incorporated within groups and clusters of galaxies. Support for this view comes from studies of the mass structure of elliptical galaxies, which are found not to show strong signs of evolution since redshift $z \approx 1$ (Koopmans et al. 2006). The halo formation rate at $z \gtrsim 1.5$, when most massive early-type galaxies formed (Renzini 2006), is well approximated by the positive term in the cosmic time derivative of the cosmological mass function (e.g., Haehnelt & Rees 1993; Sasaki 1994).

We confine our analysis to galaxy halo masses between $M_{\rm vir}^{\rm min} \simeq 2.5 \times 10^{11}\, M_\odot$, close to the mass scale at the boundary between the blue (low mass, late type) and the red (massive, early type) galaxy sequences (Dekel & Birnboim 2006) and $M_{\rm vir}^{\rm max} \approx 10^{13.2}\, M_\odot$, the observational upper limit to halo masses associated with individual galaxies (Cirasuolo et al. 2005).

The complex physics of baryons is described by a set of equations summarized in the Appendix of Lapi et al. (2006). Briefly, the model assumes that during or soon after the formation of the host dark matter (DM) halo, the baryons falling into the newly created potential well are shock-heated to the virial temperature. The hot gas is (moderately) clumpy and cools quickly in the denser central regions, triggering a strong burst of star formation. The radiation drag due to starlight acts on the gas clouds, reducing their angular momentum. As a consequence, a fraction of the cool gas falls into a reservoir around the central supermassive black hole (BH), and eventually accretes onto it by viscous dissipation, powering the nuclear activity. The energy fed back to the gas by supernova (SN) explosions and AGN activity regulates the ongoing star formation and the BH growth. Eventually, the SN and the AGN feedbacks unbind most of the gas from the DM potential well. The evolution turns out to be faster in the more massive galaxies, where both the star formation and the BH activity come to an end on a shorter timescale, due to the QSO feedback whose kinetic power is proportional, according to the model, to $M_{\rm BH}^{3/2}$.

Mao et al. (2007) found that, for the masses and redshifts of interest here, the evolution of the hot (virial temperature) gas mass, taking into account both heating and

cooling processes, is well approximated by a simple exponential law

$$M_{\text{hot}}(t) = M_{\text{hot}}(0)\, e^{-t/t_{\text{cond}}}, \tag{2.12}$$

where $M_{\text{hot}}(0) = f_{\text{cosm}}\, M_{\text{vir}}$ is the gas mass at virialization, M_{vir} being the halo mass and $f_{\text{cosm}} \approx 0.18$ the mean cosmological baryon to dark matter mass density ratio. The evolution timescale t_{cond} can be approximated as

$$t_{\text{cond}} \approx 4 \times 10^8 \left(\frac{M_{\text{vir}}}{10^{12}\, M_{\odot}} \right)^{0.2} \left(\frac{1+z}{7} \right)^{-1.5} \quad \text{yr} \ . \tag{2.13}$$

The model proved to be remarkably successful in accounting for a broad variety of data, including epoch dependent luminosity functions and number counts in different bands of spheroidal galaxies and of AGNs, the local black hole mass function, metal abundances, fundamental plane relations and relationships between the black hole mass and properties of the host galaxies (Granato et al. 2004; Cirasuolo et al. 2005; Silva et al. 2004, 2005; Lapi et al. 2006).

2 3.1.1 The virial collapse

The virial temperature of a uniform spherically symmetric proto-galactic cloud with virial mass M_{vir} (dark matter plus baryons) and mean molecular weight $\mu = (2X + 3/4Y)^{-1}$, X and Y being the baryon mass fractions in the form of hydrogen and helium (we adopt X=0.75 and Y=0.25, no metals) is

$$T_{\text{vir}} = \frac{1}{2} \frac{\mu m_p G}{k_B} \frac{M_{\text{vir}}}{R_{\text{vir}}}, \tag{2.14}$$

where m_p is the proton mass, G the gravitational constant, and k_B the Boltzmann constant. The virial radius R_{vir} is given by

$$R_{\text{vir}} = \left(\frac{4}{3} \pi \frac{\rho_{\text{vir}}}{M_{\text{vir}}} \right)^{-1/3} \tag{2.15}$$

where ρ_{vir} is the mean matter density within R_{vir}

$$\rho_{\text{vir}} = \rho_c \Omega_m \Delta (1+z)^3, \tag{2.16}$$

$\rho_c = 3H_0^2/(8\pi G)$ being the critical density. For a flat cosmology ($\Omega_m + \Omega_\Lambda = 1$), the virial overdensity Δ can be approximated by (Bryan & Norman 1998; Bullock et al. 2001)

$$\Delta = \frac{18\pi^2 + 82\omega - 39\omega^2}{\Omega(z)} \tag{2.17}$$

with $\omega = \Omega(z) - 1$, and

$$\Omega(z) = \frac{(1+z)^3 \Omega_m}{\Omega_m (1+z)^3 + \Omega_\Lambda}. \tag{2.18}$$

In the redshift range considered here ($z \geq 1.5$), we have

$$T_{\mathrm{vir}} \simeq 5 \times 10^5 \left(\frac{M_{\mathrm{vir}}}{10^{12} M_\odot} \right)^{2/3} (1 + z) \text{ K}, \tag{2.19}$$

so that for the massive objects ($2.5 \times 10^{11} M_\odot < M_{\mathrm{vir}} < 10^{13.2} M_\odot$) we are dealing with, the only relevant cooling mechanism is free-free emission.

We assume that, after virialization, the protogalaxy has a NFW density profile (Navarro, Frenk & White 1997):

$$\rho = \frac{\rho_s}{cx(1 + cx)^2} \tag{2.20}$$

where $x = r/R_{\mathrm{vir}}$,

$$\rho_s = \frac{M_{\mathrm{vir}}}{4\pi R_{\mathrm{vir}}^3 f_c} \tag{2.21}$$

with

$$f_c = \frac{\log(1 + c) - c/(1 + c)}{c^3} \tag{2.22}$$

and $c = 3$ (Zhao et al. 2003b; Cirasuolo et al. 2005).

2 3.1.2   The free-free emission

The free-free luminosity of the protogalaxy is computed integrating over its volume the emissivity given by (Rybicki & Lightman 1979):

$$j_{\mathrm{ff}} = 6.8 \cdot 10^{-38} n_e \left(\sum Z_i^2 n_i \right) C T_{\mathrm{vir}}^{-1/2} \bar{g}_{\mathrm{ff}}(T_{\mathrm{vir}}, \nu) \cdot \exp(-h_P \nu / k_B T_{\mathrm{vir}}) \text{ erg s}^{-1} \text{ cm}^{-3} \text{ Hz}^{-1}, \tag{2.22}$$

where the sum in the brackets is on all the chemical species in the gas (only H and He in our case) Z being the atomic number and n_e and n_i the number densities of electrons and of ions respectively, C is the clumping factor, for which we adopt the value ($C = 7$) given by Lapi et al. (2006), h_P is the Planck constant and $\bar{g}_{\mathrm{ff}}(T_{\mathrm{vir}}, \nu)$ is the velocity averaged Gaunt factor. For the latter we adopted the analytical approximation formulae by Itoh et al. (2000) in their range of validity. Outside such range we used the formula given by Rybicki & Lightman (1979):

$$g_{\mathrm{ff}} = \frac{\sqrt{3}}{\pi} \left[17.7 + \ln \left(\frac{T_{\mathrm{vir}}^{3/2}}{\nu} \right) \right]. \tag{2.23}$$

The gas density is assumed to be proportional to the mass density ($\rho_{\mathrm{gas}} = f_{\mathrm{cosm}} \rho$). The electron number density is

$$n_e = \frac{\rho_{gas}}{m_p}(X + Y/2), \tag{2.24}$$

m_p being the proton mass. The adopted value of the clumping factor C is assumed to be constant with radius, as in the model. This rather crude approximation stems from our ignorance of the complex structure of the gas distribution.

Finally, the flux scales with mass, redshift and frequency as

$$S_{\text{ff}}=6.6 \times 10^{-9} \bar{g}_{\text{ff}}[T_{\text{vir}}, \nu(1+z)] \left(\frac{1+z}{3}\right)^{7/2} \left(\frac{M_{\text{vir}}}{10^{12} \, M_\odot}\right)^{2/3} \cdot$$

$$\cdot \left(\frac{4.8 \times 10^{28} \text{cm}}{d_L}\right)^2 \exp\left(\frac{-1.9 \times 10^{-6}(\nu/20\,\text{GHz})}{(M_{\text{vir}}/10^{12} \, M_\odot)^{2/3}}\right) \, \text{Jy}, \tag{2.25}$$

where d_L is the luminosity distance (Hogg 1999):

$$d_L = \frac{c}{H_0}(1+z) \int_0^z \frac{dz'}{\sqrt{\Omega_m(1+z')^3 + \Omega_\Lambda}}. \tag{2.26}$$

2 3.1.3   The Sunyaev-Zel'dovich effects

According to the formula 2.4, the flux density for the thermal SZ effect, S_{tSZ}, scales with mass, redshift and frequency as

$$S_{tSZ} = 0.6 \times 10^{-7} \left(\frac{1+z}{3}\right)^5 \left(\frac{M_{\text{vir}}}{10^{12} M_\odot}\right)^{5/3} \left(\frac{4.8 \times 10^{28} \text{cm}}{d_L}\right)^2 \left(\frac{g(x)}{0.24}\right) \, \text{Jy}, \tag{2.27}$$

and may be positive or negative depending on the sign of $g(x)$. Here we will quote only positive fluxes, taking the absolute value of $g(x)$.

For a virialized cloud with $M_{\text{vir}} \simeq 10^{12} \, M_\odot$ at $z = 2$, which has a virial temperature $T_e \sim 1.4 \times 10^6$ K, a mean electron density $n_e \simeq 10^{-3} \, \text{cm}^{-3}$ and a virial radius of $\simeq 106$ kpc, the comptonization parameter is $\simeq 10^{-7}$, yielding a negative flux of $\simeq 60$ nJy at 20 GHz, on an angular scale of $\simeq 10''$.

2 3.1.4   The kinetic Sunyaev-Zel'dovich effects

The flux density for the kinetic SZ effect S_{kSZ} scales as

$$\begin{aligned} S_{kSZ} &= 5.3 \times 10^{-8} \, (|v|/393\,\text{km/s}) \, [(1+z)/3]^4 \cdot \\ & \left(M_{\text{vir}}/10^{12} M_\odot\right) \left(4.8 \times 10^{28}\text{cm}/d_L\right)^2 [h(x)/0.12] \, \text{Jy}. \end{aligned} \tag{2.28}$$

Following Sheth & Diaferio (2001) we model the distribution function of galaxy peculiar velocities, $P(v)$, as a Gaussian core with $\sigma_v = 680(1+z)^{-1/2} \, \text{km\,s}^{-1}$, extending up to $v_t = 1742(1+z)^{-1/2} \, \text{km\,s}^{-1}$, followed by exponential wings cut off at $v_{\text{max}} = 3000(1+z)^{-1/2} \, \text{km\,s}^{-1}$. Normalizing the integral of $P(v)$ to unity, we have:

$$\begin{aligned} P(v)dv &= 5.86 \times 10^{-4}(1+z)^{1/2} \, (dv/\text{km\,s}^{-1}) \cdot \\ & \cdot \begin{cases} \exp[-0.5(v/\sigma_v)^2] & \text{for } |v| \leq v_t \\ 2.065 \exp(-2.3|v|/v_0) & \text{for } v_t < |v| \leq v_{\text{max}} \end{cases} \end{aligned} \tag{2.29}$$

where $v_0 = 1000(1+z)^{-1/2} \, \text{km\,s}^{-1}$. The adopted scaling with redshift is that appropriate in the linear regime, when the effect of the cosmological constant can be neglected, as is the case in the z range of interest here.
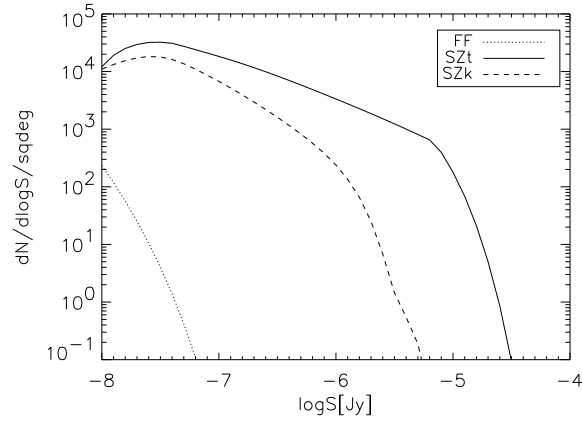
Figure 2 9 Comparison of the differential source counts at 20 GHz of thermal (solid lines) and kinetic (dashed lines) Sunyaev-Zel'dovich effects and free-free (dotted line). For SZ effects we obviously use the absolute value of the flux. The counts of the kinetic SZ effect include both positive and negative signals, and are therefore a factor of 2 larger than those given by eq. 2.37. The decline of the counts of Sunyaev-Zel'dovich effects at the faint end is due to the adopted lower redshift ($z \geq 1.5$) and halo mass ($M_{\mathrm{vir}} \geq 2.5 \times 10^{11} M_{\odot}$) limits.
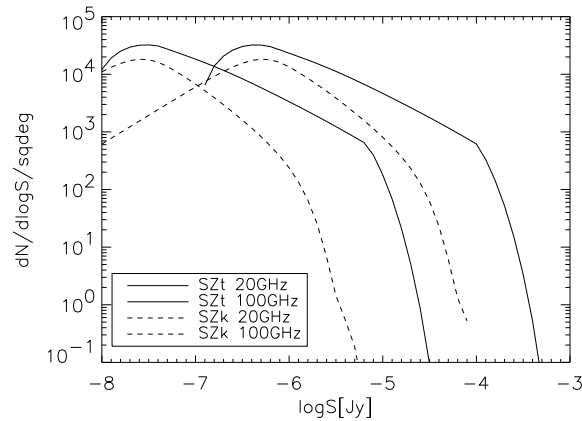
Figure 2 10 Comparison of the differential source counts at 20 GHz and 100 GHz of thermal (thin and thick solid lines respectively) and kinetic (thin and thick dashed lines) Sunyaev-Zel'dovich effects (the peak of the source counts at higher frequencies is at higher values of flux).

2 3.2   Source counts

The mean differential number counts per steradian are given by:

$$\frac{dN(S)}{d\log S} = \int_{\ln(z_0)}^{\ln(z_1)} d\ln(z)\, z \frac{dV}{dz} n[L(S,z),z] \frac{d\log L}{d\log S} \tag{2.30}$$

where $n(L,z)$ is the comoving epoch-dependent luminosity function per unit $d\log L$, and dV/dz is the comoving volume per unit solid angle:

$$\frac{dV}{dz} = \frac{c}{H_0(1+z)^2} \frac{d_L^2}{\sqrt{\Omega_m(1+z)^3 + \Omega_\Lambda}}. \tag{2.31}$$

According to our model, for any given z the free-free luminosity of a proto-spheroid and its thermal SZ signal depend only on its virial mass. The luminosity function can then be straightforwardly computed integrating the formation rate of virialized objects, $d^2N(M_{\rm vir},z)/d\log M_{\rm vir}dt$, over the duration of the ionized phase and multiplying the result by $d\log M_{\rm vir}/d\log L$. To avoid unnecessary complications we keep the free-free luminosity constant at its initial value over a time, $t_{\rm ion}$, equal to the minimum between $t_{\rm cond}$ (eq. 2.13), the expulsion time of the interstellar gas, $\Delta t_{\rm burst}$, determining the end of the star formation burst, and the expansion timescale, and zero afterwards. This simplifying assumption implies that the evolution of the hot gas mass (eq. 2.12), density, clumping factor, and temperature are neglected. It is motivated by our expectation that the effect on the free-free luminosity, hence on the counts, of the moderate decrease of the hot gas mass over the time $t_{\rm ion}$ is counterbalanced by an increase of the mean gas density and of the clumping factor, as a consequence of the shocks associated to supernova explosions and to the AGN feedback. Also, having neglected the contribution to the counts from the free-free emission at $t > t_{\rm ion}$, partly compensates the possible overestimate due to having neglected the decrease of the gas mass. In any case, a more sophisticated calculation does not appear to be warranted since, as discussed in §2 3.3.3 and 2 3.3.4, the free-free signal turns out to be too weak to be detectable, being overwhelmed by emissions associated to star formation.

Mao et al. (2007) found that $\Delta t_{\rm burst}$ (yr) can be approximated as

$$\Delta t_{\rm burst} \approx 4 \times 10^8 \left(\frac{1+z}{7} \right)^{-1.5} \cdot$$
$$\cdot \begin{cases} 1 & \text{for } M_{\rm vir} \geq 10^{12} M_\odot \\ \left(M_{\rm vir}/10^{12} M_\odot \right)^{-0.15} & \text{for } M_{\rm vir} < 10^{12} M_\odot \end{cases} \cdot \tag{2.32}$$

The mass function of ionized protospheroids at the redshift z is then:

$$\left(\frac{dN_{\rm ion}(M_{\rm vir},z)}{dM_{\rm vir}} \right)_{\rm ion} = \int_{t(z)-t_{\rm ion}}^{t(z)} dt' \frac{d^2N(M_{\rm vir},z)}{dM_{\rm vir}\, dt'}. \tag{2.33}$$

The formation rate of protospheroids is well approximated by the positive term of the derivative of the Sheth & Tormen (1999) mass function, $(dN(M_{\rm vir},z)/dM_{\rm vir})_{\rm ST}$, (Lapi et

al. 2006):

$$\frac{d^2N(M_{\rm vir}, z)}{dM_{\rm vir}dt} = \left[\frac{a\delta_c(z)}{\sigma^2(M_{\rm vir})} + \frac{2p}{\delta_c(z)}\frac{\sigma^{2p}(M_{\rm vir})}{\sigma^{2p}(M_{\rm vir}) + a^p\delta_c^{2p}(z)}\right]\left(\frac{dN(M_{\rm vir}, z)}{dM_{\rm vir}}\right)_{\rm ST}\left|\frac{d\delta_c(z)}{dt}\right|$$

(2.34)

where $a = 0.707$, $p = 0.3$, $\delta_c(z)$ is the critical overdensity for the spherical collapse, $\sigma(M_{\rm vir})$ is the rms amplitude of initial density fluctuations smoothed on a scale containing a mass $M_{\rm vir}$. In turn, the Sheth & Tormen (1999) mass function writes

$$\left(\frac{dN(M_{\rm vir}, z)}{dM_{\rm vir}}\right)_{\rm ST} = \frac{\rho}{M_{\rm vir}^2}\nu f(\nu)\frac{d\ln\nu}{d\ln M_{\rm vir}}$$

(2.35)

where ρ is the average comoving density of the universe, $\nu = [\delta_c(z)/\sigma_\delta(M_{\rm vir})]^2$, and

$$\nu f(\nu) = A[1 + (a\nu)^{-p}]\left(\frac{a\nu}{2}\right)^{1/2}\frac{e^{-a\nu/2}}{\pi^{1/2}},$$

(2.36)

with $A = 0.322$.

The calculations leading to the counts of the thermal SZ 'fluxes' are strictly analogous. In the case of the kinetic SZ effect we need also to take into account the redshift dependent distribution of peculiar velocities, and we have

$$\frac{dN(S_{\rm kSZ})}{d\log S_{\rm kSZ}} = \int_{\ln(z_0)}^{\ln(z_1)} d\ln(z)\, z\,\frac{dV}{dz}\int_{\ln(v_{\rm min})}^{\ln(v_{\rm max})}\frac{dN_{\rm ion}[M_{\rm vir}(z,v)]}{d\log M_{\rm vir}}\frac{d\log M_{\rm vir}}{d\log S_{\rm kSZ}},$$

(2.37)

where $v_{\rm min}$ is the velocity yielding a kinetic SZ 'flux' $S_{\rm kSZ}$ from a galaxy with the maximum considered mass ($M_{\rm vir} = 10^{13.2}M_\odot$) at redshift z, $dN_{\rm ion}(M_{\rm vir}, z, v)/dM_{\rm vir}$ is the differential mass function of proto-spheroidal galaxies with peculiar velocity v and redshift z, producing a kinetic SZ flux $S_{\rm kSZ}$. As before, $dN_{\rm ion}(M_{\rm vir}, z, v)/dM_{\rm vir}$ is computed integrating the formation rate of virialized objects over the duration of the ionized phase. Equation 2.30 gives the number of either positive or negative kinetic SZ signals. The comparison of the differential source counts at 20 GHz in fig. 2 9 shows that the thermal Sunyaev-Zel'dovich effect is dominant above 10^{-8} Jy. The decline of the SZ counts at faint flux levels is due to the adopted lower limits to halo masses and redshifts ($M_{\rm vir} \geq 2.5 \times 10^{11}M_\odot$ and $z \geq 1.5$). The very steep slope at the bright end comes from the high halo mass cutoff. The free-free counts are very low, indicating that this emission is very hard to detect in the radio.

As illustrated by fig. 2 10, the SZ fluxes increase with increasing frequency in the Rayleigh-Jeans region of the Cosmic Microwave Background.

2 3.3 Perspectives for searches of ionized proto-spheroidal clouds

2 3.3.1 Next generation mm-wave interferometers

In Table 2 2 we have collected some of the main properties of next generation radio interferometers working at few cm to mm wavelengths.

The Australia Telescope Compact Array (ATCA) is a 6 22m-dish array. The technical parameters we use here refer to the recently completed upgrade to the 7 mm

Table 2 2 Main properties of next generation interferometers. The maximum baseline has been calculated considering that the angular size, for the galaxies in the intervals of mass and redshift we are considering, ranges from $5''$ to $35''$, and requiring a ratio of 5 between amplitude and noise on the visibilities. 10% SKA has the same properties as SKA, but the number of baselines is 1.25×10^5.

	FULL-SKA	ALMA	ATCA	EVLA
Frequency (GHz)	10-20	100	35-50	35
Bandwidth(GHz)	4	4x2	2x2	8
Antenna diam. (m)	12	12	22	25
Efficiency	0.8	0.8	0.8	0.8
T_{sys} (K)	50	50	60-80	75
No. of polariz.	2	2	2	2
Min. baseline (m)	15	15	30.6	30
Max. baseline (km)	1.4-0.7	0.2	0.4-0.3	0.4
No. of baselines	1.25×10^7	700	10	350

receivers and the increase of the bandwidth from the present 2×128MHz up to 4 GHz (CABB). The band ranges between 30 to 50 GHz, with T_{sys} increasing from 60 K up to 80 K at the top end of the band. The system will be fully operational by 2009.

The Atacama Large Millemiter Array (ALMA) is a 50 12 m antenna array. The lower frequency band with higher priority ranges between 84 and 116 GHz, close to the maximum amplitude in flux of the negative signal of thermal Sunyaev-Zel'dovich effect. The array will be operational by 2012.

The Expanded Very Large Array (EVLA) is an improvement of the sensitivity, frequency coverage, and resolution of the existing VLA. When completed, after 2013, it will use the 27 25m dishes of VLA working in the frequency range 1-50 GHz with 8 GHz bandwidth per polarisation available in the frequency bands 18-26.5, 26.5-40, and 40-50 GHz.

The Square Kilometer Array (SKA) is a titanic project for an interferometer whose main technical specification is to have one square kilometer of detecting area. The highest frequency band should span the range 16–25 GHz. Several designs are under consideration. The parameters we use refer to the small parabolic dishes version, which is the only high frequency design being considered. The telescope is expected to be fully operational after 2020, but a '10% SKA' is expected to be operating as early as 2015. Phased array feeds in the focal plane are being considered for the lower frequency receivers. If such systems were implemented at the higher frequencies they would increase the field of view and hence the survey speed by factors of up to 50.

The angular resolution of an array of antennas is given by

$$\theta = 1.02 \frac{\lambda}{B} \tag{2.38}$$

where B is the maximum distance between two antennas. The field of view normally

corresponds to the Half Power Beam Width (HPBW) of an antenna

$$\text{HPBW} = 1.02\frac{\lambda}{D} \tag{2.39}$$

where D is the diameter of the antenna dish. For a Gaussian beam the field of view (FOV) is

$$\text{FOV} = \frac{\pi}{\ln 2}\left(\frac{\text{HPBW}}{2}\right)^2 . \tag{2.40}$$

Phased array feeds add a multiplying factor to this relation, increasing by the same factor the sky area covered in a single pointing. The noise level in an image is given by eq. 1.2 calculated for a number of baselines N_{base} short enough to have full sensitivity to observe objects with size between 5 and 35 arcsec, $\Delta\nu$ is the bandwidth and n_{pol} is the number of polarizations. Considering the NFW profile for densities enlarges the range of full sensitivity baselines in the visibility space improving the resolution without losing too much in sensitivity. We made our calculations using a reasonably conservative configuration.

Reference values of the quantities used in the calculations for the instruments mentioned above are given in Table 2 2.

Assuming as detection level of an object emitting flux S_{lim} the ratio $S_{\text{lim}}/\sigma_{\text{image}} = 5$, for a given telescope the integration time required for each pointing can be obtained by inverting eq. 1.2. The number of pointings necessary to cover a sky area A_s is

$$n_p = A_s/FOV. \tag{2.41}$$

If the integral counts of sources scale as $S^{-\beta}$, the number of sources detected in a given area scales as $t^{\beta/2}$. For a given flux, the number of detections is proportional to the surveyed area, i.e. to t. Thus, to maximize the number of detections in a given observing time we need to go deeper if $\beta > 2$ and to survey a larger area if $\beta < 2$. The number of sources detected above a given flux limit, S_{lim}, within a telescope FOV, N_{FOV}, is straightforwardly derived from the source counts. The number of such pointings necessary to detect N_s sources is $n_p = N_s/N_{\text{FOV}}(S_{\text{lim}})$ and the corresponding surveyed area is $A_s = n_p\,\text{FOV}$. The predicted integral counts of thermal and kinetic SZ effect for several frequencies, covered by the radio interferometers mentioned above, are shown in figs. 2.11(a) and 2.11(b), respectively. The scale on the right-hand side of these figures gives the corresponding area containing 100 protospheroids.

The time necessary to reach the wanted S_{lim} with $S/N = 5$ in a single pointing, t_{p}, is obtained from eq. (1.2), and the total observing time for detecting N_s sources (excluding the slew time) is obviously $t_{\text{p}}n_{\text{p}}$. In figs. 2.12(a) and 2.12(b) we show the on-source time $t_{\text{p}}n_{\text{p}}$ for $N_s = 100$ as a function of the absolute value of the thermal and kinetic SZ limiting flux for the 4 instruments in Table 2 2 at the frequencies specified in the inset. The curves have minima at the values of S_{lim} corresponding to the fastest survey capable of detecting the wanted number of sources. Clearly, it will be very time-consuming to detect 100 protospheroids with the EVLA, and unrealistic with the ATCA. On the other hand, since the 7 mm upgrade of ATCA will be operational already in 2009, it will be possible to exploit it to get the first test of the present predictions, and possibly to achieve the first detection of an SZ signal from a proto-spheroidal galaxy.
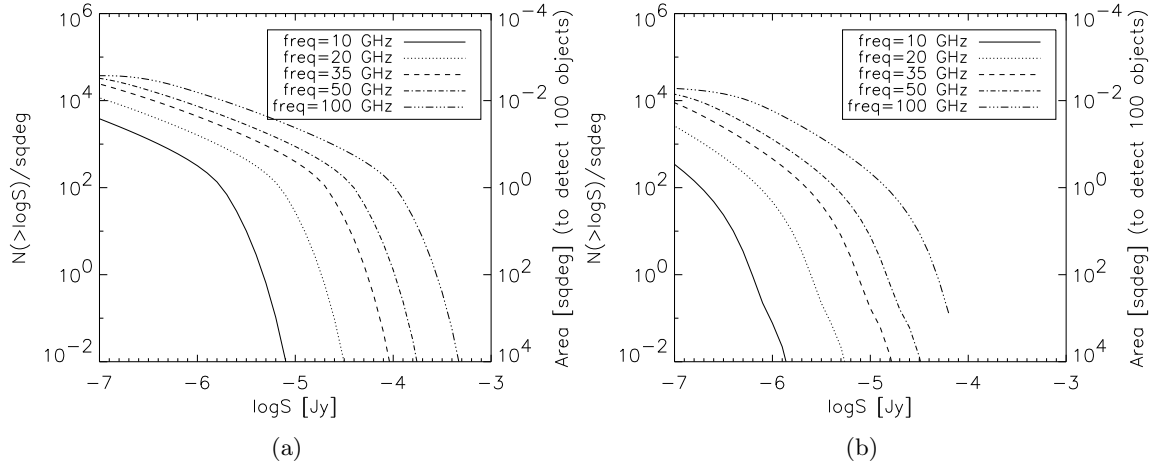
Figure 2 11 Integral counts and sky area (right-hand scale) required to detect the thermal (a) and kinetic (b) SZ effect of 100 protospheroids as a function of the absolute value of the 'flux' at 20, 35 and 100 GHz. For the kinetic SZ effect, as in fig. 2 9, the counts include both positive and negative signals; for the latter, S is obviously the absolute value of the flux.
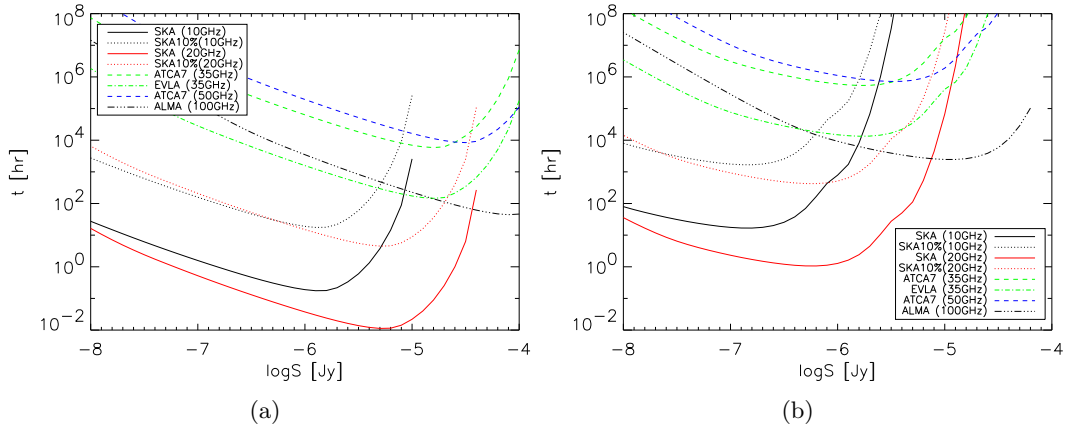
Figure 2 12 Total survey time for ALMA, SKA, EVLA and ATCA to detect 100 protospheroids in thermal (a) and kinetic (b) SZ at the frequencies specified in the inset.
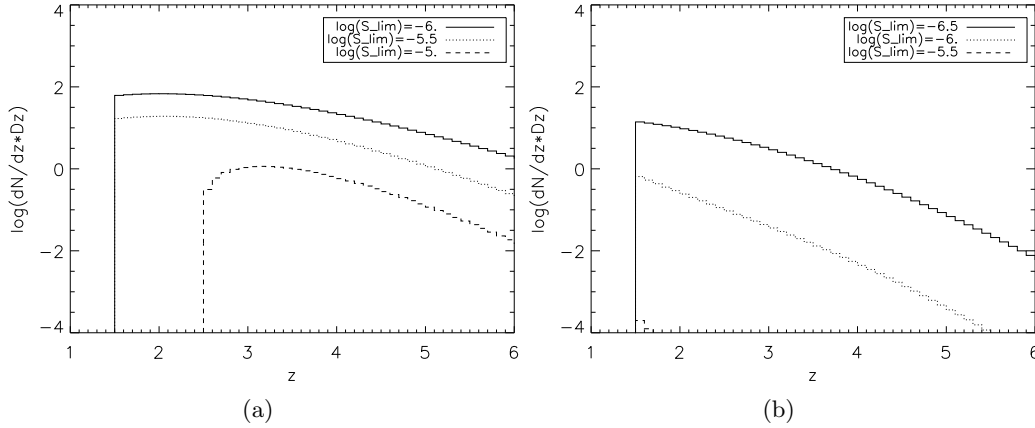
Figure 2 13 Redshift distribution (in bins of width $\delta z = 0.1$) of thermal (a) and kinetic (b) Sunyaev-Zel'dovich effects at 20 GHz for the flux limits specified in the inset.

The SKA large effective collecting area allows the detection of thermal SZ signals of 100 protospheroidal galaxies at 20(10) GHz in 1(11) minutes with 7(7) pointings reaching $S_{\lim} = 10^{-5.3}(10^{-5.9})$ Jy in a $0.46(0.47)\,\mathrm{deg}^2$ area. The 10% SKA requires 100 times more time than the full SKA but is still faster than EVLA or ALMA. If phased array feeds were available at the higher frequencies they would improve these surveying times by a factor of up to 50.

2 3.3.2   Redshift distributions

The redshift distributions of thermal and kinetic SZ effects are illustrated, for 3 values of $S_{\lim}$, in figs. 2.13(a) and 2.13(b). They are both relatively flat, as the fast decrease with increasing z of the density of massive (i.e. SZ bright) halos is partially compensated by the brightening of SZ signals (eqs. 2.27 and 2.28). Such brightening is stronger for the thermal than for the kinetic SZ. A consequence of such brightening is that the range of halo masses yielding signals above a given limit shrinks with decreasing redshift, as the minimum detectable halo mass increases. The upper limit on masses of galactic halos then translates in a lower limit to the redshift distribution for bright $S_{\lim}$.

2 3.3.3   Contaminant emissions

The adopted model envisages that the plasma halo has the same size as the dark matter halo, i.e. of order of hundreds kpc. In the central region (with size of order of 10 kpc), the gas cools rapidly and forms stars. Bressan et al. (2002) obtained a relationship between the star formation rate (SFR) and the radio luminosity at 8.4 GHz, $L_S(8.4\mathrm{GHz})$:

$$L_S(8.4\mathrm{GHz}) \simeq 3.6 \times 10^{27} \frac{\mathrm{SFR}}{M_\odot/\mathrm{yr}} \ \mathrm{erg\,s^{-1}\,Hz^{-1}}. \tag{2.42}$$

This relationship is in good agreement with the estimate by Carilli (2001) while the equations in Condon (1992) imply a radio luminosity about a factor of 2 lower, at fixed SFR. The
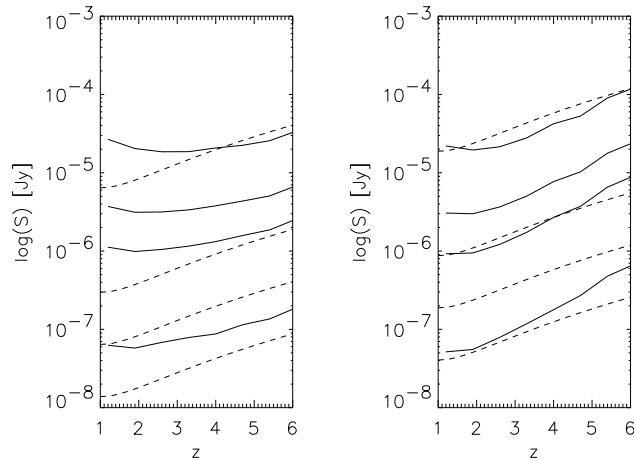
Figure 2 14 Comparison of the flux associated with star formation (solid lines) with the thermal SZ 'flux' (dashed lines) at 20GHz (left panel) and at 35GHz (right panel), as a function of the virialization redshift for four values of the virial mass ($\log(M_{\mathrm{vir}})$= 11.5, 12., 12.5, 13.2, from bottom to top).

Granato et al. (2004) model gives the SFR as a function of galactic age, t_{gal}, for any value of the halo mass and of the virialization redshift (see, e.g., fig. 1 of Mao et al. 2007). We must, however, take into account that eq. 2.42 has been derived using a Salpeter (1955) Initial Mass Function (IMF). For the IMF used by Granato et al. (2004), the radio luminosity associated to a given SFR is higher by a factor of 1.6 (Bressan, personal communication). The coefficient in eq. 2.42 was therefore increased by this factor.

The mean rest frame 8.4 GHz luminosity at given M_{vir} and z_{vir} was then obtained using the corresponding SFR averaged over t_{gal} in the renormalized eq. 2.42. Extrapolations in frequency have been obtained using, as a template, the fit to the Arp 220 continuum spectrum obtained by Bressan et al. (2002; solid line in their fig. 2). Using the continuum spectrum of M 82 (solid line in fig. 1 of Bressan et al.), the other standard starburst template, we get essentially identical results. In fig. 2 14 we compare the flux associated with star formation with the thermal SZ 'flux' [eq. (2.27)], as a function of the virialization redshift, for several values of M_{vir}. For a given halo mass, the ratio of the thermal SZ to the contaminating signal increases with frequency (and with redshift) as far as the contamination is due to radio emission associated to star formation (we do not consider here nuclear radio emission, which occurs in $\lesssim$ 10 per cent of galaxies). However, already at 20 GHz the thermal dust emission becomes important for the highest redshift sources. Such emission is more steeply increasing with frequency than the SZ signal, even in the Rayleigh-Jeans region of the CMB, and rapidly overwhelms it at $\gtrsim$ 100 GHz. The SZ/contamination ratio increases with increasing halo mass; therefore the SZ detection is easier for the more massive halos. Thus in the range 10–35 GHz the thermal SZ is expected to dominate over the contaminating signal at least for the most massive objects.

It must be noted that the star forming regions are concentrated in the core of the spheroids, on angular scales of the order or less than 1 arcsec, for the redshifts considered here. Long ($\gtrsim$ 3 km at 35 GHz for full sensitivity) baselines observation with high sensitivity

may be able to resolve the star forming region positive signal and subtract it from the image. To achieve this purpose a good sampling of the shortest spacings on the uv plane is necessary together with a good sampling of the largest ones: with the latter it might be possible to reconstruct the contaminated profile, subtract it from the former and produce an uncontaminated SZ profile. Again, the SKA at high frequencies seems to be the optimal instrument.

2 3.3.4   Confusion effects

Further constraints to the detection of SZ effects are set by confusion fluctuations. Fomalont et al. (2002) have determined the 8.4 GHz source counts down to $7.5\,\mu$Jy. For $S_{8.4\mathrm{GHz}} \lesssim 1\,$mJy they are well described by:

$$N(>S) \simeq 1.65 \times 10^{-3} S^{-1.11} \text{ arcsec}^{-2} \tag{2.43}$$

with S in μJy. The spectral index distribution peaks at $\alpha \simeq 0.75$ ($S \propto \nu^{-\alpha}$).

For all but one (SKA 10 GHz) of the considered surveys the 'optimal' depth for detecting 100 sources corresponds to 8.4 GHz flux densities within the range covered by Fomalont et al. (2002), so that the confusion fluctuations are dominated by sources obeying eq. (2.43). We then have:

$$\sigma_{\mathrm{conf}}^2 \simeq 0.2 \left(\frac{\nu}{8 \text{ GHz}}\right)^{-1.11\alpha} \frac{\omega}{100 \text{ arcsec}^2} S_{\mathrm{d}}^{0.89} \ \mu\mathrm{Jy}^2 \tag{2.44}$$

where S_{d}, in μJy, is the detection limit and ω is the solid angle subtended by the SZ signal. Equation (2.44) can be rewritten as

$$\frac{S_{\mathrm{d}}}{\sigma_{\mathrm{conf}}} \simeq 2.2 \left(\frac{\nu}{8.4 \text{ GHz}}\right)^{0.555\alpha} \left(\frac{\omega}{100 \text{ arcsec}^2}\right)^{-1/2} S_{\mathrm{d},\mu\mathrm{Jy}}^{0.555}, \tag{2.45}$$

yielding a $5\sigma_{\mathrm{conf}}$ detection limit of $\simeq 4\,\mu$Jy at 10 GHz and of $\simeq 2.3\,\mu$Jy at 20 GHz. For the 'optimal' survey depths at higher frequencies $S_{\mathrm{d}}/\sigma_{\mathrm{conf}} \gg 5$, implying that they are not affected by confusion noise due to radio sources.

On the other hand, as noted above, at high frequencies the redshifted dust emission from distant star-forming galaxies becomes increasingly important (De Zotti et al. 2005). To estimate their contribution to the confusion noise, we have used once again the model by Granato et al. (2004), with the dust emission spectra revised to yield 850μm counts consistent with the results by Coppin et al. (2006), and complemented by the phenomenological estimates by Silva et al. (2004, 2005) of the counts of sources other than high-z proto-spheroids (see Negrello et al. 2007 for further details). We find, for a typical solid angle $\omega = 100\,$arcsec^2, $5\sigma_{\mathrm{conf}}$ flux limits due to these sources of 3, 55, and $190\,\mu$Jy at 20, 35, and 50 GHz, respectively. Thus at 20 GHz we have significant contributions to the confusion noise both from the radio and from the dust emission; the overall $5\sigma_{\mathrm{conf}}$ detection limit is $S_{\mathrm{d}} \simeq 4\,\mu$Jy. At 10 GHz the contribution of dusty galaxies to the confusion noise is negligible, while at 100 GHz the confusion limit is as high as 2 mJy, implying that the detection of the galactic-scale SZ effect is hopeless at mm wavelengths.

Although high-z luminous star-forming galaxies may be highly clustered (Blain et al. 2005; Farrah et al. 2006; Magliocchetti et al. 2007), the clustering contribution to

fluctuations is negligible on the small scales of interest here (De Zotti et al. 1996), and can safely be neglected.

2 3.4 The SZ effect in protospheroids: summary and discussion

In the standard scenario for galaxy formation, the proto-galactic gas is shock heated to the virial temperature. The observational evidences that massive star formation activity must await the collapse of large halos, a phenomenon referred to as *downsizing*, suggests that proto-galaxies with a high thermal energy content existed at high redshifts. Such objects are potentially observable through the thermal and kinetic Sunyaev-Zel'dovich effects and their free-free emission. The detection of this phase of galaxy evolution would shed light on the physical processes that govern the collapse of primordial density perturbations on galactic scales and on the history of the baryon content of galaxies.

As for the latter issue, the standard scenario, adopted here, envisages that the baryon to dark matter mass ratio at virialization has the cosmic value, i.e. is about an order of magnitude higher than in present day galaxies. Measurements of the SZ effect will provide a direct test of this as yet unproven assumption, and will constrain the epoch when most of the initial baryons are swept out of the galaxies.

As mentioned, almost all semi-analytic models for galaxy formation adopt halo mass functions directly derived or broadly consistent with the results of N-body simulations, and it is commonly assumed that the gas is shock heated to the virial temperature of the halo. They therefore entail predictions on counts of SZ effects similar to those presented here. On the other hand, the thermal history of the gas is governed by a complex interplay of many astrophysical processes, including gas cooling, star formation, feedback from supernovae and active nuclei, shocks. As mentioned, recent investigations have highlighted that a substantial fraction of the gas in galaxies may not be heated to the virial temperature. Also, it is plausible that the AGN feedback transiently heats the gas to temperatures substantially above the virial value, thus yielding SZ signals exceeding those considered here. The gas thermal history may therefore be substantially different from that envisaged by semi-analytic models, and the SZ observations may provide unique information on it.

We have presented a quantitative investigation of the counts of SZ and free-free signals in the framework of the Granato et al. (2004) model, that successfully accounts for the wealth of data on the cosmological evolution of spheroidal galaxies and of AGNs (Granato et al. 2004; Cirasuolo et al. 2005; Silva et al. 2005; Lapi et al. 2006).

We find that the detection of substantial numbers of galaxy-scale thermal SZ signals is achievable by blind surveys with next generation radio interferometers. Since the protogalaxy thermal energy content increases, for given halo mass, with the virialization redshift, the SZ 'fluxes' increase rather strongly with z, especially for the thermal SZ effect, partially compensating for the rapid decrease of the density of massive halos with increasing redshift. The redshift distributions of thermal SZ sources are thus expected to have substantial tails up to high z.

There are however important observational constraints that need to be taken into account. The contamination by radio and dust emissions associated to the star formation activity depends on mass and redshift of the objects, but is expected to be stronger than the SZ signal at low and high frequencies. We conclude that the optimal frequency range

for detecting the SZ signal is from 10 to 35 GHz, where such signal dominates over the contamination at least for the most massive objects. It must be noted however that contaminating emissions have typical scales of the order of those of the stellar distributions, i.e. $< 1''$ at the redshifts of interest here (see Fomalont et al. 2006), while the SZ effects show up on the scale of the dark matter halo, which is typically ten times larger. Therefore arcsec resolution images, such as those that will be provided by the SKA, will allow to reconstruct the uncontaminated SZ signal.

The coexistence of the hot plasma halo, responsible for the SZ signal, with dust emission implies that the scenario presented in this work may be tested by means of pointed observations of high-z luminous star-forming galaxies detected by (sub)-mm surveys.

Confusion noise is a very serious limiting factor at mm wavelengths. Contributions to confusion come on one side from radio sources and on the other side from dusty galaxies. At 10 GHz only radio sources matter; a modest extrapolation of the 8.4 GHz μJy counts by Fomalont et al. (2002) gives a $5\sigma_{\rm conf}$ detection limit $S_{\rm d} \simeq 4\,\mu$Jy, for a SZ signal subtending a typical solid angle of $100\,{\rm arcsec}^2$. Fluctuations due to dust emission from high-z luminous star-forming galaxies may start becoming important already at 20 GHz; at this frequency, quadratically summing them with those due to radio sources we find again $S_{\rm d} \simeq 4\,\mu$Jy, for the same solid angle. On the other hand, the high resolution of the SKA will allow us to effectively detect and subtract out confusing sources, thus substantially decreasing the confusion effects. Beating confusion will be particularly important for searches of the weaker kinetic SZ signal.

Part 3

CMB foregrounds

3 1   The role of foregrounds for CMB observations

The millimetric wavelength band is the so called *cosmological window*, because it includes the peak of the CMB black body signal and corresponds to a minimum of the contaminating foregrounds. Because of this the millimetric wavelength range is the optimal one for CMB observations.

The crucial importance of the CMB as a source of information on the early epochs of the Universe, and, in particular, the wealth of knowledge inscribed in the anisotropy angular power spectrum (see fig.3 1) have been extensively described in the literature (see Hu & Dodelson 2002, Hu 2003 and references therein).

However, the cosmological signal is superimposed to a mixture of signals from extragalactic and Galactic emissions that, together with instrumental noise and systematics, are collected by the telescopes.

The observed signal at frequency ν can be described as:

$$\text{observedsignal}(\nu) \quad = \quad \text{beam}(\nu) * (\text{CMB} + \text{foreground1}(\nu) + \tag{3.1}$$
$$+ \quad \text{foreground2}(\nu) + ... + \text{systematics}(\nu)) + \text{noise} + ... \tag{3.2}$$

where $*$ indicates convolution.

Once the systematics due to the instrument have been removed the major limitation on a full exploitation of the capabilities of the CMB as a cosmological probe is the contamination due to astrophysical signals that originate between the observers and the last scattering surface, the so called *foregrounds*. Such signals, in fact, mask, confuse, distort the energy distribution of the CMB photons, and make the accurate reconstruction of the primordial anisotropy pattern extremely difficult.

CMB observations are performed from the ground, with single dishes or radio arrays (see for example DASI, VSA or Subrahmanian et al. 2000), with balloons (as for experiments like BOOMERang or Archeops), or from space (COBE, WMAP or Planck): a list of the experiments is maintained by Max Tegmark[1].

Some of the major differences among the various approaches reside in the different resolutions and sky coverages that could be obtained: ground based experiments could reach

---

[1] http://space.mit.edu/home/tegmark/index.html
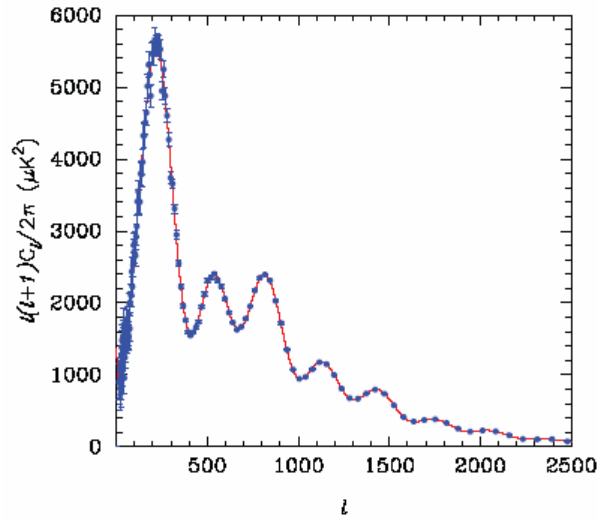
Figure 3 1 CMB power spectrum (predictions for the Planck mission, see the 'Planck Bluebook').

high angular resolution, but are limited to the sky area available at the telescope latitude; balloons could cover larger areas, sometimes down to high resolution, and could also be moved to combine several patches of the sky observed from different positions on Earth; satellites could perform all-sky surveys, but are typically limited in resolution. Satellites have also the important advantage that their observations are not contaminated by the atmosphere.

Resolution constrains the higher observable multipoles[2] in the CMB power spectrum (i.e. the smaller scales), whereas cosmic variance and sky coverage limits the spectrum knowledge towards the lower multipoles (i.e. the largest scales).

Recent technological improvements guarantee that the temperature sensitivity of the next generation of telescopes (e.g. Planck) will be limited by astrophysical foregrounds rather than by the instrumental properties.

The CMB temperature fluctuations are frequency-independent, but each foreground signal has its own spectral behaviour and spatial pattern. This fact offers a way to distinguish the foregrounds from the CMB signal, provided that we can characterize each foreground component.

Interferometric observations may reconstruct the contaminant components via observations with different resolution (i.e. with different baseline length among antennas). For balloon and satellite experiments the data are organized in maps of the observed sky region and the power spectrum is obtained from them. In this case also the component analysis should be performed on the maps generated for several frequency channels: in order to reconstruct the spectral behaviour of the components, in fact, multifrequency observations

---

[2]The CMB power spectrum is commonly described in terms of 'multipoles', l, that, on small areas of the sky, where the curvature can be neglected, correspond to the wavenumber of the two dimensional Fourier decomposition of the anisotropy pattern: the angular scale corresponds roughly to $\theta \simeq 2\pi/l$, so that low multipoles describe anisotropies on large scales and viceversa.

Table 3 1 Some of the fundamental properties of the Planck mission.

Instrument	LFI			HFI					
Detector Technology	HEMT radio receiver arrays			Bolometer detector arrays					
Frequency (GHz)	30	44	70	100	143	217	353	545	857
Bandwidth (GHz)	6	8.8	14	33	47	72	116	180	283
Beam size (deg)	0.55	0.4	0.23	0.16	0.12	0.08	0.08	0.08	0.08
Average $\Delta T/T$ per pixel	2.0	2.7	4.7	2.5	2.2	4.8	14.7	147	6700

are necessary.

Usually foregrounds are classified as 'compact' and 'diffuse' components. The first class collects all the objects which size is, roughly speaking, smaller than the beam size of the CMB telescopes. In the second category we have the Galactic synchrotron, free-free and dust emissions.

Several methods for component separation have been developed (see Leach et al. 2008 for a review of those whose properties have been investigated for the Planck mission). The knowledge of the foreground properties improves the performances of the techniques. Testing these methods on realistic simulations is crucial to evaluate their effectiveness on real data and the quality of their output. The final scientific performances of the mission could be limited, therefore, not only by the instrumental quality, but also by how effectively the astrophysical foregrounds are handled.

3 2   Foreground handling for the Planck mission

The European Space Agency is developing the Planck satellite as the definitive mission for the study of CMB temperature anisotropy on scales down to 5 arcmin and a big step forward towards all-sky measurements of CMB polarization. Planck improves on WMAP, especially on the smallest angular scales and in polarisation, thanks to better sensitivity and resolution: higher resolution, in fact, means a better knowledge up to higher multipoles; better sensitivity implies that some parameter may be directly measured, allowing to directly test the models predictions, and that, if the tensor to scalar perturbation ratio is high enough, the B-modes of polarisation may be detectable, or, at least, strongly constrained.

Furthermore, Planck is expected to map the CMB anisotropies with high sensitivity. High signal to noise ratios in the maps are essential for searches of primordial non-Gaussianities. As mentioned, the crucial step of data analysis is the characterization of foreground properties and the development of effective component separation techniques. For this purpose the Planck satellite frequency coverage extends from 30 up to 857 GHz, in 9 bands (WMAP has only 5 bands ranging from 23 to 94 GHz).

'Component separation' is a catch-all term encompassing any data processing that exploits correlations in observations made at separate frequencies, as well as external constraints and physical modelling, as a mean of discriminating between different physical

sources of emission. Planck has a number of different scientific objectives: the primary goal is a cosmological analysis of the CMB, but important secondary goals include obtaining a better understanding of the interstellar medium and Galactic emission, measurement of extragalactic sources of emission and the generation of a Sunyaev-Zel'dovich (SZ) cluster catalogue. These planned objectives will lead to a set of data products which the Planck consortium is committed to delivering to the wider community some time after the completion of the survey. These data products include maps of the main diffuse emissions and catalogues of extragalactic sources, such as galaxies and clusters of galaxies.

In the following subsection we will present some tools that we have contributed to build in the framework of the Planck consortium in order to exploit and improve the knowledge of diffuse foregrounds and of compact components. In particular:

- the Planck Sky Model (PSM), a gigantic collection of simulations of diffuse and compact components that have been broadly used, so far, to test the component separation techniques;

- a pre-launch radio source mask and catalogue covering the whole sky, built on the basis of several lower-frequency catalogues;

3 2.1   The Planck Sky Model

The Planck Sky Model (PSM) is a flexible software package developed by the working group that, within the Planck consortium, have been organized to solve the component separation issue. It is well suited for making predictions, simulations and constrained realizations of the microwave sky.

The CMB sky is based on the observed WMAP multipoles up to $l = 70$, and on a Gaussian realisation assuming the WMAP best-fit C_l at higher multipoles. It is the same CMB map used by Ashdown et al. (2007). The Galactic interstellar emission is described by a four component model of the interstellar medium comprising free-free, synchrotron, thermal and spinning dust emissions. The predictions are based on a number of sky templates which have different angular resolution. In order to simulate the sky at Planck resolution, small scale fluctuations to some of the templates have been added (see Miville–Deschênes et al. 2007 for details on the procedure that has been used).

Free-free emission is based on the model of Dickinson et al. (2003) assuming an electron temperature of 7000 K. The spatial structure of the emission is estimated using a Hα template corrected for dust extinction. The Hα map is a combination of the Southern H-Alpha Sky Survey Atlas (SHASSA) and of the Wisconsin H-Alpha Mapper (WHAM). The combined map was smoothed to obtain a uniform angular resolution of 1 degree. The Hα maps were corrected for extinction using the E$(B - V)$ all-sky map of Schlegel et al. (1998) which is a combination of a smoothed IRAS 100 μm (resolution of 6.1 arcmin) and a map at a few degrees resolution made from DIRBE data to estimate dust temperature and transform the infrared emission in extinction. As mentioned earlier, small scales were added in both templates to match the Planck resolution.

Synchrotron emission is based on an extrapolation of the 408 MHz map of Haslam et al. (1982) from which an estimate of the free-free emission was removed. In any direction in the sky, the spectral emission law of the synchrotron is assumed to follow a power law,

$T_b^{sync} \propto \nu^\beta$. A pixel-dependent spectral index β, has been used. It has been derived from the ratio of the 408 MHz map and the estimate of the synchrotron emission at 23 GHz in the WMAP data obtained by Bennett et al. (2003) using a Maximum Entropy Method technique, after having subtracted an estimate of the spinning dust component (see below).

The thermal emission from interstellar dust is estimated using model 7 of Finkbeiner et al. (1999). This model, fitted to the FIRAS data (7 degree resolution), makes the hypothesis that each line of sight can be modelled as the sum of the emission from two dust populations, one cold and one warm. Each grain population is in thermal equilibrium with the radiation field and thus has a grey-body spectrum. Once the model is fixed, the dust temperature of the two components is determined using only the flux ratio between 100 μm and 240 μm. For this purpose, the 100/240 μm map ratio published by Finkbeiner et al. (1999) has been used. Knowing the temperature and spectral index of each dust component at a given position on the sky, the 100 μm brightness at that position is used to scale the emission at any frequency. Note that the emission laws of the latter two components, synchrotron and dust, vary across the sky. The spectral index of free-free is kept constant across the sky as it only depends on the electron temperature, taken as a constant here.

A map of spinning dust emission was built separating the 'anomalous' and synchrotron emissions using WMAP polarisation data (Milville-Deschênes et al. 2008).

A map of thermal SZ spectral distortion from galaxy clusters has been added to the model, based on a cluster catalogue randomly drawn using a mass-function compatible with present-day observations and with ΛCDM parameters $\Omega_m = 0.3$, h = 0.7 and $\sigma_8 = 0.9$ (Colafrancesco et al. 1997; De Zotti et al. 2005). We have also added an estimation of the contamination of the SZ signal due to radio sources within the cluster on the basis of Massardi & De Zotti (2004) estimations. We have mainly contributed to the development of the simulation for compact components: radio sources and IR sources that will be more broadly discussed in the following subsections.

Component maps are produced at all Planck and WMAP central frequencies. They are then co-added and smoothed with Gaussian beams. Finally, inhomogeneous noise is obtained by simulating the hit counts corresponding to one year of continuous observations by Planck, using the Level-S simulations tool (Reinecke et al. 2006). The whole PSM will be release soon: by the time when Planck data will be available to the community it is the most comprehensive and realistic simulation of the whole sky available.

3 2.1.1 Radio sources in the PSM

A summary of the multi-steradian surveys used to construct an all-sky map of the radio source distribution is given in Table 1 6. Figure 3 2 illustrates their sky coverage. For the present purpose it is useful to distinguish 4 cases:

1. green points are sources with fluxes measured at both $\simeq 1$ GHz (NVSS or SUMSS) and 4.85 GHz (GB6 or PMN)

2. blue (yellow) points are sources present only in the NVSS (SUMSS) and thus with fluxes only at 1.4 (0.843) GHz

3. red points are sources with only PMN (4.85 GHz) fluxes
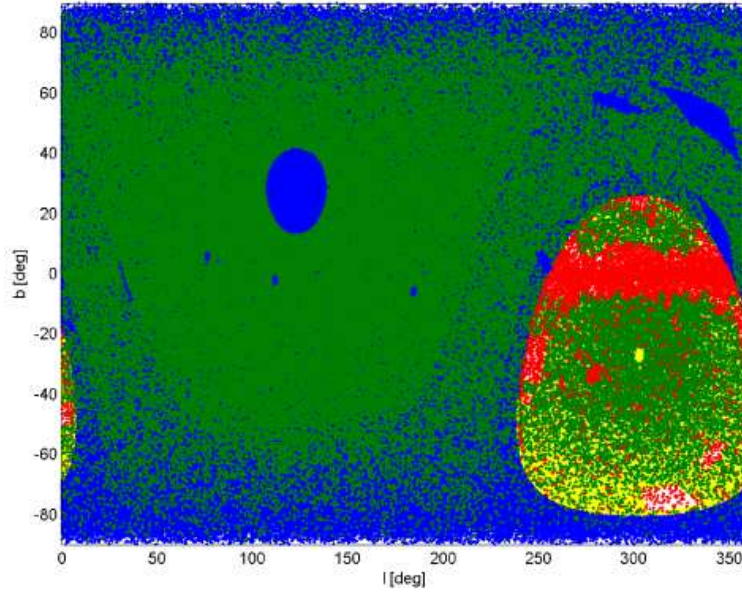
Figure 3 2 Sky coverage of the surveys listed in Table 1 6, in Galactic coordinates. Green points: sources present in both $\simeq 1\,\mathrm{GHz}$ (NVSS or SUMSS) and 4.85 GHz (GB6 or PMN) catalogs; blue points: sources in the NVSS catalog only; yellow points: sources in the SUMSS catalog only; red points: sources in the PMN catalog only; white regions: not covered by any survey.

    4. the small white regions are those not covered by any survey.

Extrapolations to Planck frequencies require the knowledge of the spectral behaviour, that is frequently quite complex (see e.g. Sadler et al. 2006). In the present data situation, however, we cannot do better than resorting to the usual power law approximation of source spectra.

        For sources of the group (1), which have measurements at 2 frequencies, the individual spectral indices α ($S_\nu \propto \nu^{-\alpha}$) can be estimated as $\alpha = -\log(S_{4.85\mathrm{GHz}}/S_{\mathrm{low}})/\log(4.85/\nu_{\mathrm{low}})$ where ν_{low} is either 1.4 GHz, if we are in the region covered by the NVSS, or 0.843 GHz if we are in the lower declination region covered by the SUMSS. However, the calculation is not as straightforward as it may appear, because the surveys at different frequencies have different resolutions, implying that a single source in a low resolution catalog can correspond to multiple sources at higher resolution. The spectral index estimates were carried out degrading the higher resolution survey to the resolution of the other. In practice, whenever the higher resolution (NVSS or SUMSS) catalogue contains more than one source within the resolution element of the lower resolution (4.85 GHz) survey, we have summed the NVSS or SUMSS fluxes, weighted with a Gaussian response function centered on the nominal position of the 4.85 GHz source, and with FWHM equal to the resolution of the 4.85 GHz survey.

        On the other hand, the low frequency surveys, and especially the NVSS, are substantially deeper than the 4.85 GHz surveys, which, furthermore, have quite inhomogeneous depths. Simply summing all the lower frequency sources within a resolution element includes a variable fraction of the background of weak sources, unresolved at 4.85 GHz, thus biasing the spectral index estimates. To correct for this, we have selected 159195 control fields, free
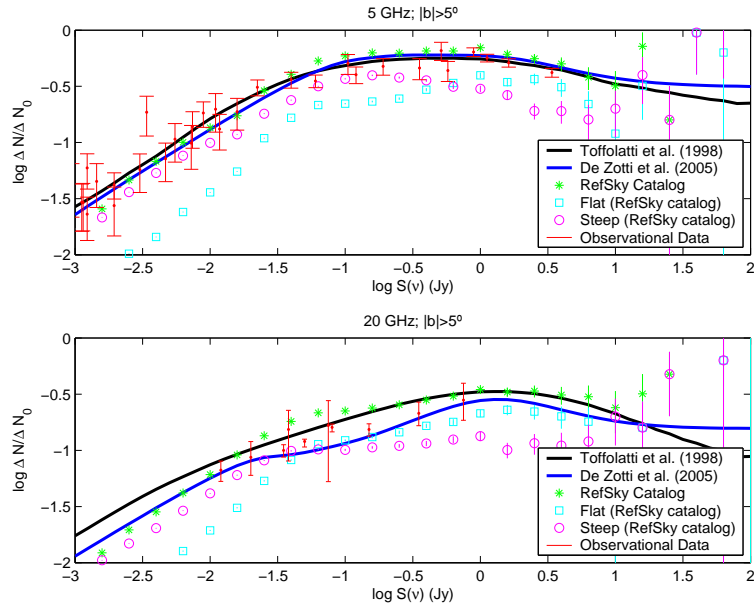
Figure 3 3 Source number counts at 5 and 20 GHz, normalized to $\Delta N_0 = S(\mathrm{Jy})^{-2.5}$, compared with models and observational data. Data at 5 GHz are from Kellermann et al. (1986), Fomalont et al. (1991) and Haarsma et al. (2000). Data in the 20 GHz panel are from the 9C survey (Waldram et al. 2003) at 15 GHz and from the ATCA survey at 18 GHz (Ricci et al. 2004); no correction for the difference in frequency was applied.

of 4.85 GHz sources, and computed the average flux of NVSS or SUMSS sources within a 4.85 GHz beam pointing on the field center, again taking into account the 4.85 GHz response function. The average fluxes of control fields, ranging from 1.67 to 3.16 mJy for the different combinations of low and high frequency catalogs (NVSS/GB6, NVSS/PMN, SUMSS/PMN), have subtracted from the summed NVSS or SUMSS fluxes associated with 4.85 GHz sources. In this way we obtained spectral indices from ~ 1 to ~ 5 GHz for a combination of complete 5 GHz selected samples with somewhat different depths, summing up to 109152 sources over about 95% of the sky.

Although this is the best we can do with the available data, it is clear that the derived individual spectral indices are uncertain, due to a combination of several factors: measurement errors, uncertainties associated to the corrections applied, that are of statistical nature, and variability (the surveys have been carried out at different epochs). As a result, the absolute values of several individual spectral index estimates turned out to be unrealistically large, and the global distribution was found to be substantially broader than indicated by accurate studies of smaller samples. Furthermore, convolving our spectral index distribution with the 1.4 GHz counts we obtain an estimate of the 5 GHz counts exceeding by an average factor of $\simeq 1.8$ those directly observed, again indicating that the spectral index distribution is spuriously broadened. Therefore, we have used the spectral index estimates only to: a) assign the sources either to the steep- or to the flat-spectrum class, the boundary value being $\alpha = 0.5$; b) determine the mean spectral index. We find $\langle \alpha_{\mathrm{steep}} \rangle = 1.18$, $\langle \alpha_{\mathrm{flat}} \rangle = 0.16$. The spectral index distributions are approximated by Gaus-
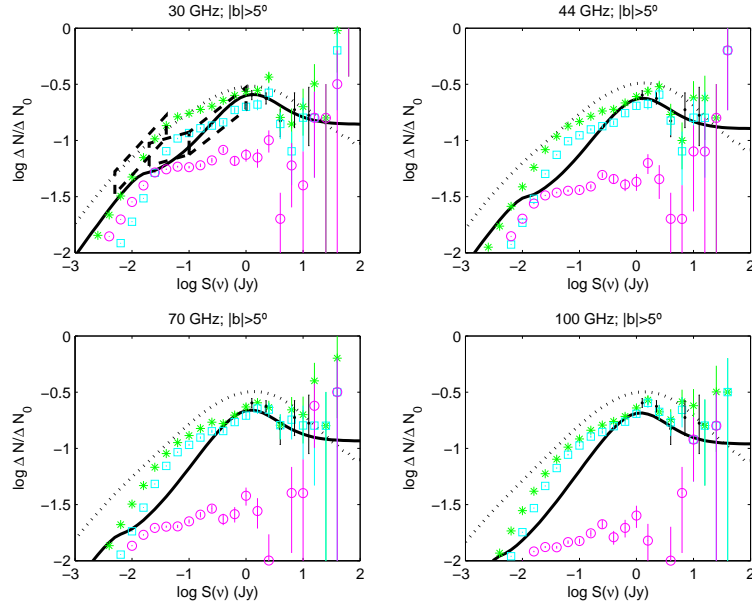
Figure 3 4 Source number counts, normalized to $\Delta N_0 = S_{\mathrm{Jy}}^{-2.5}$, at 30, 44, 70 and 100 GHz compared with the model by Toffolatti et al. (1998; upper solid curve) and with the model by De Zotti et al. (2005), updated as described in the text, and with observational data. As in Fig. 3 3, the asterisks show the total number counts of sources at $|b| > 5°$ in our maps, while the squares and the circles show the contributions of flat- and steep-spectrum sources, respectively; error bars are Poisson uncertainties. The dots with error bars, present at all frequencies, show the WMAP counts, estimated from the catalog by Hinshaw et al. (2007). At 30 GHz, the boxes show the counts estimated from (in order of decreasing fluxes) the DASI (Kovac et al. 2002), VSA (Cleary et al. 2005), and the CBI (Mason et al. 2003) experiments. The DASI and CBI measurements are at 31 GHz, the VSA ones at 34 GHz.

sians with variances $\sigma_{\mathrm{steep,flat}} = 0.3$, consistent with the results by Ricci et al. (2006). We have then extrapolated the 5 GHz fluxes to 20 GHz by assigning to each source a spectral index randomly drawn from the Gaussian distribution for its class.

Sources with flux measurements at a single frequency have been randomly assigned to either the steep- or to the flat-spectrum class in the proportions observationally determined by Fomalont et al. (1991) for various flux intervals, and assigned a spectral index randomly drawn from the corresponding distribution. The small holes in the sky coverage have been filled by randomly copying sources from other regions in proportion to the surface density appropriate for each flux interval. The same procedure was adopted to add fainter sources in the regions where the existing surveys are shallower, until a coverage down to at least $\simeq 20\,\mathrm{mJy}$ at 5 GHz over the full sky was achieved. We have checked that still fainter sources do not appreciably contribute to fluctuations in Planck channels for detection limits in the estimated range ($\simeq 200$ to $\simeq 500\,\mathrm{mJy}$; López-Caniego et al. 2006), as expected since fluctuations are dominated by sources just below the detection limit. This check was carried out computing the power spectra of fluctuations due to sources below such limits in regions covered by the NVSS (the deepest survey) and in regions covered to shallower limits: the results are indistinguishable. The regions less covered by real surveys, where the fraction of simulated sources is larger, are mostly around the Galactic plane, where they have a minor effect compared to free-free and synchrotron emissions. At Galactic latitudes $|b| > 10°$ the

Table 3 2 Best fit values of the parameters of the evolutionary models for canonical radio sources. $\log L_*$ is in $\mathrm{erg\,s^{-1}\,Hz^{-1}}$ at 5GHz, $z = 0$.

Source	luminosity function				evolution	
type	$\log n_0 (\mathrm{Mpc^{-3}})$	a	b	$\log L_*$	k_{ev}	z_{top}
FSQ	-8.989	0.658	2.938	34.043	0.224	2.254
BL Lac	-7.956	0.975	1.264	32.831	1.341	
Steep	-7.389	0.729	2.770	33.177	0.262	2.390

fraction of real sources (at least as far as positions are concerned) is of $\simeq 97\%$; over the full sky is of $\simeq 95\%$. Therefore we expect that the simulated maps faithfully reflect also the clustering properties of radio sources.

In Fig. 3 3 the source counts at 5 and 20 GHz obtained from our map are compared with observed counts, with the model by Toffolatti et al. (1998), and with an updated version of the model by De Zotti et al. (2005), allowing for a high-redshift decline of the space density of both flat-spectrum quasars (FSQs) and steep-spectrum sources (not only for FSQs as in the original model). The model adopts luminosity functions (in units of $\mathrm{Mpc^{-3}} \, (d \log L)^{-1}$) of the form

$$\Phi(L, z) = \frac{n_0}{(L/L_*)^a + (L/L_*)^b} \ . \tag{3.3}$$

and lets those of steep-spectrum sources and of FSQs evolve in luminosity as

$$L_{*,\mathrm{FSRQ}}(z) = L_*(0) 10^{k_{\mathrm{ev}} z (2 z_{\mathrm{top}} - z)} \ , \tag{3.4}$$

while for BL Lac objects a simpler evolutionary law is used:

$$L_*(z) = L_*(0) \exp[k_{\mathrm{ev}} \tau(z)] \ , \tag{3.5}$$

where $\tau(z)$ is the look-back time in units of the Hubble time, H_0^{-1}. The new values of the parameters are given in Table 3 2.

Due to the complex spectral shape of radio sources, the power-law approximation holds only for a limited frequency range. To extrapolate the fluxes beyond 20 GHz we used the multifrequency first year WMAP data (Bennett et al. 2003) to derive the distributions of differences, $\delta\alpha$, between spectral indices above and below that frequency, and no change is expected from the following update of the WMAP catalogue. Such distributions can be approximated by Gaussians with mean 0.35 and dispersion 0.3. To each source we have associated a spectral index change drawn at random from the distribution. In Fig. 3 4 we compare the number counts calculated from the extrapolated catalogue with data from different surveys at $\simeq 30\,\mathrm{GHz}$, with WMAP counts, and with model predictions.

We have also produced maps of polarized emission attributing to each source a polarization degree randomly drawn from the observed distributions for flat- and steep-spectrum sources at 20 GHz (Ricci et al. 2006), and a polarization angle randomly drawn from a uniform distribution.
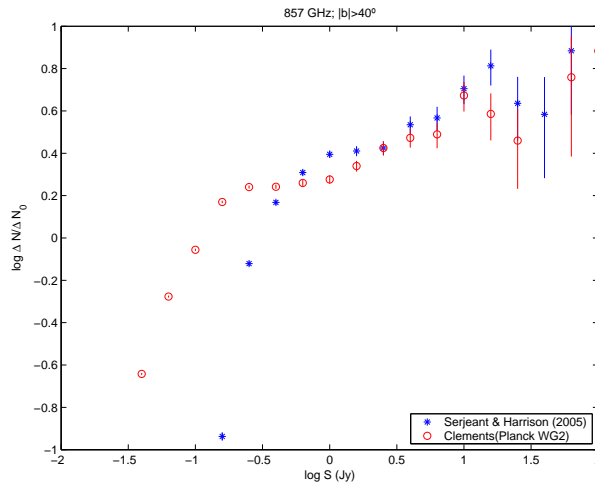
Figure 3 5 Comparison between the source number counts of Serjeant & Harrison (2005) sources and the Clements ones at 857 GHz for $|b| > 40°$.

3 2.1.2   Far-Infrared Sources

Combining far-IR (IRAS) and sub-mm (from the SCUBA Local Universe Galaxy Survey, Dunne et al. 2000) measurements, Serjeant & Harrison (2005) interpolated and extrapolated the IRAS detections to make predictions of the SEDs of all 15411 PSC-z galaxies (Saunders et al. 2000) from 50 to 1300 microns. A compilation including all FIR sources taken from the IRAS Point Source Catalog (PSC) and the Faint Source Catalog (FSC), with fluxes extrapolated to Planck frequencies was provided to the Planck working group by Dave Clements. The extrapolation was done adopting grey-body spectra $\nu^b B(\nu, T)$, $B(\nu, T)$ being the black-body function. For sources detected at only one IRAS frequency b and T were taken to be those of the average Spectral Energy Distribution of the sample by Dunne et al. (2000), i.e. $b = 1.3$ and $T = 35$ K. If the source is detected at 60 and $100 \, \mu$m, then $b = 1.3$ was still assumed but the temperature was obtained fitting the data. The two samples have been combined, keeping the Serjeant & Harrison fluxes for common sources. The resulting sample looks approximately complete down to ~ 80 mJy at 857 GHz (see Fig. 3 5), at high Galactic latitudes.

As the PSC does not contain objects where the confusion from Galactic sources is high, and thus does not penetrate the Galactic centre well, and the FSC is restricted to regions away from the Galactic plane, the source density is a function of Galactic latitude. As we did for radio sources, we have added randomly distributed sources until the mean surface density as a function of flux matched everywhere the mean of well covered regions down to $S_{857\text{GHz}} \sim 80$ mJy. The coverage gaps of the catalog (the IRAS survey missed about 4% of the sky) were filled by adding randomly distributed sources until the mean surface density as a function of flux matched the mean of well covered regions.

On the other hand, an important, and possibly dominant, contribution to (sub)-mm small-scale anisotropies comes from galaxies selected by SCUBA and MAMBO surveys (see e.g. Scott et al. 2006; Coppin et al. 2006), that are probably strongly clustered
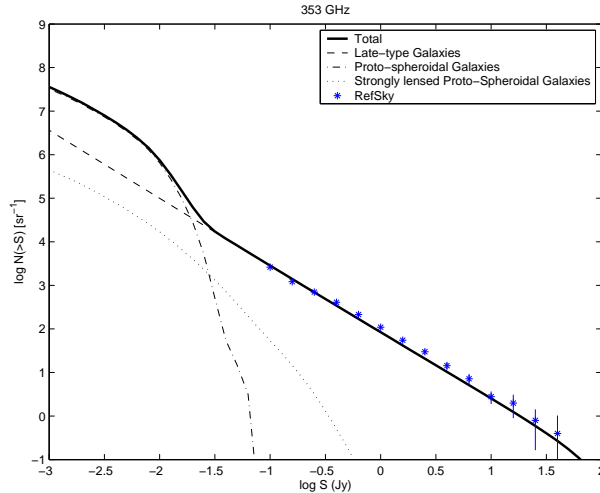
Figure 3 6 Counts at $850\,\mu$m included in the sky model. The total counts (heavy solid line) includes the contributions of un-lensed (dot-dashed line) and strongly lensed (dotted line) dusty proto-spheroids and of late-type and starburst galaxies (dashed line). Sources have been included individually down to 0.1 Jy; the asterisks show their counts as recovered counts from the simulated map, to check self-consistency. In addition we have worked out and added to the simulated map the fluctuation field due to fainter sources (that yield an important contribution to small scale fluctuations because of their very steep counts), including the effect of clustering, as described in the text.

(Negrello et al. 2004). These galaxies are interpreted as massive proto-spheroidal galaxies in the process of forming most of their stars in a gigantic starburst. We have adopted the counts predicted by the Granato et al. (2004) model, which successfully accounts for a broad variety of data including the SCUBA and MAMBO counts (although are somewhat high compared to the data by Coppin et al. 2006) and the preliminary redshift distributions (Chapman et al. 2005, Aretxage et al. 2007). The clustering properties of these sources have been modelled as in Negrello et al. (2004), using their more physical model 2. The simulation of their spatial distribution has been produced using the method by González-Nuevo et al. (2005). Once a map of the source distribution was obtained at the reference frequency, $\nu_{\rm ref}$, extrapolations to any other frequency, ν_i, were obtained via the flux-dependent effective spectral indices $\alpha = -\log(S_{\rm ref}/S_i)/\log(\nu_{\rm ref}/\nu_i)$, were S_i is defined by $n(> S_i; \nu_i) = n(> S_{\rm ref}; \nu_{\rm ref})$. The spectral indices have been computed in logarithmic steps of $\Delta \log(S_{\rm ref}) = 0.1$. We have checked that the counts computed from the extrapolated maps accurately match those yielded, at each frequency, by the model.

As first pointed out by Blain (1996), the combination of the extreme steepness of the counts determined by SCUBA surveys and of the relatively large lensing optical depth corresponding to the substantial redshifts of these sources maximizes the fraction of strongly lensed sources at (sub)-mm wavelengths. We have included such sources in our simulation by randomly distributing them with flux-dependent areal densities given by Perrotta et al. (2003) (see Fig. 3 6). The frequency extrapolations were made via the spectral indices obtained in the same way as for the proto-spheroidal galaxies.

To each source we have assigned a polarization degree of 1% and a polarization angle randomly drawn from a uniform distribution.

TQU_infrared_857GHz_MJy_sr_nside256.fits: TEMPERATURE

−4.7 ■▬▬ 1.3 Log (Mjy/sr)
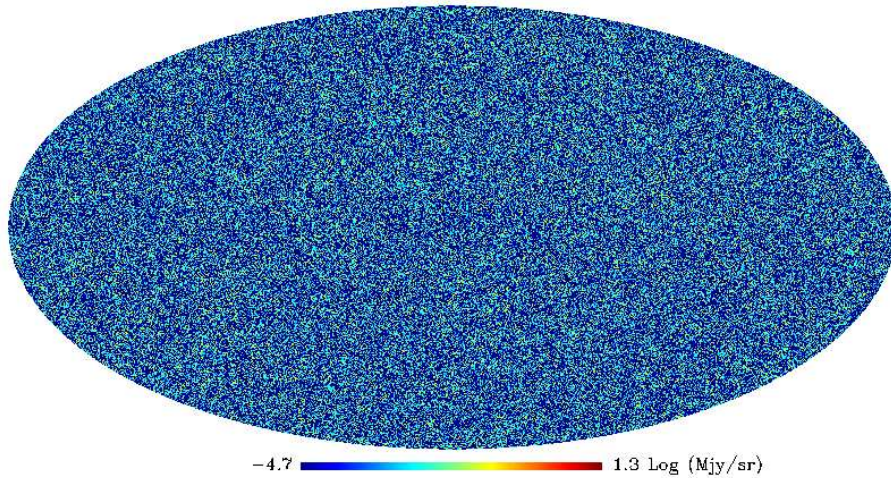
Figure 3 7 An all-sky simulation of FIR sources at 857 GHz in MJy/sr.

3 2.2   Pre–launch masks and catalogues

Compact components (and in particular radio and IR sources and galaxy cluster) should be detected and subtracted from the CMB maps. Correct subtraction requires a precise estimation of flux density (or polarised flux in case of maps of polarisation): typically, to minimize the error introduced by uncorrect subtractions, pixels in positions of sources are masked and are no longer considered in the following analysis.

As broadly debated in chapter 1 4 detection methods and blind and non-blind approaches on the map could identify complete samples, but at high flux density limits. Sources below the detection threshold still contaminate the CMB signal. This fact constitutes a limit for the investigation of the high multipoles of the CMB power spectrum. For this reason it is preferable to mask as many sources as possible. However, the number of objects, and as a consequence the number of masked pixels, increases dramatically going to lower flux limits. So that a compromise should be carefully selected.

Furthermore, as mentioned, if sources are selected at frequencies different from those at which the mask is used the masked sample may be incomplete. The lack of complete deep surveys of the whole sky in the millimetric band is a problem also for this issue. As a first approach, waiting for improvements from the AT20G whole sample at least for the Southern sky, we have developed a tool that allows the selection of a mask from a compilation of low frequency catalogues.

The CRATES catalogue (Healey et al. 2007) is a collection of observations at 8.4 GHz of flat spectrum PMN and GB6 sources and, in some regions of NVSS and SUMSS brightest objects. For this reason it covers the same area of the sky described in the previous section for the PSM compilation we have produced at 4.85 and ∼1 GHz. To the CRATES objects we have added the remaining GB6 and PMN steep-spectrum objects and

Table 3 3 Comparisons of some of the generated masks. For each mask a beam size of 5 arcmin has been used. Flux density limits are defined at 8.4 GHz.

nside	Holes mask	Gal. cut [°]	Flux sel.	Pixel fract. [%]	# Sources
128				24.7	225644
128	x	10		39.9	225644
512				3.8	225644
512	x	10		23.2	225644
1024				6.7	225644
1024	x			9.6	225644
1024	x	10		25.4	225644
2048				5.8	225644
512			at $\nu \geq 4.85$ GHz	3.7	120283
512	x		at $\nu \geq 4.85$ GHz	6.7	120283
512	x		100 mJy	3.8	25218
512	x		200 mJy	3.3	10114
512	x		300 mJy	3.2	6014
512	x		400 mJy	3.1	3167

the NVSS and SUMSS (Mauch et al. 2007 in this case) objects not associated to any of the previous catalogues (these are usually faint objects, or cover the regions non surveyed by 4.85 GHz catalogues). To avoid duplications of objects cross-correlations have been performed degrading the resolution of the catalogue to the PMN (GB6 for the Northern emisphere) one (4.2 arcmin FWHM and 3.5 arcmin respectively). This procedure produced a catalogue of 225644 sources of which 120283 have flux at 4.85 or 8.4 GHz.

The tool we have developed can also produce masks selecting sources according to their 8.4 GHz flux densities or to the spectral index among the two higher frequencies for which data are available.

An option allows to mask the full area contaminated by extended sources. A Galactic cut can also be applied and the regions not adequately covered by existing surveys can be masked. In the remaining, unmasked area the residual CMB contamination by faint point sources is estimated to be lower than the noise level. In Fig. 3.8(a) and 3.8(b) there are some examples of the masks that can be produced. In table 3 3 there is a comparison of fractions of masked pixels varying the properties of the source sample and of the mask.

Different samples should be selected for different exercises, so that, henceforth, different masks should be generated. The approach that we have followed to generate the source compilation is conservative, in order to allow any possible use of the pre-launch catalogue. Only a selection based on flux densities of ~ 1 GHz catalogue objects has been applied in order to consider only sources that are potentially affecting Planck data at the Planck frequencies.

The obtained sub-samples are, in fact, also a selection of ancillary data. By re-ordering the samples according to the Planck scanning-strategy, it will be possible to follow-up, almost simultaneously the sources as they will be observed by the satellite. That will

planckat/map2_MJy_sr_512_map.fits: UNKNOWN1
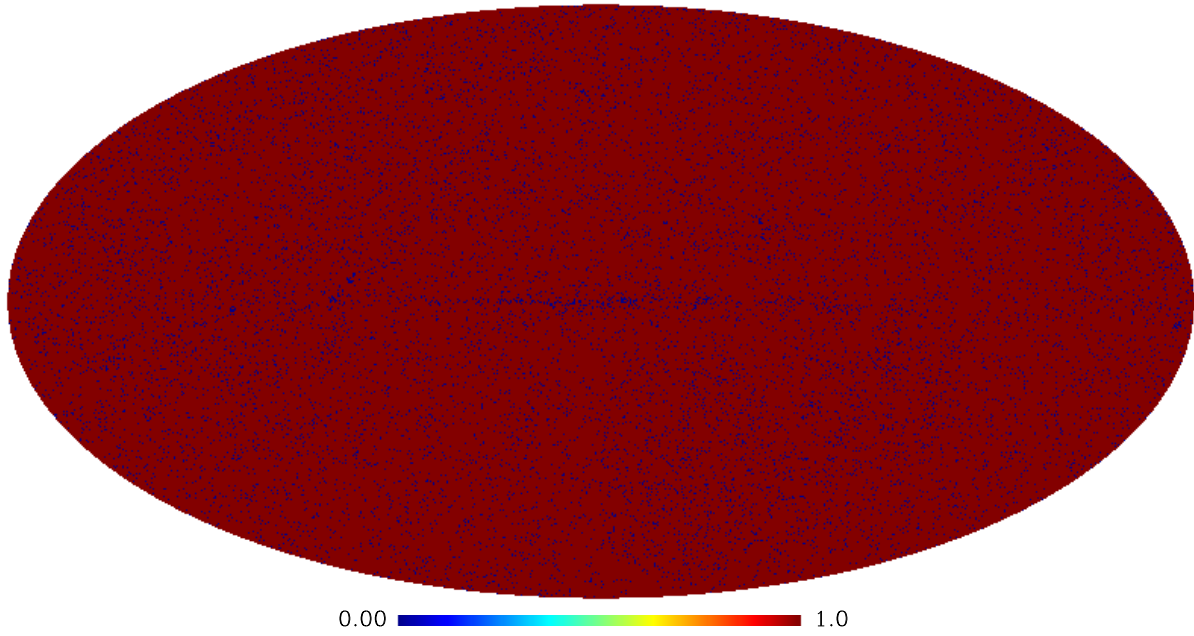
(a)

planckat/map_MJy_sr_512_map.fits: UNKNOWN1
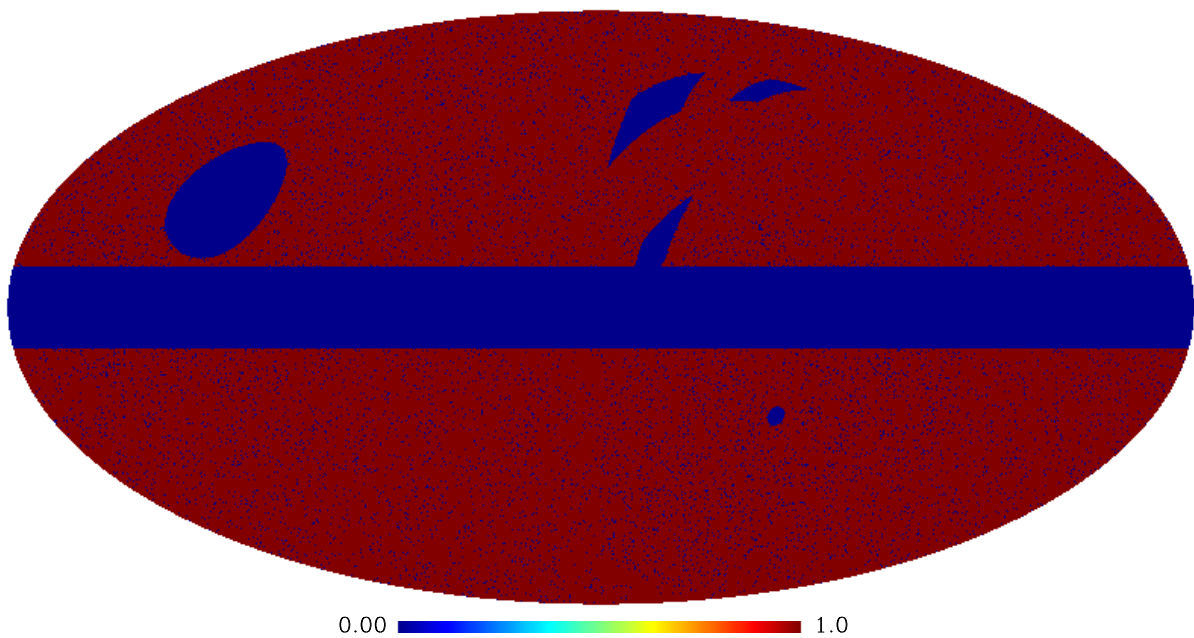
(b)

Figure 3 8 Maps of the mask produced with nside=512 in the HEALpix system (a) with all the sources, and (b) covering the holes in the PMN catalogue and with a galactic cut for $|b| < 10°$.

provide an unprecedented set of information on the spectral behaviour for a large sample that will cover the whole sky. Analogous approaches applied to several sets of objects may allow to organize several precise scientific cases and benefit from the satellite observations.

Thus, by exploiting the knowledge of foregrounds obtained with ground based telescopes it will be possible to improve the analysis on Planck (and, more in general, on any CMB-targeted mission) data, improving the outcome for cosmology, but also allowing to retrieve even more information on the same foregrounds. That feeds a 'bootstrap' process that, in the next years, may improve the knowledge of all the signals observable in the 'cosmological window' thanks to the interaction between different techniques and new data.

Summary and conclusions

A major part of the thesis work consisted in the observations, and in the reduction and analysis of the data of the Australia Telescope 20 GHz (AT20G) survey that has blindly covered the whole Southern sky to a flux limit of 50 mJy. It has been made possible by the fast scanning speed of the Australia Telescope Compact Array (ATCA) and by the 8 GHz frequency bandwidth of a prototype analogue correlator. Thanks to almost-simultaneous follow-up at 4.8, 8.6 and 20 GHz of the objects detected during the blind scan runs, we have investigated the spectral properties in total intensity and polarisation of a large sub-sample ($\gtrsim 4800$ sources) complete down to $\lesssim 80$ mJy.

The analysis for the whole sample is still on-going. We have presented the results (Massardi et al. 2008) for the 320 sources in the declination region $\delta < -15°$ with Galactic latitude $|b| > 1.5°$ and flux density $S_{20\,\mathrm{GHz}} > 0.50$ Jy that constitute the AT20G Bright Source Sample (BSS).

We found that there is a clear trend towards a steepening of spectral indices (α defined as $S_\nu \propto \nu^{-\alpha}$) at higher frequencies. The median spectral index between 1 and 5 GHz is -0.27 and increases to -0.11 between 5 and 8 GHz where the fraction of 'steep'-spectrum sources is $\simeq 8$ per cent. Between 8 and 20 GHz the median spectral index steepens to 0.16 and the fraction of 'steep'-spectrum sources almost doubles to $\simeq 15.5$ per cent. The median of the difference of the spectral indices for the BSS, ($\alpha_8^{20} - \alpha_5^8$), is 0.26 and the standard deviation of its distribution is 0.34: this implies that assuming a simple power law spectral index equal to α_5^8 to extrapolate from 8 to 20 GHz would result, on average, in a 27 per cent error in the flux density estimation.

All the follow-up measurements include polarimetry. We collected polarisation detections at 20 GHz for 213 BSS sources. The median fractional polarisation is 2.5 per cent. The median polarisation degree is found to be somewhat lower at lower frequencies: it is 2.0 per cent at 8 GHz and 1.7 per cent at 5 GHz. A similar trend was found for the sub-sample of the BSS ($\delta < -30°$) observed during a run dedicated to high sensitivity polarisation measurements with the ATCA. This observation provided more accurate short-spacing measurements of flux densities at 20 GHz, imaging and integrated flux densities. Furthermore, nine very extended sources have been selected from low frequency catalogues (PMN and SUMSS) to be observed in mosaic mode to improve the flux density and polarised flux estimation at 20 GHz.

The BSS observations showed that the fractional polarisation is independent of the flux density of the sources. Simultaneous observations in total intensity and polarisation showed that the spectral shape in polarisation is often different from the spectral shape in total intensity at any flux level.

Thus, neither the high frequency total intensity nor the polarisation behaviour can be reliably extrapolated from low frequency information. In fact, we find a broad variety of spectral shapes: most sources spectra are not power-laws so do not allow an easy extrapolation from one frequency to the other.

We have used the Bright Source Sample also as a benchmark to test the efficiency in source detection and flux density estimation of *blind* and *non-blind* detection techniques applied to the Wilkinson Microwave Anisotropy Probe (WMAP) 5-year maps (Massardi et al. submitted). The comparison with BSS data allowed us to estimate the completeness, the reliability, and the accuracy of flux density and error estimates for the samples detected with the two approaches.

We found that flux density estimates are unbiased except at the faintest flux densities ($S_{BSS} < 840\,$mJy), where the fraction of the source intensity peaks amplified by positive fluctuations due to other components (Galaxy, CMB, noise) within the WMAP beam becomes substantial and the source counts are correspondingly overestimated. This is a manifestation of the Eddington bias, enhanced by the fact that the true errors on flux density estimates turn out to be about a factor of 2 higher than the errors estimated by our procedure. The difference is due to the filtering of the maps that increases the signal-to-noise ratio by smoothing the fluctuation field. No clear-cut criterion capable of identifying sources affected by this problem using only WMAP data was found. However, the estimate of the true uncertainties obtained by comparison with the high signal-to-noise AT20G measurements, and the information on counts of sources below the WMAP detection limit provided by the AT20G (Massardi et al. 2008; Ricci et al. 2004) and 9C (Waldram et al. 2003) surveys at nearby frequencies allowed us to correct the WMAP source counts. In the K-band, the downward correction is of about 15 per cent at 2 Jy, and rapidly increases to a factor of almost 2 at 1 Jy.

At higher flux densities most (17 out of 19) of probably spurious detections are at relatively low Galactic latitudes ($|b| < 20°$), suggesting that the observed intensity peaks are largely due to small scale structure in the Galactic emission. Excluding the areas where the rms fluctuations are more than 50 per cent higher than the $|b| > 5°$ median approximately halves the number of dubious candidates, at a modest cost ($\simeq 7$–10 per cent) in terms of useful area. If all dubious sources are spurious, the reliability of the sample is 95.5 per cent.

The blind detection approach applied to the all-sky WMAP maps, excluding the Galactic plane region ($|b| < 5°$) and the areas where the rms fluctuations are more than 50 per cent higher than the median value at $|b| < 5°$, has found 488 candidate sources with SNR > 5 in at least one WMAP channel. The non-blind approach has added 28 further objects, raising the total to 516, to be compared with the 388 sources listed in the WMAP 5-yr catalogue (Wright et al. 2008) in the same sky area. If the sources that have not been previously catalogued as extragalactic or Galactic objects in lower frequency all sky surveys with comparable flux densities are all spurious, the reliability of the sample is 93.8 per cent.

This analysis illustrates the importance of the AT20G survey for the analysis of data from CMB experiments. In fact, our participation in this survey happened in the framework of the Planck Consortium activities. We have been in charge of contributing to the simulation of the radio source components for the Planck Sky Model (PSM), an all-sky simulation of the astrophysical and cosmological signals at all the Planck frequencies. Our

contribution to the PSM included also a simulation of the contamination of the SZ effect due to radio sources in clusters based on statistical estimation of the contamination (Massardi & De Zotti 2004).

A significant observational and modelling effort has been devoted also to the SZ effect that is another signal on small angular scales that, in the millimetric band, plays an important role as CMB foreground.

We have analyzed the possibility of detailed imaging of this signal in galaxy clusters from ground-based telescopes carrying out some observations of the high redshift (z= 0.823), massive ($M = 1.1 \times 10^{15} M_\odot$) galaxy cluster Cl J0152-1357 with the ATCA. The complicate structure seen in this cluster (several sub-clumps and at least two directions of on-going merging) could provide insight into the mechanisms that are active in early stages of cluster formation. We obtained a marginal detection of an unexpected offset between the SZ and X-ray peak, with a very complex data analysis involving two telescopes, mosaics and UV plane modelling. Further investigations are required to confirm our preliminary results.

We have also performed some simulations of the galaxy-scale SZ effects that should be produced in the early stages of galaxy formations when, according to current models, haloes of primordial gas virialize. We have presented a quantitative investigation of the counts of SZ and free-free signals in the framework of the Granato et al. (2004) model, that successfully accounts for the wealth of data on the cosmological evolution of spheroidal galaxies and of AGNs (Granato et al. 2004; Cirasuolo et al. 2005; Silva et al. 2005; Lapi et al. 2006).

We found that the detection of substantial numbers of galaxy-scale thermal SZ signals is achievable by blind surveys with next generation radio interferometers. Since the protogalaxy thermal energy content increases, for given halo mass, with the virialization redshift, the SZ 'fluxes' increase rather strongly with z, especially for the thermal SZ effect, partially compensating for the rapid decrease of the density of massive halos with increasing redshift. The redshift distributions of thermal SZ sources are thus expected to have substantial tails up to high z.

There are however important observational constraints that need to be taken into account. The contamination by radio and dust emissions associated to the star formation activity depends on mass and redshift of the objects, and is expected to be stronger than the SZ signal at low and high frequencies. We concluded that the optimal frequency range for detecting the SZ signal is from 10 to 35 GHz, where such signal dominates over the contamination at least for the most massive objects. It must be noted however that contaminating emissions have typical scales of the order of those of the stellar distributions, i.e. < 1 arcsec at the redshifts of interest here (see Fomalont et al. 2006), while the SZ effects show up on the scale of the dark matter halo, which is typically ten times larger. Therefore arcsec resolution images, such as those that will be provided by the SKA, will allow to reconstruct the uncontaminated SZ signal. The coexistence of the hot plasma halo, responsible for the SZ signal, with dust emission implies that this scenario may be tested by means of pointed observations of high-z luminous star-forming galaxies detected by (sub)-mm surveys. Such observations offer a unique way to investigate the earliest stages of galaxy formation, thus providing strong constraints on the models for structure formation.

Bibliography

Argüeso F., González-Nuevo J., Toffolatti L., 2003, ApJ, 598, 86

Arkin H., Colton R.R., 1970, Statistical Methods, Barnes & Noble Books, Harper & Row Pub., New York

Ashdown, M. A. J., Baccigalupi, C., Balbi, A., et al. 2007, A&A, 467, 761

Becker R. H., White R. L., Helfand D. J., 1995, ApJ, 450, 559

Bennett C. L., et al., 2003, ApJS, 148, 97

Benson A. J., Bower R. G., Frenk C. S., Lacey C. G., Baugh C. M., Cole S., 2003, ApJ, 599, 38

Binney J., 2004, MNRAS, 347, 1093

Birkinshaw M., 1999, Phys. Rep. 310:97

Birkinshaw M., Worrall D. M., Hardcastle M. J., 2002, MNRAS, 335, 142

Birkinshaw M., Lancaster K., 2005, Proc. of the International School of Physics "Enrico Fermi", "Background Microwave Radiation and Intracluster Cosmology", p. 127

Birnboim Y., Dekel A., 2003, MNRAS, 345, 349

Blain A. W., Chapman S. C., Smail I., Ivison R., 2005, proc. ESO workshop on "Multi-wavelength Mapping of Galaxy Formation and Evolution", p. 94

Bolton R. C., et al., 2004, MNRAS, 354, 485

Borgani S., Guzzo L., 2001, Natur, 409, 39

Bower R. G., Benson A. J., Malbon R., Helly J. C., Frenk C. S., Baugh C. M., Cole S., Lacey C. G., 2006, MNRAS, 370, 645

Bressan A., Silva L., Granato G. L., 2002, A&A, 392, 377

Bryan G. L., Norman M. L., 1998, ApJ, 495, 80

Bullock J. S., Kolatt T. S., Sigad Y., Somerville R. S., Kravtsov A. V., Klypin A. A., Primack J. R., Dekel A., 2001, MNRAS, 321, 559

Burbidge E. M., Gutiérrez C. M., Arp H., 2006, PASP, 118, 124

Cantor A.B., 2001, Statist. Med., 20, 2091-2097

Carilli C. L., 2001, in "Starburst Galaxies: Near and Far", L. Tacconi & D. Lutz, eds., Heidelberg: Springer-Verlag, p. 309

Carlstrom J. E., Holder G. P., Reese E. D., 2002, ARA&A, 40, 643

Cavaliere A., Fusco-Femiano R., 1976, A&A, 49, 137

Cavaliere A., Danese L., de Zotti G., 1979, A&A, 75, 322

Cavaliere A., Danese L., de Zotti G., 1977, A&A, 60, L15

Cavaliere A., Fusco-Femiano R., 1981, A&A, 100, 194

Cayón L., et al., 2000, MNRAS, 315, 757

Chen X., Wright E. L., 2007, arXiv, 712, arXiv:0712.3594

Cirasuolo M., Shankar F., Granato G. L., De Zotti G., Danese L., 2005, ApJ, 629, 816

Cleary K. A., et al., 2005, MNRAS, 360, 340

Coble K., et al., 2007, AJ, 134, 897

Colafrancesco, S., Mazzotta, P., Rephaeli, Y., Vittorio, N. 1997, ApJ, 479, 1

Cole S., 1991, ApJ, 367, 45

Cole S., Aragon-Salamanca A., Frenk C.S., Navarro J.F., Zepf S.E., 1994, MNRAS, 271, 781

Condon J. J., 1992, ARA&A, 30, 575

Condon J. J., Cotton W. D., Greisen E. W., Yin Q. F., Perley R. A., Taylor G. B., Broderick J. J., 1998, AJ, 115, 1693

Coppin K., et al., 2006, MNRAS, 372, 1621

Cooray A. R., Grego L., Holzapfel W. L., Joy M., Carlstrom J. E., 1998, AJ, 115, 1388

Croton D. J., et al., 2006, MNRAS, 365, 11

Dekel A., Birnboim Y., 2006, MNRAS, 368, 2

Dekel A., Silk J., 1986, ApJ, 303, 39

Demarco R., et al., 2005, A&A, 432, 381

De Zotti G., Franceschini A., Toffolatti L., Mazzei P., Danese L., 1996, ApL&C, 35, 289

De Zotti G., Toffolatti L., Argüeso F., Davies R. D., Mazzotta P., Partridge R. B., Smoot G. F., Vittorio N., 1999, AIPC, 476, 204

De Zotti G., Burigana C., Cavaliere A., Danese L., Granato G. L., Lapi A., Platania P., Silva L., 2004, AIPC, 703, 375

De Zotti G., Ricci R., Mesa D., Silva L., Mazzotta P., Toffolatti L., González-Nuevo J., 2005, A&A, 431, 893

De Zotti, G., Burigana, C., Negrello, M., Tinti, S., Ricci, R., Silva, L., González-Nuevo, J. & Toffolatti, L., 2006, in "The many scales in the Universe", ed. J.C. Del Toro Iniesta et al., Springer, p. 45

Dickinson, C., Davies, R. D., Davis, R. J. 2003, MNRAS, 341, 369

Dodson R., et al., 2008, ApJS, 175, 314

Duncan R. A., Sproats L. N., 1992, PASAu, 10, 16

Dunlop J. S., Peacock J. A., 1990, MNRAS, 247, 19

Dunne L., Clements D. L., Eales S. A., 2000, MNRAS, 319, 813

Eddington A. S., 1913, MNRAS, 73, 359

Ekers R. D., Goss W. M., Kotanyi C. G., Skellern D. J., 1978, A&A, 69, L21

Farrah D., et al., 2006, ApJ, 641, L17 (erratum: 2006, ApJ, 643, L139)

Feretti L., 2003, ASPC, 301, 143

Finkbeiner, D. P., Davis, M., Schlegel, D. J. 1999, ApJ, 524, 867

Fomalont E.B. et al., 1991, AJ,102, 1258-1277.

Fomalont E. B., Kellermann K. I., Partridge R. B., Windhorst R. A., Richards E. A., 2002, AJ, 123, 2402

Fomalont E. B., Kellermann K. I., Cowie L. L., Capak P., Barger A. J., Partridge R. B., Windhorst R. A., Richards E. A., 2006, ApJS, 167, 103

Fosbury R. A. E., Morganti R., Wilson W., Ekers R. D., di Serego Alighieri S., Tadhunter C. N., 1998, MNRAS, 296, 701

Gehrels N., 1986, ApJ, 303, 336

Girardi M., Demarco R., Rosati P., Borgani S., 2005, A&A, 442, 29

Granato G. L., Silva L., Monaco P., Panuzzo P., Salucci P., De Zotti G., Danese L., 2001, MNRAS, 324, 757

Granato G. L., De Zotti G., Silva L., Bressan A., Danese L., 2004, ApJ, 600, 580

Gregory P. C., Scott W. K., Douglas K., Condon J. J., 1996, ApJS, 103, 427

Griffith M. R., Wright A. E., 1993, AJ, 105, 1666

Griffith M. R., Wright A. E., Burke B. F., Ekers R. D., 1995, ApJS, 97, 347

González-Nuevo J., Toffolatti L., Argüeso F., 2005, ApJ, 621, 1

González-Nuevo J., Argüeso F., López-Caniego M., Toffolatti L., Sanz J. L., Vielva P.,
    Herranz D., 2006, MNRAS, 369, 1603

González-Nuevo J., Massardi M., Argüeso F., Herranz D., Toffolatti L., Sanz J. L., López-
    Caniego M., de Zotti G., 2008, MNRAS, 384, 711

Haarsma D. B., Partridge R. B., Windhorst R. A., Richards E. A., 2000, ApJ, 544, 641

Haehnelt M. G., Rees M. J., 1993, MNRAS, 263, 168

Hambly N. C., et al., 2001, MNRAS, 326, 1279

Haslam, C. G. T., Salter, C. J., Stoffel, H., Wilson, W. E. 1982, A&AS, 47, 1

Healey S. E., Romani R. W., Taylor G. B., Sadler E. M., Ricci R., Murphy T., Ulvestad
    J. S., Winn J. N., 2007, ApJS, 171, 61

Henkel B., Partridge R. B., 2005, ApJ, 635, 950

Hinshaw G., et al., 2007, ApJS, 170, 288

Hirabayashi H., et al., 2000, PASJ, 52, 997

Hogg D. W., 1999, astro, arXiv:astro-ph/9905116

Hogg D. W., Turner E. L., 1998, PASP, 110, 727

Hu W., 2003, AIPC, 666, 45

Hu W., Dodelson S., 2002, ARA&A, 40, 171

Huo Z.-Y., Xue S.-J., Xu H., Squires G., Rosati P., 2004, AJ, 127, 1263

Itoh N., Sakamoto T., Kusano S., Nozawa S., Kohyama Y., 2000, ApJS, 128, 125

Jackson C. A., Wall J. V., Shaver P. A., Kellermann K. I., Hook I. M., Hawkins M. R. S.,
    2002, A&A, 386, 97

Jaffe W. J., Perola G. C., 1973, A&A, 26, 423

Jee M. J., White R. L., Benítez N., Ford H. C., Blakeslee J. P., Rosati P., Demarco R.,
    Illingworth G. D., 2005, ApJ, 618, 46

Jeltema T. E., Canizares C. R., Bautz M. W., Buote D. A., 2005, ApJ, 624, 606

Jones D. H., et al., 2004, MNRAS, 355, 747

Jørgensen I., Bergmann M., Davies R., Barr J., Takamiya M., Crampton D., 2005, AJ, 129, 1249

Joy M., et al., 2001, ApJ, 551, L1

Katz N., Kereš D., Davé R., Weinberg D.H., 2003, in Rosenberg J.L., Putman M.E., eds, The IGM/Galaxy Connection: the Distribution of Baryons at z = 0. Kluwer, Dordrecht, p. 185

Katgert P., Katgert-Merkelijn J. K., Le Poole R. S., van der Laan H., 1973, A&A, 23, 171

Kauffmann G., White S. D. M., Guiderdoni B., 1993, MNRAS, 264, 201

Kellermann K., Sramek R., Shaffer D., Green R., Schmidt M., 1986, IAUS, 119, 95

Kereš D., Katz N., Weinberg D. H., Davé R., 2005, MNRAS, 363, 2

Kesteven M. J. L., Bridle A. H., Brandie G. W., 1977, AJ, 82, 541

Killeen N. E. B., Bicknell G. V., Ekers R. D., 1986, ApJ, 302, 306

Kodama T., et al., 2005, PASJ, 57, 309

Koopmans L. V. E., Treu T., Bolton A. S., Burles S., Moustakas L. A., 2006, ApJ, 649, 599

Kosowsky A., 2006, NewAR, 50, 969

Kovac J.M., Leitch E.M., Pryke C., Carlstrom J.E., Halverson N.W. & Holzapfel W.L., 2002, Nat, 420, 772

Lacey C., Silk J., 1991, ApJ, 381, 14

Laing R. A., Peacock J. A., 1980, MNRAS, 190, 903

Lamarre J. M., et al., 2003, NewAR, 47, 1017

Lapi A., Shankar F., Mao J., Granato G. L., Silva L., De Zotti G., Danese L., 2006, ApJ, 650, 42

LaRoque S. J., et al., 2003, ApJ, 583, 559

Larson R.B., 1974, MNRAS, 169, 229

Leach S.M., et al., 2008, A&A, Accepted, arXiv:0805.0269

Liang H., Subrahmanyan R., Ekers R., Pierre M., 1993, ASPC, 51, 404

Liang H., Hunstead R. W., Birkinshaw M., Andreani P., 2000, ApJ, 544, 686

Lin Y.-T., Mohr J. J., 2007, ApJS, 170, 71

Lin Y.-T., Partridge B., Pober J. C., El Bouchefry K., Burke S., Klein J., Coish J., Huffenberger K., 2008, arXiv, 805, arXiv:0805.1750

Lo K. Y., et al., 2001, AIPC, 586, 172

López-Caniego M., Herranz D., González-Nuevo J., Sanz J. L., Barreiro R. B., Vielva P., Argüeso F., Toffolatti L., 2006, MNRAS, 370, 2047

López-Caniego M., González-Nuevo J., Herranz D., Massardi M., Sanz J. L., De Zotti G., Toffolatti L., Argüeso F., 2007, ApJS, 170, 108

Ma C., Arias E. F., Eubanks T. M., Fey A. L., Gontier A.-M., Jacobs C. S., Sovers O. J., Archinal B. A., Charlot, P., 1998, AJ, 116, 516

Magliocchetti M., et al., 2002, MNRAS, 333, 100

Magliocchetti M., Silva L., Lapi A., De Zotti G., Granato G.L., Fadda D., Danese L., 2007, MNRAS, 375, 1121

Majumdar S., Subrahmanyan R., 2000, MNRAS, 312, 724

Majumdar S., Nath B. B., Chiba M., 2001, MNRAS, 324, 537 (erratum: 2001, MNRAS, 326, 1216)

Mao J., Lapi A., Granato G. L., de Zotti G., Danese L., 2007, ApJ, 667, 655

Marcillac D., Rigby J. R., Rieke G. H., Kelly D. M., 2007, ApJ, 654, 825

Mason B.S., Pearson T.J., Readhead A.C.S., et al., 2003, ApJ, 591, 540

Massardi M., De Zotti G., 2004, A&A, 424, 409

Massardi M., et al., 2008, MNRAS, 384, 775

Massardi M., Lapi A., de Zotti G., Ekers R. D., Danese L., 2008, MNRAS, 384, 701

Mather J. C., Fixsen D. J., Shafer R. A., Mosier C., Wilkinson D. T., 1999, ApJ, 512, 511

Mauch T., Murphy T., Buttery H. J., Curran J., Hunstead R. W., Piestrzynski B., Robertson J. G., Sadler E. M., 2003, MNRAS, 342, 1117

Mauch T., Murphy T., Buttery H. J., Curran J., Hunstead R. W., Piestrzynski B., Robertson J. G., Sadler E. M., 2007, yCat, 8081, 0

Maughan B. J., Ellis S. C., Jones L. R., Mason K. O., Córdova F. A., Priedhorsky W., 2006, ApJ, 640, 219

Maughan B. J., Jones L. R., Ebeling H., Perlman E., Rosati P., Frye C., Mullis C. R., 2003, ApJ, 587, 589

Middelberg E., Sault R. J., Kesteven M. J., 2006, PASA, 23, 147

Miville-Deschênes, M.-A., Lagache, G., Boulanger, F., Puget, J.-L. 2007, A&A, 469, 595

Miville-Deschênes, M.-A., Ysard, N., Lavabre, A., et al. 2008, ArXiv e-prints, 802

Morganti R., Oosterloo T. A., Reynolds J. E., Tadhunter C. N., Migenes V., 1997, MNRAS, 284, 541

Murdoch H. S., Crawford D. F., Jauncey D. L., 1973, ApJ, 183, 1

Navarro J. F., Frenk C. S., White S. D. M., 1997, ApJ, 490, 493

Negrello M., Perrotta F., González J. G.-N., Silva L., de Zotti G., Granato G. L., Baccigalupi C., Danese L., 2007, MNRAS, 323

Nie J.-Y., Zhang S.-N., 2007, ChJAA, 7, 199

O'Dea C. P., 1998, PASP, 110, 493

Oh, S. P., 1999, ApJ, 527, 16-30.

Oh S. P., Cooray A., Kamionkowski M., 2003, MNRAS, 342, L20

Orienti M., Dallacasa D., 2008, A&A, 479, 409

Pacholczyk A. G., 1970, Radio Astrophysics. W.H. Freeman, San Francisco

Perley R. A., Roser H.-J., Meisenheimer K., 1997, A&A, 328, 12

Platania P., Burigana C., De Zotti G., Lazzaro E., Bersanelli M., 2002, MNRAS, 337, 242

Reinecke, M., Dolag, K., Hell, R., Bartelmann, M., Enßlin, T. A. 2006, A&A, 445, 373

Rees M. J., Ostriker J. P., 1977, MNRAS, 179, 541

Renzini A., 2006, ARA&A, 44, 141

Rybicki G. B., Lightman A. P., 1979, "Radiative processes in astrophysics", New York Wiley

Rosa-González D., Terlevich R., Terlevich E., Friaça A., Gaztañaga E., 2004, MNRAS, 348, 669

Rosati P., Borgani S., Norman C., 2002, ARA&A, 40, 539

Rosati P., 2004, cgpc.symp, 72

Ricci R., et al., 2004, MNRAS, 354, 305

Ricci R., Prandoni I., Gruppioni C., Sault R. J., de Zotti G., 2006, A&A, 445, 465

Ruhl J., et al., 2004, SPIE, 5498, 11

Sadler E. M., et al., 2006, MNRAS, 371, 898

Sadler E. M., Ricci R., Ekers R. D., Sault R. J., Jackson C. A., de Zotti G., 2008, MNRAS, 385, 1656

Salpeter E. E., 1955, ApJ, 121, 161

Sarazin C. L., *"X ray emission from cluster of galaxies"*, 1988, Press Syndicate of the University of Cambridge

Sasaki S., 1994, PASJ, 46, 427

Sault R. J., Teuben P. J., Wright M. C. H., 1995, ASPC, 77, 433

Saunders W., et al., 2000, ASPC, 201, 223

Schlegel, D. J., Finkbeiner, D. P., Davis, M. 1998, ApJ, 500, 525

Schwartz D. A., et al., 2000, ApJ, 540, L69

Scott W. K., et al., 2004, ApJS, 155, 33

Serjeant S., Harrison D., 2005, MNRAS, 356, 192-204

Shen Z.-Q., et al., 1998, AJ, 115, 1357

Sheth R. K., Tormen G., 1999, MNRAS, 308, 119

Sheth R. K., Diaferio A., 2001, MNRAS, 322, 901

Silk, J., White, S.D.M., 1978, ApJ, 226, L103

Silva L., De Zotti G., Granato G. L., Maiolino R., Danese L., 2004, astro, arXiv:astro-ph/0403166

Silva L., De Zotti G., Granato G. L., Maiolino R., Danese L., 2005, MNRAS, 357, 1295

Somerville R.S., Primack J.R., 1999, MNRAS, 310, 1087

Spergel D. N., et al., 2006, astro, arXiv:astro-ph/0603449

Stanghellini C., O'Dea C. P., Baum S. A., Dallacasa D., Fanti R., Fanti C., 1996, IAUS, 175, 67

Stanghellini C., Dallacasa D., O'Dea C. P., Baum S. A., Fanti R., Fanti C., 2001, A&A, 379, 870

Subrahmanyan R., Kesteven M. J., Ekers R. D., Sinclair M., Silk J., 2000, MNRAS, 315, 808

Subrahmanyan R., Hunstead R. W., Cox N. L. J., McIntyre V., 2006, ApJ, 636, 172

Sunyaev R. A., Zel'dovich Y. B., 1972, CoASP, 4, 173

Sunyaev, R. A. & Zeldovich, I. B. 1980, ARA&A, 18, 537

Sunyaev, R. A. & Zeldovich, I. B. 1981, ASPRv, 1, 1

Tadhunter C., Wills K., Morganti R., Oosterloo T., Dickson R., 2001, MNRAS, 327, 227

Taylor A. C., Grainge K., Jones M. E., Pooley G. G., Saunders R. D. E., Waldram E. M., 2001, MNRAS, 327, L1

Thomas D., Maraston C., Bender R., 2002, RvMA, 15, 219

Thompson A. R., Moran J. M., Swenson G. W., 2001, Interferometry and Synthesis in Radio Astronomy. Wiley, New York

Tingay S. J., Jauncey D. L., King E. A., Tzioumis A. K., Lovell J. E. J., Edwards P. G., 2003, PASJ, 55, 351

Tinti S., Dallacasa D., De Zotti G., Celotti A., Stanghellini C., 2005, A&A, 432, 31

Tinti S., De Zotti G., 2006, A&A, 445, 889

Toffolatti L., De Zotti G., Argüeso F., Burigana C., 1999, ASPC, 181, 153

Toffolatti L. et al., 1998, MNRAS, 297, 117-127.

Urry C. M., Padovani P., 1995, PASP, 107, 803

Valenziano L., et al., 2007, NewAR, 51, 287

Vielva P., Martínez-González E., Cayón L., Diego J. M., Sanz J. L., Toffolatti L., 2001a, MNRAS, 326, 181

Vielva P., Martínez-González E., Gallegos J. E., Toffolatti L., Sanz J. L., 2003, MNRAS, 344, 89

Waldram E. M., Pooley G. G., Grainge K. J. B., Jones M. E., Saunders R. D. E., Scott P. F., Taylor A. C., 2003, MNRAS, 342, 915

Waldram E.M., Bolton R.C., Pooley G.G. & Riley J.M., 2007, MNRAS, in press (astro-ph/0706.1182)

Wechsler R.H., Bullock J.S., Primack J.R., Kravtsov A.V., Dekel A., 2002, ApJ, 568, 52

White S. D. M., Frenk C. S., 1991, ApJ, 379, 52

White S. D. M., Rees M. J., 1978, MNRAS, 183, 341

Wright A. E., Griffith M. R., Burke B. F., Ekers R. D., 1994, ApJS, 91, 111

Wright A. E., Griffith M. R., Hunt A. J., Troup E., Burke B. F., Ekers R. D., 1996, ApJS, 103, 145

Wright E. L., et al., 2008, arXiv, 803, arXiv:0803.0577

Zemcov M., Borys C., Halpern M., Mauskopf P., Scott D., 2007, MNRAS, 376, 1073

Zhao D.H., Jing Y.P., Mo H.J., Börner G., 2003b, ApJ, 597, L9

Zhao D.H., Mo H.J., Jing Y.P., Börner G., 2003a, MNRAS, 339, 12

Appendix

1 The AT20G Bright Source Sample: source tables

Tables 1 and 2 catalogue the 320 sources in the AT20G Bright Source Sample (1 3). Table 1 lists positions, flux densities, identifications with other optical or radio catalogues, and redshifts. Table 2 lists the information about polarisation (polarised flux densities, fractions and angle of polarisation). For the full sample the source names reflect the source J2000 equatorial coordinates as 'AT20G JHHMMSS-DDMMSS'. For sake of simplicity in this thesis we have referred to the sources according to their sequential number as listed in the first column of Table 1.

The content of the columns are as follows for Table 1.

- (1) Sequential number. An asterisk ('*') following the number indicates that the source is listed in the Appendix 1.1 or has been commented on in the text.

- (2–3) Right ascension and declination (J2000). The average error in right ascension and declination is 0.5 arcsec (see § 1 3.2.5).

- (4–5) Flux density at 20 GHz and its error in Jy.

- (6–7) Flux density at 8 GHz and its error in Jy.

- (8–9) Flux density at 5 GHz and its error in Jy. Whenever available we give the results of 5 and 8 GHz observations almost simultaneous to the 20 GHz ones, otherwise we refer to the best observations available for the source at each frequency.

- (10–11) Flux density at 1.4 GHz and its error from NVSS (Condon et al. 1998).

- (12–13) Flux density at 0.843 GHz and its error from SUMSS (version 2.0).

- (14–15) Redshift and its reference, obtained as discussed in § 1 3.3.6.

- (16) Optical B magnitude for sources with SuperCOSMOS[3] counterparts.

- (17) SuperCOSMOS identifications: 'G' for galaxies, 'Q' for QSOs. A blank space indicates that no identification was possible (see § 1 3.3.6).

- (18) Flags column where we collected some flags for source properties in the following order:

---

[3]http://www-wfau.roe.ac.uk/sss/

- – the epoch of the 20 GHz observations: numbers refer to the epoch reference number in Table 1 1;
- – spectral shape: 'F' for flat, 'I' for inverted,'P' for peaked, 'S' for steep,'U' for upturning, as in Table 1 2;
- – galactic position: a 'G' indicates that the source is within $10°$ from the galactic plane;
- – epoch of observation at 8 and 5 GHz respectively, in case of not simultaneous observations (numbers refer to the epoch reference number in Table 1 1): in such cases we have listed the flux densities measured in the best observation available.
- – extendedness: 'E' if the source is extended at 20 GHz, 'M' if it has been observed in the mosaic mode. The flux density for the 'M' sources corresponds to the integrated flux density of the source in the mosaic area;
- – a flag 'C' means that the source is listed in the AT calibrator manual

- (19) Alternative name from other well known catalogues (PMN, PKS) at radio frequency.

- (20) Identification number in the WMAP_1yr catalogue (Bennett et al. 2003).

    In Table 2 we collected the following columns

- (1) Sequential number as in Table 1.

- (2–3) Right ascension and declination (J2000).

- (4–5) Integrated polarised flux in Jy and its error at 20 GHz.

- (6) Fractional polarisation at 20 GHz (per cent).

- (7) Polarisation angle at 20 GHz in degrees.

- (8–9) Integrated polarised flux in Jy and its error at 8 GHz.

- (10) Fractional polarisation at 8 GHz (per cent).

- (11) Polarisation angle at 8 GHz in degrees.

- (12–13) Integrated polarised flux in Jy and its error at 5 GHz.

- (14) Fractional polarisation at 5 GHz (per cent).

- (15) Polarisation angle at 5 GHz in degrees.

Table 1: The AT20G Bright Source Sample.

Seq. #	RA	δ	S_{20GHz} [Jy]	$S_{8.6GHz}$ [Jy]	$S_{4.8GHz}$ [Jy]	$S_{1.4GHz}$NVSS [Jy]	$S_{0.843GHz}$SUMSS [Jy]	z	z Ref.	B_{Jmag}	Opt. ID	Flags	Alternative name	WMAP ID
1	00:04:35.65	-47:36:19.1	0.87 0.04	0.97 0.06	0.90 0.04	...	0.995 0.030	...	...	17.63	Q	1F....C	PKS 0002-478	...
2	00:10:35.92	-30:27:48.3	0.74 0.04	0.72 0.04	0.63 0.03	0.315 0.009	0.419 0.013	1.19	La01	19.59	Q	1F.....C	PKS 0008-307	...
3	00:11:01.27	-26:12:33.1	0.64 0.07	0.82 0.07	0.69 0.03	0.210 0.006	...	1.096	Wr83	19.53	Q	4F.....C	PKS 0008-264	...
4	00:12:59.89	-39:54:26.4	1.61 0.08	2.01 0.12	2.01 0.10	0.494 0.017	...	...	...	18.33	Q	1F....C	PKS 0010-401	202
5	00:25:49.18	-26:02:12.7	0.98 0.10	2.73 0.22	4.15 0.21	8.753 0.263	...	0.322	Ta93	20.30	G	4S....C	PKS 0023-26	...
6	00:26:16.40	-35:12:49.4	1.12 0.06	0.36 0.02	0.14 0.01	0.025 0.001	0.014 0.002	...	...	22.24	G	1L....C	PMN J0026-3512	...
7	00:38:14.72	-24:59:01.9	1.13 0.11	0.95 0.08	0.58 0.03	0.412 0.012	...	1.196	Ja84	18.90	Q	4I	PKS 0035-252	...
8	00:49:59.48	-57:38:27.6	1.87 0.09	2.14 0.11	2.00 0.10	...	2.112 0.063	1.797	Pe76	17.49	Q	2F....C	PKS 0047-579	179
9	00:51:09.50	-42:26:32.5	1.46 0.07	...	...	...	0.676	1.749	Wh88	19.13	Q	1....C	PKS 0048-427	...
10*	00:58:46.64	-56:59:11.4	0.84 0.04	0.58 0.03	0.50 0.02	...	0.485 0.015	...	...	17.91	Q	2I....C	PKS 0056-572	...
11	01:02:15.07	-80:12:40.1	0.77 0.16	0.64 0.03	0.44 0.02	...	0.113 0.004	...	...	19.73	Q	2I	PKS 0101-804	...
12	01:02:18.65	-75:46:53.0	0.71 0.15	0.55 0.03	0.53 0.03	...	0.184 0.006	1.017	Wi83	18.44	Q	2I	PKS 0101-76	171
13	01:06:45.11	-40:34:19.5	2.15 0.11	...	...	...	0.662 0.020	0.584	Wh88	18.60	Q	1....C	PKS 0104-408	...
14	01:17:48.81	-21:11:07.4	0.75 0.05	0.76 0.04	0.87 0.04	0.254 0.008	...	...	...	21.85	Q	4F....C	PKS 0115-214	...
15	01:18:57.30	-21:41:30.1	0.88 0.06	0.91 0.05	0.88 0.04	0.447 0.013	...	1.165	Wi83	19.40	Q	4F....C	PKS 0116-219	...
16	01:20:31.71	-27:01:24.6	0.62 0.04	0.82 0.04	1.04 0.05	0.934 0.028	...	...	St93	15.89	Q	4S....C	PKS 0118-272	...
17	01:24:57.37	-51:13:16.1	0.75 0.04	0.37 0.02	0.23 0.01	...	0.250 0.008	...	...	19.77	Q	2I	PKS 0122-514	...
18	01:32:43.53	-16:54:48.2	1.43 0.09	1.45 0.08	1.59 0.08	0.830 0.025	...	1.02	Wr83	18.75	Q	4F....C	PKS 0130-17	97
19*	01:33:05.77	-52:00:03.5	1.20 0.07	1.51 0.08	1.46 0.07	...	0.366 0.011	...	...	18.68	Q	2F....C	PKS 0131-522	...
20*	01:33:57.6	-36:29:34.9	>1.86 ...	...	...	...	...	0.029	RC3	13.73	G	6...MC	PKS 0131-36	...
21	01:34:32.14	-38:43:33.7	0.68 0.03	0.51 0.03	0.44 0.03	0.569 0.017	0.665 0.020	2.14	Io96	17.76	Q	1L....C	PMN J0134-3843	...
22	01:37:38.33	-24:30:53.6	1.21 0.08	1.41 0.07	1.56 0.08	1.181 0.041	...	0.837	Wr83	17.47	Q	4F....C	PKS 0135-247	...
23	01:43:10.13	-32:00:55.7	0.52 0.03	0.34 0.02	0.29 0.02	0.076 0.002	0.123 0.004	0.375	2Qz	19.89	Q	1I	PKS 0140-322	...
24	01:45:03.39	-27:33:33.9	0.57 0.04	0.79 0.04	1.00 0.05	0.923 0.028	...	1.155	Wr83	...	.	4S....C	PKS 0142-278	...
25	01:53:10.19	-33:10:26.7	0.54 0.03	0.59 0.03	0.81 0.04	1.186 0.036	1.312 0.039	0.612	Wr77	17.75	Q	1S....C	PKS 0150-334	...
26	02:04:57.76	-17:01:20.1	1.78 0.12	2.01 0.44	1.25 0.09	1.219 0.037	...	1.74	Wr83	18.18	Q	4P....C	PKS 0202-17	...
27	02:10:46.19	-51:01:01.4	3.29 0.21	2.98 0.15	3.04 0.15	...	3.493 0.105	0.999	Wi00	17.10	Q	2F....C	PKS 0208-512	158
28	02:16:48.19	-32:47:40.6	0.54 0.03	0.50 0.03	0.33 0.02	0.165 0.005	0.161 0.005	1.331	Ja02	18.88	Q	1I	PKS 0214-330	...
29	02:22:56.40	-34:41:27.7	1.02 0.05	1.23 0.06	1.23 0.06	0.683 0.021	0.713 0.022	1.49	Dr97	21.39	Q	1F....C	PKS 0220-349	137
30*	02:29:34.51	-78:47:44.0	0.84 0.18	0.80 0.04	0.73 0.04	...	0.353 0.011	...	...	19.25	Q	2F....C	PKS 0230-790	...
31	02:31:11.77	-47:46:12.0	0.77 0.04	...	...	...	0.043 0.002	...	...	17.87	Q	1	PMN J0231-4746	...
32	02:36:31.11	-29:53:55.1	0.61 0.04	0.88 0.19	0.54 0.04	0.313 0.009	0.604 0.018	2.103	2Qz	18.63	Q	4P	PKS 0234-301	...
33*	02:36:53.27	-61:36:15.2	0.51 0.03	...	...	...	...	0.466	6dF	18.18	Q	1....C	PKS 0235-618	...
34	02:40:08.13	-23:09:15.8	0.90 0.06	2.12 0.46	3.01 0.22	6.256 0.188	...	2.223	Ar67	16.57	Q	4S....C	PKS 0237-23	...
35	02:45:54.07	-44:59:39.5	0.58 0.03	0.59 0.03	0.69 0.03	...	1.967 0.059	0.280	Ma95	17.65	G	1F	PKS 0244-452	...
36	02:53:29.20	-54:41:51.4	1.93 0.12	1.65 0.08	1.43 0.07	...	0.964 0.029	0.539	Wi00	17.65	Q	2F....C	PKS 0252-549	155
37	03:03:50.64	-62:11:25.2	1.28 0.06	2.15 0.11	2.37 0.12	...	2.513 0.075	...	...	19.48	Q	1.44C	PKS 0302-623	162
38	03:09:56.12	-60:58:39.0	1.06 0.05	1.18 0.06	1.23 0.06	...	0.993 0.030	...	...	19.00	Q	1.44C	PKS 0308-611	160
39	03:11:55.33	-76:51:51.2	1.24 0.08	1.29 0.06	0.92 0.05	...	0.806 0.024	0.223	Ja78	16.09	Q	4P	PKS 0312-77	174
40	03:27:59.97	-22:02:06.3	0.53 0.03	0.68 0.03	0.67 0.03	0.641 0.019	...	2.22	Wi83	18.99	Q	4P	PKS 0325-222	...
41	03:29:54.10	-23:57:08.7	1.46 0.10	1.64 0.08	1.45 0.07	0.683 0.024	...	0.895	Ba95	19.68	Q	4F....C	PKS 0327-241	...
42*	03:34:13.62	-40:08:25.3	1.27 0.06	...	0.50 0.02	0.501 0.015	1.042 0.031	1.541	FCSS	17.51	Q	1....C	PKS 0332-403	123
43	03:36:54.12	-36:16:06.0	0.74 0.04	0.61 0.03	0.50 0.02	...	0.591 0.018	0.223	Sb05	18.40	Q	1I	PKS 0335-364	146
44	03:40:35.65	-21:19:30.8	1.04 0.07	1.29 0.06	1.25 0.06	1.075 0.038	...	...	...	16.04	Q	4F....C	PKS 0338-214	...

Table 1 – Continued

Seq. #	RA	δ	S_20GHz [Jy]	S_8.6GHz [Jy]	S_4.8GHz [Jy]	S_1.4GHz NVSS [Jy]	S_0.843GHz SUMSS [Jy]	z	z Ref.	$B_{J\,mag}$	Opt. ID	Flags	Alternative name	WMAP ID
45	03:48:38.11	-27:49:13.4	1.32 0.09	1.67 0.08	1.45 0.07	0.840 0.025	...	0.991	Wh88	20.08	Q	4F....C	PKS 0346-27	129
46	03:48:39.28	-16:10:17.2	0.94 0.06	0.96 0.05	0.87 0.04	0.437 0.013	...	...	...	18.32	G	4F.....	PKS 0346-163	.
47	03:49:57.82	-21:02:47.2	0.86 0.06	1.00 0.05	0.79 0.04	0.305 0.009	...	2.944	El01	20.48	Q	4P.....	PKS 0347-211	.
48	03:52:11.00	-25:14:50.2	0.52 0.03	0.50 0.02	0.42 0.02	0.269 0.008	...	...	...	19.58	Q	4F.....	PMN J0352-2514	.
49	04:03:53.77	-36:05:00.9	4.01 0.20	3.46 0.17	2.27 0.11	1.151 0.034	1.186 0.036	1.417	Pe76	17.04	Q	1I....C	PKS 0402-362	136
50	04:06:58.98	-38:26:27.5	1.17 0.06	1.53 0.08	1.43 0.07	0.861 0.030	0.697 0.021	1.285	St94	19.55	Q	1P....C	PKS 0405-385	141
51	04:07:33.92	-33:03:45.3	0.56 0.03	0.66 0.03	0.63 0.03	0.635 0.019	...	2.562	Dr97	19.33	Q	1F....C	PKS 0405-331	.
52*	04:08:48.75	-75:07:20.1	0.86 0.14	2.64 0.42	4.74 0.75	...	20.989 0.630	0.693	Ta93	21.40	G	4S..E.	PKS 0410-75	.
53	04:16:36.61	-18:51:08.9	0.58 0.05	0.85 0.11	0.56 0.04	1.248 0.044	...	1.536	Hu78	18.89	Q	4P....C	PKS 0414-189	.
54	04:24:42.27	-37:56:21.0	1.69 0.08	1.71 0.09	1.57 0.08	0.476 0.014	0.452 0.014	0.782	Wr77	17.96	Q	1F....C	PKS 0422-380	140
55	04:28:40.37	-37:56:19.3	1.85 0.09	1.72 0.09	1.66 0.08	0.753 0.027	1.184 0.036	1.110	He04	18.96	Q	1F....C	PKS 0426-380	.
56	04:37:01.51	-18:44:48.7	0.52 0.05	1.20 0.16	1.10 0.08	0.714 0.021	...	2.702	Wr83	19.11	Q	4P....C	PKS 0434-188	.
57*	04:37:36.56	-29:54:03.9	0.57 0.03	0.68 0.03	0.69 0.03	1.091 0.038	1.799 0.054	1.328	Wi83	...		1F....C	PKS 0435-300	.
58	04:39:00.83	-45:22:22.6	0.70 0.03	0.89 0.04	0.93 0.05	...	0.978 0.029	...	...	20.44	Q	1F....C	PKS 0437-454	.
59	04:40:17.17	-43:33:08.4	1.95 0.10	2.96 0.15	3.68 0.18	...	6.361 0.191	2.863	Mo78	19.31	Q	1S....C	PKS 0438-43	147
60	04:40:47.80	-69:52:16.6	0.51 0.08	0.29 0.01	0.23 0.01	...	0.129 0.004	...	...	19.33	Q	3L....	PMN J0440-6952	.
61*	04:50:05.45	-81:01:02.2	1.27 0.08	...	...	...	...	0.444	St94	19.31	Q	4.....C	PKS 0454-81	175
62	04:53:14.64	-28:07:37.4	1.79 0.16	3.24 0.42	2.86 0.20	2.541 0.076	...	2.559	Wi83	18.23	Q	4P....C	PKS 0451-28	131
63	04:55:50.79	-46:15:58.6	4.16 0.21	3.61 0.18	2.61 0.13	...	2.753 0.083	0.853	Su04	17.89	Q	1L....C	PKS 0454-46	151
64	04:57:03.23	-23:24:51.8	3.84 0.34	5.74 0.75	4.10 0.29	1.727 0.052	...	1.003	St89	18.85	Q	4P....C	PKS 0454-234	128
65	05:06:43.96	-61:09:41.0	1.74 0.09	1.50 0.08	1.52 0.08	...	3.102 0.093	1.093	Wr77	17.16	Q	1..42..	PKS 0506-61	154
66	05:13:49.10	-21:59:17.4	0.94 0.06	1.26 0.06	1.13 0.16	0.647 0.019	...	1.296	St89	19.95	G	4P....C	PKS 0511-220	127
67	05:15:45.23	-45:56:43.2	1.54 0.08	1.50 0.07	1.35 0.07	...	1.471 0.044	0.194	St93	18.18	G	1F.....	PKS 0514-459	.
68*	05:16:44.98	-62:07:05.1	0.83 0.05	0.70 0.03	0.65 0.03	...	0.418 0.013	...	...	21.20	Q	3.44..	PKS 0516-621	.
69*	05:19:49.7	-45:46:44.2	8.52 0.11	...	...	...	...	0.035	RC3	15.94	G	6..M.	Pictor A	150
70	05:22:34.40	-61:07:57.0	0.57 0.03	0.61 0.03	0.63 0.03	...	0.741 0.022	1.400	Wr79	18.46	Q	2F....C	PKS 0522-611	.
71*	05:22:57.94	-36:27:30.4	3.91 0.59	6.57 1.04	9.07 1.43	11.883 0.356	...	0.055	Ke85	16.09	G	1S..EC	PKS 0521-36	139
72	05:25:06.48	-23:38:11.1	0.79 0.05	0.89 0.04	0.81 0.11	0.398 0.012	...	...	...	18.36	Q	4F.....	PMN J0525-2338	.
73*	05:29:30.02	-72:45:28.2	0.55 0.04	0.58 0.03	0.59 0.03	...	0.268 0.008	0.684	Ca00	19.61	G	4.22.C	PKS 0530-727	.
74	05:36:28.45	-34:01:10.8	0.84 0.04	0.68 0.03	0.66 0.03	0.652 0.020	...	0.894	Pe76	18.00	Q	1F....C	PKS 0534-340	148
75	05:38:50.35	-44:05:08.6	5.30 0.27	4.23 0.21	3.80 0.19	...	...	3.104	Os94	15.77	Q	1F....C	PKS 0537-441	.
76	05:39:54.17	-28:39:56.3	0.68 0.04	1.14 0.06	1.28 0.18	0.862 0.026	...	1.19	SSO	19.70	G	4S....C	PKS 0537-286	.
77*	05:40:45.78	-54:18:21.7	1.13 0.06	0.99 0.05	0.71 0.04	...	0.387 0.012	0.687	Ja02	18.49	G	2I.....	PKS 0539-543	152
78*	05:50:09.55	-57:32:24.5	1.01 0.05	1.03 0.05	0.93 0.05	...	0.368 0.011	1.661	Pe98	20.26	Q	2F.....	PKS 0549-575	153
79	05:59:11.53	-45:29:40.4	0.61 0.03	0.42 0.02	0.32 0.02	0.461 0.014	...	0.687	Ja02	18.34	Q	1I.....	PKS 0557-454	.
80	06:00:31.31	-39:37:01.7	0.59 0.03	...	...	...	...	1.661	Ja02	18.85	Q	1.....	PKS 0558-396	.
81	06:04:25.13	-42:25:30.1	0.57 0.03	...	...	...	...	0.611	Ja02	20.53	Q	1....C	PKS 0602-424	.
82	06:08:59.76	-22:20:21.3	1.00 0.07	1.21 0.06	0.99 0.05	0.678 0.024	...	1.926	Wr79	21.14	Q	4P....C	PKS 0606-223	.
83	06:09:41.03	-15:42:41.6	3.98 0.26	4.91 0.24	3.76 0.19	2.742 0.082	...	0.324	Hu78	18.47	Q	4P....C	PKS 0607-15	126
84	06:20:29.31	-28:27:36.2	0.50 0.03	0.66 0.03	0.60 0.03	0.387 0.012	...	...	...	22.24	Q	4P....C	PKS 0618-252	.
85*	06:20:32.10	-25:15:17.9	0.84 0.06	1.12 0.06	1.16 0.06	1.213 0.036	...	...	...	18.32	G	4S.....	PMN J0620-2827	.
86	06:23:07.75	-64:36:20.7	1.16 0.06	0.84 0.04	0.68 0.03	...	0.326 0.013	0.128	P198	17.06	G	1.24.	PMN J0623-6436	.
87	06:27:06.73	-35:29:16.1	0.69 0.03	0.96 0.05	1.30 0.07	2.372 0.091	...	0.054	Qu95	14.93	G	1S.....	PKS 0625-35	.
88	06:29:23.76	-19:59:19.4	1.26 0.08	1.33 0.07	0.98 0.05	0.677 0.020	...	...	Sb06	20.43	G	4P....C	PKS 0627-199	.
89	06:31:11.99	-41:54:27.1	0.52 0.03	...	...	...	0.662 0.020	1.416	Ja84	18.78	Q	1....C	PKS 0629-418	130

Table 1 – Continued

Seq. #	RA	δ	S_{20GHz} [Jy]	$S_{8.6GHz}$ [Jy]	$S_{4.8GHz}$ [Jy]	$S_{1.4GHz}$ NVSS [Jy]	$S_{0.843GHz}$ SUMSS [Jy]	z	z Ref.	$B_{J\,mag}$	Opt. ID	Flags	Alternative name	WMAP ID
90	06:33:26.76	-22:23:22.6	$0.67_{0.04}$	$0.77_{0.04}$	$0.72_{0.04}$	$0.358_{0.011}$	⋯	⋯	⋯	19.56	Q	4F....	PMN J0633-2223	135
91	06:34:58.99	-23:35:12.6	$1.04_{0.07}$	$1.26_{0.06}$	$1.03_{0.05}$	$0.566_{0.017}$	⋯	⋯	⋯	22.06	Q	4P....	PMN J0634-2335	
92*	06:35:46.33	-75:16:16.9	$3.24_{0.51}$	$4.82_{0.76}$	$5.54_{0.87}$	⋯	$5.283_{0.159}$	0.653	Hu78	15.96	Q	4S...EC	PKS 0637-75	167
93	06:48:14.18	-30:44:19.3	$0.74_{0.04}$	$0.71_{0.04}$	$0.77_{0.04}$	$0.898_{0.027}$	⋯	1.153	Ho03	19.53	Q	1F...C	PKS 0646-306	
94	06:48:28.53	-17:44:05.9	$1.11_{0.07}$	$0.79_{0.04}$	$0.63_{0.16}$	$1.046_{0.031}$	⋯	⋯	⋯	20.18	Q	4IG...	PMN J0648-1744	
95	06:50:24.60	-16:37:40.0	$2.50_{0.16}$	$3.57_{0.18}$	$3.14_{0.16}$	$1.778_{0.053}$	⋯	⋯	⋯	22.09	Q	4PG...C	PKS 0648-16	
96	07:01:34.55	-46:34:36.9	$1.07_{0.10}$	$1.84_{0.57}$	$1.54_{0.36}$	⋯	$0.499_{0.015}$	0.822	Ja02	18.82	Q	1.....	PKS 0700-465	
97	07:31:06.67	-23:41:47.8	$1.39_{0.11}$	⋯	⋯	$1.047_{0.031}$	⋯	⋯	⋯	21.60	Q	4PG...C	PMN J0731-2341	
98*	07:41:45.20	-47:09:26.7	$0.58_{0.05}$	$0.58_{0.05}$	$0.61_{0.04}$	⋯	$0.396_{0.012}$	0.77	SSO	19.57	Q	1F....	PMN J0741-4709	
99	07:43:20.60	-56:19:34.2	$0.61_{0.04}$	$0.64_{0.03}$	$0.64_{0.03}$	⋯	$0.662_{0.020}$	⋯	⋯	19.38	Q	2F....C	PMN J0743-5619	
100*	07:43:31.60	-67:26:25.8	$1.22_{0.19}$	$1.87_{0.30}$	$2.34_{0.37}$	⋯	$5.638_{0.169}$	1.510	Al94	16.71	Q	1..24E.	PKS 0743-67	161
101	07:47:19.72	-33:10:46.6	$0.95_{0.09}$	⋯	⋯	$0.726_{0.022}$	⋯	⋯	⋯	⋯	·	1.G....	PKS 0745-330	
102	07:48:03.09	-16:39:50.3	$0.77_{0.06}$	$1.32_{0.41}$	$1.29_{0.30}$	$0.802_{0.024}$	⋯	⋯	⋯	18.92	Q	4PG...C	PMN J0748-1639	
103	07:56:50.65	-15:42:04.7	$0.73_{0.06}$	$1.08_{0.33}$	$1.16_{0.27}$	$0.834_{0.025}$	⋯	⋯	⋯	20.34	Q	4SG...	PMN J0756-1541	
104	08:04:51.44	-27:49:11.7	$0.90_{0.06}$	$1.01_{0.05}$	$0.71_{0.04}$	$0.847_{0.030}$	⋯	⋯	⋯	21.57	G	4PG...C	PKS 0802-276	
105	08:11:08.85	-49:29:43.6	$0.61_{0.03}$	$0.73_{0.04}$	$0.68_{0.03}$	⋯	$1.005_{0.030}$	⋯	⋯	20.79	Q	1FG...	PKS 0809-492	
106	08:16:40.41	-24:21:05.8	$0.59_{0.04}$	$0.54_{0.03}$	$0.40_{0.02}$	$0.191_{0.006}$	⋯	⋯	⋯	20.94	Q	4IG...	PMN J0816-2421	145
107	08:25:26.88	-50:10:39.0	$0.57_{0.04}$	$1.68_{0.08}$	$3.22_{0.16}$	⋯	$3.735_{0.112}$	⋯	⋯	⋯	G	2SG..C	PKS 0823-500	
108	08:26:01.60	-22:30:27.1	$0.91_{0.07}$	$1.03_{0.05}$	$0.95_{0.05}$	$0.519_{0.016}$	⋯	⋯	⋯	16.11	Q	4FG..C	PKS 0823-223	
109*	08:35:29.08	-59:53:11.5	$0.55_{0.04}$	$0.28_{0.01}$	$0.16_{0.01}$	⋯	$0.025_{0.001}$	⋯	⋯	⋯	·	2I....	PMN J0835-5953	
110	08:36:39.21	-20:16:58.9	$2.68_{0.19}$	$3.79_{0.19}$	$3.92_{0.20}$	$1.971_{0.059}$	⋯	2.752	Fr83	19.45	Q	4S....C	PKS 0834-20	144
111	08:37:00.39	-34:09:12.9	$0.76_{0.04}$	$0.61_{0.03}$	$0.57_{0.03}$	$0.259_{0.008}$	⋯	⋯	⋯	⋯	·	1FG...	PKS 0835-339	
112	08:45:02.47	-54:58:08.8	$0.92_{0.07}$	$0.98_{0.05}$	$0.82_{0.04}$	⋯	$0.835_{0.025}$	⋯	⋯	19.89	Q	2PG...C	PMN J0845-5458	
113	08:49:45.66	-35:41:01.7	$0.56_{0.03}$	$0.49_{0.02}$	$0.52_{0.03}$	$0.375_{0.013}$	⋯	⋯	⋯	20.54	Q	1FG...	PMN J0849-3541	
114	08:58:05.38	-19:50:35.5	$0.72_{0.05}$	$0.68_{0.03}$	$0.70_{0.04}$	$1.226_{0.037}$	⋯	0.659	Wh88	18.38	Q	4F....	PKS 0855-19	
115	09:00:40.02	-28:08:22.8	$0.82_{0.09}$	$1.40_{0.07}$	$2.06_{0.13}$	$1.474_{0.044}$	⋯	2.152	St93	14.74	Q	4S....C	PKS 0858-279	
116	09:04:53.33	-57:35:04.4	$1.44_{0.07}$	$1.38_{0.07}$	$1.82_{0.09}$	⋯	⋯	⋯	⋯	16.46	Q	2UG...	PKS 0903-57	
117	09:06:51.25	-20:19:57.2	$0.58_{0.07}$	$0.70_{0.03}$	$0.70_{0.04}$	$0.606_{0.018}$	⋯	⋯	⋯	18.73	Q	4F....	PMN J0906-2019	
118*	09:19:44.06	-53:40:05.1	$0.94_{0.15}$	$1.69_{0.27}$	$2.50_{0.39}$	⋯	⋯	⋯	⋯	19.00	Q	2SG.E.	PMN J0919-5340	
119	09:20:43.25	-29:56:30.6	$0.61_{0.07}$	$0.57_{0.03}$	$0.51_{0.03}$	$0.366_{0.012}$	⋯	⋯	⋯	18.36	Q	4F....	PMN J0920-2956	
120	09:21:29.41	-26:18:44.2	$2.02_{0.23}$	$2.98_{0.15}$	$3.19_{0.20}$	$1.290_{0.039}$	⋯	2.30	Wr79	18.46	Q	4S...C	PKS 0919-260	
121	09:22:46.44	-39:59:35.1	$1.31_{0.06}$	⋯	⋯	$2.615_{0.092}$	⋯	⋯	⋯	18.12	Q	1.G..C	PKS 0920-39	
122	09:27:51.90	-20:34:50.4	$0.86_{0.10}$	$0.72_{0.04}$	$0.45_{0.03}$	$0.842_{0.028}$	⋯	0.348	Pe79	16.59	Q	4I....C	PKS 0925-203	
123	09:58:02.93	-57:57:42.7	$0.52_{0.03}$	$0.29_{0.01}$	$0.45_{0.03}$	⋯	⋯	⋯	⋯	⋯	G	2UG...	PMN J0958-5757	
124	10:01:59.89	-44:38:00.2	$0.81_{0.04}$	$0.91_{0.05}$	$0.66_{0.03}$	⋯	$1.795_{0.054}$	⋯	⋯	14.11	Q	1PG...C	PKS 0959-443	
125	10:06:13.90	-50:18:13.7	$1.18_{0.06}$	$1.05_{0.06}$	$0.92_{0.05}$	⋯	⋯	⋯	⋯	20.78	Q	2FG...C	PMN J1006-5018	
126	10:07:31.36	-33:33:06.6	$0.65_{0.03}$	⋯	⋯	$0.390_{0.012}$	⋯	1.837	Ja02	20.18	G	1.....	PKS 1005-333	
127	10:14:50.33	-45:08:41.2	$0.54_{0.03}$	⋯	⋯	⋯	$0.711_{0.021}$	⋯	⋯	22.05	Q	1.G..C	PMN J1014-4508	
128	10:18:28.76	-31:23:53.3	$0.56_{0.03}$	$0.67_{0.03}$	$0.70_{0.03}$	$0.379_{0.011}$	⋯	0.794	Dr97	18.71	Q	2F...C	PKS 1016-311	
129	10:23:43.47	-66:46:47.8	$0.55_{0.03}$	$0.65_{0.04}$	$0.75_{0.04}$	⋯	$1.287_{0.039}$	2.198	Wr79	18.82	G	2FG...C	PMN J1023-6646	
130	10:35:02.15	-20:11:34.4	$1.19_{0.08}$	$1.86_{0.23}$	$1.81_{0.13}$	$0.915_{0.027}$	⋯	1.821	Ja84	18.10	Q	4P...C	PKS 1032-199	
131	10:36:53.43	-37:44:15.2	$0.81_{0.04}$	$0.60_{0.03}$	$0.37_{0.02}$	$0.328_{0.011}$	$0.326_{0.013}$	⋯	⋯	18.89	Q	1I....	PKS 1034-374	
132	10:37:16.01	-29:34:02.8	$2.68_{0.18}$	$2.51_{0.31}$	$2.01_{0.15}$	$1.113_{0.033}$	⋯	0.312	St89	16.46	Q	4I...C	PKS 1034-293	
133	10:38:40.56	-53:11:42.9	$1.68_{0.08}$	$1.52_{0.09}$	$1.43_{0.07}$	⋯	⋯	⋯	⋯	19.41	Q	2FG...C	PMN J1038-5311	
134	10:41:44.61	-47:39:60.0	$1.26_{0.06}$	$1.30_{0.06}$	$1.44_{0.07}$	⋯	$2.387_{0.072}$	⋯	⋯	18.25	Q	1FG...C	PMN J1041-4740	163

Table 1 – Continued

Seq. #	RA	δ	S_{20GHz} [Jy]	$S_{8.6GHz}$ [Jy]	$S_{4.8GHz}$ [Jy]	$S_{1.4GHz}$ NVSS [Jy]	$S_{0.843GHz}$ SUMSS [Jy]	z	z Ref.	$B_{J\,mag}$	Opt. ID	Flags	Alternative name	WMAP ID
135	10:47:42.94	-62:17:14.2	2.28 (0.11)	2.05 (0.12)	1.32 (0.07)	...	...	...	...	19.99	Q	2IG...C	PMN J1047-6217	.
136	10:48:06.58	-19:09:35.3	1.24 (0.08)	1.52 (0.19)	1.36 (0.10)	1.155 (0.035)	...	0.595	St93	18.59	Q	4F....C	PKS 1045-18	.
137	10:51:09.14	-53:44:46.2	0.77 (0.04)	1.06 (0.06)	1.31 (0.07)	...	...	...	...	21.08	G	2SG...C	PMN J1051-5344	.
138*	10:58:43.02	-80:03:53.7	2.77 (0.14)	...	...	...	0.546 (0.016)	0.582	ESO	19.08	Q	5....C	PKS 1057-79	176
139	11:01:54.42	-63:25:22.6	0.80 (0.07)	0.86 (0.05)	0.82 (0.04)	...	...	...	...	20.20	Q	3FG...C	PMN J1101-6325	.
140*	11:02:04.87	-44:04:22.6	0.77 (0.04)	...	...	...	0.113 (0.004)	0.77	SSO	20.13	Q	1......	PKS 1059-438	.
141	11:03:52.17	-53:57:00.8	0.54 (0.03)	0.65 (0.03)	0.69 (0.03)	...	1.222 (0.037)	1.666	Dr97	18.30	Q	2FG..C	PKS 1101-536	.
142	11:04:46.06	-24:31:27.5	0.52 (0.03)	0.88 (0.06)	0.85 (0.05)	0.586 (0.018)	...	1.598	Pe79	20.05	Q	4P....C	PKS B1102-242	166
143	11:07:08.73	-44:49:07.8	1.67 (0.08)	...	1.33 (0.07)	...	2.595 (0.078)	...	...	17.84	Q	1.....C	PKS 1104-445	.
144	11:07:12.85	-68:20:50.6	0.82 (0.07)	1.23 (0.07)	0.94 (0.05)	...	0.418 (0.013)	...	...	18.47	Q	3SG...C	PKS 1105-680	.
145	11:12:07.16	-57:03:39.6	0.74 (0.05)	0.97 (0.05)	1.10 (0.06)	...	...	...	...	20.08	Q	2PG..C	PMN J1112-5703	.
146	11:18:27.08	-46:34:15.3	0.96 (0.05)	0.94 (0.05)	0.79 (0.04)	0.474 (0.014)	...	0.713	Ja84	17.54	Q	1F....C	PKS 1116-46	.
147	11:20:16.08	-27:19:08.1	0.54 (0.03)	0.86 (0.06)	1.32 (0.07)	...	...	1.881	Ja02	19.33	Q	4P......	PKS 1117-270	159
148	11:27:04.36	-18:57:19.0	1.42 (0.09)	1.67 (0.11)	1.10 (0.05)	0.536 (0.016)	...	1.050	Dr97	19.17	Q	4P....C	PKS 1124-186	.
149	11:31:43.48	-58:18:53.4	1.11 (0.05)	1.40 (0.07)	0.82 (0.04)	...	...	...	...	19.06	Q	2PG..C	PMN J1131-5818	.
150	11:36:02.21	-68:27:05.4	0.57 (0.05)	0.77 (0.04)	0.58 (0.03)	...	...	...	...	...	.	3SG...C	PKS 1133-681	.
151*	11:45:53.58	-69:54:04.1	0.86 (0.04)	0.79 (0.04)	1.80 (0.10)	...	0.271 (0.008)	...	...	16.90	Q	2IG....	PKS 1143-696	.
152	11:46:08.28	-24:47:34.1	0.71 (0.05)	1.54 (0.10)	1.06 (0.05)	1.434 (0.043)	...	1.940	Dr97	17.97	Q	4S....C	PKS 1143-245	169
153	11:47:01.46	-38:12:10.7	1.38 (0.07)	1.11 (0.06)	1.37 (0.07)	1.804 (0.054)	0.823 (0.025)	1.048	St89	19.03	Q	1F....C	PKS 1144-379	.
154	11:47:33.36	-67:53:41.5	1.89 (0.09)	1.49 (0.07)	0.40 (0.02)	...	...	...	...	19.66	Q	2FG..C	PKS 1145-676	.
155	11:52:53.67	-83:44:10.7	0.52 (0.02)	0.52 (0.03)	...	...	0.148 (0.004)	...	...	...	G	1S....C	PKS 1150-834	.
156	11:54:21.79	-35:05:29.2	0.89 (0.04)	1.91 (0.10)	3.06 (0.15)	6.196 (0.186)	...	0.258	Ta93	18.81	G	.G....C	PKS 1151-34	.
157*	12:05:33.37	-26:34:04.9	0.84 (0.14)	1.18 (0.21)	1.12 (0.06)	1.654 (0.058)	...	0.789	Wr79	19.81	Q	4P..EC	PKS 1203-26	172
158	12:09:02.64	-24:06:19.8	1.15 (0.18)	1.34 (0.29)	1.12 (0.06)	0.561 (0.017)	...	1.299	Ja02	19.31	Q	4P....C	PKS B1206-238	.
159	12:09:14.90	-20:32:38.8	0.71 (0.12)	1.18 (0.25)	0.83 (0.04)	0.354 (0.011)	...	0.404	Ja02	21.68	Q	4P......	PKS B1206-202	.
160*	12:15:46.88	-17:31:45.3	1.60 (0.26)	1.94 (0.42)	1.76 (0.09)	1.662 (0.050)	7.017 (0.211)	0.529	Mu84	19.59	.	4F...C	PKS 1213-17	173
161	12:18:06.26	-46:00:30.3	0.70 (0.03)	1.43 (0.07)	2.43 (0.12)	...	0.320 (0.010)	0.11	SSO	17.88	Q	1..4.C	PKS 1215-45	.
162*	12:27:26.74	-44:36:39.8	0.54 (0.03)	...	0.58 (0.03)	...	...	...	...	22.03	Q	1......	PKS 1224-443	.
163	12:45:53.72	-16:16:44.5	0.68 (0.11)	0.75 (0.16)	1.24 (0.06)	0.516 (0.015)	...	0.633	Sa76	17.65	Q	4P......	PKS 1243-160	177
164	12:46:46.78	-25:47:49.0	1.57 (0.08)	1.47 (0.07)	2.47 (0.12)	1.165 (0.035)	...	1.275	Od91	21.52	Q	5F....C	PKS 1244-255	.
165	12:48:23.88	-19:59:18.4	0.69 (0.03)	1.61 (0.08)	1.62 (0.08)	5.136 (0.154)	...	1.02	SSO	17.24	Q	5S....C	PKS 1245-19	.
166*	12:48:28.53	-45:59:47.8	1.36 (0.07)	1.48 (0.07)	0.67 (0.03)	...	1.227 (0.037)	...	...	18.74	Q	1F......	PMN J1248-4559	.
167	12:52:43.12	-67:37:38.6	0.68 (0.06)	0.82 (0.04)	...	...	...	...	...	20.54	Q	5PG...	PKS 1249-673	.
168	12:54:37.24	-20:00:56.2	0.51 (0.03)	...	0.99 (0.05)	0.135 (0.004)	...	...	...	20.55	G	5.....	PMN J1254-2000	.
169	12:54:59.80	-71:38:18.4	0.75 (0.06)	1.01 (0.05)	2.03 (0.10)	...	1.634 (0.063)	...	...	...	G	5PG..C	PKS 1251-71	180
170	12:57:59.20	-31:55:15.2	1.46 (0.07)	1.84 (0.09)	0.52 (0.03)	1.144 (0.034)	...	1.924	Ja84	19.06	Q	1F....C	PKS 1255-316	.
171	12:58:38.27	-18:00:01.3	0.59 (0.10)	0.63 (0.14)	1.07 (0.05)	0.359 (0.011)	...	1.956	Ja02	20.50	Q	4P....C	PKS B1256-177	.
172	12:58:54.52	-22:19:30.8	0.87 (0.14)	1.15 (0.25)	...	0.793 (0.024)	...	1.306	De84	19.16	Q	4P...C	PKS 1256-220	.
173	13:03:49.22	-55:40:31.5	0.91 (0.05)	...	...	...	...	...	...	...	.	5.G...	PMN J1303-5540	.
174	13:05:27.47	-49:28:04.8	0.73 (0.04)	...	...	...	5.776 (0.173)	0.001	RC3	9.66	.	5......	PKS 1302-49	.
175	13:15:04.24	-53:34:36.0	0.87 (0.04)	...	...	...	...	...	...	...	.	5.G...	PMN J1315-5334	.
176	13:16:08.09	-33:38:58.9	1.50 (0.07)	1.22 (0.06)	1.17 (0.07)	1.278 (0.038)	...	1.210	Ja82	18.04	Q	1F....C	PKS 1313-333	182
177	13:21:12.81	-43:42:16.7	0.57 (0.03)	...	...	...	6.000 (0.016)	0.011	RC3	12.17	G	5.....	PKS 1318-434	.
178	13:21:14.02	-26:36:10.2	0.63 (0.03)	0.59 (0.03)	0.42 (0.03)	0.510 (0.015)	...	2.027	Dr97	21.10	Q	5I.....	PKS 1318-263	.
179*	13:25:27.7	-43:01:07.0	>59.30	...	...	...	342.000 (0.320)	0.001	RC3	7.30	G	6...MC	Centaurus A	.

Table 1 — Continued

Seq. #	RA	δ	$S_{20\text{GHz}}$ [Jy]	$S_{8.6\text{GHz}}$ [Jy]	$S_{4.8\text{GHz}}$ [Jy]	$S_{1.4\text{GHz}}$ NVSS [Jy]	$S_{0.843\text{GHz}}$ SUMSS [Jy]	z	z Ref.	$B_{J\,mag}$	Opt. ID	Flags	Alternative name	WMAP ID
180	13:26:49.58	-52:55:35.6	1.16 0.08	1.06 0.05	0.87 0.04	...	0.827 0.025	...	...	...	.	4IG...C	PMN J1326-5256	.
181	13:29:01.13	-56:08:02.6	0.93 0.05	...	...	...	...	...	...	...	.	5.G...C	PMN J1329-5608	.
182*	13:36:39.0	-33:57:58.2	>1.60 ...	...	...	...	...	0.012	R3C	11.42	G	6....M.	PKS 1333-33	185
183	13:37:52.37	-65:09:25.4	0.51 0.04	0.62 0.03	0.53 0.04	...	...	...	...	20.19	G	5FG...	PKS 1334-649	.
184	13:42:04.79	-20:51:29.0	0.52 0.03	0.65 0.03	0.63 0.03	0.399 0.012	...	1.582	Ja02	18.76	Q	4F....	PMN J1342-2051	.
185*	13:46:48.95	-60:24:29.1	5.30 0.84	6.14 0.97	6.58 1.04	...	...	...	...	...	.	5.G.2E.	PKS 1343-60	.
186	13:57:11.27	-15:27:29.5	0.55 0.04	0.83 0.04	0.99 0.05	0.682 0.021	...	1.890	Wi83	18.13	Q	4S....C	PKS 1354-152	.
187	14:09:50.13	-26:57:37.3	0.75 0.05	1.38 0.07	1.52 0.08	0.269 0.008	...	2.430	Dr97	21.94	Q	4S....C	PKS B1406-267	.
188	14:18:58.88	-35:09:42.9	0.63 0.03	...	...	0.414 0.012	...	1.544	Ja02	19.25	Q	5.....	PKS 1415-349	.
189	14:19:35.22	-51:54:58.8	0.75 0.04	...	...	...	0.512 0.015	...	...	...	.	5.G...	PMN J1419-5155	.
190	14:24:32.24	-49:13:49.3	2.64 0.13	4.29 0.21	5.65 0.28	...	1.130 0.034	...	...	...	.	5S....C	PKS B1421-490	.
191	14:24:55.56	-68:07:57.8	1.50 0.08	2.31 0.11	2.19 0.11	...	10.172 0.305	...	...	...	.	5.G44.	PKS 1420-679	193
192	14:27:41.31	-33:05:31.9	0.80 0.04	0.44 0.02	0.27 0.02	...	...	...	...	...	.	5I....C	PKS 1424-328	191
193	14:27:56.30	-42:06:18.9	2.75 0.14	3.03 0.15	3.11 0.15	0.161 0.005	3.911 0.117	1.522	Wh88	18.48	Q	5F....C	PKS 1424-41	.
194	14:33:21.45	-15:48:45.0	0.56 0.03	0.81 0.04	0.87 0.04	0.492 0.015	...	1.573	Dr97	...	.	5S....C	PKS 1430-155	.
195	14:38:09.46	-22:04:54.6	0.80 0.05	0.88 0.04	0.68 0.03	0.770 0.027	...	1.187	Dr97	18.75	G	4..55.C	PKS 1435-218	.
196	14:54:27.46	-37:47:33.1	1.87 0.09	1.89 0.09	1.74 0.09	0.942 0.028	1.813 0.054	0.314	6dF	16.36	G	5F....C	PKS 1451-375	.
197	14:54:32.92	-40:12:32.6	0.53 0.03	...	...	1.031 0.036	1.242 0.037	1.810	Ja02	19.01	Q	5.....C	PKS 1451-400	.
198	14:57:26.70	-35:39:10.8	0.90 0.05	...	...	0.674 0.020	1.002 0.030	1.424	Ja02	17.95	G	5.....	PKS 1454-354	.
199	15:07:04.78	-16:52:30.3	1.05 0.05	1.70 0.08	2.13 0.10	2.711 0.081	...	0.876	Hu78	18.40	G	5S....C	PKS 1504-167	.
200	15:08:38.98	-49:53:01.8	0.94 0.05	0.65 0.03	0.39 0.02	...	0.510 0.015	...	...	19.83	.	5IG..C	PMN J1508-4953	.
201	15:13:57.01	-21:14:57.7	0.54 0.10	...	0.41 0.02	0.260 0.008	...	1.179	Dr97	21.01	G	4.....C	PKS 1511-210	.
202	15:14:40.05	-47:48:28.7	0.63 0.03	0.76 0.04	0.78 0.04	...	0.405 0.012	...	...	...	.	5FG..C	PMN J1514-4748	.
203	15:17:41.76	-24:22:20.3	3.45 0.67	3.65 0.19	3.17 0.16	2.042 0.061	...	0.048	Ro77	15.63	G	4F...C	PKS 1514-24	205
204	15:22:37.72	-27:30:11.1	1.04 0.20	1.57 0.08	1.38 0.07	1.107 0.033	...	1.294	He04	18.72	Q	4P...C	PKS 1519-273	.
205	15:34:20.63	-53:51:12.7	0.84 0.04	...	...	...	...	...	...	...	.	5.G...	PMN J1534-5351	.
206	15:34:54.68	-35:26:23.8	0.73 0.04	...	...	0.272 0.008	0.186 0.006	...	...	20.25	Q	5.....	PMN J1534-3525	.
207	15:35:52.23	-47:30:21.8	0.68 0.03	...	...	...	...	...	...	...	.	5.G...	PMN J1535-4730	.
208*	15:46:44.51	-68:37:28.9	0.51 0.03	0.79 0.04	0.70 0.04	...	0.881 0.026	0.18	SSO	19.51	Q	1.....	PMN J1546-6837	.
209	15:50:58.66	-82:58:06.9	0.52 0.03	0.96 0.05	1.03 0.05	...	...	...	...	20.00	G	5..44.	PKS 1541-82	.
210	15:54:02.44	-27:04:39.8	0.60 0.12	2.47 0.12	3.48 0.17	1.394 0.042	...	2.145	Ja84	19.56	Q	4S....C	PKS 1550-269	.
211*	15:56:58.72	-79:14:04.9	0.83 0.07	0.75 0.04	0.47 0.02	...	6.165 0.185	0.150	Ta01	18.80	Q	4S....C	PKS 1549-79	.
212	15:59:41.26	-24:42:40.2	0.77 0.15	...	...	0.706 0.021	...	2.813	Wr79	19.33	Q	4I....	PKS 1556-245	.
213	16:00:19.56	-46:49:08.0	0.60 0.03	...	...	...	...	...	...	...	G	1.G...	PMN J1600-4649	.
214	16:03:50.67	-49:04:05.1	0.55 0.03	...	...	...	...	...	...	20.67	Q	1.G..C	PMN J1603-4904	.
215	16:04:31.09	-44:41:31.3	1.30 0.06	1.41 0.07	1.61 0.08	...	...	...	...	20.75	G	1FG..C	PMN J1604-4441	.
216*	16:15:05.2	-60:54:25.5	3.84 0.04	...	...	...	...	0.018	R3C	10.26	G	6.G.M.	PKS 1610-60	183
217	16:17:17.96	-58:48:06.1	2.71 0.24	3.91 0.20	4.26 0.21	...	3.281 0.098	...	...	18.23	G	2SG..C	PMN J1617-5848	.
218	16:17:49.22	-77:17:18.5	2.12 0.17	4.27 0.21	4.27 0.21	...	4.092 0.123	1.710	Hu80	19.19	G	4P...C	PKS 1610-77	.
219	16:24:18.59	-68:09:11.7	0.73 0.04	1.31 0.07	1.67 0.08	...	1.046 0.031	1.360	Th90	17.05	Q	1.52.C	PKS 1619-680	.
220	16:25:46.99	-25:27:39.3	2.06 0.29	...	...	2.521 0.076	...	0.786	di94	...	.	4.....C	PKS 1622-253	.
221*	16:26:06.04	-29:51:26.6	1.79 0.26	...	...	2.286 0.069	...	...	...	18.41	Q	4.....C	PKS 1622-29	.
222	16:36:55.26	-41:02:00.7	0.78 0.04	1.27 0.06	1.33 0.07	...	...	...	...	...	.	1.G44.	PMN J1636-4101	.
223	16:47:37.79	-64:38:01.0	0.75 0.04	0.80 0.04	0.66 0.03	...	0.649 0.020	...	...	20.05	G	3.44.C	PMN J1647-6437	.
224	16:48:42.34	-33:01:47.7	0.58 0.03	0.73 0.04	0.51 0.03	0.405 0.012	...	...	...	18.75	Q	1PG...	PKS 1645-329	.

Table 1 – Continued

Seq. #	RA	δ	S_{20GHz} [Jy]	$S_{8.6GHz}$ [Jy]	$S_{4.8GHz}$ [Jy]	$S_{1.4GHz}$ NVSS [Jy]	$S_{0.843GHz}$ SUMSS [Jy]	z	z Ref.	$B_{J\,mag}$	Opt. ID	Flags	Alternative name	WMAP ID
225	16:50:16.49	-50:44:46.2	$1.88_{0.17}$	$1.99_{0.10}$	$1.99_{0.10}$	...	...	...	...	20.95	Q	2FG...C	PMN J1650-5044	.
226*	16:50:39.55	-29:43:47.0	$1.01_{0.05}$	...	...	$0.577_{0.017}$	...	...	...	19.01	Q	5.G...C	PKS 1647-296	.
227	17:00:53.27	-26:10:52.6	$0.51_{0.10}$	...	...	$0.609_{0.018}$	...	...	...	16.50	Q	4.G...C	PKS 1657-261	.
228	17:01:44.84	-56:21:55.6	$1.16_{0.06}$	$1.79_{0.09}$	$2.02_{0.10}$	...	...	...	...	...	.	5.G22.C	PMN J1701-5621	.
229	17:03:36.34	-62:12:38.2	$1.05_{0.07}$	$1.04_{0.05}$	$1.04_{0.05}$	...	$0.731_{0.022}$	...	...	18.73	Q	2F....C	PMN J1703-6212	198
230	17:09:18.61	-35:25:21.0	$0.61_{0.03}$	$0.74_{0.04}$	$1.13_{0.06}$	$2.117_{0.064}$	...	...	...	...	.	1SG....	NVSS J170918-352521	.
231	17:09:34.40	-17:28:52.7	$0.55_{0.11}$	...	...	$0.431_{0.013}$	...	...	...	...	.	4....C	PMN J1709-1728	.
232	17:13:10.02	-34:18:27.7	$1.03_{0.06}$	$1.11_{0.06}$	$1.10_{0.05}$	$0.791_{0.024}$	...	...	...	20.60	Q	1FG....	NVSS J171309-341830	.
233	17:13:31.21	-26:58:53.4	$1.40_{0.28}$	...	...	$1.134_{0.040}$	...	...	...	19.65	Q	4.G...C	PMN J1713-2658	.
234	17:13:50.99	-32:26:08.9	$0.61_{0.03}$	$1.21_{0.06}$	$1.67_{0.08}$	$1.495_{0.045}$	...	...	...	19.82	Q	1SG....	PMN J1713-3226	.
235	17:17:36.21	-33:42:06.6	$0.69_{0.04}$	$0.61_{0.03}$	$0.58_{0.03}$	$0.624_{0.019}$	...	...	...	20.93	Q	1FG..C	PMN J1717-3342	.
236	17:23:41.10	-65:00:36.3	$2.87_{0.14}$	$4.61_{0.23}$	$5.61_{0.28}$	...	$3.724_{0.112}$	0.014	RC3	8.63	.	1..22.C	PKS 1718-649	196
237	17:33:15.32	-37:22:30.6	$0.81_{0.04}$	$1.47_{0.04}$	$0.83_{0.04}$	$0.650_{0.020}$	$0.354_{0.011}$	...	...	18.67	G	1PG...C	PMN J1733-3722	.
238	17:33:40.43	-79:35:55.7	$1.11_{0.06}$	$2.80_{0.14}$	$4.12_{0.21}$	...	$7.729_{0.232}$	...	...	...	.	5.....	PKS 1725-795	186
239	17:44:25.25	-51:44:45.2	$1.24_{0.08}$	...	...	...	$1.497_{0.045}$	...	...	...	.	2S....C	PKS 1740-517	.
240	18:02:42.66	-39:40:07.8	$1.41_{0.07}$	$1.31_{0.07}$	$1.35_{0.07}$	$2.273_{0.068}$	$0.637_{0.019}$	...	...	...	G	5.G...C	PMN J1802-3940	199
241	18:03:23.56	-65:07:36.8	$1.24_{0.06}$	...	...	...	$1.179_{0.035}$	0.069	6dF	18.18	G	1..22.C	PKS 1758-651	.
242	18:09:57.79	-45:52:41.2	$1.09_{0.05}$	$3.57_{0.18}$	$5.56_{0.28}$	...	$20.185_{0.606}$	0.062	Da79	16.89	G	1.......	PKS 1806-458	200
243	18:19:34.98	-63:45:48.2	$1.70_{0.09}$	$1.79_{0.09}$	$1.94_{0.10}$	...	$0.678_{0.020}$	...	...	16.80	G	5S....C	PKS 1814-63	.
244	18:19:45.29	-55:21:21.8	$1.23_{0.09}$	...	...	...	$0.777_{0.023}$	...	...	19.19	G	2S....C	PKS 1815-553	.
245	18:20:57.84	-25:28:12.4	$0.71_{0.04}$	$0.80_{0.04}$	$0.83_{0.04}$	$1.353_{0.048}$	...	...	...	18.56	Q	5.G...C	PMN J1820-2528	.
246*	18:29:12.57	-58:13:54.9	$0.69_{0.05}$	...	...	...	$0.374_{0.011}$	1.52	SSO	19.26	Q	2F....C	PKS 1824-582	.
247	18:32:11.13	-20:39:48.3	$0.79_{0.05}$	...	...	$1.116_{0.034}$	...	...	...	18.56	Q	4.G...C	PMN J1832-2039	.
248	18:33:39.95	-21:03:41.2	$5.50_{0.36}$	...	...	$10.896_{0.327}$	...	...	...	...	.	4.G...C	PKS 1830-211	192
249	18:34:27.29	-58:56:36.7	$1.43_{0.11}$	$1.46_{0.07}$	$1.02_{0.05}$	...	$1.290_{0.039}$	...	...	20.74	Q	2P....	PKS 1830-589	.
250	18:37:28.74	-71:08:43.0	$1.81_{0.45}$	$2.10_{0.10}$	$2.27_{0.11}$	...	$0.232_{0.007}$	1.356	Ja84	17.89	Q	2F....C	PKS 1831-711	.
251	19:03:01.33	-67:49:35.5	$0.52_{0.04}$	$0.40_{0.02}$	$0.32_{0.02}$	...	$1.184_{0.036}$	...	...	18.90	Q	1..44.	PMN J1903-6749	.
252	19:11:09.71	-20:06:55.7	$2.67_{0.20}$	$3.40_{0.17}$	$3.23_{0.16}$	$2.714_{0.081}$	...	1.119	Ha03	18.21	Q	5F....C	PKS B1908-201	.
253	19:12:40.38	-80:10:07.0	$1.07_{0.07}$	$1.08_{0.05}$	$1.03_{0.05}$	...	$0.696_{0.021}$	1.756	Go98	19.83	Q	4.22.C	PKS 1903-80	.
254	19:23:32.27	-21:04:33.4	$2.55_{0.17}$	$3.91_{0.36}$	$3.29_{0.16}$	$3.167_{0.095}$	...	0.874	Ha03	15.32	Q	4P....C	PMN J1923-2104	8
255	19:24:51.04	-29:14:30.2	$13.84_{0.91}$	...	$16.74_{0.84}$	$13.387_{0.402}$	...	0.352	Wi83	18.71	Q	4.....C	PKS B1921-293	.
256	19:30:06.08	-60:56:08.9	$0.66_{0.05}$	$0.95_{0.05}$	$1.11_{0.06}$	...	$0.764_{0.023}$	0.652	Ja78	20.57	G	1..22.C	PKS 1925-610	.
257	19:32:44.95	-45:36:38.3	$0.53_{0.03}$	$0.80_{0.04}$	$0.58_{0.03}$	...	$13.915_{0.417}$	0.231	Ta93	18.47	Q	1..44.	PKS 1929-457	.
258*	19:35:57.62	-46:20:43.8	$0.52_{0.03}$	...	...	...	$1.045_{0.031}$	0.965	Dr97	...	.	1.......	PKS 1932-46	.
259	19:37:16.22	-39:58:01.6	$1.76_{0.09}$	$2.41_{0.12}$	$1.65_{0.08}$	$1.002_{0.035}$	...	0.183	Ta93	18.15	Q	1..44.C	PKS 1933-400	.
260	19:39:24.83	-63:42:45.4	$0.95_{0.07}$	$2.99_{0.15}$	$5.93_{0.30}$	...	$13.722_{0.412}$	1.657	Ja84	18.87	G	2S....C	PKS 1934-63	.
261	19:39:26.74	-15:25:43.3	$1.20_{0.09}$	$0.89_{0.04}$	$0.62_{0.03}$	$0.608_{0.018}$	...	3.154	Os94	19.44	Q	5I....C	PKS 1936-15	.
262	19:40:25.74	-69:07:58.0	$0.52_{0.04}$	$0.80_{0.04}$	$0.87_{0.04}$	...	$1.705_{0.051}$	0.015	Gr83	18.36	G	2S....C	PKS 1935-692	.
263	19:45:24.09	-55:20:49.0	$0.78_{0.05}$	$1.01_{0.05}$	$1.06_{0.05}$	...	$0.576_{0.017}$	1.242	Ja82	8.06	G	2S....C	PKS 1941-554	.
264	19:56:59.41	-32:25:46.0	$0.84_{0.05}$	$0.96_{0.05}$	$0.91_{0.05}$	$0.473_{0.014}$	$1.423_{0.043}$	0.630	Br75	19.17	G	4F....C	PKS 1953-325	3
265	19:57:59.83	-38:45:06.8	$3.76_{0.19}$	$4.26_{0.21}$	$4.08_{0.20}$	$1.493_{0.045}$	...	0.650	Br75	18.47	Q	1..44.C	PKS 1954-388	11
266	20:00:57.08	-17:48:57.4	$2.46_{0.12}$	$2.33_{0.12}$	$2.35_{0.12}$	$0.550_{0.016}$	...	...	...	18.02	Q	5F....C	PKS 1958-179	.
267	20:03:24.04	-32:51:42.4	$0.50_{0.02}$	$0.73_{0.04}$	$0.84_{0.04}$	$0.446_{0.016}$	...	3.773	Os94	18.83	Q	1..44.C	PKS 2000-330	.
268	20:05:17.30	-18:22:03.1	$0.63_{0.03}$	$0.42_{0.02}$	$0.40_{0.02}$	$0.736_{0.026}$	...	0.868	Hu78	18.55	Q	5I.....	PKS 2002-185	.
269	20:05:55.03	-37:23:39.7	$0.66_{0.03}$	$0.71_{0.03}$	$0.63_{0.03}$	$0.320_{0.010}$	$0.279_{0.009}$	...	...	...	G	1..44.C	PKS 2002-375	.
270	20:09:25.45	-48:49:53.9	$0.88_{0.04}$	...	...	...	$1.329_{0.040}$	0.071	Fa87	15.75	G	1.....C	PKS 2005-489	.

Table 1 – Continued

Seq. #	RA	δ	S_{20GHz} [Jy]	$S_{8.6GHz}$ [Jy]	$S_{4.8GHz}$ [Jy]	$S_{1.4GHz}$ NVSS [Jy]	$S_{0.843GHz}$ SUMSS [Jy]	z	z Ref.	$B_{J\,mag}$	Opt. ID	Flags	Alternative name	WMAP ID
271	20:11:15.70	-15:46:40.2	2.10 0.11	2.31 0.12	1.55 0.08	0.546 0.016	...	1.118	Pe79	17.27	Q	5P....C	PKS 2008-159	14
272	20:24:35.58	-32:53:35.6	0.51 0.05	0.57 0.03	0.63 0.03	0.887 0.027	...	1.470	Br75	18.73	Q	5F.....	PKS 2021-330	.
273*	20:56:16.40	-47:14:47.9	1.17 0.06	...	...	...	2.223 0.067	1.489	Ja84	18.29	Q	1.....C	PKS 2052-47	208
274	20:57:41.64	-37:34:02.3	0.73 0.04	0.43 0.02	0.42 0.02	0.266 0.008	0.292 0.009	1.071	Ja02	20.69	Q	1..44.C	PKS 2054-377	.
275	21:05:44.98	-78:25:35.0	0.94 0.06	0.93 0.05	0.77 0.04	...	0.992 0.030			21.59	G	4I....C	PKS 2059-78	.
276	21:09:33.10	-41:10:20.5	1.63 0.08	...	...	...	1.782 0.054	1.058	Wh88	20.20	Q	1.....C	PKS 2106-413	.
277	21:21:13.19	-37:03:08.9	0.82 0.04	0.84 0.05	0.60 0.03	0.345 0.010	0.313 0.009			22.24	Q	1P.....	PKS 2118-372	.
278*	21:26:30.69	-46:05:48.2	0.55 0.03	0.64 0.04	0.69 0.03	...	1.467 0.044			18.12	Q	1F.....	PKS 2123-463	.
279	21:29:12.19	-15:38:40.9	0.60 0.03	1.65 0.08	1.53 0.08	0.590 0.018	...	3.268	Os94	17.61	Q	5P....C	PKS 2126-15	.
280	21:42:31.00	-24:44:38.9	1.26 0.08	0.68 0.03	0.65 0.03	0.290 0.009	...			20.53	Q	5F.....	PMN J2142-2444	.
281	21:46:29.73	-77:55:54.9	0.55 0.03	1.06 0.05	0.63 0.03	...	0.269 0.008			19.76	Q	4I.....	PKS 2141-781	184
282	21:51:21.94	-27:42:23.4	1.85 0.09	0.50 0.03	0.41 0.02	0.315 0.009	...	1.484	2QZ	17.95	Q	5I.....	PMN J2151-2742	.
283	21:51:55.58	-30:27:53.8	5.31 0.27	2.37 0.12	2.39 0.12	1.243 0.037	1.100 0.033	2.345	Wi86	18.63	Q	1..44.C	PKS 2149-306	.
284*	21:57:06.07	-69:41:23.2	1.90 0.10	...	...	...	41.200 1.455	0.027	RC3	14.10	G	6...M.	PKS 2153-69	190
285	21:58:06.28	-15:01:09.3	0.61 0.04	0.27 0.01	0.20 0.01	3.021 0.091	...	0.672	Wh88	20.67	Q	2I.....	PKS 2155-152	18
286	22:00:54.69	-55:20:08.2	2.03 0.13	0.66 0.04	0.58 0.03	...	0.263 0.008			17.91	Q	2I.....	PMN J2200-5520	.
287	22:02:56.11	-23:35:11.1	1.12 0.07	3.34 0.17	4.43 0.22	0.502 0.015	...	2.118	Ja78	18.80	Q	4.55..	PKS 2200-238	.
288	22:06:10.60	-18:35:39.5	0.80 0.05	1.41 0.07	1.54 0.08	6.398 0.192	...	0.618	Mo82	18.45	Q	4.55.C	PKS 2203-18	16
289	22:07:43.82	-53:46:34.1	0.65 0.04	...	...	...	1.526 0.046	1.215	Wi83	18.41	Q	2F.....	PKS 2204-54	.
290	22:13:02.60	-25:29:30.7	0.59 0.03	0.69 0.03	0.59 0.03	1.210 0.036	...	1.833	Wr83	19.85	Q	4.....C	PKS 2210-25	.
291	22:29:00.22	-69:10:29.7	2.00 0.10	...	...	...	0.400 0.012			17.87	Q	1.44..	PKS 2225-694	.
292*	22:30:40.34	-39:42:51.8	0.92 0.06	2.07 0.52	1.21 0.06	0.369 0.013	0.350 0.011	0.318	6df	17.61	Q	5.....	PKS 2227-399	206
293	22:35:13.28	-48:35:58.7	0.65 0.04	1.01 0.05	0.85 0.04	...	0.337 0.010	0.510	Ja84	18.59	Q	1P....C	PKS 2232-488	201
294	22:39:12.11	-57:01:01.1	1.05 0.06	...	...	...	...				.	2P.....	PKS 2236-572	.
295	22:43:26.47	-25:44:31.4	0.65 0.04	0.72 0.04	0.51 0.03	1.102 0.033	...	0.774	St93	20.38	Q	4.....C	PKS 2240-260	.
296	22:46:16.77	-56:07:46.1	1.05 0.06	1.13 0.06	1.06 0.05	...	0.477 0.014			18.70	Q	2I.....	PKS 2243-563	.
297	22:47:03.81	-36:57:46.5	0.94 0.06	1.41 0.07	1.04 0.05	1.261 0.038	1.907 0.057	2.252	Wi83	18.38	Q	4F....C	PKS 2244-37	.
298	22:48:38.67	-32:35:52.5	1.47 0.10	0.62 0.03	0.53 0.03	0.708 0.021	0.746 0.023	2.268	Pe79	21.71	Q	4I....C	PKS 2245-328	.
299	22:50:44.51	-28:06:40.0	0.52 0.03	...	...	0.305 0.009	...			19.04	Q	4.55..	PMN J2250-2806	.
300	22:56:41.26	-20:11:41.3	1.00 0.07	...	...	0.345 0.010	...				.	4.....	PKS 2254-204	19
301	22:57:10.50	-36:27:44.6	0.55 0.03	0.85 0.04	1.08 0.05	1.280 0.045	1.209 0.036	0.005	RC3	11.49	G	5S....C	PKS 2254-367	12
302	22:58:05.97	-27:58:21.7	2.04 0.13	0.40 0.02	0.40 0.02	1.248 0.038	...	0.926	Pe76	17.34	Q	4.....C	PKS 2255-282	.
303	23:03:03.02	-18:41:26.1	0.67 0.03	1.36 0.07	1.32 0.10	0.861 0.028	...	0.128	Hu78	18.29	G	5U.....	PKS 2300-18	.
304	23:03:43.46	-68:07:37.7	0.87 0.04	0.66 0.03	0.53 0.03	...	0.759 0.029	0.512	Wi86	16.26	Q	1..22..	PKS 2300-683	.
305	23:14:48.36	-31:38:38.6	0.63 0.03	0.74 0.04	0.66 0.05	0.825 0.025	0.778 0.023	1.323	Dr97	18.65	Q	1P....C	PKS 2312-319	.
306	23:15:44.24	-50:18:39.0	0.73 0.04	...	...	...	0.234 0.007			20.24	G	2F.....	PKS 2312-505	204
307	23:29:17.66	-47:30:19.2	1.42 0.07	1.84 0.09	1.99 0.10	...	3.180 0.095	1.299	Pe72	16.93	Q	1S....C	PKS 2326-477	32
308	23:31:38.69	-15:56:57.0	0.80 0.04	...	...	1.335 0.040	...	1.153	Wr83	20.72	Q	1P....C	PKS 2329-16	.
309	23:31:59.43	-38:11:47.4	0.52 0.03	0.75 0.04	0.59 0.03	0.543 0.016	0.486 0.015	1.202	Ja78	17.33	Q	1P....C	PKS 2329-384	.
310*	23:33:55.28	-23:43:40.8	0.82 0.13	1.47 0.22	0.67 0.10	0.782 0.023	...	0.047	Wi76	16.45	G	5..44EC	PKS 2331-240	.
311	23:34:44.88	-52:51:19.4	0.93 0.05	0.86 0.04	0.70 0.05	...	1.428 0.054			17.99	Q	2I.....	PKS 2332-531	195
312	23:36:12.05	-52:36:22.1	1.06 0.06	1.50 0.08	1.75 0.13	...	2.196 0.066				.	2S....C	PKS 2333-528	.
313*	23:45:12.47	-15:55:08.0	0.93 0.05	0.80 0.04	0.60 0.03	0.226 0.007	...	0.626	6dF	19.21	Q	5I.....	PMN J2345-1555	.
314	23:48:02.63	-16:31:12.0	2.45 0.16	3.29 0.78	2.49 0.12	2.641 0.079	...	0.600	Wr83	18.00	Q	4P....C	PKS 2345-16	39
315	23:54:30.18	-15:13:11.3	1.11 0.06	0.96 0.05	0.89 0.04	0.865 0.026	...	2.668	Pe79	18.49	Q	5F....C	PKS 2351-154	.

Table 1 – Continued

Seq. #	RA	δ	S_{20GHz} [Jy]	$S_{8.6GHz}$ [Jy]	$S_{4.8GHz}$ [Jy]	$S_{1.4GHz}$ NVSS [Jy]	$S_{0.843GHz}$ SUMSS [Jy]	z	z Ref.	$B_{J\,mag}$	Opt. ID	Flags	Alternative name	WMAP ID
316	23:56:00.67	-68:20:03.6	0.84 $_{0.04}$	0.93 $_{0.05}$	0.79 $_{0.06}$	...	1.126 $_{0.034}$	1.716	Pe72	17.61	Q	1..22.C	PKS 2353-68	.
317	23:57:53.41	-53:11:12.5	1.48 $_{0.08}$	1.36 $_{0.07}$	1.28 $_{0.09}$	...	1.411 $_{0.042}$	1.006	Ja84	18.63	Q	2F....C	PKS 2355-534	189
318	23:58:02.13	-45:55:18.8	0.54 $_{0.03}$	...	...	...	0.228 $_{0.007}$	...	...	18.98	Q	1......	PKS 2355-461	.
319*	23:59:04.7	-60:55:01.1	3.03 $_{0.05}$	...	...	...	...	0.096	Lo96	16.61	G	6...M.	PKS 2356-61	187
320	23:59:35.41	-31:33:44.9	0.64 $_{0.03}$	0.89 $_{0.04}$	0.93 $_{0.05}$	0.347 $_{0.010}$	0.253 $_{0.008}$	0.990	2QZ	19.08	Q	1S....C	PKS 2357-318	.

Notes: Redshift reference codes: (SSO) New redshifts from SSO 2.3m;(ESO) Edwards et al. in preparation; (2QZ) S. Croom et al. 2004 MNRAS 349, 1397; (6dF) D.H. Jones et al. 2004, MNRAS 355, 747 (6dF Galaxy Survey); (FCSS) M. Drinkwater et al. 2000 A&A 355, 900 and Fornax online catalogue; (RC3) G. de Vaucouleurs et al. 1991 Third Reference Catalogue of Bright Galaxies; (Al94) S. di Serego Alighieri et al. 1994 MNRAS 269, 998; (Ar67) H. Arp et al. 1967 ApJ 147, 840; (Ba95) J. Baker et al. 1995 MNRAS 277, 553; (Br75) I. Browne et al. 1975 MNRAS 173, 87P; (Br77) I. Browne & A. Savage 1977 MNRAS 179, 65P; (Ca00) A. Caccianiga et al., 2000, A&AS 144, 247; (Da79) J. Danziger et al. 1979 MNRAS 186, 93; (Da91) L.N. Da Costa et al. 1991 ApJS 75, 935; (di94) S. di Serego Alighieri 1994 MNRAS 269, 998; (De84) H. Dekker & S. D'Odorico 1984 ESO Messenger 37, 7; (Dr97) M. Drinkwater et al. 1997 MNRAS 284, 85; (El01) S. Ellison et al. 2001, A&A 379, 393; (Fa87) R. Falomo et al. 1987 ApJ 318, L39; (Fr83) K. Fricke et al. 1983 A&A 117, 60; (Go98) A. Goncalves et al. 1998 A&AS 127, 107; (Gr83) S. Grandi 1983 MNRAS 204, 691; (Ha03) J. Halpern et al. 2003 AJ 125, 572; (He04) J. Heidt et al. 2004 A&A 418, 813; (Hu78) R. Hunstead et al. 1978 MNRAS 185, 149; (Hu78) R. Hunstead et al. 1980 MNRAS 192, 31P; (Io96) A. Iovino et al. 1996 A&AS 119, 265; (Ja78) D. Jauncey et al. 1978 ApJ 218, L1; (Ja82) D. Jauncey et al. 1982 AJ 87, 763; (Ja84) D. Jauncey et al. 1984 ApJ 286, 498; (Ja02) C. Jackson et al. 2002 A&A 386, 97; (Ke85) W. Keel 1985 AJ 90, 2207; (La01) H. Landt et al. 2001 MNRAS 323, 757; (Lo96) J. Loveday et al. 1996 ApJS 107, 201L; (Ma95) J. Maza et al. 1995 RMxAA 31, 119; (Mo78) D. Morton et al. 1978 MNRAS 185, 735; (Mo82) D. Morton et al. 1982 MNRAS 198, 669; (Mu84) H. Murdoch et al. 1984 PASA 5, 341; (Od91) C. O'Dea et al. 1991 ApJ 380,66O; (Os94) P. Osmer et al. 1994 ApJ, 436, 678; (Pe72) B. Peterson & J. Bolton 1972 ApJ173, L19; (Pe76) B. Peterson et al. 1976 ApJ 207, L5; (Pe98) E. Perlman et al. 1998 AJ 115, 1253; (P198) W. Pietsch et al. 1998 A&A 333, 48; (Qu95) H. Quintana et al. 1995 ApJS 96, 343; (Ro77) A. Rodgers & B. Peterson 1977 ApJ 212, L9; (Sa76) A. Savage et al. 1976 MNRAS 177, 77; (Sb05) B. Sbarufatti et al. 2005 AJ 129, 559; (Sb06) B. Sbarufatti et al. 2006 AJ 132, 1; (Sc65) M. Schmidt 1965 ApJ 141, 1; (St89) M. Stickel et al. 1989 A&AS 80, 103; (St93) M. Stickel et al. 1993 A&AS 98, 393; (St94) M. Stickel et al. 1994 A&AS 105, 211; (Su04) J. Sulentic et al. 2004, A&A 423, 121; (Ta93) C. Tadhunter et al. 1993 MNRAS 263, 999; (Ta01) C. Tadhunter et al. 2001 MNRAS 327, 227; (Th90) D. Thompson et al. 1990 PASP 102, 1235; (Wh88) G. White et al. 1988 ApJ 327, 561; (Wi76) D. Wills & B. Wills 1976 ApJS 31, 143; (Wi83) B.J. Wilkes et al. 1983 PASA 5, 2; (Wi86) B.J. Wilkes 1986 MNRAS 218, 331; (Wi00) L. Wisotzki et al. 2000 A&A 358, 77; (Wr77) A. Wright et al. 1977 ApJ 211, L115; (Wr79) A. Wright et al. 1979 ApJ 229, 73; (Wr83) A. Wright et al. 1983 MNRAS 205, 793.

Table 2: The AT20G BSS: polarization data.

Seq. #	RA	δ	P_{20GHz} [Jy]	m_{20GHz} [%]	θ_{20GHz} [deg]	$P_{8.6GHz}$ [Jy]	$m_{8.6GHz}$ [%]	$\theta_{8.6GHz}$ [deg]	$P_{4.8GHz}$ [Jy]	$m_{4.8GHz}$ [%]	$\theta_{4.8GHz}$ [deg]
1	00:04:35.65	-47:36:19.1	0.017 0.003	1.7	-52	0.033 0.001	3.2	-45	0.025 0.001	2.8	-43
2	00:10:35.92	-30:27:48.3	0.040 0.003	4.1	10	0.016 0.001	2.0	-22	0.009 0.001	1.4	-37
3	00:11:01.27	-26:12:33.1	0.009 0.001	1.3	-36	0.009 0.003	1.0	-38	0.006 0.002	0.9	-1
4	00:12:59.89	-39:54:26.4	0.073 0.002	4.1	-89	0.078 0.002	3.3	-80	0.047 0.001	2.2	89
5	00:25:49.18	-26:02:12.7	0.012 0.002	0.9	26	<0.009 ...	...	...	0.038 0.003	0.8	27
6	00:26:16.40	-35:12:49.4	0.011 0.004	0.7	50	<0.004 ...	...	...	<0.003 ...	...	...
7	00:38:14.72	-24:59:01.9	0.017 0.002	1.3	87	<0.007 ...	...	...	0.008 0.001	1.0	28
8	00:49:59.48	-57:38:27.6	0.014 0.003	0.7	-22	0.069 0.001	2.8	-11	0.067 0.001	3.2	0
9	00:51:09.50	-42:26:32.5	0.029 0.003	1.8	-16	... ...	...	...	... ...	...	...
10	00:58:46.64	-56:59:11.4	0.012 0.003	1.3	-71	0.012 0.001	1.8	-81	0.003 0.001	0.5	52
11	01:02:15.07	-80:12:40.1	0.023 0.003	2.5	-33	0.014 0.001	2.0	-28	0.005 0.001	1.0	-80
12	01:02:18.65	-75:46:53.0	<0.008 ...	...	...	0.006 0.001	1.0	-19	<0.002 ...	...	...
13	01:06:45.11	-40:34:19.5	0.055 0.002	2.3	52	... ...	...	...	... ...	...	...
14	01:17:48.81	-21:11:07.4	0.013 0.002	1.3	43	0.022 0.002	2.5	49	0.022 0.002	2.3	57
15	01:18:57.30	-21:41:30.1	0.032 0.002	2.8	57	0.036 0.002	3.1	65	0.028 0.002	2.7	73
16	01:20:31.71	-27:01:24.6	0.036 0.001	5.1	-8	0.066 0.002	5.7	-2	0.071 0.002	5.7	0
17	01:24:57.37	-51:13:16.1	<0.008 ...	...	...	0.005 0.001	1.3	-70	0.006 0.001	2.5	-72
18	01:32:43.53	-16:54:48.2	0.090 0.002	3.9	34	0.064 0.002	3.3	39	0.024 0.002	1.3	48
19	01:33:05.77	-52:00:03.5	0.009 0.003	0.6	-80	0.019 0.001	1.2	64	0.045 0.001	3.1	75
20	01:33:57.6	-36:29:34.9	... ...	...	...	... ...	...	...	... ...	...	...
21	01:34:32.14	-38:43:33.7	<0.009 ...	...	...	0.010 0.001	1.6	84	0.008 0.001	1.6	-84
22	01:37:38.33	-24:30:53.6	0.010 0.001	0.8	-47	0.022 0.003	0.9	6	0.043 0.002	2.1	-15
23	01:43:10.13	-32:00:55.7	0.016 0.003	2.7	88	<0.004 ...	...	...	0.004 0.001	1.3	-27
24	01:45:03.39	-27:33:33.9	0.013 0.002	1.9	4	0.015 0.002	1.3	36	0.013 0.002	1.0	-28
25	01:53:10.19	-33:10:26.7	<0.010 ...	...	...	0.009 0.001	1.4	48	0.013 0.001	1.5	46
26	02:04:57.76	-17:01:20.1	0.064 0.002	2.3	-77	0.109 0.004	1.9	-59	0.042 0.002	2.3	-71
27	02:10:46.19	-51:01:01.4	0.050 0.002	1.4	-7	0.032 0.003	1.0	-21	0.039 0.001	1.2	-17
28	02:16:48.19	-32:47:40.6	0.022 0.003	3.6	86	0.005 0.001	0.8	-61	0.004 0.001	1.1	52
29	02:22:56.40	-34:41:27.7	0.016 0.003	1.2	-26	0.027 0.002	2.0	-5	0.036 0.001	2.8	-4
30	02:29:34.51	-78:47:44.0	0.028 0.003	2.4	59	0.012 0.001	1.4	50	0.012 0.001	1.6	44
31	02:31:11.77	-47:46:12.0	<0.006 ...	...	...	... ...	...	...	... ...	...	...
32	02:36:31.11	-29:53:55.1	0.011 0.002	1.2	-23	0.006 0.001	0.7	-70	<0.003 ...	...	...
33	02:36:53.27	-61:36:15.2	0.026 0.001	4.5	69	... ...	...	...	... ...	...	...
34	02:40:08.13	-23:09:15.8	0.030 0.002	2.7	-33	0.084 0.002	3.1	-31	0.116 0.001	3.4	-36
35	02:45:54.07	-44:59:39.5	<0.007 ...	...	...	0.013 0.001	2.0	-8	0.014 0.001	1.9	-3
36	02:53:29.20	-54:41:51.4	0.030 0.003	1.3	44	0.040 0.001	2.4	14	0.026 0.001	1.8	-2
37	03:03:50.64	-62:11:25.2	0.036 0.001	2.5	-70	... ...	...	...	... ...	...	...
38	03:09:56.12	-60:58:39.0	0.008 0.001	0.8	34	... ...	...	...	... ...	...	...
39	03:11:55.33	-76:51:51.2	0.026 0.002	1.6	71	... ...	...	...	0.015 0.001	1.6	-11
40	03:27:59.97	-22:02:06.3	0.011 0.001	1.9	49	0.018 0.001	2.3	47	0.025 0.001	3.5	48
41	03:29:54.10	-23:57:08.7	0.023 0.002	1.4	-62	0.025 0.002	1.3	22	0.007 0.001	0.4	37
42	03:34:13.62	-40:08:25.3	0.032 0.003	2.3	13	... ...	...	...	... ...	...	...
43	03:36:54.12	-36:16:06.0	0.005 0.002	0.5	16	0.008 0.001	1.3	8	0.007 0.001	1.3	43
44	03:40:35.65	-21:19:30.8	0.026 0.001	2.1	8	0.027 0.002	1.5	0	0.023 0.001	1.6	-14
45	03:48:38.11	-27:49:13.4	0.174 0.003	9.0	-77	0.088 0.002	4.0	-67	0.021 0.001	1.3	0
46	03:48:39.28	-16:10:17.2	0.043 0.002	3.5	-88	0.036 0.002	2.3	-88	0.014 0.001	1.4	47
47	03:49:57.82	-21:02:47.2	0.029 0.001	3.0	-67	0.028 0.003	1.7	-74	... ...	...	...
48	03:52:11.00	-25:14:50.2	0.013 0.001	2.0	9	<0.008 ...	...	...	0.007 0.001	1.3	47
49	04:03:53.77	-36:05:00.9	0.092 0.003	2.1	61	... ...	...	...	0.029 0.001	1.2	67
50	04:06:58.98	-38:26:27.5	0.056 0.002	4.3	14	0.037 0.001	2.2	3	0.025 0.001	1.7	-24
51	04:07:33.92	-33:03:45.3	0.012 0.002	1.8	85	0.006 0.002	0.8	-89	0.007 0.001	1.0	-86
52	04:08:48.75	-75:07:20.1	... ...	...	...	... ...	...	...	... ...	...	...
53	04:16:36.61	-18:51:08.9	0.019 0.002	1.9	-85	0.021 0.003	1.4	-69	0.005 0.001	0.8	-60
54	04:24:42.27	-37:56:21.0	0.019 0.003	0.9	-87	0.020 0.002	1.1	-71	0.020 0.001	1.3	87
55	04:28:40.37	-37:56:19.3	0.042 0.002	2.2	-46	0.070 0.001	3.8	-30	0.066 0.001	4.0	-30
56	04:37:01.51	-18:44:48.7	0.010 0.002	1.2	-37	<0.006 ...	...	...	<0.004 ...	...	...
57	04:37:36.56	-29:54:03.9	0.019 0.003	2.9	-66	0.011 0.001	1.5	-39	0.014 0.001	2.0	-46
58	04:39:00.83	-45:22:22.6	0.047 0.002	5.8	13	0.055 0.001	6.0	9	0.040 0.001	4.3	0

Table 2 – Continued

Seq. #	RA	δ	P_{20GHz} [Jy]	m_{20GHz} [%]	θ_{20GHz} [deg]	$P_{8.6GHz}$ [Jy]	$m_{8.6GHz}$ [%]	$\theta_{8.6GHz}$ [deg]	$P_{4.8GHz}$ [Jy]	$m_{4.8GHz}$ [%]	$\theta_{4.8GHz}$ [deg]
59	04:40:17.17	-43:33:08.4	0.046 0.002	2.3	4	0.073 0.002	2.4	8	0.056 0.001	1.5	-65
60	04:40:47.80	-69:52:16.6	0.025 0.004	3.5	-82	0.006 0.001	2.1	44	0.003 0.001	1.4	20
61	04:50:05.45	-81:01:02.2	... ...	...	...	... ...	...	...	... ...	...	...
62	04:53:14.64	-28:07:37.4	0.047 0.002	1.9	67	... ...	...	...	0.086 0.001	2.9	-82
63	04:55:50.79	-46:15:58.6	0.182 0.003	4.0	58	0.076 0.002	1.6	58	0.060 0.001	2.1	22
64	04:57:03.23	-23:24:51.8	0.091 0.003	2.1	-33	0.108 0.004	1.5	-30	0.052 0.002	1.1	-44
65	05:06:43.96	-61:09:41.0	0.020 0.001	1.1	-25	... ...	...	...	... ...	...	...
66	05:13:49.10	-21:59:17.4	0.077 0.001	6.2	-44	0.049 0.002	3.3	-56	0.009 0.001	0.7	-65
67	05:15:45.23	-45:56:43.2	0.074 0.003	4.4	16	0.035 0.001	2.3	3	0.023 0.001	1.7	19
68	05:16:44.98	-62:07:05.1	0.055 0.002	5.6	-22	... ...	...	...	... ...	...	...
69	05:19:49.7	-45:46:44.2	1.400 0.000	16.4	0	... ...	...	...	... ...	...	...
70	05:22:34.40	-61:07:57.0	0.018 0.002	2.9	47	0.016 0.001	2.6	65	0.019 0.001	3.1	82
71	05:22:57.94	-36:27:30.4	... ...	...	...	... ...	...	...	... ...	...	...
72	05:25:06.48	-23:38:11.1	0.004 0.002	0.3	63	<0.005 ...	...	...	<0.004 ...	...	...
73	05:29:30.02	-72:45:28.2	0.020 0.002	3.4	-27	... ...	...	...	... ...	...	...
74	05:36:28.45	-34:01:10.8	0.016 0.002	1.5	-85	0.007 0.001	0.8	-77	0.007 0.001	1.0	-80
75	05:38:50.35	-44:05:08.6	0.175 0.008	2.9	-44	0.122 0.004	2.3	-59	0.068 0.001	1.7	-44
76	05:39:54.17	-28:39:56.3	0.052 0.002	4.2	41	0.066 0.002	4.9	41	0.051 0.001	3.5	46
77	05:40:45.78	-54:18:21.7	0.034 0.002	2.8	27	0.019 0.001	1.8	20	0.012 0.001	1.8	63
78	05:50:09.55	-57:32:24.5	0.071 0.002	6.4	-9	0.055 0.001	5.3	-7	0.025 0.001	2.8	0
79	05:59:11.53	-45:29:40.4	0.008 0.002	1.1	-2	0.010 0.001	1.9	-70	0.012 0.001	3.4	-69
80	06:00:31.31	-39:37:01.7	0.018 0.002	2.8	-87	... ...	...	...	... ...	...	...
81	06:04:25.13	-42:25:30.1	0.042 0.002	7.2	-24	... ...	...	...	... ...	...	...
82	06:08:59.76	-22:20:21.3	0.009 0.001	0.8	-34	0.008 0.002	0.5	4	<0.004 ...	...	...
83	06:09:41.03	-15:42:41.6	0.221 0.005	4.5	21	0.201 0.009	3.3	43	0.103 0.005	2.4	45
84	06:20:29.31	-28:27:36.2	0.034 0.001	5.2	24	<0.006 ...	...	...	0.011 0.001	1.7	84
85	06:20:32.10	-25:15:17.9	0.053 0.001	5.1	-13	0.051 0.002	4.0	-19	0.033 0.001	2.7	-18
86	06:23:07.75	-64:36:20.7	0.005 0.001	0.4	7	... ...	...	...	... ...	...	...
87	06:27:06.73	-35:29:16.1	0.012 0.002	1.5	79	0.027 0.001	2.0	84	0.032 0.001	2.0	-84
88	06:29:23.76	-19:59:19.4	0.075 0.001	5.2	38	0.061 0.002	3.3	21	0.037 0.002	3.3	25
89	06:31:11.99	-41:54:27.1	0.004 0.001	0.7	-4	... ...	...	...	... ...	...	...
90	06:33:26.76	-22:23:22.6	0.020 0.001	2.7	-36	<0.006 ...	...	...	<0.004 ...	...	...
91	06:34:58.99	-23:35:12.6	0.046 0.002	3.9	38	0.027 0.002	1.8	63	0.012 0.001	1.1	86
92	06:35:46.33	-75:16:16.9	... ...	...	...	... ...	...	...	... ...	...	...
93	06:48:14.18	-30:44:19.3	0.020 0.002	2.1	-61	0.005 0.001	0.5	-61	0.004 0.001	0.5	82
94	06:48:28.53	-17:44:05.9	0.027 0.001	2.1	-33	0.074 0.004	3.4	-42	0.042 0.002	5.2	-28
95	06:50:24.60	-16:37:40.0	0.013 0.002	0.5	-25	0.027 0.003	0.5	-27	0.006 0.002	0.2	26
96	07:01:34.55	-46:34:36.9	0.025 0.003	2.1	83	... ...	...	...	... ...	...	...
97	07:31:06.67	-23:41:47.8	0.031 0.002	1.9	-30	0.044 0.002	2.1	6	0.050 0.001	3.1	47
98	07:41:45.20	-47:09:26.7	0.013 0.002	1.9	6	... ...	...	...	0.022 0.001	3.6	-28
99	07:43:20.60	-56:19:34.2	0.006 0.003	0.7	-58	0.004 0.001	0.6	71	<0.003 ...	...	...
100	07:43:31.60	-67:26:25.8	... ...	...	...	... ...	...	...	... ...	...	...
101	07:47:19.72	-33:10:46.6	0.026 0.002	2.2	40	... ...	...	...	... ...	...	...
102	07:48:03.09	-16:39:50.3	<0.005 ...	...	...	<0.006 ...	...	...	<0.004 ...	...	...
103	07:56:50.65	-15:42:04.7	0.013 0.002	1.2	45	0.032 0.002	2.0	-89	0.044 0.002	2.8	-75
104	08:04:51.44	-27:49:11.7	0.043 0.002	3.8	4	0.048 0.002	3.9	19	0.026 0.002	3.7	30
105	08:11:08.85	-49:29:43.6	0.019 0.002	2.8	-43	0.029 0.001	3.6	-64	<0.003 ...	...	...
106	08:16:40.41	-24:21:05.8	0.020 0.002	2.8	-28	<0.005 ...	...	...	0.012 0.001	2.9	-45
107	08:25:26.88	-50:10:39.0	<0.009 ...	...	...	0.031 0.002	1.6	1	0.055 0.001	1.6	86
108	08:26:01.60	-22:30:27.1	0.035 0.002	3.4	-2	0.060 0.001	4.7	18	0.047 0.001	4.4	59
109	08:35:29.08	-59:53:11.5	<0.008 ...	...	...	<0.004 ...	...	...	<0.003 ...	...	...
110	08:36:39.21	-20:16:58.9	0.026 0.002	0.9	23	0.031 0.002	0.6	77	0.034 0.002	0.8	56
111	08:37:00.39	-34:09:12.9	0.030 0.003	3.2	87	0.048 0.003	4.4	81	0.017 0.001	2.5	75
112	08:45:02.47	-54:58:08.8	0.064 0.003	6.1	18	0.095 0.002	8.0	18	0.068 0.001	7.5	34
113	08:49:45.66	-35:41:01.7	0.040 0.002	6.4	-85	0.034 0.002	5.4	-65	0.023 0.001	4.2	-57
114	08:58:05.38	-19:50:35.5	0.035 0.002	3.4	39	... ...	...	...	0.015 0.001	2.0	65
115	09:00:40.02	-28:08:22.8	0.129 0.002	9.9	52	... ...	...	...	0.016 0.002	0.7	-84
116	09:04:53.33	-57:35:04.4	0.095 0.005	5.2	63	0.055 0.001	4.5	-69	0.047 0.001	2.6	-71
117	09:06:51.25	-20:19:57.2	0.035 0.003	3.4	-23	0.023 0.002	2.4	-13	0.025 0.001	3.2	-46

Table 2 – Continued

Seq. #	RA	δ	P_{20GHz} [Jy]	m_{20GHz} [%]	θ_{20GHz} [deg]	$P_{8.6GHz}$ [Jy]	$m_{8.6GHz}$ [%]	$\theta_{8.6GHz}$ [deg]	$P_{4.8GHz}$ [Jy]	$m_{4.8GHz}$ [%]	$\theta_{4.8GHz}$ [deg]
118	09:19:44.06	-53:40:05.1	... ...	...	...	... ...	...	...	... ...	...	...
119	09:20:43.25	-29:56:30.6	0.008 0.002	1.0	43	<0.005 ...	...	...	0.003 0.001	0.6	-87
120	09:21:29.41	-26:18:44.2	0.100 0.002	4.2	18	0.162 0.003	4.0	7	0.103 0.002	2.9	1
121	09:22:46.44	-39:59:35.1	0.083 0.004	5.9	-87	... ...	...	...	... ...	...	...
122	09:27:51.90	-20:34:50.4	<0.010 ...	...	...	0.018 0.002	1.9	69	0.017 0.002	2.8	56
123	09:58:02.93	-57:57:42.7	<0.009 ...	...	...	<0.004 ...	...	...	<0.003 ...	...	...
124	10:01:59.89	-44:38:00.2	<0.010 ...	...	...	0.006 0.002	0.6	51	0.009 0.001	1.2	67
125	10:06:13.90	-50:18:13.7	0.011 0.003	0.9	-16	0.035 0.001	3.2	-43	0.031 0.001	3.0	-19
126	10:07:31.36	-33:33:06.6	0.012 0.002	1.5	-53	... ...	...	...	... ...	...	...
127	10:14:50.33	-45:08:41.2	0.015 0.003	2.2	-4	... ...	...	...	... ...	...	...
128	10:18:28.76	-31:23:53.3	0.019 0.004	2.5	60	0.009 0.002	0.9	-88	... ...	...	...
129	10:23:43.47	-66:46:47.8	0.015 0.001	2.6	-88	0.006 0.001	0.9	51	0.002 0.001	0.3	11
130	10:35:02.15	-20:11:34.4	0.008 0.002	0.6	-85	0.029 0.002	1.2	-58	0.029 0.001	1.5	-70
131	10:36:53.43	-37:44:15.2	<0.008 ...	...	...	<0.005 ...	...	...	0.003 0.001	0.8	-82
132	10:37:16.01	-29:34:02.8	0.075 0.002	2.0	76	0.161 0.002	4.9	63	0.118 0.002	5.0	47
133	10:38:40.56	-53:11:42.9	0.034 0.003	1.7	1	0.025 0.001	1.5	-55	0.019 0.001	1.3	19
134	10:41:44.61	-47:39:60.0	0.028 0.004	1.8	14	0.056 0.002	3.8	29	0.059 0.001	3.9	18
135	10:47:42.94	-62:17:14.2	0.087 0.003	3.4	38	0.037 0.001	1.6	-12	0.053 0.001	3.9	-18
136	10:48:06.58	-19:09:35.3	0.024 0.001	1.9	9	0.074 0.002	3.4	31	0.052 0.001	3.2	46
137	10:51:09.14	-53:44:46.2	0.025 0.003	2.5	-32	0.032 0.002	3.0	-26	0.049 0.001	3.6	-26
138	10:58:43.02	-80:03:53.7	... ...	...	...	... ...	...	...	... ...	...	...
139	11:01:54.42	-63:25:22.6	0.012 0.002	1.0	-84	0.011 0.001	1.2	-68	0.011 0.001	1.3	7
140	11:02:04.87	-44:04:22.6	0.010 0.001	1.3	-18	... ...	...	...	... ...	...	...
141	11:03:52.17	-53:57:00.8	0.007 0.003	1.0	-23	0.004 0.001	0.6	-5	0.004 0.001	0.6	28
142	11:04:46.06	-24:31:27.5	0.016 0.002	2.5	-73	0.008 0.002	0.7	-57	0.003 0.001	0.3	-77
143	11:07:08.73	-44:49:07.8	0.020 0.004	1.0	-42	... ...	...	...	... ...	...	...
144	11:07:12.85	-68:20:50.6	<0.006 ...	...	...	0.008 0.001	0.5	-4	0.002 0.001	0.2	54
145	11:12:07.16	-57:03:39.6	0.055 0.003	6.7	-80	0.069 0.001	6.7	-8	0.015 0.001	1.5	50
146	11:18:27.08	-46:34:15.3	0.039 0.005	3.3	-3	0.095 0.003	6.4	-1	0.179 0.003	8.4	-6
147	11:20:16.08	-27:19:08.1	0.024 0.002	2.7	-76	<0.008 ...	...	...	0.009 0.001	0.9	-52
148	11:27:04.36	-18:57:19.0	0.038 0.002	2.1	30	0.086 0.002	3.7	46	0.075 0.002	4.4	36
149	11:31:43.48	-58:18:53.4	0.006 0.003	0.5	-56	<0.006 ...	...	...	<0.005 ...	...	...
150	11:36:02.21	-68:27:05.4	0.028 0.002	4.6	64	0.031 0.001	3.7	55	0.026 0.001	3.0	33
151	11:45:53.58	-69:54:04.1	0.020 0.002	1.7	-82	<0.004 ...	...	...	0.002 0.001	0.4	-83
152	11:46:08.28	-24:47:34.1	0.103 0.003	5.4	-31	0.074 0.001	4.0	-29	0.060 0.001	2.9	-23
153	11:47:01.46	-38:12:10.7	0.027 0.003	1.8	20	0.011 0.002	0.9	41	0.007 0.002	0.6	-73
154	11:47:33.36	-67:53:41.5	0.035 0.002	1.6	-23	0.061 0.002	2.8	15	0.035 0.001	2.2	-36
155	11:52:53.67	-83:44:10.7	0.039 0.002	6.4	80	0.029 0.001	5.0	86	0.016 0.001	3.9	-90
156	11:54:21.79	-35:05:29.2	0.020 0.003	1.7	5	0.040 0.003	1.5	30	<0.005 ...	...	...
157	12:05:33.37	-26:34:04.9	... ...	...	...	... ...	...	...	... ...	...	...
158	12:09:02.64	-24:06:19.8	0.020 0.002	1.2	-50	0.010 0.004	0.4	-64	0.014 0.002	1.0	6
159	12:09:14.90	-20:32:38.8	0.003 0.002	0.0	0	<0.006 ...	...	...	<0.004 ...	...	...
160	12:15:46.88	-17:31:45.3	0.033 0.005	0.9	20	0.035 0.002	1.6	22	0.032 0.001	1.7	17
161	12:18:06.26	-46:00:30.3	0.081 0.003	9.5	-41	0.122 0.002	8.1	-48	... ...	...	...
162	12:27:26.74	-44:36:39.8	<0.009 ...	...	...	... ...	...	...	... ...	...	...
163	12:45:53.72	-16:16:44.5	0.074 0.003	5.9	47	0.079 0.004	5.7	21	0.038 0.002	5.0	13
164	12:46:46.78	-25:47:49.0	... ...	...	...	... ...	...	...	... ...	...	...
165	12:48:23.88	-19:59:18.4	... ...	...	...	... ...	...	...	... ...	...	...
166	12:48:28.53	-45:59:47.8	0.020 0.003	1.3	33	0.055 0.003	3.6	-70	0.054 0.002	3.2	-84
167	12:52:43.12	-67:37:38.6	... ...	...	...	... ...	...	...	... ...	...	...
168	12:54:37.24	-20:00:56.2	... ...	...	...	... ...	...	...	... ...	...	...
169	12:54:59.80	-71:38:18.4	... ...	...	...	... ...	...	...	... ...	...	...
170	12:57:59.20	-31:55:15.2	0.067 0.002	3.9	-76	0.147 0.002	5.8	-68	0.065 0.002	2.7	-75
171	12:58:38.27	-18:00:01.3	0.025 0.002	2.5	-15	0.009 0.003	0.8	-18	0.005 0.002	0.9	-12
172	12:58:54.52	-22:19:30.8	0.051 0.002	3.2	34	... ...	...	...	0.026 0.002	1.9	31
173	13:03:49.22	-55:40:31.5	... ...	...	...	... ...	...	...	... ...	...	...
174	13:05:27.47	-49:28:04.8	... ...	...	...	... ...	...	...	... ...	...	...
175	13:15:04.24	-53:34:36.0	... ...	...	...	... ...	...	...	... ...	...	...
176	13:16:08.09	-33:38:58.9	0.068 0.004	3.3	-31	0.052 0.002	3.2	-2	0.027 0.001	1.9	-11

Table 2 – Continued

Seq. #	RA	δ	P_{20GHz} [Jy]	m_{20GHz} [%]	θ_{20GHz} [deg]	$P_{8.6GHz}$ [Jy]	$m_{8.6GHz}$ [%]	$\theta_{8.6GHz}$ [deg]	$P_{4.8GHz}$ [Jy]	$m_{4.8GHz}$ [%]	$\theta_{4.8GHz}$ [deg]
177	13:21:12.81	-43:42:16.7	... ...	...	...	... ...	...	...	... ...	...	...
178	13:21:14.02	-26:36:10.2	... ...	...	...	... ...	...	...	... ...	...	...
179	13:25:27.7	-43:01:07.0	... ...	...	...	... ...	...	...	... ...	...	...
180	13:26:49.58	-52:55:35.6	0.025 0.003	0.9	-45	0.004 0.001	0.4	51	0.010 0.001	1.0	-35
181	13:29:01.13	-56:08:02.6	... ...	...	...	... ...	...	...	... ...	...	...
182	13:36:39.0	-33:57:58.2	... ...	...	...	... ...	...	...	... ...	...	...
183	13:37:52.37	-65:09:25.4	... ...	...	...	... ...	...	...	... ...	...	...
184	13:42:04.79	-20:51:29.0	0.042 0.002	6.3	48	0.028 0.002	3.1	54	<0.006 ...	...	...
185	13:46:48.95	-60:24:29.1	... ...	...	...	... ...	...	...	... ...	...	...
186	13:57:11.27	-15:27:29.5	0.007 0.002	0.9	48	<0.007 ...	...	...	0.013 0.002	1.1	-8
187	14:09:50.13	-26:57:37.3	0.018 0.001	1.8	13	0.021 0.003	1.0	8	0.030 0.004	1.7	-45
188	14:18:58.88	-35:09:42.9	... ...	...	...	... ...	...	...	... ...	...	...
189	14:19:35.22	-51:54:58.8	... ...	...	...	... ...	...	...	... ...	...	...
190	14:24:32.24	-49:13:49.3	... ...	...	...	... ...	...	...	... ...	...	...
191	14:24:55.56	-68:07:57.8	... ...	...	...	... ...	...	...	... ...	...	...
192	14:27:41.31	-33:05:31.9	... ...	...	...	... ...	...	...	... ...	...	...
193	14:27:56.30	-42:06:18.9	... ...	...	...	... ...	...	...	... ...	...	...
194	14:33:21.45	-15:48:45.0	... ...	...	...	... ...	...	...	... ...	...	...
195	14:38:09.46	-22:04:54.6	0.009 0.001	1.1	-46	... ...	...	...	... ...	...	...
196	14:54:27.46	-37:47:33.1	... ...	...	...	... ...	...	...	... ...	...	...
197	14:54:32.92	-40:12:32.6	... ...	...	...	... ...	...	...	... ...	...	...
198	14:57:26.70	-35:39:10.8	... ...	...	...	... ...	...	...	... ...	...	...
199	15:07:04.78	-16:52:30.3	... ...	...	...	... ...	...	...	... ...	...	...
200	15:08:38.98	-49:53:01.8	... ...	...	...	... ...	...	...	... ...	...	...
201	15:13:57.01	-21:14:57.7	0.039 0.003	4.5	-54	... ...	...	...	<0.027 ...	...	...
202	15:14:40.05	-47:48:28.7	... ...	...	...	... ...	...	...	... ...	...	...
203	15:17:41.76	-24:22:20.3	0.137 0.003	3.0	54	0.248 0.005	4.9	44	0.173 0.008	4.8	36
204	15:22:37.72	-27:30:11.1	0.109 0.002	7.6	-33	0.104 0.002	5.4	-27	0.043 0.003	3.1	-24
205	15:34:20.63	-53:51:12.7	... ...	...	...	... ...	...	...	... ...	...	...
206	15:34:54.68	-35:26:23.8	... ...	...	...	... ...	...	...	... ...	...	...
207	15:35:52.23	-47:30:21.8	... ...	...	...	... ...	...	...	... ...	...	...
208	15:46:44.51	-68:37:28.9	0.013 0.002	2.1	-13	... ...	...	...	... ...	...	...
209	15:50:58.66	-82:58:06.9	... ...	...	...	... ...	...	...	... ...	...	...
210	15:54:02.44	-27:04:39.8	0.016 0.002	1.7	-54	0.036 0.002	2.5	-45	<0.012 ...	...	...
211	15:56:58.72	-79:14:04.9	<0.006 ...	...	...	0.009 0.003	0.2	-9	<0.004 ...	...	...
212	15:59:41.26	-24:42:40.2	0.032 0.002	2.8	-70	<0.006 ...	...	...	0.003 0.001	0.5	71
213	16:00:19.56	-46:49:08.0	0.046 0.002	7.7	-61	... ...	...	...	... ...	...	...
214	16:03:50.67	-49:04:05.1	<0.007 ...	...	...	... ...	...	...	... ...	...	...
215	16:04:31.09	-44:41:31.3	0.060 0.002	3.8	-27	0.086 0.002	5.2	-16	0.076 0.002	4.7	-12
216	16:15:05.2	-60:54:25.5	0.169 0.000	4.4	0	... ...	...	...	... ...	...	...
217	16:17:17.96	-58:48:06.1	0.073 0.004	2.4	87	0.092 0.001	2.1	-75	0.127 0.001	2.8	-61
218	16:17:49.22	-77:17:18.5	0.033 0.002	1.4	47	0.138 0.004	1.9	59	0.133 0.002	2.5	81
219	16:24:18.59	-68:09:11.7	<0.006 ...	...	...	... ...	...	...	... ...	...	...
220	16:25:46.99	-25:27:39.3	0.060 0.002	2.3	-70	... ...	...	...	... ...	...	...
221	16:26:06.04	-29:51:26.6	0.098 0.003	4.8	17	... ...	...	...	... ...	...	...
222	16:36:55.26	-41:02:00.7	0.006 0.002	0.0	0	... ...	...	...	... ...	...	...
223	16:47:37.79	-64:38:01.0	0.131 0.003	13.8	44	... ...	...	...	... ...	...	...
224	16:48:42.34	-33:01:47.7	<0.018 ...	...	...	0.012 0.003	0.8	2	0.013 0.002	2.1	39
225	16:50:16.49	-50:44:46.2	0.103 0.005	4.7	-60	0.071 0.002	2.7	-75	0.062 0.002	2.7	81
226	16:50:39.55	-29:43:47.0	... ...	...	...	... ...	...	...	... ...	...	...
227	17:00:53.27	-26:10:52.6	0.009 0.002	1.4	-17	... ...	...	...	... ...	...	...
228	17:01:44.84	-56:21:55.6	... ...	...	...	... ...	...	...	... ...	...	...
229	17:03:36.34	-62:12:38.2	0.005 0.002	0.4	-55	0.018 0.001	1.6	-32	0.012 0.001	1.2	-12
230	17:09:18.61	-35:25:21.0	0.140 0.006	10.6	-41	0.063 0.006	3.1	-53	... ...	...	...
231	17:09:34.40	-17:28:52.7	0.107 0.002	12.7	-36	... ...	...	...	... ...	...	...
232	17:13:10.02	-34:18:27.7	0.075 0.004	4.6	86	0.152 0.006	5.8	64	0.057 0.002	3.9	43
233	17:13:31.21	-26:58:53.4	0.035 0.002	2.3	26	... ...	...	...	... ...	...	...
234	17:13:50.99	-32:26:08.9	0.025 0.003	2.8	43	0.049 0.003	3.4	38	0.062 0.002	3.2	15
235	17:17:36.21	-33:42:06.6	0.009 0.004	0.9	-39	0.026 0.004	3.5	-52	0.029 0.003	4.5	82

Table 2 – Continued

Seq. #	RA	δ	P_{20GHz} [Jy]	m_{20GHz} [%]	θ_{20GHz} [deg]	$P_{8.6GHz}$ [Jy]	$m_{8.6GHz}$ [%]	$\theta_{8.6GHz}$ [deg]	$P_{4.8GHz}$ [Jy]	$m_{4.8GHz}$ [%]	$\theta_{4.8GHz}$ [deg]
236	17:23:41.10	-65:00:36.3	<0.006 ...	...	...	... ...	...	...	... ...	...	...
237	17:33:15.32	-37:22:30.6	<0.014 ...	...	...	$0.064_{0.009}$	0.0	0	$0.034_{0.004}$	2.3	68
238	17:33:40.43	-79:35:55.7	... ...	...	...	... ...	...	...	... ...	...	...
239	17:44:25.25	-51:44:45.2	<0.012 ...	...	...	<0.004 ...	...	...	<0.003 ...	...	...
240	18:02:42.66	-39:40:07.8	... ...	...	...	... ...	...	...	... ...	...	...
241	18:03:23.56	-65:07:36.8	$0.003_{0.001}$	0.2	-3	... ...	...	...	... ...	...	...
242	18:09:57.79	-45:52:41.2	<0.015 ...	...	...	... ...	...	...	... ...	...	...
243	18:19:34.98	-63:45:48.2	... ...	...	...	... ...	...	...	... ...	...	...
244	18:19:45.29	-55:21:21.8	$0.031_{0.004}$	1.9	-50	$0.075_{0.003}$	2.9	-38	$0.064_{0.002}$	2.5	-31
245	18:20:57.84	-25:28:12.4	... ...	...	...	... ...	...	...	... ...	...	...
246	18:29:12.57	-58:13:54.9	<0.013 ...	...	...	$0.022_{0.002}$	1.7	51	$0.016_{0.001}$	1.5	53
247	18:32:11.13	-20:39:48.3	$0.098_{0.002}$	8.5	-57	... ...	...	...	... ...	...	...
248	18:33:39.95	-21:03:41.2	$0.110_{0.004}$	1.5	47	... ...	...	...	... ...	...	...
249	18:34:27.29	-58:56:36.7	$0.118_{0.004}$	7.4	-68	$0.123_{0.002}$	6.1	-62	$0.060_{0.002}$	4.2	-47
250	18:37:28.74	-71:08:43.0	$0.009_{0.004}$	0.3	-69	$0.034_{0.002}$	1.5	-81	$0.031_{0.001}$	1.3	-65
251	19:03:01.33	-67:49:35.5	$0.028_{0.001}$	5.1	15	... ...	...	...	... ...	...	...
252	19:11:09.71	-20:06:55.7	... ...	...	...	... ...	...	...	... ...	...	...
253	19:12:40.38	-80:10:07.0	$0.011_{0.004}$	0.6	17	... ...	...	...	... ...	...	...
254	19:23:32.27	-21:04:33.4	$0.079_{0.003}$	2.0	-61	$0.103_{0.004}$	1.3	-57	$0.053_{0.002}$	1.3	-66
255	19:24:51.04	-29:14:30.2	$0.148_{0.006}$	1.0	-45	... ...	...	...	$1.329_{0.009}$	2.8	45
256	19:30:06.08	-60:56:08.9	$0.023_{0.001}$	3.2	29	... ...	...	...	... ...	...	...
257	19:32:44.95	-45:36:38.3	$0.017_{0.004}$	3.0	3	... ...	...	...	... ...	...	...
258	19:35:57.62	-46:20:43.8	$0.017_{0.004}$	2.7	55	... ...	...	...	... ...	...	...
259	19:37:16.22	-39:58:01.6	$0.083_{0.002}$	4.1	87	... ...	...	...	... ...	...	...
260	19:39:24.83	-63:42:45.4	<0.007 ...	...	...	<0.004 ...	...	...	<0.004 ...	...	...
261	19:39:26.74	-15:25:43.3	... ...	...	...	... ...	...	...	... ...	...	...
262	19:40:25.74	-69:07:58.0	$0.014_{0.002}$	2.3	42	$0.006_{0.001}$	0.7	84	$0.015_{0.001}$	1.6	59
263	19:45:24.09	-55:20:49.0	<0.009 ...	...	...	<0.004 ...	...	...	<0.003 ...	...	...
264	19:56:59.41	-32:25:46.0	$0.007_{0.002}$	0.6	42	$0.026_{0.002}$	2.3	19	$0.019_{0.002}$	1.8	-10
265	19:57:59.83	-38:45:06.8	$0.117_{0.009}$	2.8	-5	... ...	...	...	... ...	...	...
266	20:00:57.08	-17:48:57.4	... ...	...	...	... ...	...	...	... ...	...	...
267	20:03:24.04	-32:51:42.4	<0.014 ...	...	...	... ...	...	...	... ...	...	...
268	20:05:17.30	-18:22:03.1	... ...	...	...	... ...	...	...	... ...	...	...
269	20:05:55.03	-37:23:39.7	<0.014 ...	...	...	... ...	...	...	... ...	...	...
270	20:09:25.45	-48:49:53.9	$0.010_{0.003}$	1.0	-54	... ...	...	...	... ...	...	...
271	20:11:15.70	-15:46:40.2	... ...	...	...	... ...	...	...	... ...	...	...
272	20:24:35.58	-32:53:35.6	... ...	...	...	... ...	...	...	... ...	...	...
273	20:56:16.40	-47:14:47.9	$0.009_{0.002}$	1.3	-78	... ...	...	...	... ...	...	...
274	20:57:41.64	-37:34:02.3	$0.035_{0.004}$	3.9	-67	... ...	...	...	... ...	...	...
275	21:05:44.98	-78:25:35.0	$0.011_{0.003}$	1.1	-40	$0.016_{0.001}$	1.6	29	$0.006_{0.001}$	0.8	26
276	21:09:33.10	-41:10:20.5	$0.150_{0.003}$	8.6	-54	... ...	...	...	... ...	...	...
277	21:21:13.19	-37:03:08.9	$0.010_{0.004}$	1.0	36	$0.007_{0.002}$	0.8	33	<0.005 ...	...	...
278	21:26:30.69	-46:05:48.2	<0.006 ...	...	...	<0.005 ...	...	...	$0.028_{0.002}$	4.0	-2
279	21:29:12.19	-15:38:40.9	... ...	...	...	... ...	...	...	... ...	...	...
280	21:42:31.00	-24:44:39.1	... ...	...	...	... ...	...	...	... ...	...	...
281	21:46:29.73	-77:55:54.9	$0.046_{0.003}$	3.0	-52	$0.004_{0.002}$	0.3	-61	$0.004_{0.001}$	0.6	-36
282	21:51:21.94	-27:42:23.4	... ...	...	...	... ...	...	...	... ...	...	...
283	21:51:55.58	-30:27:53.8	$0.023_{0.006}$	1.1	49	... ...	...	...	... ...	...	...
284	21:57:06.07	-69:41:23.2	$0.087_{0.000}$	1.6	0	... ...	...	...	... ...	...	...
285	21:58:06.28	-15:01:09.3	... ...	...	...	... ...	...	...	... ...	...	...
286	22:00:54.69	-55:20:08.2	<0.007 ...	...	...	<0.005 ...	...	...	$0.005_{0.001}$	2.2	-34
287	22:02:56.11	-23:35:11.1	$0.033_{0.003}$	2.4	-63	... ...	...	...	... ...	...	...
288	22:06:10.60	-18:35:39.5	$0.235_{0.005}$	3.9	43	... ...	...	...	... ...	...	...
289	22:07:43.82	-53:46:34.1	$0.060_{0.002}$	4.5	-13	$0.059_{0.002}$	4.1	-35	$0.067_{0.001}$	3.9	-47
290	22:13:02.60	-25:29:30.7	$0.020_{0.002}$	1.6	-30	... ...	...	...	... ...	...	...
291	22:29:00.22	-69:10:29.7	$0.003_{0.001}$	0.5	3	... ...	...	...	... ...	...	...
292	22:30:40.34	-39:42:51.8	... ...	...	...	... ...	...	...	... ...	...	...
293	22:35:13.28	-48:35:58.7	$0.018_{0.003}$	0.8	-76	... ...	...	...	$0.007_{0.001}$	0.6	-35
294	22:39:12.11	-57:01:01.1	$0.029_{0.003}$	2.7	2	$0.026_{0.002}$	2.1	-17	$0.030_{0.001}$	3.3	-6

Table 2 – Continued

Seq. #	RA	δ	P_{20GHz} [Jy]	m_{20GHz} [%]	θ_{20GHz} [deg]	P_{8.6GHz} [Jy]	m_{8.6GHz} [%]	θ_{8.6GHz} [deg]	P_{4.8GHz} [Jy]	m_{4.8GHz} [%]	θ_{4.8GHz} [deg]
295	22:43:26.47	-25:44:31.4	0.032 0.002	3.9	-54	... ...	...	...	... ...	...	...
296	22:46:16.77	-56:07:46.1	0.068 0.003	5.4	59	0.012 0.001	1.3	46	0.007 0.001	1.2	-71
297	22:47:03.81	-36:57:46.5	0.005 0.002	0.4	-13	0.013 0.001	1.1	13	0.012 0.001	1.1	68
298	22:48:38.67	-32:35:52.5	0.013 0.002	0.8	-69	0.036 0.002	2.2	-82	0.014 0.001	1.3	88
299	22:50:44.51	-28:06:40.0	0.043 0.001	7.8	-44	... ...	...	...	... ...	...	...
300	22:56:41.26	-20:11:41.3	0.031 0.002	2.2	78	... ...	...	...	... ...	...	...
301	22:57:10.50	-36:27:44.6	... ...	...	...	... ...	...	...	... ...	...	...
302	22:58:05.97	-27:58:21.7	0.029 0.002	1.3	-67	... ...	...	...	... ...	...	...
303	23:03:03.02	-18:41:26.1	... ...	...	...	... ...	...	...	... ...	...	...
304	23:03:43.46	-68:07:37.7	0.030 0.001	3.0	64	... ...	...	...	... ...	...	...
305	23:14:48.56	-31:38:38.6	<0.009 ...	...	...	0.015 0.003	1.6	80	0.019 0.001	3.1	82
306	23:15:44.24	-50:18:39.0	0.055 0.003	6.4	35	0.051 0.001	6.6	32	0.033 0.001	4.9	37
307	23:29:17.66	-47:30:19.2	0.045 0.002	2.9	-49	0.034 0.002	1.4	-43	0.094 0.001	3.9	-39
308	23:31:38.69	-15:56:57.0	... ...	...	...	... ...	...	...	... ...	...	...
309	23:31:59.43	-38:11:47.4	0.021 0.004	3.5	40	0.020 0.002	2.3	59	0.009 0.001	1.4	-88
310	23:33:55.28	-23:43:40.8	... ...	...	...	... ...	...	...	... ...	...	...
311	23:34:44.88	-52:51:19.4	0.008 0.003	0.8	8	0.012 0.001	1.3	-62	0.005 0.001	0.8	75
312	23:36:12.05	-52:36:22.1	0.030 0.002	2.5	49	0.004 0.001	0.2	-86	0.002 0.001	0.1	-59
313	23:45:12.47	-15:55:08.0	... ...	...	...	... ...	...	...	... ...	...	...
314	23:48:02.63	-16:31:12.0	0.021 0.002	0.8	10	... ...	...	...	0.054 0.002	1.4	1
315	23:54:30.18	-15:13:11.3	... ...	...	...	... ...	...	...	... ...	...	...
316	23:56:00.67	-68:20:03.6	<0.006 ...	...	...	... ...	...	...	... ...	...	...
317	23:57:53.41	-53:11:12.5	<0.009 ...	...	...	0.027 0.001	1.8	-13	0.038 0.001	2.8	-20
318	23:58:02.13	-45:55:18.8	0.005 0.002	0.8	85	... ...	...	...	... ...	...	...
319	23:59:04.7	-60:55:01.1	0.053 0.000	1.7	0	... ...	...	...	... ...	...	...
320	23:59:35.41	-31:33:44.9	<0.007 ...	...	...	0.006 0.001	0.7	50	0.014 0.001	1.5	-55

1.1 The AT20G BSS: individual sources notes

Source 61 : PKS 0454−81 appears in the scan maps, but the follow-up data were degraded by bad weather and we didn't have the opportunity to re-observe it. For this source we obtained a flux density measurement from its observations as a secondary calibrator in October 2006.

Source 92 (PKS 0637-752) is a quasar with an asymmetric jet seen in radio and Xray images (Schwartz et al. 2000). The tabulated flux density is dominated by the core with about 10 per cent in the 15 arcsec jet. It is one of the largest (100 kpc) and most luminous jets known.

Source 109 (PMN J0835−5953) has a highly inverted radio spectra, with spectral index $\alpha_5^{20} = +0.88$, but has no obvious optical counterpart. Although the Galactic latitude is relatively low ($b = 11°$), the optical extinction is only 1.1 mag in the B band. The lack of optical ID suggests this could be a distant radio galaxy rather than a QSO.

Source 151 (PKS 1143−696) is a resolved double in the SUMSS image, and is also double in the 20 GHz image. The SUMSS source is larger than the ATCA beam at 20 GHz, suggesting that the measured flux density may be a lower limit to the true value. The position of the low-frequency radio centroid is slightly different from the AT20G position.

Source 211 (PKS 1548−79) is a relatively nearby ($z = 0.15$) galaxy with an unresolved radio source which has a steep spectrum in our 5, 8 and 20 GHz data. The galaxy

has strong optical emission lines, and has been studied in detail by Tadhunter et al. (2001).

Source 221 appears to be one component of a source (PKS 1622−29) which is double (component separation ∼ 1.5 arcmin) in the NVSS image. Both components fall within the ATCA 5 GHz beam, but the 20 GHz image is centred on the eastern component and the other component falls outside the primary beam. Our measured 20 GHz flux density is therefore an underestimation of the total flux density.

Source 258 The AT20G source (corresponding to PKS 1932−46) is flagged as extended, and the image appears to show a compact double. The source is a 30 arcsec double at 5 GHz (Duncan & Sproats 1992). The optical position given in NED is associated with a $z = 0.231$ galaxy at (J2000) 19:35:56.5 −46:20:41, which is offset by 3.2 arcsec from the AT20G position but appears to be the correct ID.

Source 273 (PKS 2052−47) is a $z = 1.5$ QSO which is also detected as both an X–ray and a gamma–ray source. Since this source is an ATCA calibrator, its flux density has been monitored at several epochs during 2002–7. The calibrator data suggest that our AT20G observation of this object in October 2004 took place during the declining stage of a flaring phase, during which the flux density of the source changed rapidly. This fast change in flux and polarisation properties is clearly visible in our data, with the 20 GHz flux density decreasing by a factor of 2.5 in two days. This makes it difficult to give a reliable value for the flux density and fractional polarisation of this source.

Source 292 (PKS 2227−3952) is a resolved triple in the SUMSS image. The low-frequency emission extends somewhat beyond the 20 GHz ATCA beam, but the source is not flagged as extended here, since the 20 GHz flux is dominated by the core.

Source 310, flagged as extended, appears to be the core of a well known and highly-extended radio galaxy PKS 2331−240. The optical ID is a galaxy at z=0.0477. The extended flux is well outside of the primary beam used for these observations and the flux densities listed correspond mainly to the core.

Source 319 (PKS 2356−61) is a FRII galaxy characterized by four bright regions of emissions that are slightly asymmetric about the core (Burke et al.).

2   The New Extragalactic WMAP Point Source 5-year catalogue: source list

The content of the columns for the NEWPS_5yr catalogue are as follows.

- (1) Sequential number.

- (2–3) Right ascension and declination (J2000).

- (4–5) Galactic longitude and latitude.

- (6–9) Flux density at 23, 33, 41, 61 GHz in mJy.

- (10–13) Errors on flux density at 23, 33, 41, 61 GHz in mJy.

- (14–17) Ratio between the value of the noise map in the position of the source (σ_{pixel}) and the σ_{median} (see 1 4.4). The present catalogue is result of a selection for $r = \sigma_{\mathrm{pixel}}/\sigma_{\mathrm{median}} < 1.5$.

- (18) Flag column where we collected some flags in the following order:

  - four flags for blind 'B' and non-blind 'N' detections at 23, 33, 41, 61 GHz respectively.

  - 'L' for sources within 5 degrees from the Large Magellanic Cloud (RA=5.3929 δ=-69.7561)

  - 'W' for objects within a beam unit (at 23 GHz 21.35 arcmin)from a WMAP_5yr source

  - object identification: 'e' for extragalactic, 'g' for galactic, 'u' for not clearly identified objects.

- (19) Redshift obtained from the NED database.

- (20) Identification in well–known catalogues.

2.1 The NEWPS catalogue: individual sources notes

 # 76 : The source is in the region of Fornax A that probably contributes to the detected flux density.

 # 79, 83, 86, 88 and 90 : The detections are in the region of the California Nebula and are probably part of its structure. Except for the #90, that is within a beam unit from the center of the Nebula, the other detections have been classified as "unidentified".

 # 274 : The source is in the region of Virgo A that probably contributes to the detected flux density.

Table 3: The NEWPS.5yr catalogue.

#	RA	δ	l	b	S_{23}	S_{33}	S_{41}	S_{61}	σ_{23}	σ_{33}	σ_{41}	σ_{61}	r_{23}	r_{33}	r_{41}	r_{61}	flags	z	Id.
1	0.0652	68.6173	118.6020	6.1460	947	967	.	2141	159	174	.	250	.	.	.	1.35	...BG..u	.	...
2	0.0706	-47.6401	324.0430	-67.5070	2523	2672	2604	2328	170	224	200	257	0.95	1.04	1.01	1.02	BN...We	.	PKS 0002-478
3	0.1029	-6.3719	93.4960	-66.6210	1253	1235	1274	.	163	217	198	.	0.98	1.03	1.02	.	BBBB..We	0.3470	PKS 0003-066
4	0.1777	11.0522	107.0640	-50.5590	1182	1385	970	1144	153	190	185	227	0.91	0.92	0.94	0.95	BBBN..We	0.0893	PKS J0010+1058
5	0.2155	-39.9448	332.4160	-74.9010	974	.	.	.	165	.	.	.	0.98	.	.	.	B....We	.	PKS 0010-401
6	0.3252	20.2997	112.8470	-41.9460	1140	.	.	.	163	.	.	.	0.97	.	.	.	B....We	0.2840	PKS 0017+200
7	0.3278	26.0203	114.0680	-36.3040	.	.	.	.	.	.	.	.	.	.	.	.	N.....e	1.7810	PKS J0019+2602
8	0.3286	73.5179	120.6480	10.7870	.	1469	.	.	.	254	.	.	.	1.33	.	.	.N...e	0.3220	GB6 J0019+7327
9	0.4348	-26.1011	41.7750	-84.2420	904	.	.	1443	157	.	.	238	0.94	.	.	0.95	B....We	.	PKS 0023-26
10	0.4401	-35.1350	335.1410	-80.3720	1299	1190	1505	.	153	190	185	.	0.92	0.95	0.94	.	BBBB..We	1.3170	PMN J0026-3512
11	0.4910	5.9198	112.9880	-56.5270	1210	1427	.	.	163	217	.	.	0.97	1.05	.	.	BB....We	0.2196	PKS 0027+056
12	0.6349	-2.1247	115.0860	-64.7930	.	.	937	1184	.	.	185	236	.	.	1.02	0.95	.N...e	1.1960	PKS J0038-0207
13	0.6410	-24.9722	68.7030	-86.3750	.	.	.	.	.	.	.	.	.	.	.	.	.B...We	1.1410	PKS J0038-2459
14	0.6925	57.1919	121.5860	-5.6540	935	.	1164	.	166	.	184	.	0.99	.	0.94	.	B...G.e	0.1740	GB6 J0042+5708
15	0.7225	52.0529	121.6660	-10.7990	888	.	1353	1177	166	.	173	221	0.99	.	0.88	0.89	B....We	0.0008	GB6 J0043+5203
16	0.7947	-25.2878	98.1300	-87.9760	1097	985	1061	1248	157	193	168	212	0.93	0.94	0.86	0.85	BBBB..We	.	PKS 0045-25
17	0.8291	-73.1107	303.1030	-44.0170	1882	1728	.	.	174	202	.	.	1.03	0.98	.	.	BBBB...g	1.7970	PKS 0046-734
18	0.8320	-57.5991	303.3330	-59.5280	1583	1418	.	.	153	185	.	.	0.91	0.91	.	.	BBBB..We	1.7490	PKS 0047-579
19	0.8493	-42.3519	303.2690	-74.7760	912	975	.	.	151	184	.	.	0.90	0.92	.	.	BN...We	1.9750	PKS 0048-427
20	0.8544	-8.3937	122.8070	-69.7110	1133	.	.	.	176	.	.	.	1.06	.	.	.	B....We	0.5370	PKS 0048-071
21	0.8552	-9.4743	122.8290	-72.3460	1023	1091	.	.	176	212	.	.	1.04	1.07	.	.	BN...We	.	PKS 0048-09
22	0.8755	56.6334	123.0830	-6.2380	.	.	8903	5994	.	.	236	288	.	.	1.16	1.19	.BBG..g	.	NGC 0281
23	0.9579	30.3067	124.4770	-32.5470	919	1122	1130	.	176	215	209	.	1.04	1.04	1.07	.	BBB...g	0.0164	GB6 J0057+3021
24	0.9595	-1.3762	126.4550	-64.2060	.	.	.	.	.	.	.	.	.	.	.	.	.B...We	0.0450	PKS 0055-01
25	0.9842	-57.0436	300.8580	-60.0540	.	.	853	2121	.	.	168	226	.	.	0.86	.	B.B..We	0.0180	PKS 0056-572
26	1.0094	-72.1988	301.9470	-44.9120	2160	1588	1156	1518	174	202	173	261	1.03	0.98	0.88	0.91	BBBB..We	.	PKS 0057-724
27	1.1082	-40.5591	290.8510	-76.2140	2412	2629	2257	.	154	189	175	.	0.91	0.92	0.91	1.05	BBBB..We	0.5840	PKS 0104-408
28	1.1411	1.5814	131.7350	-60.9990	1956	1817	1841	.	173	222	206	.	1.03	1.08	1.05	.	BBB...We	2.0990	PKS 0106+01
29	1.1478	13.3392	129.4440	-49.3120	1474	1160	.	1452	179	223	.	256	1.06	1.08	.	1.03	BB....We	0.0597	PKS J0108+1320
30	1.2569	-1.3837	136.5220	-63.6210	1528	1175	1197	.	166	218	193	.	0.99	1.06	0.99	.	B....We	1.3650	PKS J0115-0127
31	1.2705	-11.5351	144.6040	-73.3550	839	1171	.	.	160	194	.	.	0.98	0.94	.	.	.B...e	0.6700	PKS 0113-118
32	1.3131	-21.5196	213.2800	-81.6210	788	.	.	.	152	.	.	.	0.92	.	.	.	B....e	1.1610	PKS 0116-219
33	1.3434	-26.9793	213.3800	-53.5050	1182	.	1133	.	174	.	212	.	1.04	.	1.08	.	BBB...We	0.5590	PKS 0118-272
34	1.3623	11.8058	134.6050	-50.3780	879	1181	.	1421	173	221	.	243	1.03	1.07	.	.	BB....We	0.5700	PKS 0119+11
35	1.3651	4.3836	137.2280	-57.6400	921	.	.	.	183	.	.	.	1.09	.	.	.	B......e	0.6370	PKS 0119+041
36	1.3724	25.0790	131.7330	-37.2640	1213	.	.	.	186	.	.	.	1.08	.	.	.	B......e	2.0250	PKS 0119+247
37	1.4234	-0.1526	141.1510	-61.8170	.	.	.	.	.	.	.	.	.	.	.	.	N....We	1.0765	PKS 0122-00
38	1.5427	-16.9582	168.1250	-76.0770	1908	1699	1835	.	166	194	193	.	0.99	0.95	0.98	0.99	BBBB..We	1.0200	PKS 0130-17
39	1.5466	-51.9512	288.3220	-63.9880	852	1241	.	.	142	181	.	.	0.85	0.85	.	.	BB....We	0.0200	PKS 0131-522
40	1.5580	-36.4433	261.7980	-77.1100	788	.	.	.	152	.	.	.	0.91	.	.	.	B....We	.	PMN J0133-3629
41	1.6138	47.9132	130.7530	-74.2680	3898	3756	3331	2631	208	222	203	288	1.24	1.08	1.04	1.15	BBBB..We	0.8590	GB6 J0136+4751
42	1.6295	-24.5600	201.6700	-79.2690	1408	1379	1967	1692	155	199	185	239	0.92	0.97	0.96	0.97	BBBB..We	0.8370	PKS 0135-247
43	1.8264	5.8719	148.1520	-54.1280	959	.	995	.	168	.	189	.	1.00	.	1.06	.	B.N..We	2.3450	PKS 0146+056

Table 3 – Continued

#	RA	δ	l	b	S_{23}	S_{33}	S_{41}	S_{61}	σ_{23}	σ_{33}	σ_{41}	σ_{61}	r_{23}	r_{33}	r_{41}	r_{61}	flags	z	Id.
44	1.8786	22.1612	141.1590	-38.5320	1218	1498	1353		183	232	224		1.13	1.12	1.14		BBB...We	1.3200	PKS 0149+21
45	2.0871	15.1755	148.0830	-44.0630	1238	1288	1212	1500	187	224	202	281	1.11	1.09	1.03	1.12	BBBB...We	0.4050	PKS 0202+14
46	2.0882	-17.0788	186.2610	-70.1980	923		1053		155		167		0.90		0.89		B.B..We	1.7400	PKS 0202-17
47	2.0890	32.1895	140.6360	-28.1290	1637	1645	1124	2250	183	232	224	210	1.09	1.12	1.14	0.82	BBB...We	1.4660	GB6 J0205+3212
48	2.1750	-51.0021	276.1510	-61.8170	2940	2823	2906		145	173	164		0.11	0.88	0.83		NNNB..We	0.9990	PKS 0208-512
49	2.2809	-8.3080	173.9470	-62.3840			976				188				0.97		B....e	0.6065	PKS 0214-085
50	2.3018	1.6310	162.3560	-54.4680	1056				155				0.92				.....We	1.7150	PKS 0215+015
51	2.3038	73.8375	128.9710	11.9920	2353	1788	1639	1396	225	204	174	225	1.34	0.99	0.89	0.90	BBBB...e	2.3670	GB6 J0217+7349
52	2.3539	35.8532	142.6650	-23.5540	1104	1170			175	216			1.04	1.05			BB...We	0.6846	GB6 J0221+3556
53	2.3796	-34.7410	239.8400	-69.0460	978				141				0.84				B...We	1.4900	PKS 0220-349
54	2.3828	43.0029	140.2100	-16.7770	1786	1247	1548		152	214	212		1.05	1.05	1.04		NBN...We	0.0212	GB6 J0223+4259
55	2.4288	34.4025	144.2010	-24.5450	1027				175				1.04				B.....e	2.9100	GB6 J0226+3421
56	2.5227	-47.7768	266.2710	-61.6190				1136				209				0.83	...B..We		PMN J0231-4746
57	2.5269	13.3551	157.0670	-42.7800	1359		1092		187		202		1.11		1.03		B.B..We	2.0590	PKS 0229+13
58	2.6282	28.8108	149.4210	-28.5390	3858	3376	3336	2587	199	236	235	314	1.18	1.15	1.19	1.23	BBBB..We	1.2130	GB6 J0237+2848
59	2.6427	16.6351	156.7360	-39.1040	1688	1862	1476		190	242	239		1.15	1.17	1.21		BBB...We	0.9400	PKS 0235+164
60	2.6655	4.3301	166.8630	-49.0630	874				169				1.08				N....e	0.9780	PKS 0237+040
61	2.6811	-8.3220	182.0530	-58.0080	1227				158				0.94				B.....We	0.0050	PKS 0238-084
62	2.7066	-0.0710	172.0820	-52.0240	921				158				0.94				B.....e	0.0037	PKS J0242-0000
63	2.7505	-44.9407	258.6130	-61.1940		890				176				0.86			.B...We	0.2800	PKS 0244-452
64	2.8926	-54.7461	272.5470	-54.5720	2309	2442	2361	1998	149	189	166	210	0.87	0.92	0.84	0.84	BBBB..We	0.5390	PKS 0252-549
65	2.9930	-0.2401	177.1140	-49.1450	1147	1324	1093		176	225	203		1.05	1.09	1.03		BBB..We	2.0012	PKS 0256-005
66	3.0571	47.2703	144.9620	-9.8770	1183				191				1.06				N.G..e		GB6 J0303+4716
67	3.0609	-62.2369	280.3030	-48.6740	1488	1345	1370	1278	153	183	159	205	0.91	0.89	0.82	0.82	BBBB..We	0.0286	PKS 0302-623
68	3.1396	4.1733	174.7810	-44.4800	1124	1279	1076		176	225	203		1.05	1.09	1.04		BBB...We	0.8630	PKS J0308+0406
69	3.1556	10.5435	169.1980	-39.6330	1047	1317	1348	1494	182	232	204	267	1.08	1.13	1.04	1.07	BBBB..We		PKS 0306+102
70	3.1566	-60.8722	278.0580	-49.0590	1223	1189	873		153	183	159		0.91	0.90	0.81		BBB..We	0.6640	PKS 0308-611
71	3.2112	1.5535	178.4980	-45.5330			1035				193				1.04		.N..We	0.2230	PKS 0310+013
72	3.2174	-76.8736	293.3860	-37.5040	966	1156	957		163	189	173		0.97	0.93	0.89		BBB..We		PKS 0312-77
73	3.3290	41.5292	150.5560	-13.2530	10198	9281	7870	5450	248	277	237	279	1.47	1.17	1.09	1.12	BBBB..We	0.0175	GB6 J0319+4130
74	3.3722	-37.1774	240.1220	-56.7660		5217	3069	1752		229	180	218		1.08	0.91	0.87	.BBB..We	0.0058	Fornax A
75	3.3793	12.3994	170.7480	-36.0600	1461	1407	1290		203	245	231		1.21	1.12	1.18		BNB..e	2.6620	PKS 0319+12
76	3.4098	-37.2630	240.1860	-56.3100				1176				218				0.87	...B..e		PMN J0324-3716
77	3.4193	22.3883	163.5850	-28.0970	917		1196		172		223		1.22		1.21		N.N..We	2.0600	GB6 J0325+2223
78	3.4970	-23.9914	216.9460	-54.2860	1096	1291	1279		149	190	185		0.88	0.92	0.95		BBB..We	0.8950	PKS 0327-241
79	3.5118	31.8654	158.2600	-19.8670	1127				222				1.32				B....u		...
80	3.5657	-40.1363	244.7710	-54.1300	1393	1391	1380	1270	150	229	180	218	0.89	1.11	0.92	0.87	BBBB..We	1.4450	PKS 0332-403
81	3.6060	-12.9958	201.1450	-49.0020	981		1147		172		195		0.99		1.00		B.B..We	1.3030	PKS 0334-131
82	3.6105	32.3174	159.0160	-18.7410		1643	1783			238	224			1.16	1.14		.BB..e	1.2580	GB6 J0336+3218
83	3.6497	31.3069	160.0960	-19.2180	1357				222				1.32				B.....u		...
84	3.6526	-1.7176	187.8650	-42.4920	2429	2446	1907	1422	161	214	198	260	0.96	1.08	1.01	1.04	BBBB..We	0.8520	PKS 0336-01
85	3.6725	-21.4220	213.9150	-51.2630	1029	1122	1083		149	190	185		0.88	0.92	0.95		BBB...We	0.2230	PKS 0338-214
86	3.7221	31.8733	160.4730	-18.1930	2703	2352	1372		222	238	224		1.32	1.16	1.14		BBB..u		...
87	3.8160	-27.7730	224.4720	-50.8300	975		915	1556	147		167	211	0.87		0.89	0.85	B.NB.We	0.9910	PKS 0346-27

Table 3 – Continued

#	RA	δ	l	b	S_{23}	S_{33}	S_{41}	S_{61}	σ_{23}	σ_{33}	σ_{41}	σ_{61}	r_{23}	r_{33}	r_{41}	r_{61}	flags	z	Id.
88	3.9732	36.6366	159.7070	-12.5520	1349	.	1621	.	203	.	268	.	1.28	.	1.37	.	B....u	..	...
89	3.9793	10.5121	179.7400	-31.0300	.	.	.	2100	.	.	.	292	.	.	.	1.17	B....We	0.0304	PKS J0358+1025
90	4.0415	36.3478	160.5310	-12.2160	.	.	3088	.	.	.	268	292	.	.	1.37	.	..BB...g	.	NGC 1499
91	4.0660	-36.0650	237.7150	-48.4700	3442	3661	3764	3755	175	219	174	233	1.00	1.07	0.89	0.92	BBBB..We	1.4170	PKS 0402-362
92	4.0935	-13.1185	205.7470	-42.6360	1974	1725	1461	.	172	208	195	.	1.02	1.01	1.00	.	BBB...We	0.5705	PKS 0403-13
93	4.1170	-38.4379	241.2820	-47.8830	1212	1227	938	.	173	203	174	.	1.04	0.99	0.89	.	BBB...We	1.2850	PKS 0405-385
94	4.1621	-75.0947	288.9090	-36.0930	843	.	.	.	159	.	.	.	1.22	.	.	.	N.....We	0.6930	PKS 0410-75
95	4.1920	76.9082	133.4680	18.3370	1051	.	.	.	165	.	.	.	0.95	.	.	.	B.....We	0.5985	NVSS J041045+765645
96	4.2786	-20.8726	216.9170	-43.0150	852	.	.	.	166	.	.	.	0.98	.	.	.	B.....We	0.8080	PKS 0413-21
97	4.3100	38.0243	161.7120	-8.7870	.	.	3405	3249	.	.	268	292	.	.	1.37	1.17	.BBG..e	0.0485	3C 111
98	4.3909	-1.2953	195.2720	-33.0750	.	8129	7393	6318	.	261	248	313	.	1.27	1.27	1.25	.BBB..We	0.914	PKS 0420-01
99	4.3962	2.3081	191.7540	-31.0490	1154	.	.	.	229	.	.	.	1.36	.	.	.	B.....We	2.2770	PKS 0420+022
100	4.4066	41.8321	159.7670	-5.3220	1237	1613	1244	.	175	232	209	.	1.00	1.41	1.28	.	BB.G..e	.	GB6 J0423+4150
101	4.4155	-38.0085	240.7530	-44.3580	1471	1310	1129	1303	175	219	174	233	1.04	1.05	0.89	0.93	BBBB..We	0.7820	PKS 0422-380
102	4.4202	0.6819	193.5760	-31.6430	.	1728	1854	.	183	207	248	.	1.08	1.00	1.27	.	BBB...We	0.3100	PKS 0422+00
103	4.4828	-37.9160	240.6810	-43.5590	.	1364	1103	1195	.	219	174	233	.	1.07	0.89	0.93	BBB..We	1.1100	PKS 0426-380
104	4.5011	35.3117	165.3040	-9.0060	.	.	1641	.	.	.	268	.	.	.	1.37	.	.B.G..g	.	NGC 1579
105	4.5524	5.3387	190.3810	-27.4140	2511	2653	2261	2180	214	226	220	281	1.27	1.10	1.14	1.13	BBBB..We	0.0330	PKS 0433+0521
106	4.6163	29.7445	170.5110	-35.1760	3516	2311	1600	.	239	233	214	.	1.42	1.13	1.09	.	BBB...e	0.2177	GB6 J0437+2940
107	4.6483	-12.9147	209.8440	-35.1760	797	1009	.	.	148	191	.	.	0.88	0.93	.	.	BB...e	1.2770	PKS 0436-129
108	4.6665	-43.5359	248.3890	-41.6190	2485	2086	2135	1391	173	203	174	224	1.03	0.99	0.89	0.90	BBBB..We	2.8630	PKS 0438-43
109	4.7045	-0.2745	197.1240	-28.5310	998	.	1445	.	183	.	248	.	1.08	.	1.23	.	B.B..We	0.8440	PKS 0440-00
110	4.7105	36.0793	166.4380	-6.5910	.	.	.	1587	.	.	268	292	.	.	.	1.16	..BG.g	...	IRAS 04395+3601
111	4.8210	11.3449	187.4590	-20.7170	2093	1994	2063	1923	214	226	220	281	1.27	1.10	1.12	1.13	BBBB..e	1.2070	PKS 0446+11
112	4.8500	-81.0268	293.8430	-31.3350	1799	1795	1416	1470	163	189	173	225	1.09	0.94	0.89	0.91	BBBB..We	0.4440	PKS 0454-81
113	4.8870	-69.3698	280.8020	-35.5500	2541	1991	1442	.	205	202	175	.	1.22	1.00	0.89	.	BBB.L.g	.	NGC 1722
114	4.8874	-28.0854	228.9680	-37.0060	1636	1416	1246	.	170	209	185	.	1.01	1.01	0.94	.	BBB...We	2.5590	PKS 0451-28
115	4.9331	-46.3050	252.0180	-38.7900	4022	3963	3846	3280	237	254	223	272	1.41	1.15	1.10	1.07	BBBB..We	0.8528	PKS 0454-46
116	4.9461	-23.3902	223.6580	-34.9520	2486	2519	2500	1639	170	209	185	231	1.01	1.01	0.94	0.92	BBBB..We	1.0030	PKS 0454-234
117	4.9535	-66.3832	277.1390	-36.0320	4137	3409	3075	2146	217	215	172	207	1.29	1.04	0.88	0.83	BBBB.L.g	.	PKS 0456-665
118	5.0252	-2.0307	201.5330	-25.2520	1214	1140	1141	.	200	218	213	.	1.19	1.06	1.09	.	BBB...We	2.2860	PKS 0458-02
119	5.0568	-25.3321	177.7370	-9.7990	1198	.	.	.	239	.	.	.	1.42	.	.	.	B..G..e	0.2775	PKS 0459+25
120	5.1137	-61.1079	270.4830	-36.0700	2069	1681	1754	.	217	215	172	.	1.29	1.04	0.88	.	BBB...We	1.0930	PKS 0506-61
121	5.1649	-68.9031	279.7660	-34.2470	1060	1034	.	.	205	202	.	.	1.25	1.03	.	.	BB...L.g	.	PKS 0510-689
122	5.1656	18.0408	184.6910	-12.7940	1066	1591	1406	.	170	238	215	.	1.01	1.16	1.10	.	BB....e	0.4160	PKS 0507+17
123	5.2335	-21.9275	223.5150	-35.0716	.	1002	.	.	.	194	.	.	.	1.01	.	.	BN....We	1.2960	PKS 0511-220
124	5.2514	-45.8866	251.6500	-35.4670	.	.	1029	.	.	.	200	.	.	.	1.14	.	.N....We	0.1940	PKS 0514-459
125	5.2766	-69.3105	280.0860	-33.5740	.	1154	.	.	.	202	.	.	.	0.98	.	.	B..L.u	.	...
126	5.3258	-45.7428	251.5480	-34.6800	6521	4886	4032	2708	237	254	223	272	1.41	1.23	1.14	1.09	BBBB...We	0.0350	Pictor A
127	5.3287	-69.6190	280.3810	-33.2430	.	.	909	.	.	.	175	.	.	.	0.89	.	.B.L.g	.	PKS 0519-696
128	5.3660	-67.9578	278.3830	-33.3510	.	1792	1885	1636	.	215	172	207	.	1.03	0.88	0.86	BBB.L.g	0.0553	PKS 0522-679
129	5.3843	-36.4112	240.5570	-32.6880	4098	3661	3684	3374	180	203	188	242	1.07	0.98	0.96	0.97	BBBB..We	.	PKS 0521-36
130	5.4211	-66.1511	276.1870	-33.3110	1360	1342	982	.	217	215	172	.	1.29	1.04	0.88	.	BBB.L.g	.	PKS 0525-66
131	5.4343	-48.4931	254.9690	-33.7900	919	1156	1163	.	156	198	181	.	0.93	0.96	1.07	.	BBB...We	.	PKS 0524-485

Table 3 – Continued

#	RA	δ	l	b	S_{23}	S_{33}	S_{41}	S_{61}	σ_{23}	σ_{33}	σ_{41}	σ_{61}	r_{23}	r_{33}	r_{41}	r_{61}	flags	z	Id.
132	5.4562	-12.6758	215.1800	-24.2960	1406	1530	1598	.	180	207	202	.	1.07	1.21	1.32	.	BBB...g	.	PKS 0525-127
133	5.4928	21.6073	184.2780	-6.9740	7470	.	.	.	625	.	.	.	0.07	.	.	.	N..G.u	.	.
134	5.4946	-25.1916	228.4050	-28.3820	771	.	.	.	153	.	.	.	1.01	.	.	.	N.....e	2.8130	PKS 0528-250
135	5.5098	13.6372	191.2310	-11.0290	2382	2512	2236	2351	241	238	215	299	1.43	1.16	1.10	1.20	BBBB...e	2.0600	PKS 0528+134
136	5.5161	-71.1291	281.9380	-32.0380	.	1241	1238	.	.	202	175	.	.	0.98	0.89	.	BB.L.g	.	PKS 0531-711
137	5.5216	12.4709	192.3360	-11.4930	.	2016	.	.	.	282	.	.	.	1.37	.	.	B....u	.	.
138	5.5438	7.5655	196.8210	-13.7330	.	1576	1339	.	.	310	231	.	.	1.37	1.18	.	.NB...e	1.2540	PMN J0532+0732
139	5.5478	48.4578	162.0600	8.2150	1092	1379	.	.	189	206	.	.	1.12	1.00	.	.	BB..G.e	1.1620	GB6 J0533+4822
140	5.5746	-67.6115	277.7740	-32.2300	.	.	1714	.	.	.	172	.	.	.	0.88	.	.B.L.g	.	PKS 0535-676
141	5.6402	-69.1260	279.4980	-31.6950	.	32077	27720	22740	.	396	294	389	.	1.48	1.19	0.97	.BBB.L.g	.	PKS 0539-691
142	5.6513	-44.0757	250.0790	-31.0460	5683	5912	5466	4326	237	254	223	272	1.41	1.23	1.14	1.09	BBBB.We	0.8940	PKS 0537-441
143	5.6604	-28.7095	232.9660	-27.3650	840	.	.	.	152	.	.	.	0.91	.	.	.	B....We	3.1040	PKS 0537-286
144	5.6706	-5.6862	209.8790	-18.4160	7871	.	.	.	730	.	.	.	0.06	.	.	.	N.....u	.	.
145	5.6803	-54.2430	261.9700	-31.8540	1554	1529	1315	1198	156	198	181	199	0.93	0.96	0.93	0.94	BBBN.We	0.5450	PKS 0539-543
146	5.7193	49.8797	161.7080	10.3900	1968	1363	1466	.	189	206	203	.	1.12	1.00	1.04	.	BBB...We	.	GB6 J0542+4951
147	5.7820	0.1184	205.3120	-14.2590	.	.	2196	1582	.	.	263	296	.	.	1.34	1.18	..BB..g	.	NGC 2068
148	5.8373	-57.5774	265.9500	-30.7180	1274	1054	1068	.	156	187	181	.	0.93	0.96	0.93	.	BNB..We	.	PKS 0549-575
149	5.8701	0.7997	205.3340	-12.7720	.	.	1553	.	.	.	263	.	.	.	1.34	.	..B...u	.	.
150	5.9258	39.7592	171.7140	7.2910	2724	2184	1512	1296	191	215	208	252	1.14	1.04	1.06	1.04	BBBNG.We	2.3650	GB6 J0555+3948
151	5.9517	-13.3258	219.0220	-17.9690	936	.	.	.	180	.	.	.	1.07	.	.	.	B.....e	.	PKS 0555-132
152	6.1159	67.3767	146.7430	20.7850	862	.	.	.	159	.	.	.	0.94	.	.	.	B....We	1.9700	GB6 J0607+6720
153	6.1260	-6.3702	213.6670	-12.6440	.	.	7168	5913	.	.	263	296	.	.	1.34	1.18	..BB..g	.	PKS 0605-06
154	6.1385	-8.5524	215.7610	-13.4410	1563	1459	1584	.	202	230	217	.	1.20	1.12	1.11	.	BBB...e	0.8720	PKS 0605-08
155	6.1490	-22.3471	228.9300	-18.9740	1013	1038	.	.	152	185	.	.	0.91	0.92	.	.	BN...We	1.9260	PKS 0606-223
156	6.1660	-15.6790	222.6090	-16.1090	3717	3505	3183	2362	202	230	217	254	1.20	1.12	1.11	1.02	BBBB.We	0.3240	PKS 0607-15
157	6.2415	61.9106	152.4860	19.5730	829	.	.	.	159	.	.	.	0.94	.	.	.	B.....u	.	.
158	6.3519	-25.2987	232.9180	-17.5180	812	.	.	.	152	.	.	.	0.91	.	.	.	B....We	1.9000	PKS 0618-252
159	6.3887	-64.6799	274.3970	-27.3070	886	.	.	.	140	.	.	.	0.83	.	.	.	B....We	0.1288	PMN J0623-6436
160	6.4431	-35.3960	243.3230	-20.0370	791	.	.	.	155	.	.	.	0.92	.	.	.	B....We	0.0545	PKS 0625-35
161	6.4857	-19.9166	228.5470	-13.6870	1419	1262	1140	1336	196	202	182	224	1.16	0.98	0.93	0.90	BBBB.We	.	PKS 0627-199
162	6.5850	-75.3022	286.4000	-27.2030	4301	3655	3601	2602	166	192	174	210	0.99	0.93	0.87	0.86	BBBB.We	0.6530	PKS 0637-75
163	6.6110	-20.5155	229.8560	-12.3280	1190	.	.	.	196	.	.	.	1.16	.	.	.	B....We	0.0551	PKS 0634-20
164	6.6576	73.3794	141.3130	25.0640	800	.	901	.	154	.	169	.	0.92	.	0.86	.	B.B..We	1.8500	GB6 J0639+7324
165	6.7771	44.8223	171.1270	17.9490	2978	2532	2154	1478	181	218	213	280	1.07	1.06	1.09	1.12	BBBB.We	3.3960	GB6 J0646+4451
166	6.8394	-16.6223	227.6970	-7.7260	3071	2783	2467	1942	196	202	182	224	1.16	0.98	0.93	0.90	BBBBG..e	.	PKS 0648-16
167	7.0026	17.1177	198.5220	9.5880	969	.	.	.	174	.	.	.	1.04	.	.	.	B.G..e	0.8220	GB6 J0700+1709
168	7.0393	-46.7061	256.9840	-17.6270	1025	.	1012	.	168	.	169	.	1.00	.	0.91	.	B.B..e	.	PKS 0700-465
169	7.1577	-36.2552	247.5630	-12.3140	1730	1178	.	.	232	208	.	.	1.38	1.01	.	.	BB....u	.	.
170	7.1984	-37.7986	249.2070	-12.5180	1342	.	.	.	232	.	.	.	1.38	.	.	.	B.....u	.	.
171	7.3278	-52.1071	263.3300	-17.0190	837	.	.	.	155	.	.	.	0.92	.	.	.	B.....u	.	.
172	7.3311	-62.2878	273.3870	-20.6390	726	.	.	.	140	.	.	.	0.83	.	.	.	B.....u	.	PMN J0719-6218
173	7.3503	4.0552	212.6770	8.4240	899	.	.	.	164	.	.	.	0.98	.	.	.	B..G.We	.	PMN J0721+0406
174	7.3581	71.3678	143.9520	27.9860	1712	1748	1899	1651	154	188	169	225	0.91	0.91	0.93	0.93	BBBN..We	0.3000	GB6 J0721+7120
175	7.4279	14.4421	203.6650	14.0040	904	.	.	.	164	.	.	.	0.98	.	.	.	B.....e	.	PKS 0722+145

Table 3 – Continued

#	RA	δ	l	b	S23	S33	S41	S61	σ23	σ33	σ41	σ61	r23	r33	r41	r61	flags	z	Id.
176	7.4309	-0.7934	217.5890	7.2860	1255	1427	1094	.	178	213	212	.	1.06	1.04	1.08	.	BBB.G.We	0.1280	PKS 0723-008
177	7.4538	67.7516	148.0750	28.3230	775	.	.	.	148	.	.	.	0.90	.	.	.	N....We	0.8460	GB6 J0728+6748
178	7.4795	-36.3383	249.3740	-8.8550	1199	.	.	.	232	.	.	.	1.38	.	.	.	B...G.e	.	PKS 0727-36
179	7.5835	50.3245	167.7930	27.2800	838	1213	.	.	167	210	.	.	0.99	1.01	.	.	BB....e	0.7200	GB6 J0733+5022
180	7.6321	17.7216	201.8110	18.0340	1407	1487	.	.	170	219	.	.	1.01	1.07	.	.	BB....We	0.424	GB6 J0738+1742
181	7.6458	-43.1030	256.3570	-10.2760	.	.	1027	.	.	.	197	.	.	.	1.01	.	.B...u	.	...
182	7.6554	1.6472	216.9660	11.3990	1740	1965	2154	1901	178	213	212	260	1.06	1.04	1.08	1.04	BBBB..We	0.1910	PKS 0736+01
183	7.6926	31.2451	188.6190	23.6780	1132	1148	.	.	173	228	.	.	1.03	1.11	.	.	BB....We	0.6313	GB6 J0741+3112
184	7.7424	-67.4295	279.5020	-20.0360	1126	920	.	.	140	172	.	.	0.83	0.87	.	.	BN...We	1.5100	PKS 0743-67
185	7.7583	10.1688	209.8080	16.5730	1108	.	.	.	164	.	.	.	0.98	.	.	.	B....We	2.6240	PKS 0742+10
186	7.7690	-0.8175	220.0020	11.7650	1353	1154	.	.	178	213	.	.	1.06	1.04	.	.	BB....We	0.9940	PKS 0743-006
187	7.8002	-36.1482	251.0770	-5.3570	2275	.	1570	1224	343	.	230	242	0.04	.	1.18	1.00	N.BNG.u	.	...
188	7.8478	12.5542	208.1260	18.7760	2686	2506	2473	1749	177	221	212	272	1.05	1.08	1.08	1.09	BBBB..We	0.8890	PKS 0748+126
189	7.8782	53.8492	164.2340	30.4540	950	.	.	.	163	.	.	.	0.97	.	.	.	B....We	.	GB6 J0753+5353
190	7.9538	9.9974	211.2730	19.1070	1616	1553	1525	1410	177	221	212	275	1.05	1.08	1.08	1.09	BBBN..We	0.2660	PKS 0754+100
191	8.0955	61.7744	155.0030	32.4000	865	.	.	.	151	.	.	.	0.92	.	.	.	B....We	3.0330	GB6 J0805+6144
192	8.1347	-7.8599	229.0250	13.1210	1257	1289	1140	1248	156	198	184	243	0.92	0.96	0.94	0.97	BBBB..We	1.8370	PKS 0805-07
193	8.1448	49.8945	169.1040	32.5730	969	.	1099	.	189	.	214	.	1.12	.	1.11	.	B.N...e	1.4360	GB6 J0808+4950
194	8.2347	48.2688	171.1210	33.3300	1005	.	.	.	189	.	.	.	1.12	.	.	.	B....We	0.8710	GB6 J0813+4813
195	8.2825	-24.3866	244.3890	6.1540	895	.	.	.	176	.	.	.	1.05	.	.	.	B...G.We	.	PMN J0816-2421
196	8.3904	22.3053	201.4510	29.6530	1043	.	.	.	179	.	.	.	1.06	.	.	.	B....We	0.9510	PKS 0820+22
197	8.4157	39.2953	182.1220	34.1980	1331	.	.	.	174	.	.	.	1.03	.	.	.	B....We	1.2156	GB6 J0824+3916
198	8.4266	3.1418	221.2020	22.3270	1661	2021	2005	1723	168	221	220	280	1.00	1.07	1.12	1.12	BBBB..We	0.5060	PKS 0823+033
199	8.5211	24.1981	200.0380	31.9670	1325	1368	1501	.	179	231	235	.	1.06	1.12	1.20	.	BBB...We	0.9404	GB6 J0830+2410
200	8.5298	-4.5595	220.6270	24.3570	.	.	1190	.	.	.	220	.	.	.	1.12	.	.N...e	0.2900	PKS 0829+046G4
201	8.5387	-52.6972	269.3480	-7.6360	.	1385	.	.	.	275	.	.	.	1.34	.	.	.B.G..u	.	...
202	8.5805	55.5110	162.3050	36.5520	1036	.	.	.	163	.	.	.	0.97	.	.	.	B....We	0.2411	GB6 J0834+5534
203	8.6107	-20.2938	243.5780	12.2230	2827	2339	2377	1724	176	199	195	242	1.05	0.97	1.00	0.97	BBBB..We	2.7520	PKS 0834-20
204	8.6279	58.4631	158.5980	36.6390	827	.	.	.	163	.	.	.	0.97	.	.	.	B....We	2.1010	GB6 J0837+5825
205	8.6789	13.2141	212.9530	30.1280	1865	1950	1946	.	195	238	228	.	1.16	1.16	1.16	.	BBB...We	0.6808	PKS 0838+13
206	8.7054	70.9279	143.4760	34.4880	1686	1800	1823	1579	151	187	188	234	0.90	0.91	0.95	0.94	BBBB..We	2.1720	GB6 J0841+7053
207	8.7915	-7.0513	233.6770	21.8640	925	.	.	.	163	.	.	.	0.97	.	.	.	B....We	.	PMN J0847-0703
208	8.9132	20.0570	206.8700	35.7990	3951	4451	3661	4125	195	238	228	303	1.16	1.16	1.16	1.21	BBBB..We	0.3060	PKS 0851+202
209	9.0143	-28.0683	253.3190	11.8720	1104	.	.	.	185	.	.	.	1.10	.	.	.	B....e	2.1520	PKS 0858-279
210	9.0365	-14.2358	242.2190	20.7170	1218	1333	1126	.	174	218	207	.	1.03	1.06	1.06	.	BBB...We	1.3330	PKS 0859-14
211	9.0597	46.8960	172.9760	41.6410	950	.	.	.	161	.	.	.	0.96	.	.	.	B....e	1.4700	GB6 J0903+4650
212	9.0697	42.5798	178.7570	41.8530	1016	.	.	.	202	.	.	.	1.41	.	.	.	N....e	.	GB6 J0904+4238
213	9.0702	-57.5116	276.0010	-7.0600	1200	1130	938	.	166	183	173	.	0.99	0.89	0.88	.	BBB.G.e	0.6950	PKS 0903-57
214	9.1341	-20.3785	248.2620	18.0340	1003	.	.	.	174	.	.	.	1.03	.	.	.	B....We	.	PMN J0907-2026
215	9.1547	1.3333	228.9880	30.9350	2234	2055	2019	2072	175	223	219	298	1.04	1.08	1.10	1.17	BBBB..We	1.0244	PKS 0906+01
216	9.1619	42.9720	178.2220	42.8670	1203	1315	1238	.	210	234	214	.	1.41	1.25	1.09	.	NNB...We	0.6702	GB6 J0909+4253
217	9.2510	2.7563	228.4280	32.9060	1247	1413	1163	.	175	223	207	.	1.04	1.08	1.06	.	BB...We	0.4270	PKS 0912+029
218	9.3066	-12.0344	242.9220	25.1880	2158	1318	.	.	174	218	207	.	1.03	1.06	1.06	.	BBB...We	0.0548	PKS 0915-11
219	9.3431	44.6854	175.7260	44.7480	1415	1583	1474	.	238	258	214	.	1.41	1.25	1.09	.	BBB...We	2.1899	GB6 J0920+4441

Table 3 – Continued

#	RA	δ	l	b	S₂₃	S₃₃	S₄₁	S₆₁	σ₂₃	σ₃₃	σ₄₁	σ₆₁	r₂₃	r₃₃	r₄₁	r₆₁	flags	z	Id.
220	9.3567	-26.3220	255.0670	16.4590	1586	1433	1346	.	185	200	188	.	1.01	0.98	0.97	.	BBB...We	2.3000	PKS 0919-260
221	9.3568	62.3696	152.0810	40.9350	871	.	899	.	151	.	175	.	0.90	.	0.91	.	B.B..We	1.4460	GB6 J0921+6215
222	9.3835	-40.0512	265.4250	7.1810	1205	1107	1058	.	211	208	181	.	1.25	1.01	0.93	.	BBB.G..e	0.5910	PKS 0920-39
223	9.4491	39.0317	183.7190	46.1430	6576	5204	5016	3781	238	258	214	271	1.41	1.25	1.09	1.08	BBBB..We	0.6952	GB6 J0927+3902
224	9.8086	40.6757	180.9830	50.2060	1399	1316	1384	.	238	258	201	.	1.41	1.25	1.07	.	BBN...We	1.2490	GB6 J0948+4039
225	9.9282	-41.0463	270.7660	10.5980	1114	.	.	.	211	.	.	.	1.25	.	.	.	B....e	.	PMN J0954-4108
226	9.9299	69.6955	141.3980	40.5520	1348	1075	887	.	160	203	170	.	0.95	0.99	0.87	.	BBB...We	0.0006	GB6 J0955+6940
227	9.9515	25.2541	205.5320	51.0380	994	1074	.	.	170	204	.	.	1.01	1.03	.	.	BB....e	0.7120	87GB 095400.5+252927
228	9.9598	55.4250	158.5450	47.9050	1071	1040	1016	.	161	206	189	.	0.93	0.95	0.93	.	BBB...We	0.8955	GB6 J0957+5522
229	9.9624	47.4545	170.0420	50.6260	1635	1235	1289	.	143	183	169	.	0.85	0.95	0.86	.	BBB...We	1.8817	GB6 J0958+4725
230	9.9795	65.5291	145.7890	43.1500	964	.	.	.	151	.	.	.	0.90	.	.	.	B....We	0.3680	GB6 J0958+6534
231	10.2295	23.0947	210.4750	54.2250	1171	.	.	.	170	.	.	.	1.01	.	.	.	B....We	0.5650	GB6 J1014+2301
232	10.2589	-45.1665	276.2140	9.4650	935	.	.	.	174	.	.	.	1.04	.	.	.	B..G.We	.	PMN J1014-4508
233	10.2911	35.8925	188.1640	56.2680	1043	.	.	.	166	.	.	.	0.98	.	.	.	B.....We	1.2279	NVSS J101811+354240
234	10.3897	39.9802	180.5240	56.8790	1019	.	.	.	166	.	.	.	0.99	.	.	.	B....e	1.2540	GB6 J1023+3947
235	10.4158	-18.6672	261.1080	32.0570	.	.	979	.	.	.	188	.	.	.	1.01	.	N...g	.	PKS 1022-183
236	10.5402	41.3600	177.2820	58.2250	879	.	.	.	166	.	.	.	0.99	.	.	.	B.....We	1.1169	GB6 J1033+4115
237	10.5930	-20.1884	264.5540	32.3730	888	.	.	.	163	.	.	.	0.97	.	.	.	B....e	2.1980	PKS 1032-199
238	10.6237	-29.5070	270.9470	24.9340	1520	1578	1409	1267	176	211	201	247	1.05	1.03	1.03	0.99	BBBB..We	0.3120	PKS 1034-293
239	10.6445	5.2162	241.6820	51.5500	1639	1668	1412	.	187	219	206	.	1.11	1.05	1.05	.	BBB...We	.	PKS 1036+054
240	10.6868	6.2301	241.0170	52.6720	1507	1701	1364	.	187	219	206	.	1.11	1.05	1.05	.	BBB...We	1.2700	PKS 1038+064
241	10.6941	-47.6902	281.4390	9.6920	1230	993	.	.	174	195	.	.	1.04	0.95	.	.	BN.G.We	.	PMN J1041-4740
242	10.7171	24.2116	211.4300	60.9960	945	.	.	.	170	.	.	.	0.98	.	.	.	B.....We	0.5600	GB6 J1043+2408
243	10.8031	-19.1565	266.7670	34.9180	1356	.	1193	.	163	.	198	.	1.01	.	1.03	.	B.N..We	0.5950	PKS 1045-18
244	10.8054	71.7406	135.4450	42.2680	1366	1471	1276	1280	160	203	170	228	0.95	0.99	0.87	0.92	BBBN..We	1.1500	GB6 J1048+7143
245	10.8906	81.1040	128.2510	34.7700	829	.	.	.	157	.	.	.	0.93	.	.	.	B....We	0.7060	NVSS J105811+811433
246	10.9802	1.5561	251.6170	52.8220	4769	4350	4405	3840	187	219	206	270	1.11	1.06	1.05	1.08	BBBB..We	0.8900	PKS 1055+01
247	10.9844	-80.0577	298.0200	-18.2750	2271	2307	2268	2346	165	204	177	226	0.98	0.99	0.91	0.91	BBBB..We	.	PKS 1057-79
248	11.1219	-44.8213	284.2000	14.2300	1566	1435	927	.	174	195	174	.	1.03	0.94	0.90	.	BBB...We	1.5980	PKS 1104-445
249	11.3067	-46.5790	286.7340	13.3460	923	.	.	.	171	.	.	.	1.02	.	.	.	B....We	0.7130	PKS 1116-46
250	11.3135	-12.5328	270.4240	44.4140	1019	.	.	.	171	.	.	.	1.02	.	.	.	B....We	1.739	PKS 1115-12
251	11.3233	12.5502	242.4790	63.9860	1010	1768	1095	.	159	203	200	.	0.94	1.05	1.00	.	B.N..We	2.1290	PKS 1116+12
252	11.4493	-18.9692	276.7010	39.5610	1478	1930	1482	.	171	203	193	.	1.02	0.98	1.03	.	BBB...We	1.0500	PKS 1124-186
253	11.5020	-14.7886	275.2610	43.6710	1984	1930	1805	1308	171	203	193	213	1.02	0.98	0.99	1.00	BBBN..We	1.1840	PKS 1127-14
254	11.5111	38.2472	174.5320	69.7630	1227	1097	1025	.	156	188	179	.	0.91	0.92	0.94	.	BNB...We	1.7414	GB6 J1130+3815
255	11.7809	40.0016	164.9330	74.1370	1105	1182	924	.	156	196	179	.	0.92	0.92	0.93	.	BBB...We	1.0880	GB6 J1146+3958
256	11.7870	-38.1496	289.2650	23.0120	2163	2427	1902	1677	167	207	198	246	0.99	1.01	1.01	0.98	BBBB..We	1.0480	PKS 1144-379
257	11.8411	-79.5838	300.0820	-17.0510	872	.	.	.	165	.	.	.	1.04	.	.	.	B....Wu	.	...
258	11.8548	-0.3571	272.7400	58.9430	931	.	.	.	163	.	.	.	0.99	.	.	.	B....We	1.9762	PKS 1148-00
259	11.8726	-8.7255	279.1120	51.3930	993	.	.	.	169	.	.	.	0.97	.	.	.	N.....e	2.3700	PKS B1149-084
260	11.8876	49.5616	145.5460	64.9340	2153	2080	2120	1714	150	183	173	213	0.89	0.89	0.88	0.86	BBBB..We	0.3339	GB6 J1153+4931
261	11.9098	81.0847	125.6190	35.7450	1373	1225	1036	.	157	193	186	.	0.93	0.94	0.95	.	BBB...We	1.2500	NVSS J115312+805829
262	11.9640	16.6119	250.4680	73.7370	.	1226	.	.	.	205	.	.	.	1.00	.	.	B....We	1.0500	PKS 1155+169
263	11.9930	29.2427	199.4200	78.3860	1899	2126	1958	1889	169	203	186	243	1.00	0.97	0.94	0.97	BBBB..We	0.7290	GB6 J1159+2914

Table 3 – Continued

#	RA	δ	l	b	S_{23}	S_{33}	S_{41}	S_{61}	σ_{23}	σ_{33}	σ_{41}	σ_{61}	r_{23}	r_{33}	r_{41}	r_{61}	flags	z	Id.
264	11.9995	73.0582	128.0690	43.5530	800				157				0.90				N.....e	0.9700	GB6 J1200+7300
265	12.1511	-24.0361	290.6610	37.8240	1241		1017		175		200		1.00		1.01		B.N..We	1.2990	PKS B1206-238
266	12.2004	-52.6302	296.8820	9.7780	2396	1559	1108		223	212	200		1.32	1.03	1.02		BBB.G..u		...
267	12.2644	-17.5627	291.0100	44.4840	1469	1315	1059		162	209	199		0.96	1.02	1.02		BBB...We		PKS 1213-17
268	12.3166	48.5766	137.1390	67.6470	764				150				0.89				B....We	1.0760	GB6 J1219+4830
269	12.3250	5.7568	281.9300	67.3170	2435	1857	1818	1413	180	234	220	262	1.07	1.14	1.13	1.04	BBBN..We	0.0074	PKS 1216+06
270	12.3627	-4.3235	284.3870	66.1210	969				180				1.07				B.....We	0.0052	PMN J1221+0428
271	12.4265	-83.2129	302.1190	-20.3820	834				165				0.98				B.....We		PKS 1221-82
272	12.4853	2.0440	289.9570	64.3520		18110	16673	14019		387	275	357		1.38	1.16	1.09	.BBB..We	0.1583	PKS 1226+02
273	12.5117	12.0924	284.0000	74.1970			3663				227				0.99		.N....e	0.0043	Virgo A
274	12.5134	12.4471	283.6960	74.5430		15330	12708	8821		338	275	307		1.33	1.20	1.21	.BBB..We	0.0065	NGC 4476
275	12.6563	7.5449	294.0750	70.2090	1072	1206			166	234			1.03	1.14			BB....We	0.4000	PKS 1236+077
276	12.6769	-10.4372	298.5740	52.3430	842				162				0.96				B......e	0.7520	PKS 1237-10
277	12.7745	-16.1300	301.1910	46.7250	818			1396	159			268	0.94			1.07	B.B..e		PKS 1243-160
278	12.7865	-25.7919	301.7330	37.0700	1354	1497	1589	1430	163	211	201	266	0.97	1.03	1.03	1.07	BBBB..We	0.6330	PKS 1244-255
279	12.9096	11.7539	305.8280	74.6080	900				169				1.00				B.....We	0.8734	PKS 1252+11
280	12.9365	-5.7617	305.1070	57.0900			18472	16635			334	438			1.36	1.20	.BB..We	0.5362	PKS 1253-05
281	12.9655	-31.9295	304.5380	30.9220	1184	981	1151		174	189	211		1.03	1.02	1.04		BNB...We	1.9240	PKS 1255-316
282	12.9785	-22.3645	305.1420	40.4760	885				159				0.94				B......We	1.3060	PKS 1256-220
283	13.0296	57.8733	120.2480	59.2010	849				145				0.86				B.....We		87GB 130049.5+580435
284	13.1024	-49.4246	305.3890	13.3770	1542		1354		279		238		1.32		0.95		N.B..We	0.0018	PKS 1302-49
285	13.1565	11.8724	319.2400	74.1730	839				157				0.98				N.....e		PKS 1307+121
286	13.1760	32.3923	85.8450	83.2990	2516	2489	2194	1482	152	184	189	225	0.90	0.91	0.94	0.91	BBBB..We	0.9960	GB6 J1310+3220
287	13.2415	-53.5014	306.4010	9.2150	1138				223				1.32				B..G..e		PMN J1315-5334
288	13.2711	-33.5977	308.8410	28.9890	1639	1527	1933	1750	174	205	211	264	1.03	1.00	1.08	1.05	BBBB..We	1.2100	PKS 1313-333
289	13.3809	-44.6821	308.7900	17.8320	3348		1217		400		214		0.05		1.10		N.B...e	1.95	PKS 1320-446
290	13.4067	-10.7662	315.9400	51.2710	871				171				1.01				B.....We	0.8720	PKS B1321-105
291	13.4216	-43.0247	309.4830	19.4160			31910	24660			428	552			1.31	1.17	.BB..e	0.0018	Centaurus A
292	13.4409	-52.9637	308.2660	9.5450	1540	1682	1107	1404	212	216	202	237	1.26	1.04	1.03	0.95	BBBBG..e		PMN J1326-5256
293	13.4562	22.0685	3.0900	80.3970	1107				151				0.90				B.....We	1.4000	GB6 J1327+2210
294	13.5192	25.1378	22.5660	80.8700	1203	1254			151	202			0.90	0.94			BB....We	1.0550	PKS 1328+25
295	13.5268	30.5104	56.3320	80.5780	2410	1893	1506	1185	146	182	178	230	0.89	0.91	0.95	0.92	BBBB..We	0.8493	GB6 J1331+3030
296	13.5542	1.9931	326.4230	62.9420	1454	1063	1331		159	198	196		0.95	0.96	0.98		BBB...We	0.2155	PKS 1330+02
297	13.5553	27.3571	36.7380	80.6910	920				164				0.98				B.....We		GB6 J1333+2725
298	13.6058	-33.8969	313.4840	28.0530	1717	1290			244	239			1.45	1.16			BB....We	0.0124	PKS 1333-33
299	13.6311	-12.9512	320.0980	48.3670	6159	6153	6211	5738	218	249	226	288	1.29	1.21	1.16	1.15	BBBB..We	0.5390	PKS 1335-127
300	13.7335	66.0069	114.6160	50.2640	890				158				0.94				B.....We	0.7660	87GB 134217.7+661742
301	13.7939	12.2907	347.2680	70.1600	1020	1170			151	193			0.90	0.95			BB....We	0.1217	PKS 1345+12
302	13.9126	-10.6895	327.1410	49.1830	1578	1304	1161		187	204	206		1.11	1.14	1.05		BNB...We	0.3320	PKS 1352-104
303	13.9380	76.6918	118.1320	39.8260	773	1006	1041		152	190	171		0.90	0.93	0.87		BBB...We		NVSS J135755+764320
304	13.9508	19.4189	9.2780	73.0980	1659	1604	1481	1421	151	202	193	220	0.91	0.96	0.94	0.95	BBBN..We	0.7200	PKS 1354+19
305	14.1460	-7.8600	333.8300	50.3150	1215	1301	1064		187	221	206		1.04	1.07	1.05		BBB...We	1.4940	PKS 1406-076
306	14.1594	-27.0515	323.6430	32.6590	896				170				1.01				B.....We	2.4300	PKS B1406-267
307	14.1955	52.3415	97.5980	60.6570	903				148				0.88				B.....We	0.4641	GB6 J1411+5212

Table 3 – Continued

#	RA	δ	l	b	S_{23}	S_{33}	S_{41}	S_{61}	σ_{23}	σ_{33}	σ_{41}	σ_{61}	r_{23}	r_{33}	r_{41}	r_{61}	flags	z	Id.
308	14.2681	13.4104	2.3870	65.9360	991	1145	.	.	162	201	.	.	0.96	0.97	.	.	BB....We	0.2467	PKS 1413+135
309	14.3260	54.3410	98.2910	58.3680	963	.	871	1126	148	.	169	209	0.88	.	0.85	0.84	B.NB..We	0.1525	GB6 J1419+5423
310	14.3261	38.3636	69.8450	68.4150	1021	1193	981	1308	148	179	166	208	0.88	0.87	0.85	0.82	BBBB..We	1.8314	GB6 J1419+3822
311	14.3264	27.0526	37.7810	70.4060	1030	1075	.	.	144	185	.	.	0.85	0.91	.	.	BB....We	.	GB6 J1419+2706
312	14.4098	-49.2851	318.1530	10.8140	2134	1863	1553	1417	212	216	202	237	1.26	1.05	1.03	0.95	BBBB...e	1.8400	PKS B1421-490
313	14.4229	-68.1252	311.5320	-6.8360	1346	1196	1142	.	163	195	169	.	0.97	0.95	0.86	.	BBB.G..e	.	PKS 1420-679
314	14.4619	-42.1471	321.3900	17.2480	3011	2786	2618	2420	176	222	199	269	1.04	1.06	1.01	1.04	BBBB..We	1.5220	PKS 1424-41
315	14.4619	-33.0211	325.2250	25.6490	1041	1438	1404	.	176	222	199	.	1.04	1.08	1.02	.	BBB...We	.	PKS 1424-328
316	14.6162	63.6269	105.1610	49.7020	695	.	.	.	136	.	.	.	0.87	.	.	.	B.....We	2.0680	GB6 J1436+6336
317	14.6421	-22.1140	333.3000	34.3660	1041	1060	.	.	165	208	.	.	0.98	1.03	.	.	BB....e	1.1870	PKS 1435-218
318	14.7192	52.0021	90.4720	57.5030	857	.	.	.	155	.	.	.	0.90	.	.	.	B.....We	0.1411	GB6 J1443+5201
319	14.7662	-16.2977	338.8970	38.4470	1038	.	.	.	165	.	.	.	0.98	.	.	.	B.....We	.	PKS B1443-162
320	14.7697	17.4159	18.8010	61.8170	.	888	.	.	.	177	.	.	.	0.93	.	.	.N....e	0.1020	NVSS J144635+172107
321	14.9043	-37.9240	328.1240	18.8670	1320	.	1102	.	176	.	199	.	1.04	.	1.02	.	B.B...e	0.3140	PKS 1451-375
322	14.9510	-35.5580	329.8720	20.6580	930	.	929	.	176	.	199	.	1.04	.	0.86	.	B.B...We	1.4240	PKS 1454-354
323	14.9957	71.6585	109.9210	42.0770	1421	1414	.	.	158	202	.	.	0.94	0.98	.	.	BB....We	0.9050	GB6 J1459+7140
324	15.0510	-41.9821	327.5850	14.5030	2403	1618	1648	.	196	213	197	.	1.16	1.03	1.01	.	BBB...g	.	PKS 1459-41
325	15.0713	10.4734	11.3200	54.5980	1663	1511	1215	.	154	191	183	.	0.92	0.94	0.95	.	BBB...We	1.8390	PKS 1502+106
326	15.0885	3.4686	2.3090	50.2330	.	1083	.	.	.	206	.	.	.	1.00	.	.	.N....e	0.4088	PKS 1502+036
327	15.1005	37.5288	61.6860	59.9190	736	.	.	.	137	.	.	.	0.82	.	.	.	B.....e	0.6715	NVSS J150609+373051
328	15.1197	-16.7791	343.7360	35.1220	1558	1494	1108	.	174	221	211	.	1.03	1.07	1.10	.	BBN...We	0.8760	PKS 1504-167
329	15.1775	-5.6004	353.9620	43.0630	1176	1177	1176	.	173	212	211	.	1.01	1.02	1.05	.	BBB...We	1.1850	PKS 1508-05
330	15.2108	-9.0062	351.3260	40.2400	1902	1583	1942	1594	168	209	202	261	1.00	1.01	1.03	1.05	BBBB..We	0.3600	PKS 1510-08
331	15.2338	-10.2324	350.5840	39.1030	984	1140	.	.	166	221	.	.	1.03	1.07	.	.	NB....We	1.5130	PKS 1511-100
332	15.2442	-47.9509	326.2600	8.3280	1461	1504	1349	.	196	213	197	.	1.16	1.03	1.01	.	BBB.G..e	.	PMN J1514-4748
333	15.2795	0.2456	1.4000	45.9650	1549	1480	1350	1384	173	212	211	260	1.03	1.03	1.08	1.04	BBBB..We	0.0524	PKS 1514+00
334	15.2978	-24.3832	340.7080	27.5460	.	2233	2176	2107	.	232	210	258	.	1.19	1.08	1.05	.BBB..We	0.0486	PKS 1514-24
335	15.6374	-33.3284	338.6350	17.7380	1119	.	.	.	210	.	.	.	1.49	.	.	.	B.....u	.	...
336	15.6807	14.7778	24.3050	48.7880	1120	.	.	.	159	.	.	.	0.95	.	.	.	B.....We	0.6050	PKS 1538+149
337	15.8227	2.5453	10.7430	40.8910	2862	2916	2259	1681	177	206	185	255	1.05	1.00	0.95	1.02	BBBB...We	0.4144	PKS 1546+027
338	15.8256	50.6148	80.1970	49.0300	1024	.	943	.	158	.	164	.	0.93	.	0.84	.	B.B...We	2.1750	GB6 J1549+5038
339	15.8456	5.4431	14.2320	42.1940	2453	1926	1697	1955	177	206	185	255	1.05	1.00	0.95	1.02	BBBB..We	1.4220	PKS 1548+056
340	15.8939	13.0006	23.8710	45.2230	809	.	.	.	159	.	.	.	0.95	.	.	.	B.....e	1.2900	PKS 1551+130
341	15.9458	-79.2182	311.1820	-19.4490	913	.	.	.	171	.	.	.	1.02	.	.	.	B.....e	0.1501	PKS 1549-79
342	16.1514	10.4953	23.0860	40.7240	2145	2097	1735	1288	159	193	179	239	0.95	0.96	0.93	0.96	BBBB...We	1.2260	PKS 1606+10
343	16.2238	34.2067	55.1350	46.4310	4194	3498	3233	2872	174	218	182	231	1.03	1.06	0.93	0.92	BBBB..We	1.3971	GB6 J1613+3412
344	16.2527	-60.8553	325.3340	-7.1850	2739	1874	1302	.	199	207	204	.	1.18	1.04	1.04	.	BBB.G..e	0.0182	PKS 1610-60
345	16.3169	-77.2748	313.4880	-18.8930	2302	1853	1817	1427	171	185	165	220	1.02	0.90	0.84	0.88	BBBB..We	1.7100	PKS 1610-77
346	16.3452	-25.4865	351.3190	17.1500	.	3028	2084	.	.	296	248	.	.	1.45	1.26	.	.BB...u	.	...
347	16.4002	-68.1303	320.7410	-12.9630	790	.	.	.	156	.	.	.	1.18	.	.	.	N.....We	1.3600	PKS 1619-680
348	16.4297	-25.4600	352.1410	16.3190	.	.	2383	1780	.	.	252	278	.	.	1.29	1.11	..BB...e	0.7860	PKS 1622-253
349	16.4311	-29.8350	348.7990	13.3680	.	.	1320	1484	.	.	252	278	.	.	1.29	1.11	..BB...e	0.8150	PKS 1622-29
350	16.4320	-24.4003	352.9900	16.9990	.	6038	4574	.	.	296	248	.	.	1.44	1.26	.	.BB...g	.	IC 4603
351	16.5343	-24.7441	353.6750	15.7210	.	1736	1305	.	.	310	252	.	.	1.46	1.23	.	.BB...u	.	...

Table 3 – Continued

#	RA	δ	l	b	S_{23}	S_{33}	S_{41}	S_{61}	σ_{23}	σ_{33}	σ_{41}	σ_{61}	r_{23}	r_{33}	r_{41}	r_{61}	flags	z	Id.
352	16.5497	82.4571	115.6740	31.2250	1295	1428	1308	.	153	181	173	.	0.91	0.88	0.88	.	BBB...We	0.0247	NVSS J163226+823220
353	16.5922	38.0941	61.0360	42.2800	4078	4398	3831	3279	174	218	182	231	1.03	1.06	0.93	0.92	BBBB..We	1.8135	GB6 J1635+3808
354	16.6286	47.1918	73.3060	41.8910	1008	.	.	.	162	.	.	.	0.96	.	.	.	B....We	0.7400	GB6 J1637+4717
355	16.6420	57.4371	86.7520	40.3010	1354	1410	1450	1670	158	190	164	209	0.90	0.89	0.83	0.82	BBBB..We	0.7506	GB6 J1638+5720
356	16.6561	-24.3578	355.0900	14.6980	.	2851	1401	.	.	292	236	.	.	1.42	1.21	.	.BB...e	...	IRAS 16367-2356
357	16.7067	-6.3165	10.9180	24.9600	.	1349	1081	.	.	249	215	.	.	1.21	1.10	.	.BB...e	...	PMN J1642-0621
358	16.7171	68.9383	100.6640	36.5480	1552	1583	1771	1754	138	174	156	185	0.82	0.85	0.80	0.74	BBBB..We	0.7510	GB6 J1642+6856
359	16.7208	39.7646	63.3990	40.8950	6697	6039	5177	4426	187	220	191	239	1.11	1.07	0.96	0.96	BBBB..We	0.5928	GB6 J1642+3948
360	16.7318	-24.1514	355.9300	14.0260	.	1498	.	.	.	292	.	.	.	1.42	.	.	B....e	...	IRAS F16410-2355
361	16.7329	-77.2173	314.4610	-19.9210	987	976	852	.	171	185	165	.	1.02	0.90	0.84	.	BBB...We	0.0427	PKS 1637-77
362	16.8503	5.0211	23.0620	28.9860	1880	1386	1037	.	162	201	197	.	0.96	1.03	1.02	.	BBB...We	0.1540	Hercules A
363	16.8999	39.7658	63.6100	38.8360	1383	1054	.	.	156	189	.	.	0.93	0.92	.	.	BB....We	0.0336	GB6 J1653+3945
364	16.9606	57.1596	85.8100	37.8100	.	874	.	.	.	173	.	.	.	0.84	.	.	B....We	1.2810	GB6 J1657+5705
365	16.9609	47.9452	74.1170	38.5010	899	.	.	.	159	.	.	.	0.95	.	.	.	B....We	...	NVSS J165746+480832
366	16.9703	7.7005	26.7170	28.6400	1480	1282	1285	1302	162	201	197	248	0.96	0.98	1.00	0.99	BBBB..We	0.6210	PKS 1655+077
367	16.9812	5.2336	24.3200	27.3620	1098	.	.	.	206	.	.	.	1.23	.	.	.	B....We	0.8790	PKS 1656+053
368	17.0202	-56.4365	332.2630	-8.7620	1229	1071	.	.	195	202	.	.	1.16	0.98	.	.	BB.G..e	.	PMN J1701-5621
369	17.0540	-62.2795	328.0340	-12.4380	1511	1471	1699	1315	199	207	204	235	1.18	1.01	1.04	0.94	BBBB..We	.	PMN J1703-6212
370	17.1145	-14.2454	7.5010	15.5370	.	.	1106	.	.	.	204	.	.	.	1.13	.	.N...e	.	PMN J1707-1415
371	17.3396	-0.9466	21.2200	19.6830	5486	3629	3070	2078	206	224	204	257	1.23	1.09	1.04	1.03	BBBB...e	0.0304	PKS 1717-00
372	17.4041	-65.0056	327.0040	-15.8810	2421	1983	1482	.	199	207	204	.	1.18	1.01	1.04	.	BBB...We	0.0144	PKS 1718-649
373	17.4545	45.4876	71.4000	33.3110	829	1074	.	.	159	201	.	.	0.95	0.98	.	.	BB....We	0.7170	GB6 J1727+4530
374	17.4761	4.4496	27.3110	20.4430	.	1066	1054	.	.	200	204	.	.	1.09	1.04	.	.NB...e	0.2960	PKS 1725+044
375	17.5086	-21.5635	4.4350	6.8130	.	1544	1720	.	.	292	236	.	.	1.42	1.21	.	BB.G..g	.	PKS 1727-21
376	17.5346	-44.3789	345.4560	-5.9130	1409	.	.	.	245	.	.	.	1.45	.	.	.	B..G..u	...	...
377	17.5482	-13.0704	12.0210	10.8490	.	4656	4348	3230	.	249	221	277	.	1.21	1.13	1.11	BBB....e	0.9020	PKS 1730-13
378	17.5691	38.9557	64.0060	31.0440	1289	1239	1201	1402	156	189	172	228	0.93	0.92	0.88	0.91	BBBB..We	0.9700	GB6 J1734+3857
379	17.5924	-79.6365	313.6110	-23.3590	900	1032	937	.	171	186	165	.	1.02	0.90	0.84	.	BNB..We	.	PKS 1725-795
380	17.6129	6.4186	30.1630	19.5140	1148	1055	.	.	177	203	.	.	1.14	1.02	.	.	BB....e	1.2070	PKS 1734+063
381	17.6658	47.6842	74.2820	31.4030	879	.	982	.	159	.	170	.	0.95	.	0.88	.	B.N..We	.	GB6 J1739+4738
382	17.6758	52.1701	79.5330	31.7570	1214	1286	1248	1169	159	201	172	223	0.95	0.98	0.88	0.89	BBBB..We	1.3750	GB6 J1740+5211
383	17.7341	-3.7901	21.6390	13.1350	.	5345	5032	4111	.	252	217	260	.	1.23	1.11	1.04	BBB...e	1.0540	PKS 1741-03
384	17.7351	-51.6508	340.2200	-11.4020	1053	.	.	.	195	.	.	.	1.16	.	.	.	B....e	0.6300	PKS 1740-517
385	17.8106	70.1408	100.5750	30.7090	.	.	.	1085	.	.	.	185	.	.	.	0.74	...B..We	0.7700	GB6 J1748+7005
386	17.8592	9.6278	34.8990	17.6340	3992	4334	4320	4473	177	203	196	251	1.05	0.99	1.00	1.00	BBBB...e	0.3220	PKS 1749+096
387	17.8938	44.1043	70.6450	28.4800	834	.	.	.	159	.	.	.	0.94	.	.	.	B....We	0.8710	GB6 J1753+4410
388	17.8948	28.7739	54.1030	24.4550	2139	1876	2189	2285	144	185	164	218	0.86	0.90	0.84	0.87	BBBB..We	.	GB6 J1753+2847
389	17.9987	78.5072	110.0880	29.1020	2071	1693	1720	.	153	181	173	.	0.91	0.91	0.88	.	BBB...We	0.6800	NVSS J180045+782804
390	18.0081	38.9094	65.2830	26.0460	1028	.	895	.	154	.	161	.	0.92	.	0.86	.	B.N..We	2.0920	GB6 J1800+3848
391	18.0229	44.1562	71.0270	27.1310	1161	1314	1433	1478	154	194	172	213	0.92	0.94	0.88	0.85	BBBB..We	0.6630	GB6 J1801+4404
392	18.0331	-39.6756	352.3780	-8.3060	1861	1844	1692	1680	245	235	215	261	1.45	1.14	1.10	1.05	BBBBG..e	0.2960	PMN J1802-3940
393	18.0700	-64.9983	328.9900	-19.6500	1253	1186	1236	.	154	179	174	.	0.91	0.87	0.89	.	BBB...We	.	PKS 1758-651
394	18.1030	69.8509	100.1620	29.2240	1580	1436	1215	1123	138	174	156	185	0.82	0.85	0.80	0.74	BBBB..We	0.0510	GB6 J1806+6949
395	18.1667	-45.8368	347.5080	-12.4510	1376	1364	1099	.	245	235	215	.	1.45	1.14	1.10	.	BBB...e	0.0696	PKS 1806-458

Table 3 – Continued

#	RA	δ	l	b	S_{23}	S_{33}	S_{41}	S_{61}	σ_{23}	σ_{33}	σ_{41}	σ_{61}	r_{23}	r_{33}	r_{41}	r_{61}	flags	z	Id.
396	18.1976	6.7999	34.5460	11.8800	1048	.	.	.	206	.	.	.	1.23	.	.	.	B....g	.	GB6 J1812+0651
397	18.3235	-63.7526	330.8550	-20.7410	1805	1563	1034	1237	154	179	190	243	0.92	0.96	0.97	0.97	BBBB..We	0.0627	PKS 1814-63
398	18.3383	-55.3305	339.2370	-17.8450	961	.	.	.	155	.	.	.	1.04	.	.	.	B.....We	.	PKS 1815-553
399	18.4081	56.9080	85.8120	26.0420	1574	1392	1353	1413	152	193	168	219	0.90	0.94	0.86	0.86	BBBB..We	0.6640	GB6 J1824+5650
400	18.4339	-36.7950	357.1580	-11.2030	974	1075	.	1478	183	208	.	264	1.18	1.05	.	1.06	NN.B..e	.	PMN J1826-3651
401	18.5004	48.7335	77.2350	23.4220	2813	2652	2612	2031	152	193	168	219	0.90	0.94	0.86	0.88	BBBB..We	0.6920	GB6 J1829+4844
402	18.5589	-21.0858	12.1300	-5.6960	5080	4119	.	.	220	238	.	.	1.30	1.16	.	.	BB..G.e	2.5070	PKS 1830-21
403	18.5828	32.7618	61.3620	17.4870	858	.	.	.	144	.	.	.	0.86	.	.	.	B.....We	0.0578	GB6 J1835+3241
404	18.5863	-58.8535	336.4680	-20.9540	853	.	1139	.	155	.	190	.	0.92	.	0.97	.	B.B...We	.	PKS 1830-589
405	18.6339	-71.1287	323.7150	-24.4970	1603	1383	1271	.	154	179	174	.	0.91	0.87	0.89	.	BBB...We	1.3560	PKS 1831-711
406	18.7048	79.7730	111.4400	27.0680	1193	1000	955	.	164	185	172	.	0.94	0.92	0.87	.	BBB...We	0.0561	3C 390.3
407	18.7060	68.2236	98.6000	25.8820	1098	1141	1053	.	173	192	166	.	1.03	0.90	0.81	.	BBB...We	0.4720	GB6 J1842+6809
408	18.8085	32.4587	62.1940	14.7330	846	1037	1003	.	143	186	171	.	0.98	0.91	0.86	.	NBN...We	0.7980	GB6 J1848+3219
409	18.8275	67.1087	97.5140	25.0100	1367	1463	1331	1082	150	177	155	194	0.89	0.86	0.79	0.78	BBBB..We	0.6570	GB6 J1849+6705
410	18.8419	28.3263	58.4750	12.6810	1211	.	.	.	165	.	.	.	0.98	.	.	.	B.....We	2.5600	GB6 J1850+2825
411	19.0476	31.8831	62.9180	11.7250	1080	941	.	.	165	185	.	.	0.98	0.95	.	.	BN....We	0.6350	GB6 J1902+3159
412	19.1845	-20.1358	16.8460	-13.2060	2251	2299	2552	2316	220	238	215	283	1.30	1.14	1.10	1.11	BBBB...e	1.1190	PKS B1908-201
413	19.2973	-80.1582	314.0010	-27.8240	868	.	.	.	171	.	.	.	1.02	.	.	.	B.....We	0.3460	PKS 1910-80
414	19.3938	-21.1116	17.1530	-16.2880	2416	2446	2495	2540	220	238	215	283	1.30	1.16	1.10	1.12	BBBB..We	0.8740	PMN J1923-2104
415	19.4118	-29.2075	9.3660	-19.5650	.	.	10978	10133	.	.	256	327	.	.	1.17	1.10	..BB..We	0.3520	PKS J1924-2914
416	19.4505	73.9373	105.5780	23.5840	3368	3098	2531	2474	173	192	166	200	1.03	0.94	0.85	0.80	BBBB..We	0.3021	GB6 J1927+7357
417	19.4557	61.2947	92.7210	19.4660	1122	1002	1066	.	150	177	155	.	0.89	0.86	0.79	.	BBB...We	.	GB6 J1927+6117
418	19.5119	-60.8729	335.8950	-28.1770	808	.	.	.	145	.	.	.	0.92	.	.	.	N.....e	0.9650	PKS 1925-610
419	19.6162	-39.9382	359.1770	-25.3030	1211	1491	1445	.	174	211	201	.	1.04	1.02	1.03	.	BBB...We	1.6570	PKS 1933-400
420	19.6611	-15.4971	24.1250	-17.5170	1068	.	.	.	179	.	.	.	1.06	.	.	.	B.....We	0.1830	PKS 1936-15
421	19.6633	-63.7180	332.7420	-29.4320	948	.	.	.	154	.	.	.	0.92	.	.	.	B.....We	3.1540	PKS 1934-63
422	19.6867	-69.1415	326.5100	-29.6280	736	.	.	.	139	.	.	.	0.82	.	.	.	B......e	0.0590	PKS 1935-692
423	19.8715	2.5335	42.2910	-12.3080	963	.	.	.	165	.	.	.	0.98	.	.	.	B......We	.	PKS 1949+02
424	19.8868	40.1015	75.0300	6.4570	1852	.	.	.	185	.	.	.	1.10	.	.	.	B...G.u	0.0581	...
425	19.9643	-55.2309	342.6950	-31.3060	818	.	.	.	161	.	.	.	0.96	.	.	.	B......e	.	PKS 1954-55
426	19.9699	-38.7112	1.6340	-28.9870	3501	3585	2904	2479	178	215	201	260	1.06	1.05	1.03	1.04	BBBB..We	0.6300	PKS 1954-388
427	20.0173	-17.7994	24.0350	-23.1280	2176	1978	1814	1641	179	217	213	273	1.06	1.05	1.09	1.09	BBBB..We	0.6500	PKS 1958-179
428	20.0750	43.2256	78.8170	6.2600	.	2694	.	.	.	304	.	.	.	1.48	.	.	.B.G.u	.	...
429	20.1017	77.8118	110.4120	22.6790	926	953	878	.	173	185	172	.	1.00	0.90	0.88	.	BBB...We	0.3420	NVSS J200531+775243
430	20.1778	72.5384	105.4310	20.1500	869	1057	998	1019	173	192	166	184	1.03	0.94	0.85	0.80	BBBN..We	.	GB6 J2009+7229
431	20.1922	-15.8458	27.0690	-24.6870	1749	1511	1369	1401	179	217	213	273	1.06	1.05	1.09	1.09	BBBB..We	1.1800	PKS 2008-159
432	20.2776	45.7759	82.1520	5.8100	.	2482	.	.	.	304	.	.	.	1.48	.	.	.B.G.u	.	...
433	20.3605	61.5884	96.0270	13.8090	.	1304	1096	.	.	224	179	.	.	1.09	0.91	.	.BB...We	0.2270	GB6 J2022+6137
434	20.4159	17.1774	59.3520	-11.6970	.	1028	.	.	.	195	.	.	.	0.98	.	.	N....We	1.0500	GB6 J2024+1718
435	20.5778	-68.6947	326.3000	-34.4440	739	.	.	.	139	.	.	.	0.82	.	.	.	B.....We	.	PKS 2030-689
436	20.5903	10.8956	55.3700	-17.2690	.	1272	.	.	.	198	.	.	.	0.96	.	.	B......We	0.6010	PKS 2032+107
437	20.6465	51.3164	88.8220	6.0160	1359	1826	1832	1824	.	224	179	218	0.96	1.09	1.11	0.92	BBBG..e	1.6860	GB6 J2038+5119
438	20.8317	31.9118	74.8150	-7.6030	1961	1101	.	.	225	218	.	.	1.33	1.06	.	.	BB.G..g	.	NGC 6979
439	20.8456	29.1597	72.7530	-9.4600	.	.	.	.	225	.	.	.	1.33	.	.	.	B..G.u	.	...

Table 3 – Continued

#	RA	δ	l	b	S23	S33	S41	S61	σ23	σ33	σ41	σ61	r23	r33	r41	r61	flags	z	Id.
440	20.8712	55.4041	93.3070	6.9560	1152				224				1.09				B..G..e		[WB92] 2051+5507
441	20.9403	-47.2811	352.5440	-40.4050	2090	2278	2279	1853	158	192	180	232	0.94	0.93	0.92	0.93	BBBB..We	1.4890	PMN J2056-4714
442	20.9536	31.1171	75.1880	-9.3130			1089				193				0.99		..B.G..g		NGC 6995
443	21.0218	3.6775	52.6260	-26.5860	1038	999	1078		159	198	196		0.93	0.96	1.00		BBB..We	1.0130	PKS 2059+034
444	21.0303	-28.0284	17.7800	-39.6040	904				160				0.94				B.....e	0.0396	PKS 2058-28
445	21.1241	-25.4226	21.4740	-40.1850	977				166				0.97				B.....e	0.0388	PKS 2104-25
446	21.1518	35.6612	80.3070	-8.2140	1080				208				1.23				B...G.We	0.2023	GB6 J2109+3532
447	21.1631	-41.1539	0.7030	-42.8800	1555	1710	1364		162	206	192		0.96	1.00	0.98		BBB...We	1.0580	PKS 2106-413
448	21.2233	59.3034	98.1530	7.3730		1134				179				0.91			.B.G..u		...
449	21.2919	60.0141	99.0340	7.4840		1560	1498	1173		247	193	224		1.20	0.99	0.90	.BBBG..u		...
450	21.3978	25.1250	74.5390	-17.6780	923				153				0.91				B....We	0.1016	PKS 2121+24
451	21.4003	5.5659	58.0300	-30.1910	2092	1711	1705		200	275	207		1.19	1.33	1.06		BBB...We	1.8780	PKS 2121+053
452	21.5032	-9.3858	43.5370	-39.4280	954				186		263		1.13		1.09		B.N..e	0.7800	PKS 2127-096
453	21.5253	-12.0962	40.5540	-40.9310	2793	2262	2434	1447	186	230	214	280	1.10	1.12	1.10	1.12	BBBB..We	0.5010	PKS 2128-12
454	21.5719	-1.8700	52.4330	-36.5240	1970	1935	1633	1412	195	227	211	264	1.16	1.10	1.08	1.06	BBBB..We	1.2850	PKS 2131-021
455	21.6138	0.6962	55.5030	-35.6170	4771	3634	2909	1484	195	275	211	264	1.16	1.16	1.08	1.06	BBBB..We	1.9320	PKS 2134+004
456	21.6552	14.3900	72.1620	-27.5910	2105	1704	1686	1348	153	195	188	243	0.91	0.95	0.97	1.00	BBBN..We	2.4270	PKS 2136+141
457	21.7287	17.7587	73.3880	-27.0870	1163	1024			153	192			0.91	0.95			BN....We	0.2111	GB6 J2143+1743
458	21.7992	6.9911	63.6580	-34.0260	8227	7588	7542	6144	235	275	237	288	1.39	1.33	1.10	1.15	BBBB..We	0.9900	PKS 2145+06
459	21.8270	-78.0190	313.3560	-35.1450	1183	1068	996		160	191	174		0.95	0.93	0.89		BBB...We		PKS 2145-78
460	21.8668	-30.5180	16.9970	-50.8090	1483	1565	1442	1482	155	193	192	248	0.92	0.94	0.98	1.00	BBBB..We	2.3450	PKS 2149-306
461	21.8919	47.3551	94.4540	-5.4380				2058				323				1.29	...BG..g		GB6 J2153+4716
462	21.9609	-69.7154	321.2520	-40.6710	3838	2753	2408	1909	171	191	167	215	0.95	0.93	0.86	0.86	BBBB..We	0.0282	PKS 2153-69
463	21.9682	-15.0489	40.5970	-48.0310	2415	1861	1572		186	230	214		1.10	1.12	1.10		BBB...We	0.6720	PKS 2155-152
464	22.0505	42.2397	92.6120	-10.5060	3584	3205	3525	3050	211	215	185	224	1.25	1.05	0.95	0.90	BBBB..We	0.0686	GB6 J2202+4216
465	22.0515	-23.6537	28.5450	-51.9940	799				159				0.94				B.....e	2.1180	PKS 2200-238
466	22.0559	31.7154	85.9450	-18.8280	2577	2493	2192	1911	173	207	193	251	1.03	1.01	0.98	1.01	BBBB..We	0.2950	GB6 J2203+3145
467	22.0624	17.4343	75.7340	-29.6790	1586	1641	1523	1667	183	226	205	266	1.08	1.10	1.05	1.07	BBBB..We	1.0750	PKS 2201+171
468	22.1050	-18.6129	36.6530	-51.2000	1752	1603	1202		159	201	207		0.94	0.98	1.07		BBB...We	0.6185	PKS 2203-18
469	22.1235	-53.8256	339.8590	-49.8620	1176	928			145	180			0.86	0.89			BB....We	1.2060	PKS 2204-54
470	22.1961	23.8430	82.1190	-26.1050	1481	1469	1090		173	207	193		1.03	1.01	0.98		BBB...We	1.1250	PKS 2209+236
471	22.2157	-25.3092	26.6990	-54.5520	915				159				0.94				B....We	0.0624	PKS 2209-255
472	22.3164	-3.6735	58.9760	-46.7200	2495	2151	2012	1773	202	235	216	272	1.20	1.14	1.11	1.08	BBBB..We	0.9010	PKS 2216-03
473	22.3227	26.4378	85.4000	-25.1380	886				173				0.99				B.....u		...
474	22.3535	63.3287	106.9850	5.2080			3322	1606			383	310			1.23	0.97	..BBG..g		...
475	22.4255	21.2863	83.1270	-30.0850	890	1054			165	201			0.98	0.98			BB...We	1.9590	PKS 2223+21
476	22.4262	-4.9220	58.9460	-48.7830	4993	4970	4197	3549	202	235	216	272	1.20	1.14	1.11	1.09	BBBB..We	1.4040	PKS 2223-05
477	22.4941	-8.5035	55.2770	-51.6720	2097	2392	2377	2746	170	220	213	273	1.01	1.05	1.08	1.09	BBBB..We	1.5595	PKS 2227-08
478	22.4964	-20.9382	36.0030	-57.1810	948				159				0.94				B....Wg		PKS 2226-211
479	22.5303	65.3938	109.0610	6.3540		1897	1047			247	193			1.20	0.99		BB.G..u		...
480	22.5304	39.3176	95.5100	-16.0070	818				158				1.25				N....e	0.0170	87GB 222906.4+390556
481	22.5452	11.7543	77.4820	-38.5810	3620	4055	4124	4148	183	226	205	266	1.11	1.06	1.04	1.05	BBBB..We	1.0370	PKS 2230+11
482	22.5861	-48.5590	344.5600	-56.0750	2029	2231	2228	1774	145	185	178	221	0.86	0.90	0.91	0.89	BBBB..We	0.5100	PKS 2232-488
483	22.6012	28.4695	90.0470	-25.6230	1264	1155	1052		152	192	187		0.91	0.93	0.96		BBB..We	0.7950	GB6 J2236+2828

Table 3 – Continued

#	RA	δ	l	b	S_23	S_33	S_41	S_61	σ_23	σ_33	σ_41	σ_61	r_23	r_33	r_41	r_61	flags	z	Id.
484	22.6665	-56.8997	331.8500	-52.2080	943	1130	831	.	146	180	163	.	0.87	0.88	0.83	.	BBB...We	...	PKS 2236-572
485	22.7155	-25.7375	28.3220	-61.2760	819	.	.	.	159	.	.	.	0.94	.	.	.	B.....e	0.7740	PKS 2240-260
486	22.7680	-12.1059	53.8270	-57.0200	1838	1984	1844	.	170	220	213	.	0.98	1.07	1.08	.	BBB...We	0.6320	PKS 2243-123
487	22.7909	-36.9710	4.4780	-62.0970	904	.	.	.	155	.	.	.	0.96	.	.	.	N.....e	2.2520	PKS 2244-37
488	22.8976	16.1648	86.0960	-38.1560	7718	7758	7752	7808	224	245	225	298	1.24	1.19	1.08	1.16	BBBB..We	0.8590	PKS 2251+15
489	22.9296	42.0311	101.0080	-15.8640	966	.	.	.	149	.	.	.	0.89	.	.	.	B.....We	1.4760	GB6 J2255+4202
490	22.9355	-20.1048	41.6230	-62.7390	931	.	.	.	169	.	.	.	1.01	.	.	.	B.....We		PKS 2254-204
491	22.9723	-27.9425	24.4680	-64.9710	5311	4806	4716	4040	185	218	196	251	1.10	1.06	1.00	1.01	BBBB..We	0.9260	PKS 2255-282
492	23.0547	-68.0833	317.0610	-45.9650	.	.	886	.	.	.	167	.	.	.	0.85	.	.B..We	0.5120	PKS 2300-683
493	23.2452	-31.6529	14.9840	-68.4980	824	.	.	.	162	.	.	.	1.03	.	.	.	B.....e	1.3230	PKS 2312-319
494	23.2526	-50.2929	334.8270	-60.4510	.	939	941	.	.	180	168	.	.	0.88	0.83	.	.BN...We	.	PKS 2312-505
495	23.3477	5.3113	85.5330	-50.8640	847	.	.	.	162	.	.	.	0.96	.	.	.	B.....e	0.6220	PKS 2318+049
496	23.3568	27.4569	99.5110	-31.2880	871	.	.	.	166	.	.	.	0.99	.	.	.	B.....e	1.2530	GB6 J2322+2732
497	23.3885	51.0476	109.1000	-9.4420	856	.	877	.	149	.	162	.	0.89	.	0.86	.	B.N.G.We	.	NVSS J232226+505752
498	23.3924	-3.2429	77.7980	-58.1910	923	.	.	.	162	.	.	.	0.96	.	.	.	B.....e	1.4100	PKS 2320-035
499	23.4523	9.6979	91.0260	-47.8830	1047	1686	1207	.	192	211	199	.	1.07	1.01	1.01	.	BBB...We	1.8430	PKS 2325+093
500	23.4526	-14.8498	60.7290	-66.8690	951	1093	.	.	163	209	.	.	0.97	1.02	.	.	BB....e	2.4650	PKS 2325-150
501	23.4898	-47.5185	335.6810	-47.2800	1108	967	1220	.	163	191	184	.	0.97	0.93	0.94	.	BBB...We	1.2990	PKS 2326-477
502	23.5114	10.8371	92.9560	-47.0570	966	.	.	.	155	.	.	.	1.07	.	.	.	B.....We	1.4890	PKS 2328+10
503	23.5283	-15.8844	60.1550	-68.3590	1179	.	.	.	163	.	.	.	0.97	.	.	.	B.....We	1.1530	PKS 2329-16
504	23.5713	-23.6804	39.8480	-72.2570	842	.	.	.	162	.	.	.	1.01	.	.	.	N.....We	0.0477	PKS 2331-240
505	23.5727	7.6570	91.9710	-50.5230	1140	1129	1211	.	170	209	.	241	1.01	1.01	.	1.01	BN.N..We	0.4010	PMN J2334+0736
506	23.5854	-1.5781	84.1240	-58.5770	.	1224	1034	.	.	213	201	.	.	1.03	0.98	.	.BN...We	1.1840	PKS 2332-017
507	23.5940	-52.7195	326.6870	-60.7720	1111	.	.	.	146	.	.	.	0.87	.	.	.	B.....We	.	PKS 2333-528
508	23.7807	9.4530	97.5480	-50.2080	1152	1051	.	.	155	206	.	.	0.92	1.00	.	.	BB....We	0.6770	PKS 2344+09
509	23.8059	-16.5037	65.7270	-71.9400	1817	1762	1822	1638	163	209	205	261	0.97	1.02	1.04	1.03	BBBB..We	0.6000	PKS 2345-16
510	23.8329	38.8641	110.0310	-22.4630	812	915	1094	.	154	172	.	.	0.94	0.90	.	.	B.....We	1.0320	87GB 234649.1+383240
511	23.8876	81.7981	120.7580	19.1730	.	.	.	.	.	172	.	.	.	0.90	.	.	N.....We	1.3440	NVSS J235622+815252
512	23.9031	45.8584	112.6210	-15.8640	1620	1098	1094	.	166	202	198	.	0.99	0.98	1.01	.	BBB...We	1.9920	GB6 J2354+4553
513	23.9151	68.1014	117.6800	5.8080	.	.	.	1423	.	.	.	250	.	.	.	1.35	...BG..e	.	87GB 235426.3+673455
514	23.9653	-53.2446	320.1220	-62.0610	1326	1082	1204	.	159	187	173	.	0.93	0.92	0.88	.	BBB...We	1.0060	PKS 2355-534
515	23.9692	-10.3014	83.6770	-69.0070	1171	.	.	.	172	.	.	.	1.02	.	.	.	B.....We	1.6391	PKS 2355-106
516	23.9874	-60.8690	314.0140	-55.1220	1909	1345	1030	.	153	192	168	.	0.91	0.93	0.86	.	BBB...We	0.0963	PKS 2356-61